

UNIVERSITY OF OKLAHOMA

GRADUATE COLLEGE

THE PREDICTION AND ASSIMILATION OF POLARIMETRIC RADAR DATA
USING ENSEMBLE-BASED METHODS

A DISSERTATION

SUBMITTED TO THE GRADUATE FACULTY

in partial fulfillment of the requirements for the

Degree of

DOCTOR OF PHILOSOPHY

By

BRYAN JAMES PUTNAM

Norman, Oklahoma

2016

THE PREDICTION AND ASSIMILATION OF POLARIMETRIC RADAR DATA
USING ENSEMBLE-BASED METHODS

A DISSERTATION APPROVED FOR THE
SCHOOL OF METEOROLOGY

BY

Dr. Ming Xue, Chair

Dr. Guifu Zhang

Dr. Youngsun Jung

Dr. Howard Bluestein

Dr. S. Lakshmivarahan

Dedication

This dissertation is dedicated to JP.

Acknowledgements

I would first like to thank my advisors, Dr. Ming Xue and Dr. Guifu Zhang. I sincerely appreciate the opportunity they have given me to advance both my education and career and complete a life-long goal during both my master's degree and doctorate. I can still remember the first time I met with Dr. Xue prior to graduate school, and the research examples he showed me of convective-scale modeling were exactly what I was looking to do as a research assistant. This area of research is current and very relevant and I am thankful they chose me to further it. Not only have they given me the guidance and means to grow as a scientist through my research, but they have also provided me with several opportunities outside of school to travel and present my work at conferences. A trip to Japan, and others, are life experiences I did not imagine sharing when I first began as a graduate student. I will be forever grateful.

Second, I thank Dr. Youngsun Jung. Youngsun has always been available for help and advice. I would have never been able to get started on my research without her. I reflect back to when I first began and recall all the things I didn't know about different research subjects and the ARPS model and see how much I have learned in 7 years. The best measure of my growth is how often I no longer need to ask questions.

Third, I thank my additional committee members, Dr. Howie Bluestein and Dr. S Lakshmivarahan. I am thankful for their guidance and time in pursuing my degree. I also appreciate what I learned in their classes and the relationships I developed with them during this time, which played a significant role in why I wanted them as committee members. I was able to take all three classes Dr. Bluestein offers, which contributed to my education in synoptic, mesoscale, and convective-scale meteorology.

All three subjects are among my favorites, and the classes provided a complete summary of elements necessary for forecasting convection. I also learned a great deal about data assimilation in Dr. Lakshmivarahan's class which furthered my understanding of my primary area of research.

I would also like to thank Dr. Nate Snook. Nate has provided countless hours of aid for addressing problems with my research, setting up experiments, and reviewing my written work. Out of all his support, the help with assembling publication quality figures will be what I most remember, which can sometimes be the most challenging aspect of putting together a paper. I am thankful for the many times he helped me when he had no obligation to do so.

I thank the secretaries and professional assistants that have helped me with my classes, schedules, requirements, and travel. This includes Marcia Pallutto, Celia Jones, Christie Upchurch, Jo Ann Mehl, Krysta Bruehl, Lauren White, Kacie Shoemaker, Debra Farmer, and Eileen Hasselwander. I transferred between research groups multiple times and never had to do anything because of their efficient work. I would also like to thank Chris Cook for swift expert technical support.

Finally, I must thank both my family and friends. I thank my parents, Jim and Peggy Putnam, and sister Stephanie Putnam, for their unconditional love and support, especially during the rough times. Graduate school can be very stressful and they were always ready to help with any other burdens or problems I encountered. I am also very thankful for my friends, both inside and outside the program. Inside the program, Vivek Mahale, Derek Stratman, Jim Kurdzo, Jennifer Newman, Tim Bonin, and Chris Schwarz, and I have been together throughout graduate school. They were always very

supportive and helpful as we worked and succeeded together in class and in research. The time outside of school we spent together, more often than not laughing, was also a significant stress reliever. My friends outside of school, including Brandon Lawson, Brett Wallace, Kristina Wallace, Matt Neville, and Emmale Davis mattered more to me than they will ever know, if for so much as providing a way to leave my troubles or struggles behind for a while and enjoy life.

The funding for this research was provided by National Science Foundation (NSF) grant AGS-1046171 and National Oceanic and Atmospheric Administration (NOAA) grant NA11OAR4320072. Computing resources were provided from Extreme Science and Engineering Discovery Environment (XSEDE) services and included the National Institute for Computational Sciences (NICS) Kraken supercomputer and the Texas Advanced Computing Center (TACC) Stampede supercomputer.

Table of Contents

Acknowledgements	iv
Table of Contents	vii
List of Tables	x
List of Figures.....	xi
Abstract	xxiii
Chapter 1 Introduction	1
1.1 Background.....	1
1.2 Dissertation Overview	6
Chapter 2 Simulation of Polarimetric Radar Variables and Evaluation of Microphysics Schemes in Ensemble Forecasts	10
2.1 Introduction	10
2.2 Methodology	15
2.2.1 Overview of the 2013 CAPS SSEF	15
2.2.2 Polarimetric simulation and general experiment settings	17
2.2.3 Spring experiment microphysics schemes	18
2.2.4 Polarimetric radar observations	20
2.3 Evaluation of simulation results.....	22
2.3.1 The 20 May 2013 mesoscale convective system case	24
2.3.1.1 Qualitative evaluation of forecasts.....	24
2.3.1.2 Quantitative evaluation of forecasts.....	33
2.3.2 The 20 May 2013 supercell case	42
2.3.2.1 Qualitative evaluation of forecasts.....	43
2.3.2.2 Quantitative evaluation of forecasts.....	48
2.4 Summary and conclusions.....	53
Chapter 3 Probabilistic Prediction of Polarimetric Radar Variables in EnKF- Initialized Ensemble Forecasts of a Mesoscale Convective System	57
3.1 Introduction	57
3.2 Experimental case and method	63

3.2.1 System overview.....	63
3.2.2 Forecast model settings.....	65
3.2.3 Data sources	66
3.2.4 Ensemble Kalman filter settings.....	67
3.2.5 Microphysics schemes used and their configurations	68
3.3 Results of experiments.....	69
3.3.1 Ensemble forecasts of radar reflectivity	70
3.3.1.1 Qualitative evaluation of reflectivity mosaics	70
3.3.1.2 Probabilistic forecasts for reflectivity	72
3.3.1.3 Quantitative evaluation of reflectivity forecasts.....	76
3.3.2 Ensemble forecasts of polarimetric variables.....	81
3.3.2.1 Qualitative evaluation of predicted polarimetric variables	81
3.3.2.2 Probabilistic forecasts of polarimetric variables.....	87
3.3.2.3 Quantitative verification of polarimetric variables	88
3.4 Summary and conclusions.....	92
 Chapter 4 Assimilation of Polarimetric Radar Data using EnKF: Experiment Setup and Sensitivity Testing.....	 97
4.1 Introduction.....	97
4.2 Overview of case studies.....	104
4.2.1 The 20 May 2013 New Castle-Moore, OK tornadic supercell case	104
4.2.2 The 10 May 2010 Moore-Harrah, OK and Norman-Pink, OK tornadic supercells case	105
4.3 Method	108
4.3.1 Prediction model and microphysics scheme	109
4.3.2 Experiment configuration and EnKF settings	110
4.3.2.1 20 May 2013 experiment configuration	110
4.3.2.2 10 May 2010 experiment configuration	114
4.3.3 Dual-pol observation assimilation settings	119
4.3.4 Radar data processing	120
4.3.5 Observation operators	121
4.4 Dual-pol assimilation sensitivity tests	124
4.4.1 The 20 May 2013 tornadic supercells case	126
4.4.1.1 Observation assimilation order	126
4.4.1.2 Model error treatment methods	127
4.4.1.3 Radar configuration.....	135
4.4.1.4 Radar observation filtering	138
4.4.2 The 10 May 2010 tornadic supercells case	144
4.4.2.1 Model error treatment methods	145
4.4.2.2 Radar observation filtering	149

4.5 Conclusions	153
Chapter 5 Assimilation of Polarimetric Radar Data using EnKF: Evaluation of Analyses	156
5.1 Introduction	156
5.2 The 20 May 2013 tornadic supercells case.....	157
5.2.1 Evaluation of analyzed dual-pol variables	157
5.2.2 Evaluation of model microphysical state	161
5.3 The 10 May 2010 tornadic supercells case.....	167
5.3.1 Evaluation of analyzed dual-pol variables	168
5.3.2 Evaluation of model microphysical state	172
5.4 Summary and conclusions.....	177
Chapter 6 Summary and Conclusions	179
6.1 Summary.....	179
6.2 Future work	186
References.....	189
Appendix A Example Calculation of Forward Operator for Polarimetric Radar Observation Assimilation	205

List of Tables

Table 2.1. Reference table for which predicted model variables are used to calculate the intercept (N_0) and shape (α) parameters for rain (r), snow (s), graupel (g), and hail (h) from each of the microphysics scheme considered. The values are either fixed and listed, or calculated as a function of mixing ratio (q), number concentration (N_i), and/or air temperature (T). Schemes which do not contain a given hydrometeor category are listed as not applicable (NA).

Table 4.1. Table of radar volume start times for each assimilation cycle for the 20 May 2013 case.

Table 4.2. Table of conventional observation error values for both the 20 May 2013 and 10 May 2010 experiments.

Table 4.3 Table of radar volume start times for each assimilation cycle for the 10 May 2010 case.

Table 4.4. Table of calculated average RMSEs over the assessment window period for both the Z_{DR} and lowest tilt domains for the 20 May 2013 case. Blue cells indicate RMSEs lower than the control experiment and orange cells indicate RMSEs higher than the control experiment.

Table 4.5. Table of calculated average RMSEs over the assessment window period for both the Z_{DR} and lowest tilt domains for the 10 May 2013 case. Blue cells indicate RMSEs lower than the control experiment and orange cells indicate RMSEs higher than the control experiment.

List of Figures

Fig. 2.1. Model domain for 2013 CAPS Spring Experiment storm scale ensemble forecasts.

Fig. 2.2. Mosaics of observed (a) reflectivity (dBZ), (b) differential reflectivity (dB), and (c) specific differential phase ($^{\circ} \text{ km}^{-1}$) at a $.5^{\circ}$ tilt before ground clutter/biological scatterer removal and (d-f) after. The locations of the WSR-88D radars used are included as black dots in (a).

Fig. 2.3. Mosaics of observed (a) reflectivity (dBZ), (b) differential reflectivity (dB), and (c) specific differential phase ($^{\circ} \text{ km}^{-1}$) at a $.5^{\circ}$ tilt 0400 UTC 20 May 2013 and simulated values at the same tilt locations from the (d-f) TOM, (g-i) MY, (j-l) MOR, (m-o) WDM, and (p-r) WSM forecasts. Features of interest referenced in the text are noted by arrows. Locations of WSR-88D sites used for both the observed and simulated variable plots are noted with black dots in (a).

Fig. 2.4. Mosaic of hydrometeor classification using fuzzy logic for (a) observations at a $.5^{\circ}$ tilt 0400 UTC 20 May 2013 as well as classification of highest simulated linear reflectivity at the same tilt locations for (b) TOM, (c) MY, (d) MOR, (e) WDM, and (f) WSM forecasts. Features of interest referenced in the text are noted by arrows. Locations of WSR-88D sites used for both the observed and simulated variable plots are noted with black dots in (a).

Fig. 2.5. Histograms of observed (a) reflectivity (dBZ), (b) differential reflectivity (dB), and (c) specific differential phase ($^{\circ} \text{ km}^{-1}$) mosaic values at a $.5^{\circ}$ tilt from Fig. 3 as well as percentile histograms of simulated values at the same tilt locations from the (d-f) TOM, (g-i) MY, (j-l) MOR, (m-o) WDM, and (p-r) WSM

forecasts distributed into bins based on the observed percentiles (noted by the solid black line)

Fig. 2.6. Scatter plot of (a) observed reflectivity (dBZ) and differential reflectivity (dB) mosaic values at a $.5^\circ$ tilt from Fig. 3 as well as scatter plots of simulated values at the same tilt locations from the (b) TOM, (c) MY, (d) MOR, (e) WDM, and (f) WSM forecasts.

Fig. 2.7. Fractions skill scores for the TOM, MY, MOR, WDM, and WSM forecast results at increasing neighborhood radii for (a) reflectivity values exceeding 15 dBZ, (b) reflectivity values exceeding 40 dBZ, (c) differential reflectivity values exceeding 2.5 dB, and (d) specific differential phase values exceeding $0.6^\circ \text{ km}^{-1}$ for the mosaics in Fig. 3. The black line indicates skill greater than a random forecast.

Fig. 2.8. As in Fig. 7, but with the FSS scores calculated based on percentile values relative to the observations.

Fig. 2.9. Mosaics of observed (a) reflectivity (dBZ), (b) differential reflectivity (dB), and (c) specific differential phase ($^\circ \text{ km}^{-1}$) at a $.5^\circ$ tilt 2100 UTC 20 May 2013 and simulated values at the same tilt locations from the (d-f) TOM, (g-i) MY, (j-l) MOR, (m-o) WDM, and (p-r) WSM forecasts. Features of interest referenced in the text are noted by arrows, numbers, and letters. Locations of WSR-88D sites used for both the observed and simulated variable plots are noted with black dots in (a).

Fig. 2.10. Mosaic of hydrometeor classification using fuzzy logic for (a) observations at a $.5^\circ$ tilt 2100 UTC 20 May 2013 as well as classification of highest simulated

linear reflectivity at the same tilt locations for (b) TOM, (c) MY, (d) MOR, (e) WDM, and (f) WSM forecasts. Features of interest referenced in the text are noted by arrows. Locations of WSR-88D sites used for both the observed and simulated variable plots are noted with black dots in (a).

Fig. 2.11. 2D plots of maximum updraft helicity ($\text{m}^2 \text{s}^{-2}$) at 2100 UTC 20 May 2013 for (a) TOM, (b) MY, (c) MOR, (d) WDM, and (e) WSM. Features of interest referenced in the text are noted by arrows.

Fig. 2.12. Histograms of observed (a) reflectivity (dBZ), (b) differential reflectivity (dB), and (c) specific differential phase ($^{\circ} \text{km}^{-1}$) mosaic values at a $.5^{\circ}$ tilt from Fig. 9 as well as percentile histograms of simulated values at the same tilt locations from the (d-f) TOM, (g-i) MY, (j-l) MOR, (m-o) WDM, and (p-r) WSM forecasts distributed into bins based on the observed percentiles (noted by the solid black line).

Fig. 2.13. Fractions skill scores for the TOM, MY, MOR, WDM, and WSM forecast results at increasing neighborhood radii for (a) reflectivity values exceeding 15 dBZ, (b) differential reflectivity values exceeding 2.5 dB, and (c) specific differential phase values exceeding $0.4^{\circ} \text{km}^{-1}$ for the mosaics in Fig. 9. The black line indicates skill greater than a random forecast.

Fig. 2.14. As in Fig. 13, but with the FSS scores calculated based on percentile values relative to the observations.

Fig. 3.1. Mosaic of observed reflectivity (dBZ) from KAMA, KDYX, KFWS, KLBB, KTLX, and KVNK at 0200 UTC at about 2 km above ground. The locations of all radars assimilated are marked. Also, notable MCS features including the line

end vortex (LEV), leading convective line, leading stratiform region, and trailing stratiform region are given. Reproduced from Putnam et al. (2014).

Fig. 3.2. Mosaic of (a,d,g) observed reflectivity (dBZ) as in Fig. 1 as well as probability matched ensemble mean reflectivity for (b) EXP_S and (c) EXP_D at 0300 UTC/1-h forecast, (d-f) 0400 UTC/2-h forecast, and (g-f) 0500 UTC/3-h forecast.

Fig. 3.3. Probability of reflectivity exceeding 20 dBZ at 2 km AGL for EXP_S at (a) 1 h, (b) 2 h, and (c) 3 h forecast times and (d-f) EXP_D. The thick black line outlines observed reflectivity exceeding 20 dBZ.

Fig. 3.4. Probability of reflectivity exceeding 40 dBZ at 2 km AGL for EXP_S at (a) 1-h, (b) 2-h, and (c) 3-h forecast times and (d-f) EXP_D. The thick black line outlines observed reflectivity exceeding 40 dBZ.

Fig. 3.5. Area under the relative operating characteristic curve (AUC) for EXP_S (red line and shading) and EXP_D (blue line and shading) at (a) 1-h, (b) 2-h, and (c) 3-h forecast times at 2 km AGL for the full experiment domain and also (d-f) a subdomain covering Oklahoma.

Fig. 3.6. Reliability diagrams calculated for reflectivity exceeding 20 dBZ for EXP_S (red line) and EXP_D (blue line) at (a) 1-h, (b) 2-h, and (c) 3-h forecast times at 2 km AGL for the full experiment domain and also (d-f) a subdomain covering Oklahoma.

Fig. 3.7. Sharpness diagrams calculated for reflectivity exceeding 20 dBZ for EXP_S (red) at (a) 1-h, (b) 2-h, and (c) 3-h forecast times and (d-f) EXP_D (blue) at 2

km AGL for the full experiment domain and also (g-l) a subdomain covering Oklahoma.

Fig. 3.8. (a) Observed reflectivity (dBZ) and simulated reflectivity from (b) EXP_S and (c) EXP_D at 0300 UTC/1-h forecast at a 0.5° tilt from KOUN, as well as (d-f) differential reflectivity (dB) and (g-i) specific differential phase ($^\circ\text{km}^{-1}$).

Fig. 3.9. As in Fig. 8 but at 0400 UTC with 2-h forecast results.

Fig. 3.10. As in Fig. 8 but at 0500 UTC with 3-h forecast results.

Fig. 3.11. (a) Observed reflectivity (dBZ) and simulated reflectivity from (b) EXP_S member 14 and (c) EXP_D member 39 at 0400 UTC/2-h forecast at a 0.5° tilt from KOUN, as well as observed (d) and simulated (e-f) differential reflectivity (dB).

Fig. 3.12. Probability of differential reflectivity exceeding 2.3 dB at a 0.5° tilt for EXP_S at (a) 1-h, (b) 2-h, and (c) 3-h forecast times and for (d-f) EXP_D.

Fig. 3.13. Area under the relative operating characteristic curve (AUC) for differential reflectivity (dB) for EXP_S (red line and shading) and EXP_D (blue line and shading) at (a) 1-h, (b) 2-h, and (c) 3-h forecast times at a 0.5° tilt as well as for (d-f) specific differential phase ($^\circ\text{km}^{-1}$).

Fig. 3.14. Histograms of observed (black) KOUN and simulated reflectivity (dBZ) values from EXP_S (red) and EXP_D (blue) at (a) 0300, (b) 0400, and (c) 0500 UTC at a 0.5° tilt as well as (d-f) observed and simulated differential reflectivity (dB) values and (g-i) observed and simulated specific differential phase ($^\circ\text{km}^{-1}$) values. The values in EXP_S and EXP_D are normalized by the size of each ensemble.

Fig. 4.1. (a) 500 mb wind barbs, wind fields (colorfill, 20 knot interval), height contours (60-dam interval), and air temperature (red dashed lines, 2 ° C intervals) as well as (b) Mixed layer CAPE (red contours) and CIN (colorfill) (J kg^{-1}) analyses from the Storm Prediction Center (SPC) at 2000 UTC 20 May 2013.

Fig. 4.2. (a) 2100 UTC 10 May 2010 and (b) 0000 UTC 11 May 2010 Storm Prediction Center surface analyses. Note the marked locations of the warm front, dryline, cold front, and surface low.

Fig. 4.3. Norman Weather Service Office tornado damage survey paths from 10 May 2010 tornado outbreak.

Fig. 4.4. 20 May 2013 experiment domain and location of radars included. Observed reflectivity (Z , dBZ) at the 0.5 ° tilt from KTLX at 1938 UTC 20 May 2013 is included.

Fig. 4.5. Diagram of experiment timeline including the spin-up forecast, assimilation window, 30 minute assessment period, and times of tornadoes from the storms of interest.

Fig. 4.6. 10 May 2010 experiment domain and location of radars included. Observed reflectivity (Z , dBZ) at the 0.5 ° tilt from KOUN at 2250 UTC 10 May 2010 is included.

Fig. 4.7. Diagram of experiment timeline including the spin-up forecast, assimilation window, 30 minute assessment period, and times of tornadoes from the storms of interest.

Fig. 4.8. Time plot of analyzed (a) Z (dBZ) and (b) Z_{DR} (dB) RMSE values calculated over the Z_{DR} domain for experiments CZZDR and OZZDR over the assessment window (1930 – 2000 UTC).

Fig. 4.9. (a) Reflectivity (dBZ) and (b) differential reflectivity (dB) at the 0.5° tilt from KTLX at 1938 UTC as well as from the ensemble mean analyses of experiments (c-d) CZZDR and (e-f) OZZDR at 1940 UTC.

Fig 4.10. Time plot of analyzed Z (dBZ) RMSE values for the (a-b) Z_{DR} domain and (b-c) lowest tilt domain and analyzed Z_{DR} (dB) RMSE values for the (e-f) Z_{DR} domain and (g-h) lowest tilt domain calculated over the assessment window (1930 – 2000 UTC) for the model error treatment experiments.

Fig. 4.11. (a) Reflectivity (dBZ) and (b) differential reflectivity (dB) at the 0.5° tilt from KTLX at 1938 UTC as well as from the ensemble mean analyses of experiments (c-d) CZ and (e-f) MZ and (g-h) PZ at 1940 UTC.

Fig. 4.12. (a) Reflectivity (dBZ) and (b) differential reflectivity (dB) at the 0.5° tilt from KTLX at 1938 UTC as well as from the ensemble mean analyses of experiments (c-d) CZZDR and (e-f) MZZDR and (g-h) PZZDR at 1940 UTC.

Fig 4.13. Time plot of analyzed Z (dBZ) RMSE values for the (a-b) ZDR domain and (b-c) lowest tilt domain and analyzed ZDR (dB) RMSE values for the (e-f) ZDR domain and (g-h) lowest tilt domain calculated over the assessment window (1930 – 2000 UTC) for the radar configuration experiments.

Fig. 4.14. (a) Reflectivity (dBZ) and differential reflectivity (dB) at the 0.5° tilt from KTLX at 1934 UTC as well as from the ensemble mean analyses of experiments (c-d) CZ and (e-f) RCZ at 1935 UTC.

Fig. 4.15. (a) Reflectivity (dBZ) and (b) differential reflectivity (dB) at the 0.5° tilt from KTLX at 1934 UTC as well as from the ensemble mean analyses of experiments (c-d) CZZDR and (e-f) RCZZDR at 1935 UTC.

Fig 4.16. Time plot of analyzed Z (dBZ) RMSE values for the (a-b) Z_{DR} domain and (b-c) lowest tilt domain and analyzed Z_{DR} (dB) RMSE values for the (e-f) Z_{DR} domain and (g-h) lowest tilt domain calculated over the assessment window (1930 – 2000 UTC) for the radar filtering experiments.

Fig. 4.17. (a) Reflectivity (dBZ) and (b) differential reflectivity (dB) at the 0.5° tilt from KTLX at 1938 UTC and from the ensemble mean analysis of (c-d) CZ at 1940 UTC as well as the filtered (e) reflectivity and (f) differential reflectivity from KTLX and the ensemble mean analysis of (g-h) RFZ.

Fig. 4.18. (a) Reflectivity (dBZ) and (b) differential reflectivity (dB) at the 0.5° tilt from KTLX at 1938 UTC and from the ensemble mean analysis of (c-d) CZZDR at 1940 UTC as well as the filtered (e) reflectivity and (f) differential reflectivity from KTLX and the ensemble mean analyses of (g-h) RFZZDR and (i-j) RFREZZDR.

Fig 4.19. Time plot of analyzed Z (dBZ) RMSE values for the (a-b) Z_{DR} domain and (b-c) lowest tilt domain and analyzed Z_{DR} (dB) RMSE values for the (e-f) Z_{DR} domain and (g-h) lowest tilt domain calculated over the assessment window (2230 – 2301 UTC) for the model error treatment experiments.

Fig. 4.20. (a) Reflectivity (dBZ) at the 0.5° tilt from KTLX at 2246 UTC and (b) differential reflectivity (dB) from KOUN at 2246 UTC as well as from the ensemble mean analyses of experiments (c-d) CZ and (e-f) PZ at 2248 UTC.

Fig. 4.21. (a) Reflectivity (dBZ) at the 0.5° tilt from KTLX at 2246 UTC and (b) differential reflectivity (dB) from KOUN at 2246 UTC as well as from the ensemble mean analyses of experiments (c-d) CZZDR and (e-f) PZZDR at 2248 UTC.

Fig 4.22. Time plot of analyzed Z (dBZ) RMSE values for the (a-b) Z_{DR} domain and (b-c) lowest tilt domain and analyzed Z_{DR} (dB) RMSE values for the (e-f) Z_{DR} domain and (g-h) lowest tilt domain calculated over the assessment window (2230 – 2301 UTC) for the radar filtering experiments.

Fig. 4.23. (a) Reflectivity (dBZ) at the 0.5° tilt from KTLX at 2246 UTC and (b) differential reflectivity (dB) from KOUN at 2246 UTC and from the ensemble mean analysis of (c-d) CZ at 2248 UTC as well as the filtered (e) reflectivity and (f) differential reflectivity from KTLX and KOUN and the ensemble mean analyses of (g-h) RFZ.

Fig. 4.24. (a) Reflectivity (dBZ) at the 0.5° tilt from KTLX at 2246 UTC and (b) differential reflectivity (dB) from KOUN at 2246 UTC and from the ensemble mean analysis of (c-d) CZZDR at 2248 UTC as well as the filtered (e) reflectivity and (f) differential reflectivity from KTLX and KOUN and the ensemble mean analyses of (g-h) RFZ and (i-j) RFREZZDR.

Fig. 5.1. (a) Reflectivity and (b) differential reflectivity (dB) at the 0.5° tilt from KTLX at 1938 UTC as well as from the ensemble mean analyses of (c-d) M20Z and (e-f) M20ZZDR at 1940 UTC.

Fig. 5.2. (a) Reflectivity (dBZ) and (b) differential reflectivity (dB) at the 0.5° tilt from KTLX at 1938 UTC and the difference between the (c) analysis reflectivity and

the observations and (d) differential reflectivity and the observations for M20Z and (e-f) M20ZZDR at 1940 UTC.

Fig. 5.3. (a) Differential reflectivity (dB) at the 0.5° tilt from KTLX at 1938 UTC and difference in differential reflectivity between (b) M20Z and M20ZZDR at 1940 UTC.

Fig. 5.4. (a) Differential reflectivity (dB) at the 0.5° tilt from KTLX at 1938 UTC as well as mean mass diameter (mm) at the first model level above the surface for the ensemble mean analysis of (b) M20Z and (c) M20ZZDR at 1940 UTC. Reflectivity contours are overlaid on the mean mass diameter plots in 20 dBZ intervals.

Fig. 5.5. (a) Differential reflectivity at the 0.5° tilt from KTLX at 1938 UTC as well as rain intercept parameter (mm^{-4} , 10Log_{10} scale) at the first model level above the surface for the ensemble mean analysis of (b) M20Z and (c) M20ZZDR at 1940 UTC. Reflectivity contours are overlaid on the intercept parameter plots in 20 dBZ intervals.

Fig. 5.6. Individual rain DSDs at each model grid point from the first level above surface for (a) M20Z and (b) M20ZZDR at 1940 UTC as well as (c) simulated and (d) analyzed differential reflectivity reference images from M20Z and M20ZZDR as plotted from the 0.5° tilt of KTLX with a black box indicating the region from which the DSDs are included.

Fig. 5.7. As in Fig. 5.6, but for a different reference area indicated by the black box in (c-d).

Fig. 5.8. (a) Retrieved rain intercept parameter values (mm^{-4} , 10Log_{10} scale) from KTLX observations at the 0.5° tilt as well as calculated rain intercept parameter values at the first model level above the surface for the ensemble mean analysis of (b) M20Z and (c) M20ZZDR at 1940 UTC. Reflectivity contours are overlaid on the intercept parameter plots in 20 dBZ intervals. Also, (d) observed differential reflectivity from the 0.5° tilt of KTLX and (e) hydrometeor classifications of the observations from KTLX.

Fig. 5.9. (a) Reflectivity (dBZ) and (b) differential reflectivity (dB) at the 0.5° tilt from KOUN at 2246 UTC as well as from the ensemble mean analyses of (c-d) M10Z and (e-f) M10ZZDR at 2248 UTC.

Fig. 5.10. (a) Reflectivity (dBZ) and (b) differential reflectivity (dB) at the 0.5° tilt from KOUN at 2246 UTC and the difference between the (c) analysis reflectivity and the observations and (d) differential reflectivity and the observations for M10Z and (e-f) M10ZZDR at 2248 UTC.

Fig. 5.11. (a) Differential reflectivity (dB) at the 0.5° tilt from KTLX at 2246 UTC and difference in differential reflectivity between (b) M10Z and M10ZZDR at 2248 UTC

Fig. 5.12. (a) Reflectivity (dBZ), (b) differential reflectivity (dB), and (c) specific differential phase ($^\circ \text{ km}^{-1}$) at the 0.5° tilt from KOUN at 2246 UTC as well as from the ensemble mean analyses of (d-f) M10Z and (g-i) M10ZKDP at 2248 UTC.

Fig. 5.13. (a) Differential reflectivity (dB) at the 0.5° tilt from KOUN at 2246 UTC as well as mean mass diameter (mm) at the first model level above the surface for

the ensemble mean analysis of (b) M10Z and (c) M10ZZDR at 2248 UTC. Reflectivity contours are overlaid on the mean mass diameter plots in 20 dBZ intervals.

Fig. 5.14. (a) Differential reflectivity at the 0.5° tilt from KOUN at 2246 UTC as well as rain intercept parameter (mm^{-4} , 10Log_{10} scale) at the first model level above the surface for the ensemble mean analysis of (b) M10Z and (c) M10ZZDR at 2248 UTC. Reflectivity contours are overlaid on the intercept parameter plots in 20 dBZ intervals.

Fig. 5.15. (a) Observed specific differential phase at the 0.5° tilt from KOUN at 2246 UTC as well as rain mixing ratio (g kg^{-1}) at the first model level above the surface for the ensemble mean analysis of (b) M10Z and (c) M10ZZDR at 2248 UTC. Reflectivity contours are overlaid on the mixing ratio plots in 20 dBZ intervals.

Abstract

Accurately representing the microphysical state of precipitation using bulk microphysics schemes, including the hydrometeor particle size distributions (PSDs), is vital to improving convective-scale forecasts. In this dissertation, results will be presented from three related projects that combine the use of dual-polarimetric (dual-pol) radar observations and ensemble forecast methods to evaluate and improve the forecast model microphysical state. The dual-pol variables provide additional information on hydrometeor types and their PSDs compared to reflectivity (Z) alone.

In the first project, simulated dual-pol variables from several members of the 2013 CAPS Storm Scale Ensemble Forecasts (SSEF) that use different microphysics schemes are compared to dual-pol observations. The microphysics schemes vary significantly and include single-moment (SM) WSM6, partially double-moment (DM) Thompson and WDM6, and fully DM Milbrandt and Yau and Morrison. Both a mesoscale convective system (MCS) and supercell case are considered due to the different patterns in the dual-pol variable fields unique to each case. Results show that the forecasts using the Morrison scheme and the Milbrandt and Yau scheme have patterns of high differential reflectivity (Z_{DR}) indicative of size sorting that match similar patterns in the observations. The dual-pol variables also help highlight biases in the forecasts including the under-prediction of liquid water content and the over-prediction of particular hydrometeor types such as graupel.

In the second project, probabilistic forecasts of simulated dual-pol variables are performed. Ensemble forecasts of a mesoscale convective system (MCS) from 9 May 2007 are initialized from ensemble Kalman filter (EnKF) analyses using both SM and

DM microphysics schemes. Qualitative analysis of simulated Z_{DR} shows that the DM experiment better represents the PSDs of the convective and stratiform precipitation regions, while the K_{DP} fields show that the SM experiment over-forecasts liquid water content in the convective areas. Quantitative ensemble forecast verification methods using dual-pol variables are considered for the first time and reveal the challenges associated with evaluating dual-pol fields that have very fine-scale details.

Finally, in the third project, dual-pol variables are assimilated using the EnKF and a DM microphysics scheme for two supercell cases: 10 May 2010 and 20 May 2013. For each case, both Z_{DR} and K_{DP} are assimilated in separate experiments in addition to Z and radial velocity (V_r) and compared to a control experiment that assimilates only Z and V_r . The results show that the simulated dual-pol fields in the analyses of the dual-pol experiments better represent documented polarimetric signatures, such as the Z_{DR} arc, compared to the control experiment. Additionally, comparisons of model microphysical variables and mean mass diameter between the dual-pol and control experiments show that the dual-pol experiments have an improved microphysical state. For example, the mean mass diameter of raindrops in the Z_{DR} experiment is increased along the Z_{DR} arc. This work, as far as we know, represents the first to directly assimilate dual-pol radar observations into the convective-scale model for real cases.

Chapter 1 Introduction

1.1 Background

Recent advances in computer power and observations systems have led to a combination of both finer grid scale convection allowing model (CAM) ensemble forecasts and advanced data assimilation (DA) methods using weather radar observations. In particular, data assimilation methods that use an ensemble of forecasts, such as the ensemble Kalman filter (Evensen 1994; 2003), have become widely used in CAM assimilation studies. Ensemble forecasts allow for comparisons of diverse model physics settings and provide a means to gauge uncertainty in the forecast, which in turn is used in new DA methods such as the EnKF that require a good estimate of model error present for success. Developing new methods to understand and account for uncertainty in analyses and forecasts is of particular importance for CAMS since the highly non-linear processes considered lead to rapid error growth in forecasts (Lorenz 1969).

Previous DA and forecast studies that use reflectivity (Z) and radial velocity (V_r) have played a vital role in real-time forecasting. Analyzing Z can help determine the location and intensity of precipitation while V_r observations can directly impact the flow fields and improve analysis of convergence and divergence as well as mid-level rotation (i.e. the mesocyclone of a supercell) and low-level rotation (a strong indication of a tornado). These parameters have also been widely used in real case EnKF DA studies to analyze the behavior of storm systems and supercells as well as initialize model forecasts to varying success (Dowell et al. 2004; Dowell et al. 2004; Aksoy et al. 2009; Dowell and Wicker 2009; Lei et al. 2009; Lei et al. 2009; Aksoy et al. 2010 Dowell et

al. 2011; Snook et al. 2011; Dawson et al. 2012; Snook et al. 2012; Yussouf et al. 2013; Tanamachi et al. 2013; Wheatley et al. 2014; Snook et al. 2015; Yussouf et al. 2015). However, one area of particular importance in CAM DA and forecasts where these parameters do not contain enough information is with the cloud microphysical state. A good evaluation of the microphysical state of convection includes information on both the types of hydrometeors present and their particle size distributions (PSDs). Z alone cannot provide this information due to the diversity in types and sizes of hydrometeors present in precipitation.

In the past few years, the WSR-88D radar network has been upgraded to dual-polarimetric (dual-pol) capabilities, which provide several additional new measurable parameters besides the three traditional parameters of Z , V_r , and spectrum width that were previously available (ROC 2013). While there have been an increased number of studies involving the EnKF and dual-pol radar observations separately, the combination of dual-pol observations and ensemble DA and forecasts has yet to be thoroughly investigated. More specifically, there have only been a limited number of studies that have investigated the information the dual-pol observations provide for evaluating and improving analyses of the model microphysical state (Jung et al. 2008b, Jung et al. 2012; Li and Mecikalski 2012; Putnam et al. 2014).

The new dual-pol variables include differential reflectivity (Z_{DR}), specific differential phase (K_{DP}), and correlation coefficient (ρ_{HV}) which provide valuable additional information on the types and size of hydrometeors present (Bringi and Chandrasekar 2001). For example, Z_{DR} , the ratio of the horizontal and vertically polarized waves, is indicative of the axis ratio of hydrometeors present in the radar

volume. For example, raindrops become more oblate as they increase in size, leading to a higher value in horizontal Z compared to the vertical and thus Z_{DR} values increase. On the other hand, dry hail typically tumbles as it falls, and the differing orientations within the radar volume result in similar horizontal and vertical Z values, leading Z_{DR} values at or near zero. K_{DP} is the derivative of differential phase Φ_{DP} , which is a measure of the return time between the horizontal and vertically polarized waves. The speed of the waves is slowed by the presence of liquid water, which for oblate raindrops decreases the speed of the horizontal wave compared to the vertical and increases K_{DP} values. Higher values of K_{DP} suggest a greater amount of liquid water, or rain, present as well as a higher rainfall rate. Finally, ρ_{HV} , or the co-polar correlation coefficient between the horizontal and vertical wave, is impacted by diversity between the hydrometeors present in the radar volume. For example, there is a very high amount of diversity in the melting layer, where hydrometeors of different sizes, shapes, and water content to ice content ratios are present. These regions have lower ρ_{HV} values compared to regions of pure rain.

Specific patterns of dual-pol variable values occur in severe convection due to dynamical and microphysical processes, known as polarimetric signatures (Kumjian and Ryzhkov 2008). For example, the size-sorting of hydrometeors due to storm relative wind shear in the forward flank of supercells results in larger hydrometeors falling adjacent to the updraft while smaller hydrometeors are advected further downshear in the forward flank. The larger raindrops at the surface increase Z_{DR} values, known as the ‘ Z_{DR} ’ arc. The dual-pol variables can also be used with fuzzy logic algorithms to classify the dominant hydrometeor types present. In combination, these variables

provide a detailed description of the types and sizes of hydrometeors present for evaluating the microphysical state of convection. While the distributions of rain and ice hydrometeors in the model are known based on the model microphysical state variables, any substantive evaluation of the model microphysical state compared to observations requires this additional information from the observations.

Cloud microphysics (MP) schemes play a vital role in CAM analysis and forecast. In fact, while there is currently some disagreement over the use of the term ‘convective scale’ models because of differences in opinions with regard to the scales that are actually resolved (Bryan et al. 2003; Lean et al. 2008; Dudhia 2011; Bryan and Morrison 2012; Xue et al. 2013). Regardless, the use of MP schemes without cumulus parameterization sets CAMs apart from lower-resolution models that require inclusion of cumulus parameterizations, such as Kain-Fritsch (Kain and Fritsch 1993) and Betts-Miller-Janjic (BMJ, Janjic 1994). There is a wide variety of MP schemes available and their differences can have a significant impact on data assimilation and subsequent forecasts. Specifically, most MP schemes represent hydrometeor PSDs in bulk form and the amount of independent information predicted by the MP scheme defines the number of degrees of freedom associated with the PSDs that a model can represent. Single-moment MP schemes predict only one moment of the PSD of each hydrometeor species while more advanced multi-moment (MM) schemes predict additional moments of the hydrometeor PSD, and thus are able to represent a broader spectrum of PSDs and microphysical processes more accurately. For instance, the size sorting of hydrometeors requires an adjustment in both the size and number of hydrometeors present in a distribution which cannot be accomplished with a SM scheme that uses a fixed intercept

parameter; proper representation of size sorting requires at least a double-moment (DM) scheme.

The new dual-pol observations as well as advanced MP schemes available for use provide valuable new information and tools for evaluating and improving forecasts, but they are not directly connected; the model state variables associated with cloud MP schemes are not directly observed. The critical connection between the model microphysical state variables and dual-pol observations are the forward or observation operators that link the model state to observations. For polarimetric radar data, these are also known as a polarimetric radar data simulator (PRDS), which simulates the observed dual-pol variables based on the MP state variables as well as other important assumptions not predicted in the model including axis ratio relations, canting angles, and the interaction or scattering of the radar wave by the volume of hydrometeors present. Additionally, most MP schemes do not predict mixed-phase hydrometeors, so a melting model must be included to account for when both rain and ice hydrometeors are present at a similar grid point in the model. The PRDS developed by Jung et al. (Jung et al. 2008a) and Jung et al. (Jung et al. 2010) is used in this work because of its ability to represent multi-moment (i.e. more than a SM) MP schemes, as well as that it includes a detailed melting model and advanced T-matrix scattering calculations compared to other PRDSs currently available. The PRDS can be used to both evaluate the analysis and forecast microphysical state with dual-pol observations and serve as the forward operator to assimilate dual-pol observations to optimally analyze the atmospheric microphysical state for the improved initialization of forecasts.

There are several important areas and aspects to consider to advance current research using ensembles, advance microphysics schemes, and dual-pol variables to evaluate and improve the model microphysical state. The available model microphysical state variables have a significant impact on the simulated variables and it is vital that the simulated variables are consistent with the MP scheme used in order to properly represent the microphysical processes and hydrometeor PSDs. Additionally, advanced MM MP schemes are required in order for the MP scheme processes and particle size distributions to represent observed polarimetric signatures and patterns (Kumjian and Ryzhkov 2012; Jung et al. 2012). Therefore, the focus of this work is on advanced DM MP schemes in order to take advantage of the dual-pol observations available, particularly for assimilation. In turn, the comparisons between simulated variables using SM and DM schemes with dual-pol observations will reveal the significant advantage that a DM scheme has over a SM scheme. Finally, the EnKF method is chosen for assimilation since it does not require an adjoint model as in 3DVAR or 4DVAR, which are extremely difficult to develop for ice microphysics schemes, and the ability to easily use non-linear and complex observation operators for polarimetric observations.

1.2 Dissertation Overview

This dissertation seeks to investigate the information and impacts the simulation and assimilation of observed dual-pol parameters can provide to the ensemble analyses and forecasts of the model microphysical states using MM microphysics schemes. This includes developing new methods for comparing model assimilation and forecast results as well as assimilating dual-pol observations. To accomplish this goal, work was carried

out in several areas that combine the simulation and/or assimilation of dual-pol parameters with various MP schemes in ensemble forecasts and the EnKF data assimilation processes. The progression of studies advances the use of dual-pol variables in current research. The dual-pol variables are first used for evaluation of ensemble forecasts, then assessed in terms of their probabilistic predictions, and finally assimilated to improve the estimation of model microphysical state.

In the first study to be documented in Chapter 2, dual-pol parameters are simulated from forecasts of a CAM ensemble produced by the Center for Analysis and Prediction of Storms (CAPS), the Storm Scale Ensemble Forecast (SSEF), as part of the NOAA Hazardous Weather Testbed (HWT) Spring Experiment (Kong 2013). The ensemble members differ in the use of radar DA, boundary conditions, as well as model physics parameterizations to assess forecast sensitivity to different model parameterizations. In particular, several members differ only in MP scheme and provide a basis to compare and contrast the MP scheme performance and sensitivities. The proper simulation of dual-pol parameters from various microphysics schemes has yet to be considered and plays a vital role in this area of research even if assimilation is not used. Not only will information from these simulations allow for an in depth comparison and potentially beneficial updates to the schemes, the simulation comparisons can also be used as a tool to investigate how the various microphysics schemes in each forecast replicate typical dual-pol parameter values and signatures by forecasts for choosing schemes for future dual-pol parameter assimilation work. It is also desirable to eventually provide new dual-pol forecast tools and both qualitative and quantitative methods of presenting the simulated dual-pol variables are considered.

These include comparing results using a fuzzy logic HCA algorithm and the fractions skill score (FSS). The recent upgrade of the WSR-88D network to dual-pol capabilities provides the widespread observations needed to evaluate the microphysical state of forecasts on this scale.

In the second study (Chapter 3), ensemble forecasts initialized from an EnKF analysis are performed for an MCS case using both SM and DM MP schemes. The spread in the ensemble provides a measure of uncertainty in order to produce probabilistic forecasts of dual-pol variables which can be compared with observations. Previous studies have considered ensemble forecast products with the EnKF (Dawson et al. 2012; Snook et al. 2012; Yussouf et al. 2013; Wheatley et al. 2014; Snook et al. 2015) but have focused mainly on probabilistic forecasts of vorticity and not microphysics related variables. The probabilistic methods include qualitative assessments of probabilities thresholds as well as quantitative methods such as the relative operating characteristic (ROC) area under curve (AUC) score and reliability diagrams.

In the final study (Chapters 3 and 4), dual-pol observations (Z_{DR} and K_{DP}) are assimilated for the first time using the EnKF, an advanced DM ice microphysics scheme, and the Jung et al. (2010) observations operators which include actual T-matrix scattering amplitudes. A new method to pre-calculate a portion of the operator using look-up tables of the scattering amplitudes and PSD parameters is developed to assimilate the observations with the same computation expense as prior research with a simplified version of this operator (Jung et al. 2012). Two high impact supercell storm cases are considered: 10 May 2010 and 20 May 2013. Since this is a new area of

research, Chapter 4 contains sensitivity experiments to first narrow down the best model, observation, and EnKF settings. These include different EnKF model error treatment methods, different filtering methods of the dual-pol observations, different dual-pol observation errors, and different radar configurations. The analyses from the best experiments are investigated in Chapter 5. Particular attention is paid to the impact the additional dual-pol variables have on the microphysical state compared to control experiments. This includes such aspects as rain mean mass diameter, rain mixing ratio, and comparisons of the model PSDs with retrieved PSD parameters from the dual-pol observations.

Chapter 2 Simulation of Polarimetric Radar Variables and Evaluation of Microphysics Schemes in Ensemble Forecasts

2.1 Introduction

The national WSR-88D S-band weather radar network has completed its polarimetric upgrade, providing unprecedented polarimetric radar variable measurements over the CONUS (ROC 2013). The polarimetric radar variables provide additional information about the cloud hydrometeor types and their particle size distributions (PSDs) compared to reflectivity (Z), in particular information on hydrometeor size and diversity. They include: 1) differential reflectivity (Z_{DR}) that is sensitive to hydrometeor shape and orientation; 2) specific differential phase (K_{DP}) that is sensitive to rainwater content/rain rate; and 3) cross-correlation coefficient (ρ_{hv}) that is sensitive to diverse and mixed-phase hydrometeors (Bringi and Chandrasekar 2001). Common dynamical and microphysical processes lead to patterns in these variables which occur at specific locations and in specific circumstances within convective storms, referred to as polarimetric signatures (Kumjian and Ryzhkov 2008). For example, there is a relative Z_{DR} maximum along the right forward flank of supercells due to hydrometeor size sorting, known as the Z_{DR} arc. In mesoscale convective systems (MCS), high Z_{DR} is observed on the leading edge of the convective line due to the size sorting of larger drops that fall ahead of the system (Park et al. 2009).

Note: This Chapter is an extended version of our paper: Putnam, B. J., M. Xue, Y. Jung, G. Zhang, and F. Kong, 2016: Simulation of polarimetric radar variables from 2013 CAPS spring experiment storm scale ensemble forecasts and evaluation of microphysics schemes. *Mon. Wea. Rev.*, Conditionally accepted.

The hydrometeor variables in microphysics (MP) schemes of numerical weather prediction (NWP) models are typically not directly observed. One way to evaluate the model prediction of hydrometeor fields and the MP parameterization schemes is to simulate polarimetric variables from the model output and compare them with observations. The model state variables, including MP variables, are connected to observed polarimetric fields by the so-called polarimetric radar data simulator (PRDS) (Jung et al. 2008a; Jung et al. 2010, hereafter JXZ10), or the observation operators in data assimilation terminology. These operators are derived from scattering calculations of polarized radar radio waves by hydrometeor particles within each radar sampling volume.

Most MP schemes represent hydrometeor PSDs in bulk form using the simplified gamma distribution

$$N(D)_x = N_{0x} D_x^{\alpha_x} e^{(-\Lambda_x D)} , \quad (2.1)$$

which defines the number of particles of hydrometeor x with diameter D in a unit volume (Ulbrich 1983; Milbrandt and Yau 2005a). Three free parameters govern the distribution: 1) the slope parameter Λ_x ; 2) the intercept parameter N_{0x} ; and 3) the shape parameter α_x . MP schemes can be broadly categorized by the number of these free parameters that they derive from predicted microphysical variables for each species. For example, mixing ratio (q) is proportional to the third PSD moment (mass) and is used to solve for Λ_x . Single-moment (SM), double-moment (DM), and triple-moment (TM) schemes predict one, two, and three moments of the PSD and can therefore determine one, two or three of the PSD parameters, respectively. Parameters that are not derived from predicted variables are either diagnosed or set as constant. Another significant

feature of a given MP scheme is the number of hydrometeor species included. Five categories are most commonly considered in ice MP schemes: cloud water (c), cloud ice (i), rain water (r), snow (s), and graupel (g) or hail (h), and some but relatively few schemes (e.g., the Milbrandt and Yau (MY) scheme (Milbrandt and Yau 2005b)) include graupel and hail as separate species.

It is important that the observation operators developed for a PRDS are consistent with the MP scheme used so that the simulated variables reflect the model microphysical state and dynamical processes. Increasing the number of model variables predicted (e.g., moving from a SM to a DM scheme) increases the amount of predicted microphysical information that can and should be used in the operators. Some schemes, including Thompson (Thompson et al. 2008) and WDM6 (Lim and Hong 2010) schemes are partially double moment, predicting a second moment for rain (number concentration, N_{rr}) but only one moment for other hydrometeor species. Though most SM and DM schemes set $\alpha_x = 0$ by default, resulting in an exponential distribution, WDM6 uses $\alpha_r = 1$ for rain and the Thompson scheme uses a combined exponential and gamma distribution for snow.

Limitations of MP schemes may preclude the model from replicating certain polarimetric signatures and highlight microphysical state differences. Some current schemes, including the Thompson, WSM6 (Hong and Lim 2006), WDM6, and Morrison (Morrison et al. 2005; Morrison et al. 2009) schemes, contain a graupel category but not hail, and are unable to replicate the decrease in Z_{DR} associated with large, dry hail (Kumjian and Ryzhkov 2008; Johnson et al. 2016a). Additionally, Wacker and Seifert (Wacker and Seifert 2001) and Milbrandt and Yau (2005a) have

shown that SM MP schemes cannot represent sedimentation, or size sorting, and thus a DM or higher order scheme is required to produce polarimetric signatures associated with size sorting (JXZ10; Kumjian and Ryzhkov 2012). Jung et al. (2012) demonstrated that the Z_{DR} arc signature could be replicated with the DM MY scheme but not a SM Lin (Lin et al. 1983) scheme when the states of a supercell are estimated using a cycled ensemble Kalman filter. Putnam et al. (2014) showed for an MCS case that the size sorting of large drops and subsequent increase in Z_{DR} in the convective line compared to the stratiform region could be replicated by the DM MY scheme but not the SM Lin scheme.

Since the spring of 2007, the Center for Analysis and Prediction of Storms (CAPS) at the University of Oklahoma has been producing storm-scale ensemble forecasts (SSEF) for the CONUS (Kong et al. 2007; Xue et al. 2007) as part of the NOAA Hazardous Weather Testbed (HWT) Spring Experiment (Weiss et al. 2007; Clark et al. 2012). In the spring of 2013, the SSEF system had a 4 km convection-permitting grid spacing, allowing explicit representation of convective storms (Kong 2013). The system used a variety of microphysics (MP) schemes among its ensemble members, including several that predicted two moments of some of the hydrometeor species within the schemes. One set of special products produced from the ensemble forecast output were simulated polarimetric radar variables using the PRDS developed at CAPS. The availability of polarimetric observations from the upgraded WSR-88D network and the PRDS with the ability to simulate polarimetric variables from a variety of microphysics schemes provided an unprecedented opportunity to compare and

contrast the ability of the various microphysics schemes commonly used in convective-scale forecasts in reproducing known polarimetric signatures.

The purpose of this paper is to document the real-time implementation of the PRDS, evaluate the simulated polarimetric variables and polarimetric variable forecasts within the SSEF system against WSR-88D polarimetric observations, and to infer strengths and weaknesses of MP schemes as implemented in the 2013 ensemble. Biases identified with the microphysics schemes can help the scheme developers to improve their schemes, and help the scheme users to interpret their simulation results in their research. As observed quantities are often more intuitive to forecasters, simulated polarimetric variables can be used by forecasters to monitor and nowcast severe weather when the association of polarimetric signatures with weather events/features is well recognized. Towards that end, knowledge gained on the behavior of the MP schemes and the PRDS can help forecasters better understand the dual-pol forecast products.

Up to the time of this exercise, CAPS's PRDS had mainly been used with the MY DM scheme (Jung et al. 2012; Putnam et al. 2014); this effort represents the first time that multiple DM schemes are evaluated in a common framework in terms of their ability to produce polarimetric radar signatures for real cases. The recent study of Johnson et al. (2016a) had a similar goal but it was based on a set of idealized supercell simulations therefore no real radar observations could be used for comparison. Since significant polarimetric radar signatures are relatively local and isolated within convective systems, simple grid-point-based evaluation scores typically applied to precipitation forecasts, such as the equitable threat score, are not very revealing, especially when different types of convective systems are mixed together (different

types of convective systems tend to produce different kinds of polarimetric signatures in different parts of the systems). Because of the many challenges facing objective evaluations of the forecast of polarimetric signatures, which tend to be highly localized and in the current forecasts contain significant biases, we choose to focus on two cases from the CAPS 2013 Spring Experiment only in this study: one case with MCSs and one case with supercells. Focusing on two cases allows us to perform more detailed subjective evaluations and at the same time access the objective evaluation methods and procedures. Such a study would provide the groundwork for future studies evaluating the MP and PRDS performances over the entire Spring Experiment period.

The rest of this Chapter is organized as follows. The methodologies, including the general design of the CAPS SSEF, the PRDS and MP schemes used, and the quality control of observations, are given in section 2.2. Section 2.3 presents evaluation results for the MCS and supercell cases. A summary and conclusion reviewing notable trends in polarimetric size sorting signatures and biases in graupel and water content is given in section 2.4. Some challenges faced in evaluation are also noted.

2.2 Methodology

2.2.1 Overview of the 2013 CAPS SSEF

The 2013 CAPS SSEF forecasts were run as part of the NOAA HWT Spring Experiment (Kong 2013). Official forecasts began on 6 May 2013 and continued through 7 June 2013. Daily 48-hour forecasts initialized at 0000 UTC were run on a CONUS domain using a horizontal grid spacing of 4 km with 51 vertical levels (Fig. 2.1). Twenty nine ensemble members were run using three mesoscale NWP models: the WRF-ARW model (version 3.4.1, 26 members, Skamarock et al. 2008), the U.S. Navy

COAMPS model (2 members, Hodur 1997), and the CAPS Advanced Regional Prediction System (ARPS, version 5.3, 1 member, Xue et al. 2003). This paper focuses on the WRF-ARW members since the COAMPS and ARPS members used single-moment microphysics schemes only.

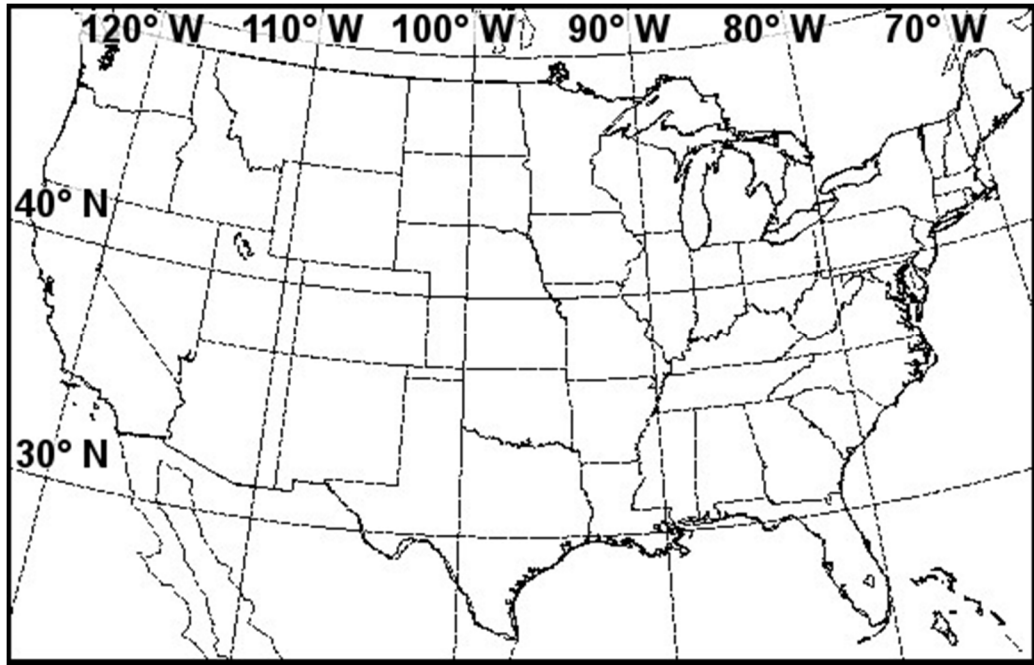


Fig. 2.1. Model domain for 2013 CAPS Spring Experiment storm scale ensemble forecasts

The 26 WRF-ARW members varied in terms of their initial conditions (IC), boundary conditions (BC), and physics packages. The control member IC was obtained by assimilating surface, upper-air, and WSR-88D radar observations using the ARPS 3DVAR and complex cloud analysis system (Xue et al. 2003; Gao et al. 2004; Hu et al. 2006a,b), with the NCEP 12 km NAM (Rogers et al. 2009) 0000 UTC analysis used as the background, and used a BC that was obtained from the 0000 UTC NAM forecast. An additional 11 members used this IC and BC while 13 members used this IC and BC with added perturbations derived from the 2100 UTC NCEP Short-Range Ensemble

Forecasts (SREF, Du et al. 2006). One member was initialized from the NAM analysis directly. For the purpose of investigating the performance of various physics packages in the WRF, the subset of members which used the same IC and BC as the control member differed in their use of land surface, boundary layer, radiation, and microphysics schemes. Since MP scheme differences are the focus of this study, polarimetric variable simulations were performed for the control and for those members that differed from the control only in their choice of MP scheme (the arw_cn, arw_m20, arw_m21, arw_m22, and arw_m26 members) (Kong 2013). These members used the NOAH land surface model (Chen and Dudhia 2001) and the Mellor–Yamada–Janjic boundary layer scheme (MYJ, Mellor and Yamada 1982; Janjic 2002). More details on the MP schemes used are provided in section 2.2.3.

2.2.2 Polarimetric simulation and general experiment settings

The PRDS originally developed for the ARPS output (Jung et al. 2008a; JXZ10) was adapted and applied to the WRF output with several different MP schemes. The PRDS calculations include only the rain, snow, graupel, and hail categories, when applicable. Despite the important role that cloud water and cloud ice play in precipitation processes, the radar returns from these hydrometeors are minimal. Important details of the PRDS, including the axis-ratio relation, canting angle of particles, the melting model, and radar scattering amplitudes, are briefly summarized here.

The PRDS operators include complex scattering amplitudes calculated using the T-matrix method (Vivekanandan et al. 1991; Bringi and Chandrasekar 2001) for both rain and ice species via numerical integration over the PSDs. The raindrop axis ratio

decreases with diameter based on the relation in Brandes et al. (2002); this ratio is set to 0.75 for hail, graupel, and snow. The mean canting angle for all hydrometeor types is 0° with a standard deviation of 0° for rain, 20° for snow, and ranging from 0° to 60° for hail and graupel depending on the water fraction. Since most MP schemes do not predict mixed-phase hydrometeors, a mixing ratio fraction of wet (melting) snow, wet hail, or wet graupel is considered present when rain (q_r) coexists at a particular model grid point with snow (q_s), hail (q_h), or graupel (q_g), creating mixed-phase mixing ratios denoted q_{rs} , q_{rh} and q_{rg} . The water fraction model used there for the mixed phases is described in detail in Jung et al. (2008a), and the water fraction model used during the 2013 CAPS Spring Experiment does not vary across the size spectrum. The density (ρ) of each mixed-phase species increases as the fractional amount of rain increases and the dielectric constant is calculated using the Maxwell-Garnett mixing formula (Maxwell-Garnett 1904). These variables are used in separate calculations of Z_{rs} , Z_{rh} , and Z_{rg} for mixtures, in addition to Z_r , Z_s , Z_g , and Z_h , with the log of the sum giving the final simulated Z . A radar wavelength of 107 mm is used to match the WSR-88D S-band network. For reference, from JXZ10, Z is calculated using equation (3), Z_{DR} from the quotient of (3) and (4), and K_{DP} from (6).

2.2.3 Spring experiment microphysics schemes

The 2013 SSEF WRF-ARW members used 6 different MP schemes: the MY, Morrison, Thompson, WDM6, NSSL (Mansell 2010), and WSM6 schemes. The NSSL scheme has not yet been added to the PRDS because its representation of hydrometeor PSDs is a lot more complex than the other schemes. The original PRDS operators were already compatible with the WSM6 and MY schemes. The Morrison scheme follows the

same PSD and has the same predicted moments as MY (excluding hail) so it was easily implemented. Modifications were required for the other schemes. The Thompson and WDM6 schemes predict N_t and q for rain but only predict q for the remaining categories as used in the PRDS (prediction of N_{tr} was added to the Thompson scheme subsequent to Thompson et al. (2008)). WDM6 diagnoses N_{0s} using temperature and uses a fixed value for N_{0g} . WDM6 also uses a fixed shape parameter of 1.0 for α_r . The Thompson scheme has been further updated since Thompson et al. (2008) to use temperature and the mean volume diameter of rain to diagnose N_{0g} .

Additionally, the Thompson scheme deviates from the typical representation of the bulk PSD for snow. The PSD is composed of the sum of an exponential and gamma distribution, given as

$$N(D)_s = \frac{M_2^4}{M_3^3} \left[\kappa_0 e^{\frac{M_2}{M_3} \Lambda_0 D} + \kappa_1 \left(\frac{M_2}{M_3} D \right)^{\alpha_s} e^{\frac{M_2}{M_3} \Lambda_1 D} \right], \quad (2.2)$$

where κ_0 , κ_1 , Λ_0 , Λ_1 , and α_s are constants and M is a given moment of the distribution. The sum is used to represent the ‘super-exponential’ portion of observed snow PSDs in which the number of snowflakes with small diameters rapidly increases with decreasing size. The calculation of M is unique to the Thompson scheme and presents an additional challenge in the melting model. The third moment of the distribution, used to calculate Λ in the PSD, does not include ρ (which is modified for the rain/snow mixed-phase PSD in the melting model). Developing a method to represent this PSD that must transition between the combined exponential and gamma snow PSD and the exponential rain PSD requires further study. For now, the rain/snow mixed-phase PSD is represented as an exponential distribution with Λ derived from the rain/snow mixing ratio, q_{rs} , and uses a typical fixed value for N_{0s} originating from the Lin (3×10^6 , Lin et

al. 1983) scheme. Table 2.1 summarizes whether N_0 and α are derived using predicted microphysical moments, diagnosed, or a fixed value for each hydrometeor category for each MP scheme.

Scheme	N_{0r}	N_{0s}	N_{0g}	N_{0h}	α_r	α_s	α_g	α_h
<i>Thompson</i>	$F(q_r, N_{tr})$	$F(q_s, T)$	$F(q_g, T)$	NA	0	0.6357	0	NA
<i>MY</i>	$F(q_r, N_{tr})$	$F(q_s, N_{ts})$	$F(q_g, N_{tg})$	$F(q_h, N_{th})$	0	0	0	0
<i>Morrison</i>	$F(q_r, N_{tr})$	$F(q_s, N_{ts})$	$F(q_g, N_{tg})$	NA	0	0	0	NA
<i>WDM6</i>	$F(q_r, N_{tr})$	$F(T)$	$4 \times 10^6 \text{ m}^{-4}$	NA	1	0	0	NA
<i>WSM6</i>	$8 \times 10^6 \text{ m}^{-4}$	$F(T)$	$4 \times 10^6 \text{ m}^{-4}$	NA	0	0	0	NA

Table 2.1. Reference table for which predicted model variables are used to calculate the intercept (N_0) and shape (α) parameters for rain (r), snow (s), graupel (g), and hail (h) from each of the microphysics scheme considered. The values are either fixed and listed, or calculated as a function of mixing ratio (q), number concentration (N_i), and/or air temperature (T). Schemes which do not contain a given hydrometeor category are listed as not applicable (NA).

2.2.4 Polarimetric radar observations

The upgraded WSR-88D radars provide domain-wide polarimetric observations which are used for comparison to the simulated variables. Z and Z_{DR} observations are filtered using a 5-point along-the-radial median filter, while K_{DP} is calculated from similarly filtered differential phase (Φ_{DP}) observations using the least squares fit method of Ryzhkov and Zrnich (1996). Nine range gates are used when $Z > 40$ dBZ and 25 range gates are used for $Z < 40$ dBZ.

The availability of polarimetric observations allows for extensive quality control of the data using fuzzy logic (Park et al. 2009). The fuzzy logic method uses ranges of polarimetric radar data values and weights to determine the most likely hydrometeor type of the observation. The Z , Z_{DR} , ρ_{hv} , standard deviation (SD) of Z (1 km running average), and $SD(\Phi_{DP})$ (2 km running average) membership functions are used along

with their respective weights. The confidence vectors are not included. Additionally, the temperature profile and the presence of frozen hydrometeors from the forecast model are used to help further narrow down potential hydrometeor types before classification. For example, frozen categories are not considered at heights where full melting has occurred in the forecast and rain-associated categories are not considered above the freezing level. The MY forecast member was chosen since this scheme included the most number of hydrometeor categories and produced reasonable results. Those observations that are determined to be ground clutter, anomalous propagation, or biological scatterers are removed. This is important since SSEF forecasts begin at 0000 UTC and short term forecasts in the late spring/early summer months will be at a time when observed radar blooms due to birds and insects are prominent (Lakshmanan et al. 2007). An example of Z , Z_{DR} , and K_{DP} observations at an elevation angle of 0.5° before and after the removal of non-meteorological echoes for one of the cases evaluated in this study, at 0400 UTC 20 May 2013, is given in Fig. 2.2. The locations of the WSR-88D radars used are included as black dots in Fig. 2.2a. Obvious clutter from the late evening radar bloom (10 pm Central Standard Time) is almost completely removed. Data points that are determined to be a three body scatter spike are also removed (Mahale et al. 2014).

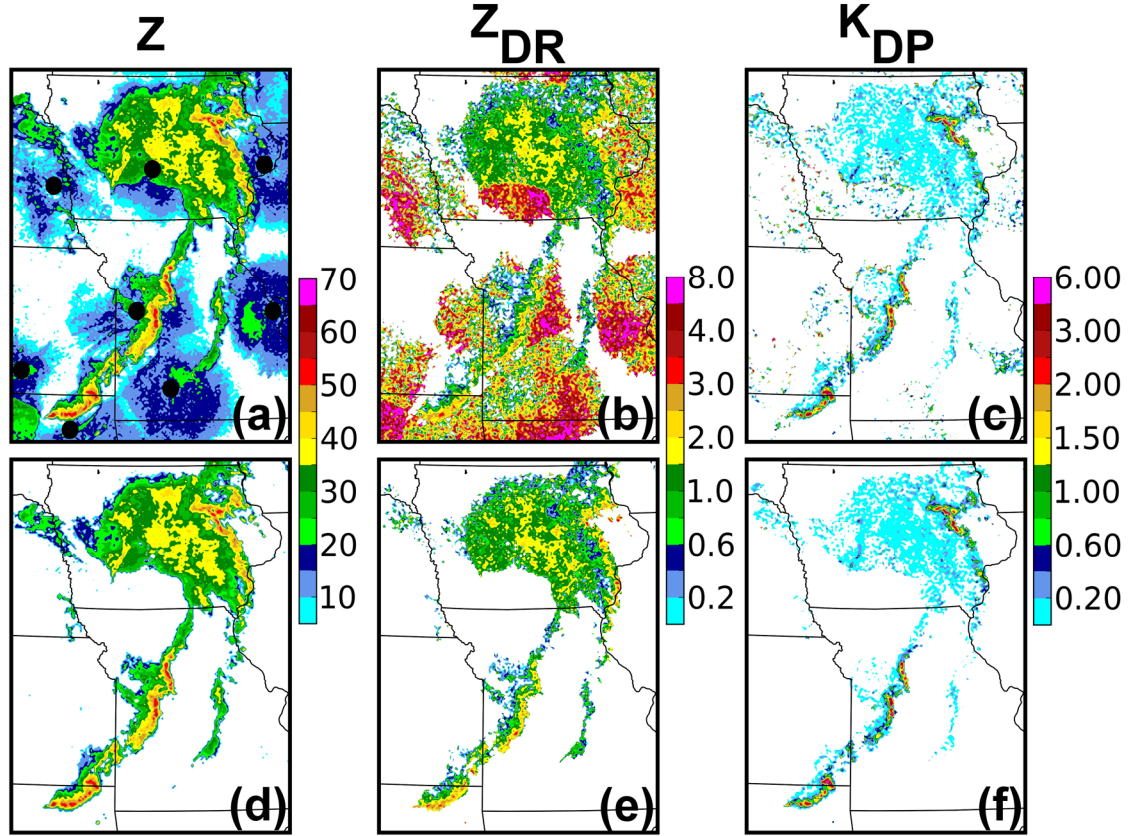


Fig. 2.2. Mosaics of observed (a) reflectivity (dBZ), (b) differential reflectivity (dB), and (c) specific differential phase ($^{\circ} \text{ km}^{-1}$) at a $.5^{\circ}$ tilt before ground clutter/biological scatterer removal and (d-f) after. The locations of the WSR-88D radars used are included as black dots in (a).

2.3 Evaluation of simulation results

In this section, results for two example cases chosen from the 2013 Spring Experiment are evaluated. The first is a four-hour forecast initialized at 0000 UTC 20 May 2013 for a series of MCSs. The second is a 21-hour forecast of several supercell thunderstorms also initialized at 0000 UTC 20 May 2013. These cases provide two different convective modes that contain distinct and different polarimetric signatures for evaluation. Additionally, the first case is a short-term forecast with sufficient lead time to allow for microphysical processes such as size sorting to develop while not too long for the storm systems originally initialized from radar data to dissipate. The divergence

between the ensemble of model solutions and the observations is also relatively small at this point. Because of the early evening initialization time, a similar situation is difficult to find for supercell thunderstorms, which typically dissipate or grow upscale at night. For these reasons, the 21-hour long forecasts valid in the afternoon of 20 May were chosen. It was also a point of emphasis to choose cases that had storm systems that were well placed so more focus could be on the differences in the polarimetric variable values and not storm structure and placement. For convenience, the chosen ensemble members (section 2.2.1) are referred to by their respective microphysics schemes: TOM (Thompson), MY (Milbrandt and Yau), MOR (Morrison), WDM (WDM6), and WSM (WSM6).

In this study, the forecast results are compared to the observations by creating a 0.5° elevation mosaic of observed and simulated radar data from all WSR-88D sites within the domain from data in a ‘gridtilt’ format for direct comparison. The simulated variables are left on the model grid in the horizontal but mapped (via weighted average) in the vertical to the elevations or tilts of each radar using the beam pattern weighting function given in Xue et al. (2006). Conversely, the radar observations are interpolated to the model grid points in the horizontal but left on the radar elevation levels in the vertical. As a result, both model and radar data are transferred to a common ‘gridtilt’ space with respect to individual radars. A 0.5° elevation mosaic is created by combining the lowest available elevation angles (0.5°) from the WSR-88D radars located within the domain, using the observation closest to the surface where two or more radars overlap. The 0.5° elevation angle is chosen and the closest-to-the-surface value is used because polarimetric signatures associated with hydrometeor size sorting

are most prevalent near the surface. This is similar to how the ‘reflectivity at lowest altitude’ or ‘RALA’ product is produced in the Multi-Radar Multi-Sensor (MRMS) system (Smith et al. 2016). A near-surface constant height mosaic will have large areas of missing observations because the radar beam height increases with distance. Additionally, vertical interpolation of radar elevation level data to a constant model level can have large error as the radar beam width increases with distance from the radar (Sun and Crook 2001).

2.3.1 The 20 May 2013 mesoscale convective system case

Height falls associated with an upper level trough moving into the central plains and ample low level moisture led to the development of multiple areas of severe thunderstorms during the mid-afternoon of 19 May 2013. Over time, these clusters grew upscale to form several MCSs that stretched from the upper Mississippi valley south into Oklahoma. The most intense of these system resulted from storms initially forming over central Kansas that continued into eastern Iowa. At 0400 UTC 20 May this system exhibited the elements of a classic MCS including leading convection and trailing stratiform precipitation (Fritsch and Forbes 2001). Additional linear convective storms formed along an outflow-reinforced cold front that stretched southwestward into northern Oklahoma. Widespread damaging wind and hail was reported across the Midwest, and several tornadoes were reported in southwestern Missouri (SPC 2014b).

2.3.1.1 Qualitative evaluation of forecasts

A mosaic of observed and simulated Z , Z_{DR} , and K_{DP} in the gridtilt format described at the beginning of section 2.3 is plotted in Fig. 2.3. Locations of WSR-88D radar sites used for both the observed and simulated variable plots are included in Fig.

2.3a. Overall, the observed features are well placed in the five forecasts. However, the intensity and structure of the forecast precipitation differ from the observations, and differ among the forecast members. The MY and MOR members produce more widespread, high Z in the convective areas (Fig. 2.3g,j) in eastern Iowa compared to the observations but show a decrease in intensity in the stratiform precipitation region further west in central Iowa. Z in WDM and WSM is lower than in MY and MOR in the convective areas and more closely matches the observations (Fig. 2.3m,p). However, the stratiform precipitation over Iowa is almost non-existent in WDM, and is significantly under-forecast in WSM. Lim and Hong (2010) found that WDM had low rain rates in the stratiform region of a 2D simulated MCS due to higher rain number concentrations and increased evaporation. The WSM and WDM forecasts are overall very similar as only warm rain processes are DM in WDM. Putnam et al. (2014) found that a DM MY forecast, which predicts a second moment for snow and cloud ice, better maintained separate convective and stratiform precipitation regions in an MCS compared to a SM Lin forecast due in part to improved transport of frozen hydrometeors between the convective towers and stratiform precipitation region. The TOM Z appears most reasonable in terms of both intensity and coverage (Fig. 2.3d). The placement and structure of convection in western Missouri and northern Oklahoma, and the associated Z intensity, match the observations well. However, the convective region in eastern Iowa is disorganized with no discrete linear convective line ahead of the trailing precipitation.

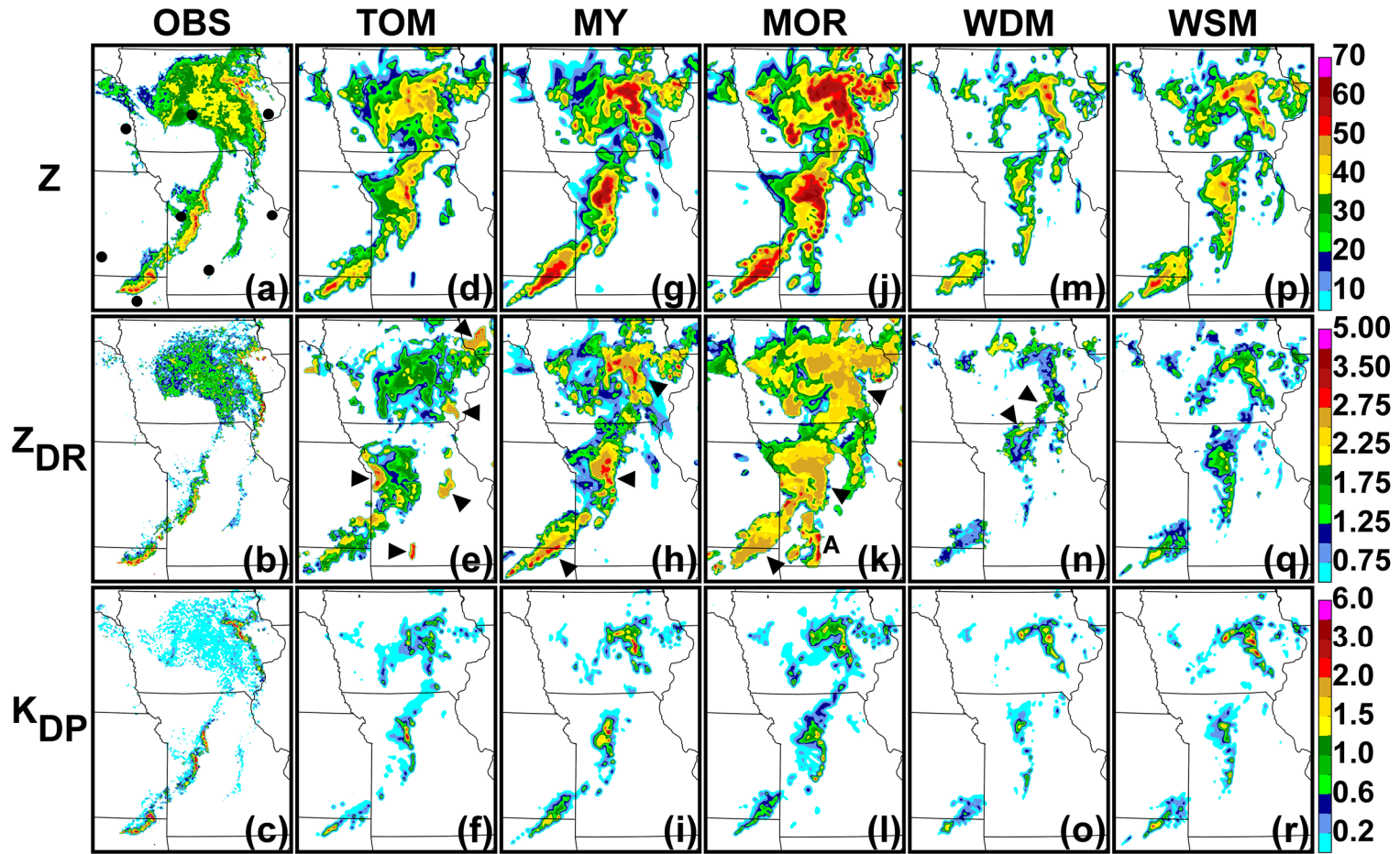


Fig. 2.3. Mosaics of observed (a) reflectivity (dBZ), (b) differential reflectivity (dB), and (c) specific differential phase ($^{\circ}$ km⁻¹) at a $.5^{\circ}$ tilt 2100 UTC 20 May 2013 and simulated values at the same tilt locations from the (d-f) TOM, (g-i) MY, (j-l) MOR, (m-o) WDM, and (p-r) WSM forecasts. Features of interest referenced in the text are noted by arrows, numbers, and letters. Locations of WSR-88D sites used for both the observed and simulated variable plots are noted with black dots in (a).

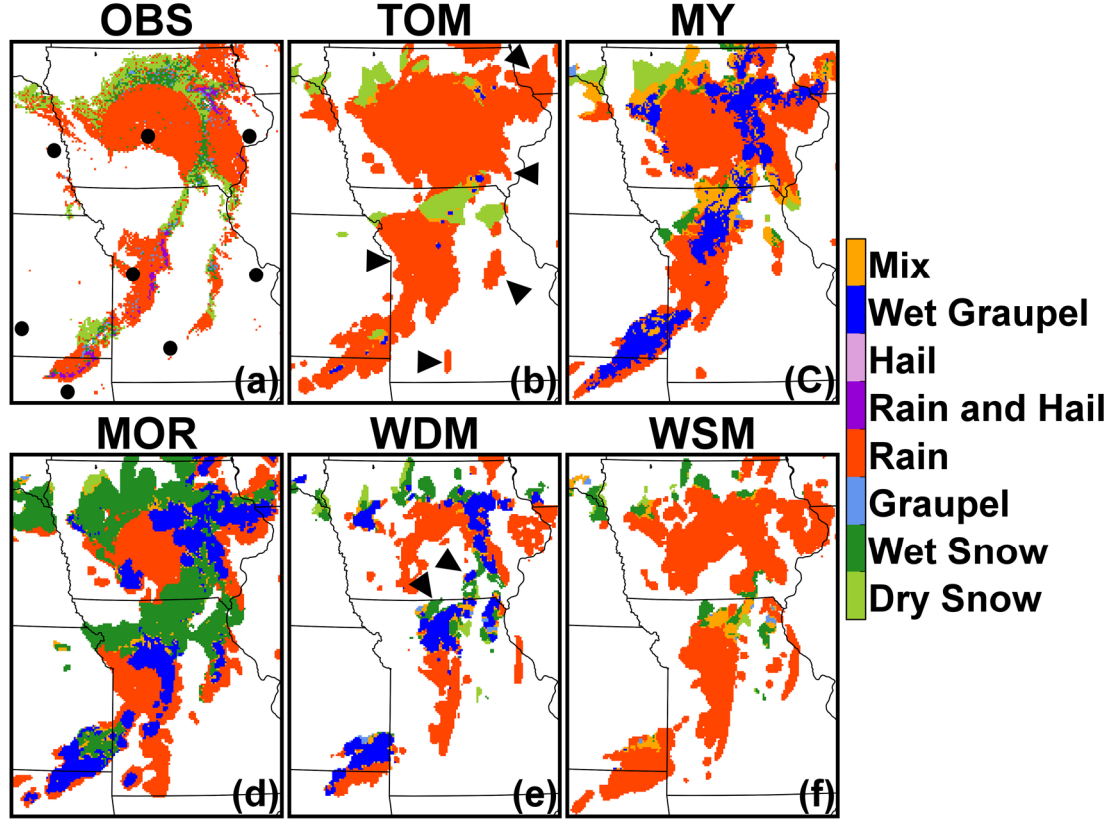


Fig. 2.4. Mosaic of hydrometeor classification using fuzzy logic for (a) observations at a .5° tilt 0400 UTC 20 May 2013 as well as classification of highest simulated linear reflectivity at the same tilt locations for (b) TOM, (c) MY, (d) MOR, (e) WDM, and (f) WSM forecasts. Features of interest referenced in the text are noted by arrows. Locations of WSR-88D sites used for both the observed and simulated variable plots are noted with black dots in (a).

The range of Z may be due to different hydrometeors sizes, types, and water contents; simulated Z_{DR} and K_{DP} provide further insight to better differentiate the microphysical states of the members. Additionally, observed Z_{DR} and K_{DP} can be used to diagnose the hydrometeor categories using the fuzzy logic method described in section 2.2.4 (Fig. 2.4). For the forecasts, the dominant category is determined based on which hydrometeor type provides the majority contribution to the linear simulated Z , including the diagnosed mixed phase species described in section 2.2.2. If no category contributes at least 50% to Z , the category is considered a ‘mix’. Since the model MP

scheme categories do not match the Park et al. (2009) HCA categories, hail, wet (melting) graupel, and ‘mix’ are added to the classification list for identification when present in the PRDS results. Additionally, the forecast rain category does not differentiate between the ‘big drop’ and ‘heavy rain’ categories so all rain is combined into one category and wet (melting) hail from the PRDS results is considered ‘rain and hail’. Non-meteorological categories are not included, as they were removed during quality control.

Observed Z_{DR} is generally greater than 2.0 dB in the convective regions with a maximum of around 3.0 dB and is less than 2.0 dB in the stratiform regions (Fig. 2.3b). This matches the typical observed Z_{DR} pattern in an MCS caused by differing rain PSDs; areas of convective precipitation have high Z_{DR} due to the presence of large raindrops, with the maxima occurring along the leading edge of the convective line where the largest drops (which have the greatest terminal velocity) fall, while the stratiform region, which is not supported by an intense updraft, contains moderate precipitation with small to medium-sized raindrops and lower Z_{DR} (Zhang et al. 2008). MY and MOR have the highest simulated Z_{DR} in convective regions, comparable to the observations, but the coverage of these high values is more widespread (Fig. 2.3h,k). The widespread high Z_{DR} matches the areas of over-forecast high Z where the presence of larger raindrops in intense convection would be expected. The high Z_{DR} , along with very high Z , is also indicative of large oblate wet graupel, the dominant hydrometeor category (Fig. 2.4c-d). MY predicts hail but shows a similar high bias in wet graupel as MOR. The MY scheme implemented in the WRF as used in the CAPS SSEF was modified from Milbrandt and Yau (2005b) to include a strict minimum size threshold

for hail. Hail below this threshold is converted back to graupel and this threshold has been shown to result in forecasts that produce little, if any, hail (Van Weverberg et al. 2012). This may explain the presence of too much graupel compared to the observations in this case. It should also be noted that the Morrison scheme in the WRF does have an option to treat dense ice as hail instead of graupel, but in the SSEF it is treated as graupel. Z_{DR} tends to increase towards the leading edge of the convective lines in southeastern Kansas and northeastern Oklahoma, as well as in central Missouri and eastern Iowa for MOR (indicated by arrows in Fig. 2.3h,k); high Z_{DR} at the leading edge of convection is a commonly found polarimetric signature associated with size sorting. However, there are many convective areas where large drops are embedded within the convection and a size sorting signature is not evident. MOR has a strong size sorting signature in southwestern Missouri (indicated by ‘A’ in Fig. 2.3k), but this corresponds with low Z and weak precipitation. It is not unusual to see high Z_{DR} in developing convection as size-sorting begins to occur, but this may also be a result of the drop breakup scheme in MOR. In MOR, the self-collection of raindrops is initiated based on q_r . As a result, in low precipitation regions with small q_r , the raindrops may easily increase to their maximum size and break up. These spikes in Z_{DR} were also noted in Johnson et al. (2016a).

There is a more significant difference in the microphysical state of MOR and MY in the stratiform precipitation region in central Iowa. There is widespread moderate Z_{DR} in MOR, only 0.5 dB less than the Z_{DR} in the convective line to the east, while Z_{DR} decreases away from the leading convective lines in MY, similar to the observations. The distinguishing Z_{DR} that differentiates the PSDs of the convective and stratiform

regions is more prominent in MY; this matches the findings of Putnam et al. (2014). Insufficient size sorting by the DM MOR forecast highlights MP scheme challenges that extend beyond simply adding a second moment.

Z_{DR} in TOM and WDM shows no clear organization based on the structure of the convective systems (Fig. 2.3e,n). There is little difference between Z_{DR} in the convective and stratiform regions, and no clear size sorting signatures that match the observations. In fact, the highest Z_{DR} in TOM is in an area of light precipitation on the rear side of the convective line in Western Missouri, to the north and south of the convection in Iowa, and in isolated light showers in Missouri (indicated by arrows in Fig. 2.3e). Relatively high Z_{DR} values are often seen with developing storms like those in Missouri, but the remaining noted Z_{DR} patterns do not match the observations. Dawson et al. (2014) found that the size-sorting of hail and graupel had a greater impact on low-level Z_{DR} signatures than the size-sorting of rain. Both TOM and WDM are only SM for graupel (they do not include hail) and thus there is no size-sorting of graupel. Despite the apparent lack of size sorting, which is one of the features tied to maintaining a stratiform precipitation region in Putnam et al. (2014), TOM still represents the coverage of the convective and stratiform precipitation regions relatively well. Wheatley et al. (2014) found in their real case EnKF study of an MCS that the Thompson scheme replicated the convective and stratiform regions well due to broad and intense development of snow aloft. Thompson is not DM for snow, but it does use a unique snow PSD and diagnostic N_{0s} , and TOM contains stratiform coverage similar to that produced by the fully DM MOR and MY results. WDM also has areas where high Z_{DR} is located on the rear edge of convection in northern Missouri and southern Iowa

(indicated by arrows in Fig. 2.3n). In fact, Z_{DR} is relatively low in the most intense areas of convection ($Z > 40$ dBZ), indicating a large number of small to moderate-sized drops. Given that wet graupel is the dominant category present (indicated by arrows in Fig. 2.4e), it is likely that the wet graupel that exists is small and shedding small raindrops. This differs from MOR and MY, which also show a significant contribution to Z from wet graupel but have much higher Z_{DR} values, indicating larger wet graupel and a significant difference in the graupel PSDs between the schemes.

Z_{DR} differs more substantially between WDM and WSM compared to Z (Fig. 2.3m-n,p-q). The Z_{DR} maxima from the two schemes are about the same, but in WSM Z and Z_{DR} have a monotonic relationship, with the highest Z_{DR} co-located with the highest Z ; this is because the WSM scheme with a fixed N_0 is incapable of size sorting. WDM does not improve upon WSM, however, compared to the observations, since Z and Z_{DR} do not differ between convective and stratiform precipitation regions and the size sorting signatures appear in the wrong locations. The only difference between WDM and WSM is that WDM is DM for rain, further emphasizing the impact that the size sorting of graupel has on low-level rain PSDs and the associated Z_{DR} signatures.

Simulated K_{DP} is generally lower in all members compared to observations with values mostly less than $2.0^\circ \text{ km}^{-1}$. A few more intense convective areas ($Z > 50$ dBZ) in MY and WSM have K_{DP} higher than $2.0^\circ \text{ km}^{-1}$ (Fig. 2.3i,r) which agrees more closely with the observations (Fig. 2.3c). MY and MOR have similar Z_{DR} maxima but generally lower K_{DP} compared to the observations so the rain PSDs must contain a lower concentration of small to moderate-sized drops (Fig. 2.3c,i,l). The convective regions in MY, MOR, and WDM contain significant wet graupel (Fig. 2.4c-e). Low Z_{DR} and K_{DP}

are indicative of small wet graupel in WDM (Fig. 2.3n) while significantly higher Z_{DR} in MY and MOR (Fig. 2.3h,k) suggests larger wet graupel but with a low water ratio. Low Z_{DR} is also indicative of the lack of large raindrops in WDM due to the gamma distribution with a short tail in the large drop's end. WSM has lower Z_{DR} but similar K_{DP} (Fig. 2.3f,r) compared to MY and similar Z_{DR} but higher K_{DP} compared to TOM, indicating a higher concentration of small to moderate-sized drops due to a large fixed N_{0r} . A high bias in graupel compared to observations (Fig. 2.4a) could potentially explain low K_{DP} (as compared to an all-rain scenario), but WSM, as well as TOM, have similarly low K_{DP} values in areas of pure rain.

Another significant difference in the forecasts compared to the observations is the lack of significant K_{DP} in the stratiform precipitation region over central Iowa. Those members that show this trailing precipitation (TOM, MY, MOR) only have noteworthy K_{DP} where Z exceeds 35 dBZ (Fig. 2.3f,i,l); the observations exhibit low (but consistent) K_{DP} throughout the stratiform region (Fig. 2.3c). Although the melting layer differs between the forecasts, which could contaminate the K_{DP} results, K_{DP} is also lower in areas of pure rain. In MOR, Z_{DR} is higher than observed in this area, indicating PSDs with a few larger raindrops and lower water content overall (Fig. 2.3k). Z_{DR} in TOM and MY is closer to the observations but similarly low K_{DP} values suggest an overall low bias among the DM schemes in the concentration of moderately-sized raindrops and their water content (Fig. 2.3f-i). The use of a triple-moment (TM) microphysics scheme with an effectively variable shape parameter would provide greater flexibility to represent a wider range of possible PSDs, including those with a greater number of moderately-sized drops and higher liquid water content/rain rate.

2.3.1.2 Quantitative evaluation of forecasts

Although forecast errors at all scales continuously grow as forecast length increases, the error growth rate is much larger for smaller scale phenomenon (e.g., convective cells). Additionally, diagnostic metrics are highly sensitive to displacement errors for storm scale forecasts, especially for fine-scale structures, making one-to-one quantitative verification even more difficult. A few different methods of quantitative comparison that help account for these errors are considered.

Percentile histograms of simulated Z , Z_{DR} , and K_{DP} are calculated over the domain used in Fig. 2.3 to gauge the overall distribution of values (Fig. 2.5). The histograms are created by first ranking all observed and simulated values individually and then distributing the simulated values within 10 bins representing the observed percentiles between 0.0 and 1.0. For reference, the observed histograms for each variable are provided in Fig. 2.5a-c and a black line indicating the number of observed values per bin is provided for all simulated results. There is a high bias in the simulated Z results relative to the largest observed Z values, indicative of strong convective precipitation, especially for MY and MOR (Fig. 2.5g,j). Qualitative comparisons suggested that the convective regions contained more intense precipitation over a larger area and that wet graupel contributed to high Z . The observed distribution peaks at around 35 dBZ (Fig. 2.5a), which corresponds to Z from the large region of stratiform precipitation in central Iowa and contributes to the number of values in the middle percentiles. The MOR and TOM distributions are most similar to the observations in this mid-range, though all forecasts have at least some low bias. MOR has a consistent high bias for low and high Z due to an over-forecast of precipitation coverage (Fig.

2.5j). Conversely, WDM has a consistent low bias at nearly all percentiles, lacking the stratiform precipitation and significantly under-forecasting precipitation coverage overall (Fig. 2.5m).

The observed distribution of Z_{DR} peaks around 1 dB, and extends up to 4 dB (Fig. 2.5b). TOM, and particularly MY and MOR, have a high bias in the higher percentiles due to the over-forecast east-west extent of the convective lines. MOR has a significant bias above the 90th percentile (Fig. 2.5k) related to the large drops in the stratiform region, oblate wet graupel in the convective region, and over-forecast in precipitation coverage overall. On the other hand, WDM and WSM have a similar low bias above the 50th percentile. The low bias in WSM may be related to the relatively high fixed N_{0r} of $8 \times 10^6 \text{ m}^{-4}$ (Fig. 2.5q). Although WDM is DM for rain, it follows a similar behavior as the SM WSM, which was also noted in the qualitative evaluation.

The K_{DP} histograms for the ensemble members all follow a similar trend relative to one another with a steadily increasing number of values up to the 90th percentile. The forecasts better match the observations in the mid to upper range of percentiles. There is a low bias in the lowest percentiles due to the lack of significant K_{DP} in the stratiform regions in the forecasts. Additionally, above the 90th percentile, which represents the highest observed K_{DP} values in the convective regions, there is a low bias in all members but MY. In general, all members have simulated K_{DP} values lower than observed in both stratiform and intense convection regions due to apparent lower liquid water contents (TOM and WSM) and contamination by graupel (MOR and WDM).

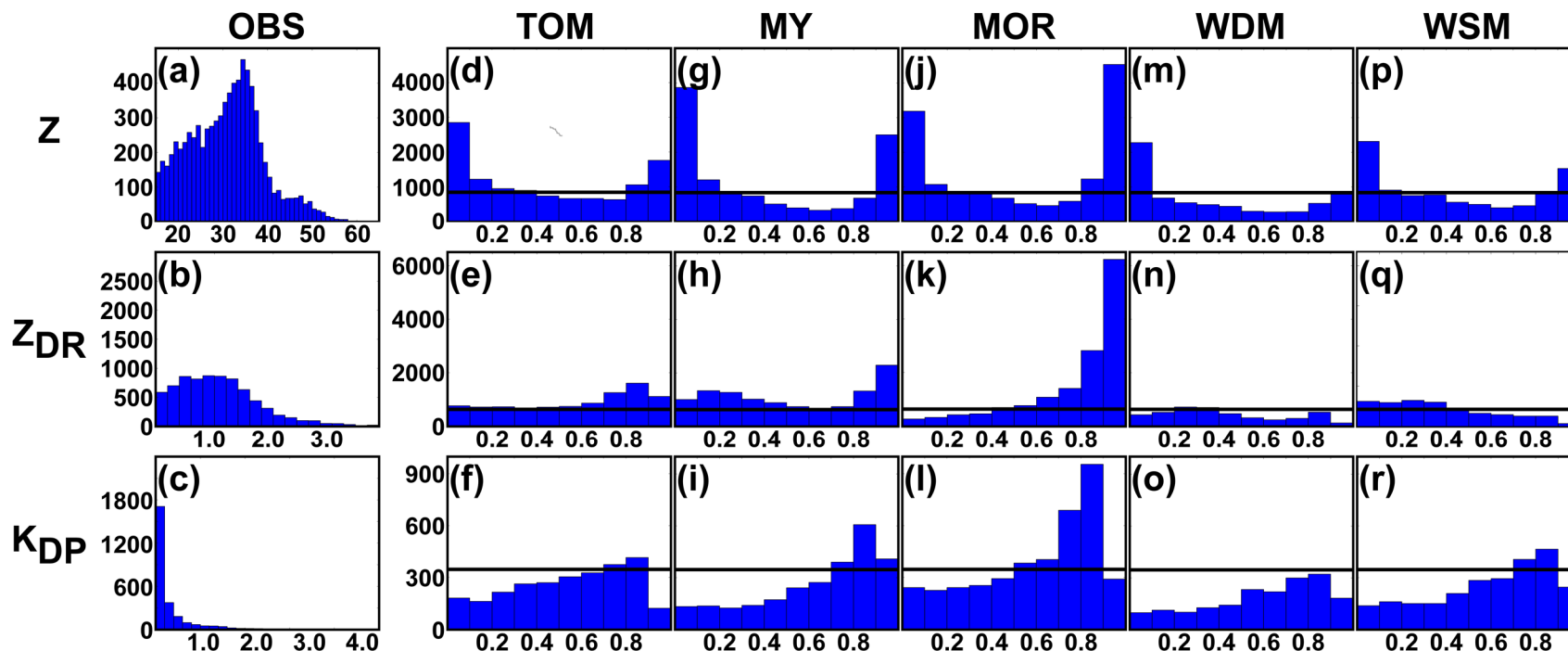


Fig. 2.5. Histograms of observed (a) reflectivity (dBZ), (b) differential reflectivity (dB), and (c) specific differential phase ($^{\circ} \text{km}^{-1}$) mosaic values at a $.5^{\circ}$ tilt from Fig. 2.3 as well as percentile histograms of simulated values at the same tilt locations from the (d-f) TOM, (g-i) MY, (j-l) MOR, (m-o) WDM, and (p-r) WSM forecasts distributed into bins based on the observed percentiles (noted by the solid black line).

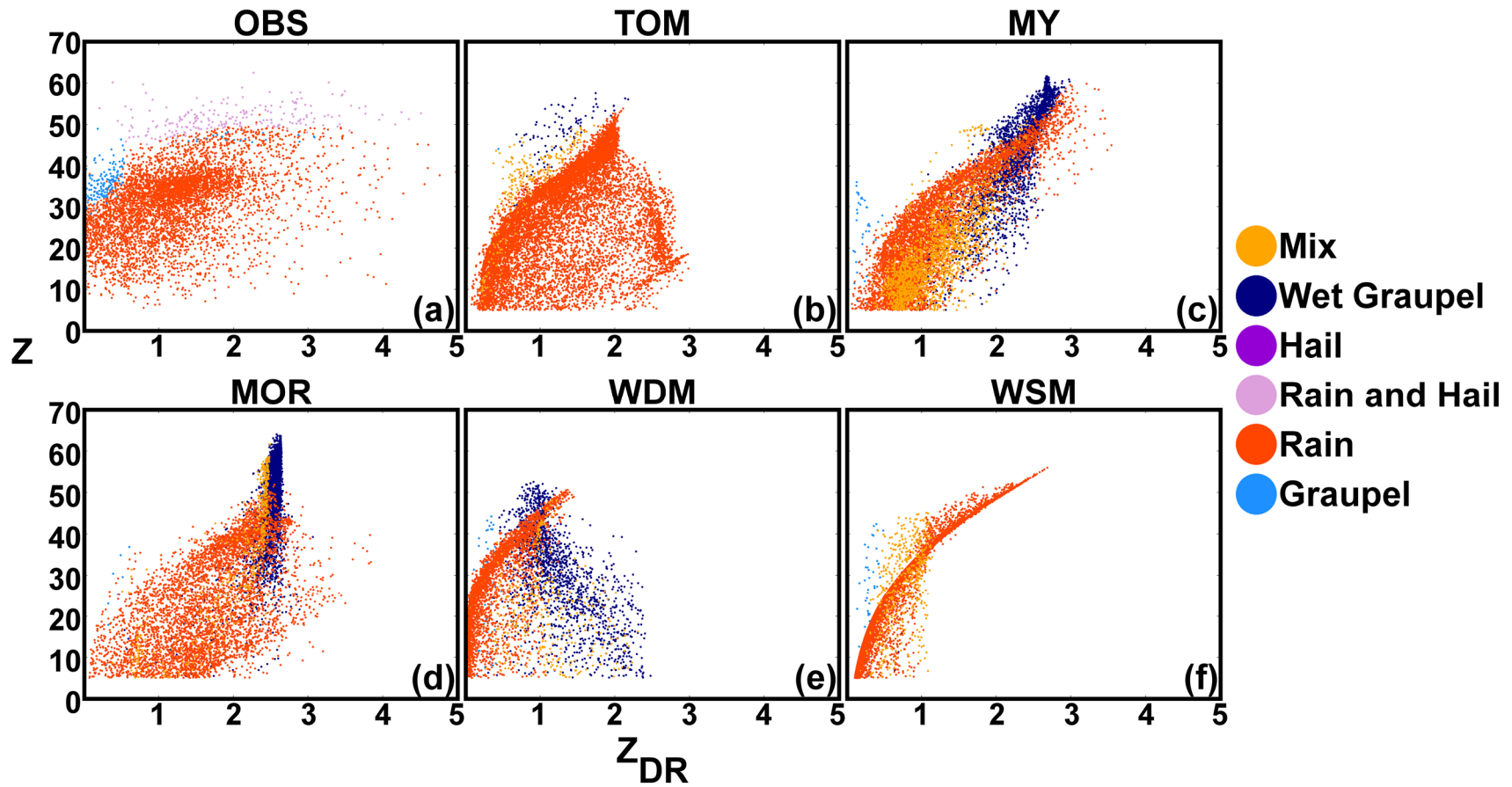


Fig. 2.6. Scatter plot of (a) observed reflectivity (dBZ) and differential reflectivity (dB) mosaic values at a 0.5° tilt from Fig. 2.3 as well as scatter plots of simulated values at the same tilt locations from the (b) TOM, (c) MY, (d) MOR, (e) WDM, and (f) WSM forecasts.

Another quantitative measure to evaluate the PSDs is scatterplots of Z versus Z_{DR} at a given location for the observations and forecasts (Fig. 2.6). Data points where $Z > 5$ dBZ from the Fig. 2.3 domain are considered and are categorized by dominant hydrometeor type using the same process as for Fig. 2.4. TOM, MY, and MOR show a broad overall distribution of Z and Z_{DR} value combinations similar to the observations. The additional free PSD parameter in the DM scheme allows for greater flexibilities in the range of possible PSDs in the forecast. The high density of data points for rain in the observations results from the broad region of stratiform precipitation (Fig. 2.6a). TOM, MOR, and MY, which performed well in terms of stratiform precipitation in the qualitative evaluation, have a similar concentration of data points for rain. The distribution in MOR is shifted toward slightly higher Z and Z_{DR} due to the widespread coverage of more moderate to large raindrops in the stratiform region. The large amount of melting ice species (snow, graupel, or a mix of both (Fig. 2.6d)) leads to the over-forecast convective intensity in MOR based on a comparison of the hydrometeor types associated these values in Figs. 2.3j and 2.4d; the same is true to a lesser extent with MY (Fig. 2.6c). The Z_{DR} maxima displaced from the leading edge of the convection in WDM results from wet snow and graupel (Fig. 2.6e, indicated by arrows in Figs. 2.3n and 2.4e), while that with TOM is mainly associated with rain (Fig. 2.6b, indicated by arrows in Figs. 2.3e and 2.4b).

WDM and WSM exhibit very similar distributions (Fig. 2.6e-f). There is little spread in the data points in WSM given the one-to-one relationship between Z and Z_{DR} in a SM scheme. Again, WDM, being only DM for rain, and with a diagnostic N_{0s} , exhibits the least variation compared to the more complex TOM and fully DM MOR

and MY. Most of the variation in both WSM and WDM is associated with the presence of mixed-phase precipitation where changing liquid and frozen water contents will lead to various Z and Z_{DR} combinations.

Since traditional numerical measures like root mean square error (RMSE) will indicate poor results when spatial errors are present, neighborhood methods have been developed to account for placement errors when the overall storm structure is otherwise good (Ebert 2008). One of these techniques, the fractions skill score (FSS, Roberts 2008; Roberts and Lean 2008), has been considered in past studies involving the CAPS SSEF and is used again here (Schwartz et al. 2009a; Cintineo et al. 2014). The FSS is calculated by finding the fraction of forecast grid points in a neighborhood with a given radius that exceeds a threshold value compared to the observations. The FSS is designed so that as the radius for the neighborhood increases to the size of the domain the score will asymptote towards an ideal finite value of 1. If there is bias present in the forecast, then the score will be less than 1, except for relatively small scale neighborhoods (Mittermaier and Roberts 2010). A forecast can be considered to have measurable skill when:

$$FSS > 0.5 + \frac{O_{domain}}{2}, \quad (2.3)$$

where O_{domain} is the domain-wide fraction of grid points where observations exceed the given threshold (Roberts and Lean 2008).

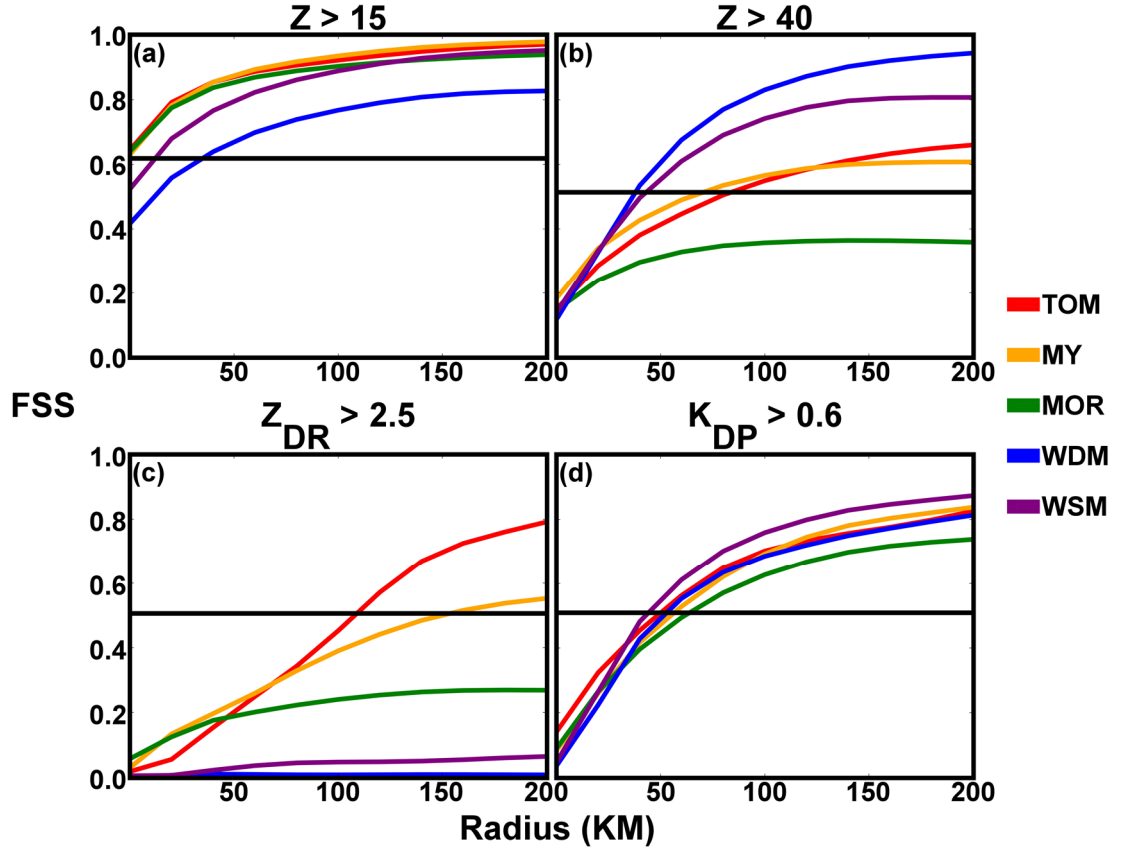


Fig. 2.7. Fractions skill scores for the TOM, MY, MOR, WDM, and WSM forecast results at increasing neighborhood radii for (a) reflectivity values exceeding 15 dBZ, (b) reflectivity values exceeding 40 dBZ, (c) differential reflectivity values exceeding 2.5 dB, and (d) specific differential phase values exceeding $0.6 \text{ } ^\circ \text{ km}^{-1}$ for the mosaics in Fig. 2.3. The black line indicates skill greater than a random forecast.

The FSS is calculated over the Fig. 2.3 domain for several thresholds for radii ranging from 0 to 200 km to account for the regional nature of MCS coverage (Fig. 2.7). Overall precipitation coverage, including both the convective and stratiform regions, is assessed using a threshold of $Z > 15$ dBZ (Fig. 2.7a). All forecasts perform well at this threshold. TOM, MY, and MOR show skill with initial scores around 0.65 that increase to around 0.9 at the 100 km radius. WDM has the worst score overall, averaging around 0.2 less than other members, likely due to the low precipitation coverage bias. When the Z threshold is increased to 40 dBZ to assess the prediction of

intense convective precipitation (Fig. 2.7b), there is more spread between the members, and all members exhibit very poor scores for small radii when large spatial errors are present. Interestingly, WDM has the highest score for the 100 km radius due to less extensive east-west coverage bias of the convective lines compared to the other members. WDM under-forecasts precipitation overall but matches the observations better in the convective regions. TOM and MY show some skill using a 100 km radius, but do not improve much with increased radii. MOR, which exhibits substantial high Z bias due to the over-forecast of intense convective precipitation, has no measurable skill.

A Z_{DR} threshold of 2.5 dB is chosen to assess convective regions in the observations where the largest drops are present, specifically the maxima seen with the polarimetric signatures associated with size sorting on the leading edges of convective lines (Fig. 2.7c). Scores are generally poor; the only skillful forecasts are TOM, which shows skill at a 100 km radius, and MY, which shows skill at a 150 km radius. This result indicates the coverage and intensity of significant Z_{DR} in TOM in convective regions is closest to the observations without over-forecasting large drops overall within the stratiform region. However, the qualitative evaluation in section 2.3.1.1 showed Z_{DR} in TOM is displaced and large radii neighborhoods miss these fine-scale details. MOR is likely negatively impacted by the high Z_{DR} coverage bias in the stratiform region and greater east-west extent of convective regions. WDM and WSM are biased towards small hydrometeor sizes.

Similarly to Z_{DR} , a threshold of $0.6^\circ \text{ km}^{-1}$ for K_{DP} is chosen to highlight the convective cores where higher liquid water content is present (Fig. 2.7d). The K_{DP}

maximum is generally lower in all members than in the observations and skill scores at higher thresholds will be very poor. All members have skill for radii greater than 50 km (Fig. 2.7d). Thus, convective regions with high K_{DP} are relatively well placed, with the caveat that graupel contamination may affect the upper range of these values. The better FSS scores for K_{DP} compared to Z_{DR} are likely due to the more direct linkage between high liquid water content and intense convection while Z_{DR} patterns associated with size sorting are not co-located with Z maxima. Z_{DR} provides a more stringent assessment of microphysical processes and states.

Since the range of simulated polarimetric variable values in each forecast may not match the overall range of the observations, the FSS scores are calculated again for the same thresholds using percentiles (Fig. 2.8). The percentile value in the observations consistent with each numeric threshold is used as the threshold to assess the forecast percentile values. This method normalizes the scores for those forecasts which do not produce values as high as the observations, as in the Z_{DR} values for WDM and WSM. The scores for $Z > 15$ dBZ and $K_{DP} > 0.6^\circ \text{ km}^{-1}$ are very similar to the previous results. However, the new scores are improved significantly for the $Z > 40$ dBZ convective assessment and $Z_{DR} > 2.5$ dB which are more affected by maximum value biases. More specifically, those forecast members that showed no skill without using percentiles (MOR for $Z > 40$ dB; TOM, WDM, and WSM for $Z_{DR} > 2.5$ dB) now show skill at higher radii when using percentiles. The most significant improvement is in WDM and WSM; these members have a low bias compared to the other members for high Z_{DR} values. The percentile calculations show the highest Z_{DR} values from WDM and WSM forecasts are well placed compared to the observations but underestimated in value.

Future quantitative assessment methods of polarimetric variables may need to take into account maximum and minimum value biases.

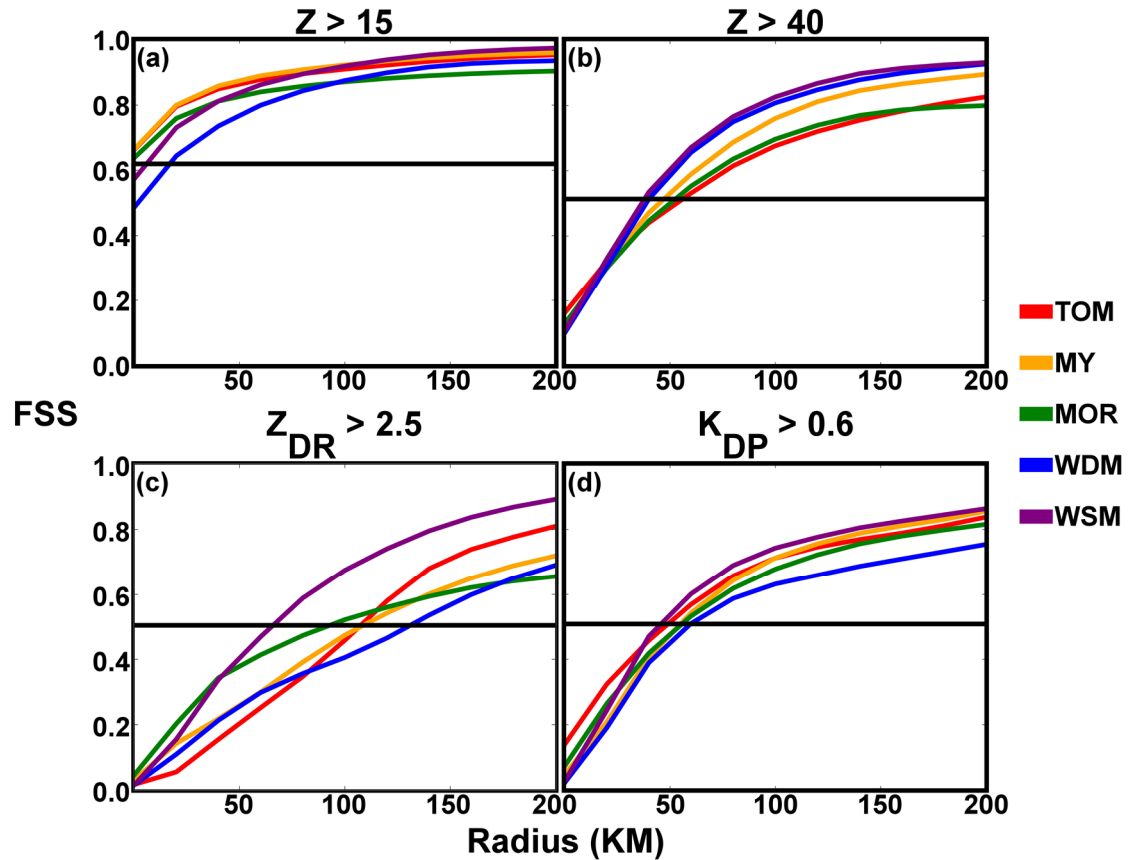


Fig. 2.8. As in Fig. 2.7, but with the FSS scores calculated based on percentile values relative to the observations.

2.3.2 The 20 May 2013 supercell case

Several supercell thunderstorms developed along a stationary cold front and dry line across the southern plains early afternoon 20 May 2013, the most intense of which occurred over central and southern Oklahoma. Dewpoints in the low 70s (F) and 5000 J kg⁻¹ of CAPE combined with winds in excess of 50 kts at 500 hPa associated with an upper level trough to create a volatile severe weather environment. The most intense storm, which produced an EF-5 tornado, formed near the dry line/cold front intersection

as the cold front stalled shortly before 2000 UTC. The tornado killed 24 people and caused over 1 billion dollars in damage across the southern Oklahoma City metropolitan area (NWS 2014). Additional tornadoes were reported across Oklahoma as well as widespread large hail reports over southern Oklahoma (SPC 2014a).

2.3.2.1 Qualitative evaluation of forecasts

Mosaics of 0.5° tilt observed and simulated Z , Z_{DR} , and K_{DP} for all members at 2100 UTC (Fig. 2.9) as well as hydrometeor classifications using the same process in section 2.3.1.1 (Fig. 2.10) are evaluated. Locations of WSR-88D radar sites within the domain used to create the observed and simulated variable mosaics are included in Figs. 2.9a and 2.10a. The placement and coverage of forecast convection are worse than in the MCS case due to the longer forecast lead time, the isolated nature of discrete supercell storms, and that storm development is not directly influenced by assimilated radar data at the initial condition time. The Z patterns for the southern Oklahoma storms in MY and MOR (indicated by ‘A’ in Fig. 2.9g,j) both exhibit classic supercell structure with a hook-echo/rear flank downdraft, indicative of the presence of a mesocyclone. It should be noted that the structures are rather large compared to the observations; this is often seen in forecasts using a 4 km grid spacing (Lean et al. 2008, Johnson et al. 2013). TOM, WDM, and WSM have a line of cells that are smaller and low-precipitation in comparison but have supercell characteristics (Fig. 2.9d,m,p). For reference, a plot of the Spring Experiment hourly max updraft helicity product (Kain et al. 2008; Kong 2013) for 2100 UTC is included (Fig. 2.11); the high values greater than $150 \text{ m}^2 \text{ s}^{-2}$ for the southern Oklahoma storm in all members are indicative of a mesocyclone (indicated by arrows in Fig. 2.11). As in the MCS case, WDM under-

forecasts the precipitation coverage, while MOR forecasts the most intense precipitation. Z in the observations (Fig. 2.9a) generally peaks at a higher value ($Z > 50$ dBZ) than in the model forecasts; MOR is most similar to the observations. However, the high Z in MOR is due to the presence of wet graupel (Fig. 2.10d), while high Z observations are mostly due to rain and hail. There is spurious convection in the northwest corner of the domain in all members.

The observed Z_{DR} is generally higher on the right (southeastern) edge of the forward flanks of the observed cells (Fig. 2.9b), exhibiting a distinctive Z_{DR} arc. Z_{DR} is lower in the center of the forward flanks of the central Oklahoma storms, possibly due to a hail-induced Z_{DR} hole, but the hydrometeor classification algorithm identifies little hail (Fig. 2.10a). The lower Z_{DR} is associated with higher K_{DP} (Fig. 2.9c), indicating moderately-sized drops and a high rain rate. Z_{DR} increases along the right forward flank of the dominant southern Oklahoma storm in MOR, MY, and to a lesser extent in WDM (indicated by arrows in Fig. 2.9h,k,n), while other convective cells are less organized and don't show this signature. The forecasts also don't show quite the same degree of increase in Z_{DR} between the center and right forward flanks as in the observations. As in the MCS case, there is a bias toward large drops and oblate, wet graupel in MOR (Fig. 2.10d). There is wet graupel in MOR, MY, and WDM along the right forward flank (indicated by arrows in Fig. 2.9c-e); Dawson et al. (2014) showed that the size sorting of melting hail and graupel had a substantial impact on the model representation of the Z_{DR} arc. MOR shows the highest Z_{DR} farther downwind the forward flank than the extent of the wet graupel, consistent with Dawson et al. (2014; see their Fig. 17). Wet graupel is present along the entire right forward flank in MY and WDM, and the

maximum Z_{DR} is not located along the immediate edge. Dawson et al. (2014) also found hail better replicated the observed coverage and intensity of the Z_{DR} arc compared to graupel which can lead to an over-extensive forward flank, as seen in this case.

TOM and WSM did not exhibit the same Z_{DR} pattern as the observations (Fig. 2.9e,q). There is a one-to-one relationship in WSM where high Z_{DR} occurs with high Z in the center of the cells. Similar to the MCS case, a relative Z_{DR} maximum occurs along the edges of smaller cells with less intense precipitation TOM, MOR, and WDM. This occurs in the southwest portion of the domain for MOR and TOM, in northwest Oklahoma for MOR, and in central Oklahoma for TOM and WDM (indicated by 1, 2, and 3 in Fig. 2.9e,k,n, respectively). As noted for the MCS case, high Z_{DR} is sometimes associated with aggressive size sorting in developing convection. The drop breakup scheme in MOR may have also contributed to the spikes in Z_{DR} values associated with weak precipitation in that case. The Z_{DR} in TOM appears particularly misplaced; there is a large area of Z_{DR} exceeding 2.5 dB that occurs between the more intense precipitation associated with the storm cells. The PSDs in this region are heavily weighted toward a few large drops given the low Z . Compared to MY and MOR, TOM, WSM, and WDM are not DM for graupel, which was noted to have an impact on size sorting in supercells.

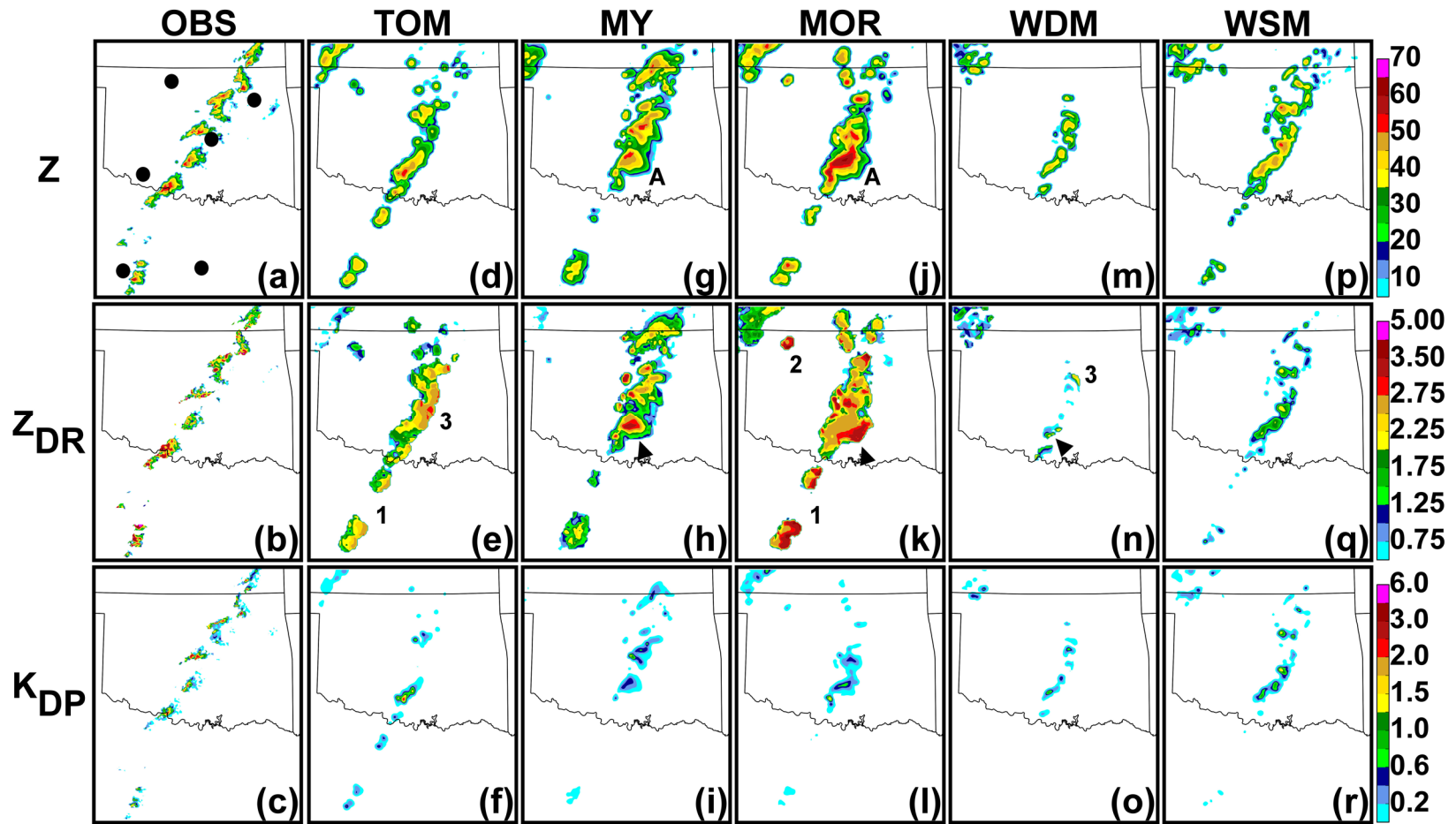


Fig. 2.9. Mosaics of observed (a) reflectivity (dBZ), (b) differential reflectivity (dB), and (c) specific differential phase ($^{\circ} \text{km}^{-1}$) at a $.5^{\circ}$ tilt 2100 UTC 20 May 2013 and simulated values at the same tilt locations from the (d-f) TOM, (g-i) MY, (j-l) MOR, (m-o) WDM, and (p-r) WSM forecasts. Features of interest referenced in the text are noted by arrows, numbers, and letters. Locations of WSR-88D sites used for both the observed and simulated variable plots are noted with black dots in (a).

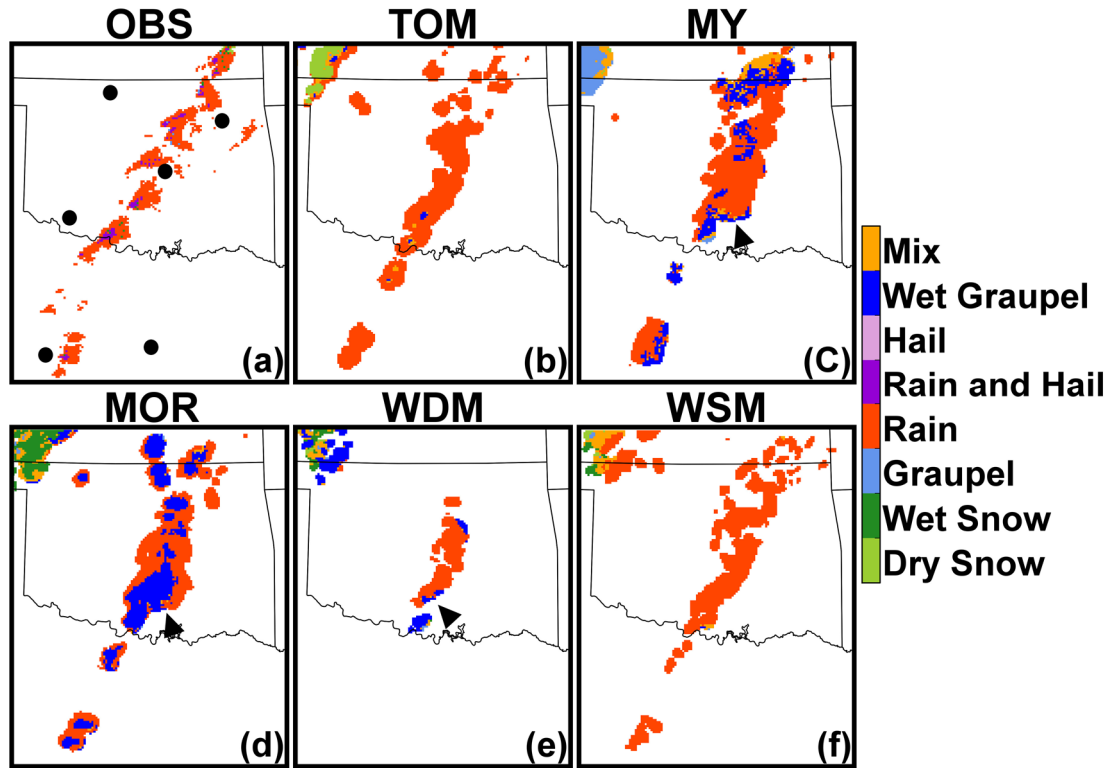


Fig. 2.10. Mosaic of hydrometeor classification using fuzzy logic for (a) observations at a .5° tilt 2100 UTC 20 May 2013 as well as classification of highest simulated linear reflectivity at the same tilt locations for (b) TOM, (c) MY, (d) MOR, (e) WDM, and (f) WSM forecasts. Features of interest referenced in the text are noted by arrows. Locations of WSR-88D sites used for both the observed and simulated variable plots are noted with black dots in (a).

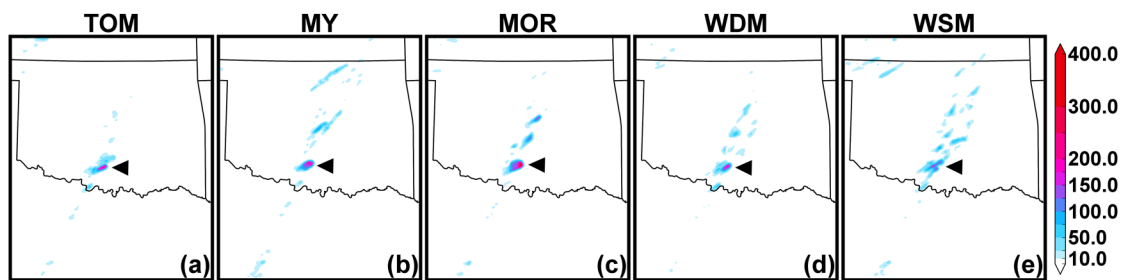


Fig. 2.11. 2D plots of maximum updraft helicity ($\text{m}^2 \text{s}^{-2}$) at 2100 UTC 20 May 2013 for (a) TOM, (b) MY, (c) MOR, (d) WDM, and (e) WSM. Features of interest referenced in the text are noted by arrows.

K_{DP} is under-forecast in all members compared to the observations. The observations peak above $3.0^{\circ} \text{ km}^{-1}$ (Fig. 2.9c), while only TOM has a maximum above $1.75^{\circ} \text{ km}^{-1}$ (Fig. 2.9f). Of note, the highest K_{DP} values are not co-located with the highest Z_{DR} values in the southern Oklahoma storm in MY and MOR (Fig. 2.9i,l). K_{DP} has a relative maximum in the center of the storm but decreases in the right forward flank where Z_{DR} is higher, another indication that size sorting has resulted in a few large raindrops in the Z_{DR} arc compared to elsewhere in the forward flank. Although there is some graupel present in the forecast that may contaminate the K_{DP} results, particularly in MOR, most of the forecast convection is classified as pure rain, suggesting liquid water content is under-forecast overall.

2.3.2.2 Quantitative evaluation of forecasts

As in Section 2.3.1.2, percentile histograms (Fig. 2.12) and FSSs (Fig. 2.13) are considered for quantitative evaluation. Both are calculated over a sub-domain that focuses on the line of supercells that extends from southeast Kansas to northwest Texas. The MY and MOR histograms show an over-forecast of precipitation coverage (Fig. 2.12g,j); this over-forecast is present but confined to lower percentiles in TOM and WSM (Fig. 2.12d,p). Given this circumstance, the mostly even distribution of intensities in the observations (Fig. 2.12a) is matched relatively well by these members. The WDM precipitation coverage is under-forecast so substantially that the Z distribution is lower than the observations for all percentiles (Fig. 2.12m).

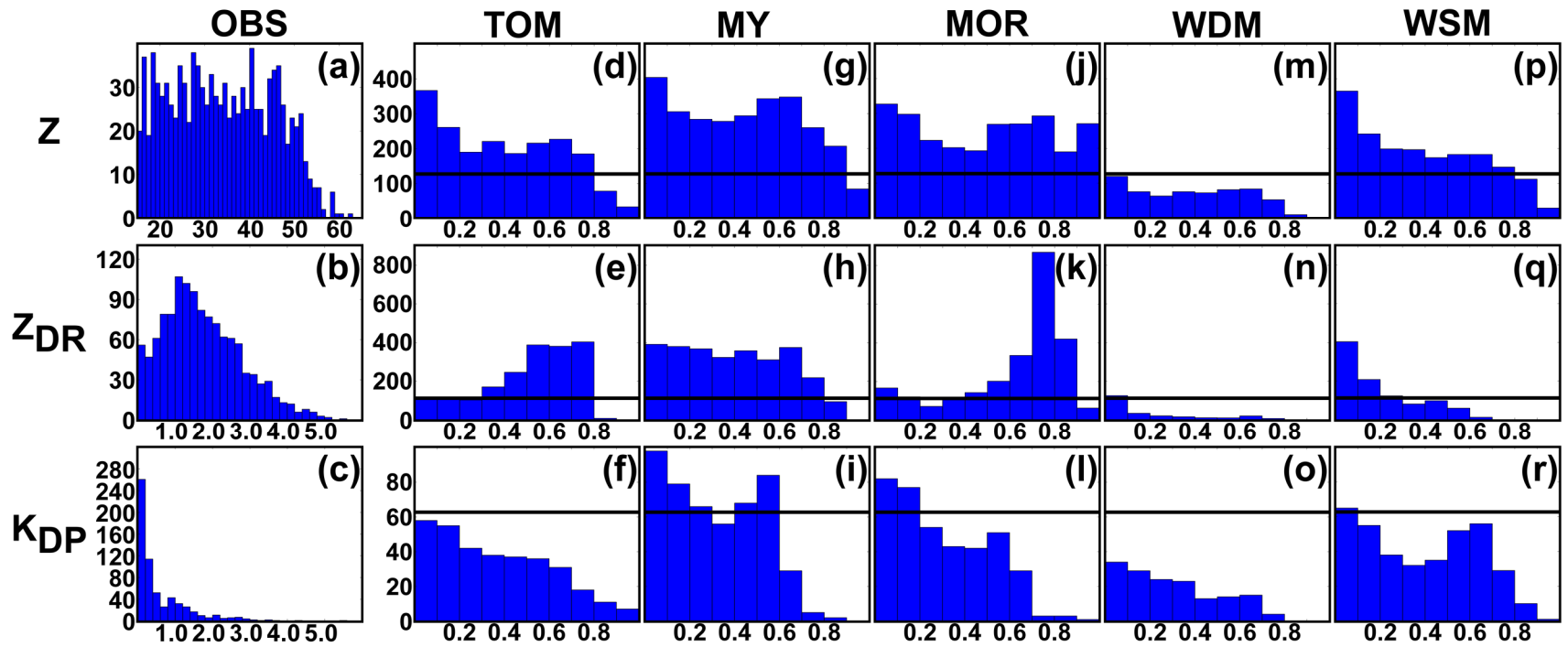


Fig. 2.12. Histograms of observed (a) reflectivity (dBZ), (b) differential reflectivity (dB), and (c) specific differential phase ($^{\circ}$ km⁻¹) mosaic values at a $.5^{\circ}$ tilt from Fig. 2.9 as well as percentile histograms of simulated values at the same tilt locations from the (d-f) TOM, (g-i) MY, (j-l) MOR, (m-o) WDM, and (p-r) WSM forecasts distributed into bins based on the observed percentiles (noted by the solid black line).

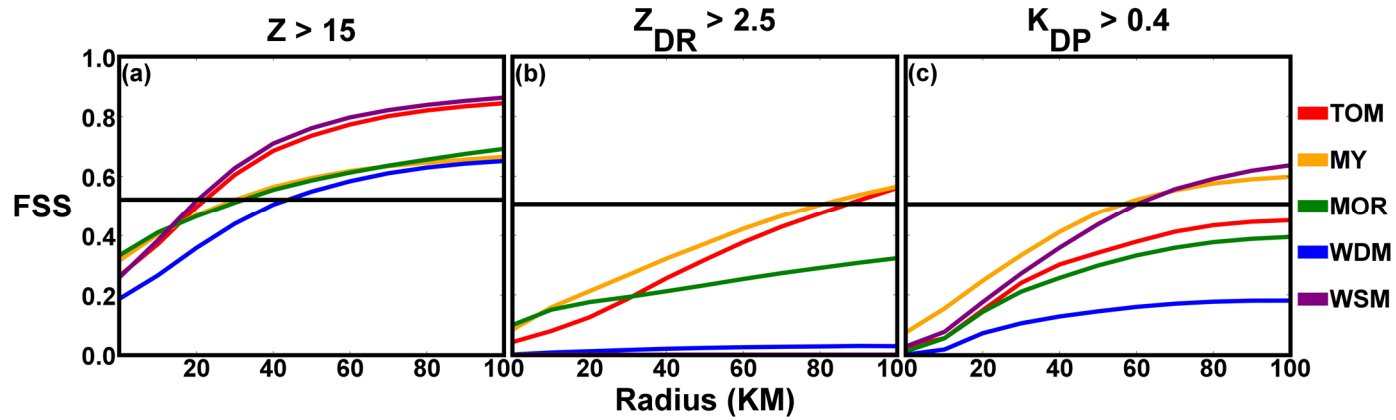


Fig. 2.13. Fractions skill scores for the TOM, MY, MOR, WDM, and WSM forecast results at increasing neighborhood radii for (a) reflectivity values exceeding 15 dBZ, (b) differential reflectivity values exceeding 2.5 dB, and (c) specific differential phase values exceeding $0.4 \text{ } ^\circ \text{ km}^{-1}$ for the mosaics in Fig. 2.9. The black line indicates skill greater than a random forecast.

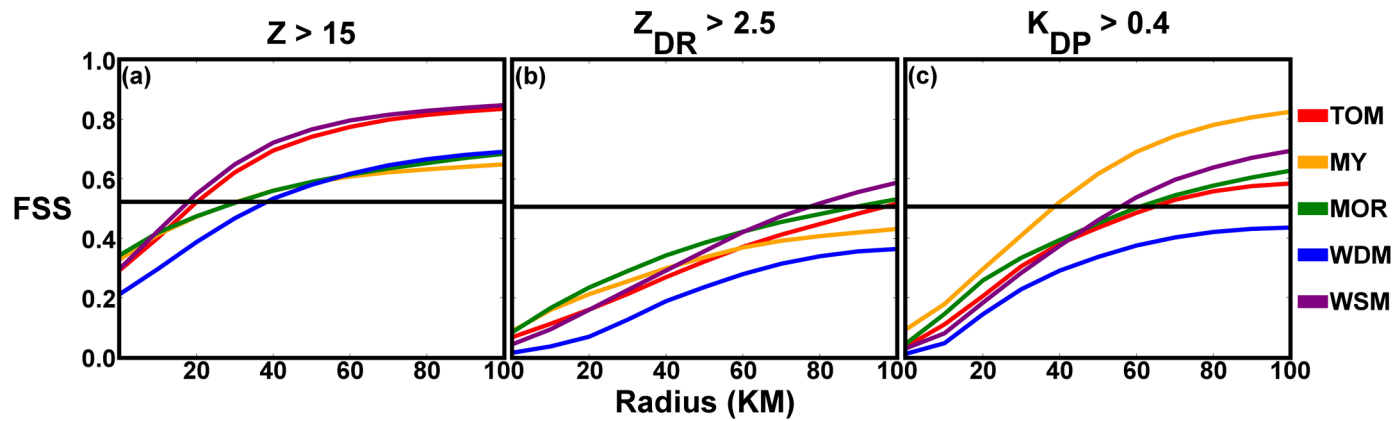


Fig. 2.14. As in Fig. 2.13, but with the FSS scores calculated based on percentile values relative to the observations.

There is a high bias in the amount of Z_{DR} values due to the greater precipitation coverage in TOM, MY, and MOR. Z_{DR} in MY actually has a relatively even distribution compared to the observations with the caveat that the over-forecast of precipitation coverage leads to a higher number of values overall (Fig. 2.12h). After considering the grid scale, simulated Z_{DR} in MY represents the varying degree of maximum raindrop size in the rain PSD well. MOR has a significant peak at the 70th percentile (Fig. 2.12k), corresponding to the widespread Z_{DR} around 2.5 dB and greater in the central forward flank regions where wet graupel is present (Fig. 2.10d). Z_{DR} in WSM, for all but the lowest percentiles, is lower than the observations compared to TOM, MOR, and MY (Fig. 2.12q); this is expected given the fixed intercept parameters used in this SM scheme. Z_{DR} in WDM has a significant low bias (Fig. 2.12n) due to small raindrops and small, wet graupel in precipitation under-forecast in coverage and intensity.

In the K_{DP} distributions, all members but WDM have a similar number of values compared to the observations for low K_{DP} percentiles, but their distributions quickly decrease for the higher percentiles (Fig. 2.12f,i,l,r). Similarity between the model and observed distributions for low K_{DP} is somewhat misleading; forecast K_{DP} is too low in regions of heavy precipitation and insignificant in light precipitation, where low K_{DP} is seen in the observations. All forecast members appear to have generally lower liquid water contents than the observations in pure rain areas.

The FSS is calculated for radii only up to 100 km due to the more localized nature of the supercell case. All members show some skill for radii of 20-40 km or more for a Z threshold of 15 dBZ (Fig. 2.13a). WSM and TOM have noticeably higher scores than the other members because the precipitation coverage is more similar to the

observations; precipitation coverage is over-forecast in MY and MOR and under-forecast in WDM. The qualitative evaluation showed more realistic Z and Z_{DR} patterns in MY and MOR compared to WSM and TOM but the size of the supercells in the former cases was notably larger. Members generally show no skill for Z_{DR} (Fig. 2.13b). The K_{DP} threshold (Fig. 2.13c) is decreased slightly compared to the MCS case since the simulated values are lower overall ($.4^{\circ} \text{ km}^{-1}$ instead of $.6^{\circ} \text{ km}^{-1}$). MY and WSM, as in the MCS case, have the best skill for K_{DP} for large radii ($> 60 \text{ km}$), but these scores are not high ($< .7$). Issues of grid-scale and storm placement leave many quantitative challenges for the simulated polarimetric variables, especially in terms of Z_{DR} patterns for a supercell case.

Fig. 2.14 replicates the FSS calculations for Fig. 2.13 using percentile values. As in the MCS case, those forecasts with very poor scores for $Z_{DR} > 2.5 \text{ dB}$ due to lower maximum values than the observations (WDM and WSM) show significant improvement. However, all forecasts still show little to no skill overall. The spatial extent and coverage of Z_{DR} signatures for the supercell case appear more difficult to match than the MCS case. Unlike the MCS case, the K_{DP} scores are also improved for all members. The histograms for each case show that the distribution of K_{DP} values is a better match in the MCS case than for the supercell case where there is a greater low bias in K_{DP} values. The use of percentiles helps better match the observed and forecast distributions for comparison so that all but WDM show at least some skill at the larger radii values. It is clear the poor K_{DP} scores when percentiles aren't used are due to the low bias of values in the forecast.

2.4 Summary and conclusions

Polarimetric variables are simulated from the CAPS spring experiment storm scale ensemble forecasts (SSEF) for evaluation of both single-moment (SM) and double-moment (DM) model microphysics (MP) schemes. An existing polarimetric radar data simulator (PRDS, Jung et al. 2008a; Jung et al. 2010) is modified to add several new MP schemes including Thompson (TOM), Morrison (MOR), and WDM6 (WDM); Milbrandt and Yau (MY) and WSM6 (WSM) were already included. Careful attention is paid in the simulation to the hydrometer types and particle size distributions (PSDs) of each scheme to properly represent the forecast microphysical state. Two cases are considered: a 4-hour forecast for a series of mesoscale convective systems (MCS) from 20 May 2013 and a 21-hour forecast of supercell thunderstorms from the 20 May 2013 Oklahoma tornado outbreak. Simulated reflectivity (Z), differential reflectivity (Z_{DR}), and specific differential phase (K_{DP}) from a single ensemble member forecast using each scheme with otherwise similar model settings are compared to observations from the recently upgraded WSR-88D radar network.

Z_{DR} in MOR and MY in the supercell case, as well as classification of the hydrometeors present, produce results consistent with Dawson et al. (2014), which demonstrated the role that the size sorting of graupel plays in the formation of the Z_{DR} arc. The other schemes examined are not DM for graupel and do not show this pattern. In addition, the two schemes that best represent polarimetric size sorting signatures (MY and MOR) also show better coverage of stratiform precipitation compared to the SM WSM scheme. TOM, only DM for rain with a unique snow PSD and diagnostic N_{0s} , shows incorrect size sorting signatures but still represents the stratiform precipitation

region well. Qualitative and quantitative evaluation shows that WDM, despite being DM for rain, has a similar one-to-one relationship between Z and Z_{DR} as WSM and no stratiform precipitation development. The other DM schemes include more complex diagnostic equations (TOM) or are fully DM (MY and MOR), demonstrating that size sorting of hydrometeor categories in addition to rain is as important in improving the forecast microphysical state. TOM, MOR, and WDM all have incorrect Z_{DR} maxima associated isolated, weak convection on the back side of convective lines where isolated large drops are not expected.

Notable biases are present in each scheme. Z and Z_{DR} in the stratiform precipitation region of the MCS are too high in TOM, MY, and particularly MOR, indicating that the forecast rain PSDs contain too many large drops for stratiform rain. The MY, MOR, and WDM forecasts contain a large amount of wet (melting) graupel in convective areas, as determined by the coexistence of rain and graupel in the model, while the observations have a little hail but mostly rain in similar locations. MY and WDM also show this bias, though the coverage is not as broad. These areas of wet graupel contribute to more extensive intense Z compared to the observations. MY includes a hail category but contains a similarly significant amount of graupel, likely due to a strict minimum hail size threshold in the scheme. Finally, simulated K_{DP} values are lower in all members for both cases, particularly in intense convective precipitation regions. K_{DP} increases with large amounts of moderate sized drops and higher liquid water contents, but large raindrops and graupel with a low water ratio are apparent in MOR and MY, while WDM and WSM have a bias toward small raindrops and graupel. Additionally, K_{DP} is a measurement related to mass in a volume, and with a low-

resolution 4 km grid the volumes will be quite large and miss more localized maxima that may be present.

There are several challenges inherent in large-domain convective-scale forecasts that can hamper our ability to gain information about the different microphysics schemes from the simulated variables. A poor forecast of storm structure for a given supercell or MCS will be missing notable polarimetric value patterns. For example, TOM, WDM, and WSM have poor supercell structures that make Z_{DR} arc comparisons more difficult. Previous studies have shown that forecasts performed using 4 km horizontal grid spacing may miss some fine-scale details in convection (Bryan et al. 2003), result in larger scale structures (Lean et al. 2008, Johnson et al. 2013), and impede processes such as development of trailing stratiform precipitation (Bryan and Morrison 2012; Xue et al. 2013). Other studies that have considered simulated polarimetric variables use a smaller grid scale than 4 km: 2 km in Putnam et al. (2014), 1 km in Jung et al. (2012), and 1 km in Li and Mecikalski (2012). These patterns may also be displaced compared to observations, making quantitative comparisons difficult.

Forecast members show some skill in terms of the fractions skill score (FSS) for Z and K_{DP} in the MCS case but higher scores require larger radii, and all forecasts exhibit very poor skill for Z_{DR} in both cases. Although qualitative comparisons indicate that MY and MOR represent Z_{DR} patterns relatively well, substantial spatial error leads to FSS scores with no skill. Normalizing the FSS using percentile values results in a significant improvement in skill for forecasts that do not contain simulated values as high as the observations. Future studies should continue to adapt these methods as forecasts are refined and improved before general statistics can be produced for all forecasts over

the Spring Experiment period. Such information could be used in the future to provide additional forecast products as well as serve research purposes like determining which MP scheme may best represent polarimetric signatures in supercells for use in dual-pol data assimilation experiments.

Finally, we point out that there are also many uncertainties with the polarimetric radar simulator. There are various assumptions made on the water drop aspect ratio, canting angle of snow, hail, and graupel, and water fraction for mixed phase species. These are some of the aspects that still need refinement and tuning, and they can affect the microphysics evaluation. Dawson et al. (2014) developed an alternative water fraction model for the mixed phases that depends on the size spectrum. The relative performance of this model should be evaluated in the future.

Chapter 3 Probabilistic Prediction of Polarimetric Radar Variables in EnKF-Initialized Ensemble Forecasts of a Mesoscale Convective System

3.1 Introduction

A major focus in recent convective scale numerical weather prediction (NWP) research has been improving both the forecast initial conditions and the microphysics parameterizations that are important for convective-scale predictions; both areas address major challenges identified for the Warn-on-Forecast paradigm by Stensrud et al. (2013). Data assimilation (DA), which is an indispensable part of convective-scale NWP, aims to improve the forecast initial condition by optimally combining available observations and a background model state to produce the best possible estimate of the atmospheric state. One popular DA method for convective-scale NWP is the ensemble Kalman filter (EnKF, Evensen 1994; 2003), which uses an ensemble of forecasts to estimate the background error covariance. The application of EnKF methods for the assimilation of radar observations has produced successful results for a variety of real storm cases (e.g., Dowell et al. 2004; Dowell and Wicker 2009; Lei et al. 2009; Aksoy et al. 2009; Aksoy et al. 2010; Dowell et al. 2011; Snook et al. 2011; Dawson et al. 2012; Jung et al. 2012; Snook et al. 2012; Yussouf et al. 2013; Tanamachi et al. 2013; Putnam et al. 2014, hereafter P14; Wheatley et al. 2014; Snook et al. 2015; Yussouf et al. 2015).

Note: This Chapter is an extended version of our paper: Putnam, B. J., M. Xue, Y. Jung, N. A. Snook, and G. Zhang, 2016: Ensemble probabilistic prediction of a mesoscale convective system and associated polarimetric radar variables using single-moment and double-moment microphysics schemes and EnKF radar data assimilation. *Mon. Wea. Rev.*, Submitted.

Additionally, microphysics parameterization (MP) schemes are used in convective-scale NWP models for the explicit prediction of fields describing the type and amount of hydrometeors present within the simulated storms. Most MP schemes represent the hydrometeor particle size distribution (PSD) in bulk form via the simplified gamma distribution:

$$N(D)_x = N_{0x} D_x^{\alpha_x} e^{(-\Lambda_x D)}, \quad (3.1)$$

where $N(D)_x$ is the number of particles of hydrometeor species x with diameter D in a unit volume, and Λ_x , N_{0x} , and α_x are the slope, intercept, and shape parameters, respectively (Ulbrich 1983; Milbrandt and Yau 2005a). MP schemes are often characterized by the number of PSD moments that are explicitly predicted and used to derive the same number of PSD parameters. Single-moment schemes (SM) usually predict the third moment of the distribution, the hydrometeor mixing ratio (q_x), while specifying the intercept and shape parameters; double-moment (DM) schemes also predict the zeroth moment, the total number concentration (N_{tx}), so that both the slope and intercept parameters can be updated. The shape parameter is specified in DM schemes.

The use of DM scheme for EnKF-based convective-scale NWP has been shown to improve storm structure and evolution during the analysis cycles as well as forecasts for both supercell and mesoscale convective system (MCS) cases. Dawson et al. (2009) showed that DM and triple-moment (TM) schemes produced better predictions of a supercell storm than a SM scheme. Xue et al. (2010) first successfully applied EnKF to the estimation of model states associated with a DM scheme using simulated radar observations of a supercell, while Jung et al. (2012) first successfully used a DM

scheme for EnKF radar DA for a real supercell storm. For the 8 May 2003 Moore, Oklahoma supercell, Yussouf et al. (2013) found that both a fully DM scheme (which predicts total number concentration for graupel, N_{tg}) as well as a semi-DM scheme (which diagnoses intercept parameter for graupel, N_{og}) produced more small graupel than a SM scheme; this graupel was advected farther downwind, forming a broader forward flank downdraft (FFD), in agreement with observations. For MCS cases, P14 and Wheatley et al. (2014) found that DM MP schemes improved the development of trailing stratiform precipitation compared to a SM scheme. A dramatic increase in the formation and detrainment of snow and ice from the leading convective towers rearward over the stratiform region resulted in much broader stratiform coverage.

Recently, simulated dual-polarization (dual-pol) radar variables have been used to evaluate microphysical states estimated through data assimilation and predicted by convective scale models for real cases, by comparing these variables to observations (Jung et al. 2012; Li and Mecikalski 2012; Dawson et al. 2014; P14; Posselt et al. 2015; Putnam et al. 2016). The dual-pol variables contain additional information on PSDs over reflectivity (Z), specifically information about the size, content, and diversity of hydrometeors present in the radar volume. For example, differential reflectivity (Z_{DR}) values are dependent on the horizontal-to-vertical axis ratio of hydrometeors; values are higher for large, oblate raindrops and low for dry, tumbling hail (Bringi and Chandrasekar 2001). Additionally, specific differential phase (K_{DP}) is sensitive to the amount of liquid water the radar pulse interacts with.

Dynamical and microphysical processes can lead to significant variation in hydrometeor PSDs over small spatial scales. For example, the size-sorting of

hydrometeors associated storm-relative wind shear in the forward flank of supercells leads to a significant increase in the number of large raindrops in low-level rain PSDs that can be identified by an increase Z_{DR} values known as the Z_{DR} arc (Kumjian and Ryzhkov 2008; Kumjian and Ryzhkov 2012; Dawson et al. 2014). This signature is indistinguishable in the observed Z pattern. Jung et al. (2012), in an EnKF data assimilation study of a supercell storm that occurred on 29 May 2004 in central Oklahoma, showed that using a DM MP scheme (Milbrandt and Yau 2005b) allowed the model to replicate observed dual-pol signatures such as the Z_{DR} arc. P14 found that simulated Z_{DR} patterns in the final EnKF analysis of an MCS produced using a DM scheme better represented the distribution of large, oblate raindrops in the leading convective line and small to medium sized raindrops in the trailing stratiform region compared to an analysis produced using a SM scheme. The SM analysis failed to capture this distinction, overestimating raindrop size in the stratiform region.

The P14 study, which considered DM schemes and simulated dual-pol variables, focused exclusively on deterministic forecasts of simulated Z . The current study expands upon P14 by performing and examining ensemble forecasts of the 8-9 May 2007 MCS case in terms of both Z and dual-pol radar variables. Ensemble forecasts offer additional benefits compared to deterministic forecasts, including the ability to produce probabilistic forecasts for precipitation events instead of a binary hit or miss forecast. Ensemble forecasts are integral to the Warn-on-Forecast vision outlined in Stensrud et al. (2009), providing the basis for operational probabilistic prediction of hazards associated with severe convection in the near future. Probabilistic forecasts help account for the uncertainties related to both the initial condition and the prediction

model (including the microphysics), so as to provide a means of measuring the level of confidence in the prediction.

One of the advantages of EnKF methods is that they inherently provide an ensemble of analyses suitable for initializing an ensemble of forecasts (Kalnay 2002). Analyses from well-tuned EnKF systems provide a good representation of flow-dependent background error that properly characterizes the analysis uncertainty (Kalnay et al. 2006). EnKF-initialized ensemble forecasts have been used to produce convective-scale probabilistic forecasts in several recent studies. For tornadic storms, probabilistic forecasts have focused on the low-level vorticity; Dawson et al. (2012) and Yussouf et al. (2013; 2015; 2016) showed that the ensemble probability of vorticity exceeding certain thresholds predicted the observed damage paths of tornadoes well in supercell cases, while Snook et al. (2012; 2015) obtained similarly successful results for an MCS case. Snook et al. (2012; 2015) also examined and demonstrated the benefits of using multiple SM MP schemes in EnKF ensembles for probabilistic forecasts of Z, while Yussouf et al. (2016) showed the assimilation of radar data in a continuous-update-cycle EnKF DA system provides significant improvement during the first three hours of probabilistic quantitative precipitation forecasts.

In previous convective-scale EnKF studies using DM MP schemes, little attention has been given to probabilistic prediction of simulated radar variables or quantitative probabilistic forecast skill scores, especially in terms of simulated dual-pol variables. Dawson et al. (2012), Yussouf et al. (2013), and Wheatley et al. (2014) conducted ensemble forecasts using DM MP schemes, but only examined individual member or ensemble mean forecasts, not probabilistic forecasts of Z. Recent studies by

Yussouf et al. (2015; 2016) showed promise for probabilistic prediction of radar variables; the authors produced probabilistic forecasts of Z exceeding 40 dBZ using the semi-DM Thompson (Thompson et al. 2004; Thompson et al. 2008) scheme for the 27 May 2011 tornado outbreak and 31 May 2013 central Oklahoma supercell case that matched the locations of observed supercells well. However, no quantitative probabilistic forecast skill scores for Z were presented. Putnam et al. (2016) simulated dual-pol variables from the CAPS storm-scale ensemble forecasts for Hazardous Weather Testbed Spring Experiment (Kong 2013) for several members that differed only in the use of MP schemes. The study emphasized the differences among the different MP schemes in their ability to simulate dual-pol radar signatures, but ensemble probabilistic forecasting of dual-pol radar variables was not investigated.

In this study, we examine for an MCS case ensemble forecasts produced by a forecast model employing SM and DM MP schemes during the EnKF DA cycles as well as in the subsequent forecasts. We evaluate the probabilistic forecasting skills in terms of dual-pol radar variables. As far as we know, probabilistic forecasting in terms of the dual-pol radar variables has not been examined before, at least in formal literature.

The remainder of this Chapter is organized as follows: Section 3.2 reviews the 8-9 May 2007 MCS case and the experiment design, and briefly summarizes the methods used in the SM and DM ensemble forecasts. In section 3.3, we assess the skills of the ensemble probabilistic forecasts obtained with the SM and DM schemes. Finally, section 3.4 summarizes the findings. The challenges associated with probabilistic

forecasting and evaluation of highly localized dual-pole signatures are also discussed and some suggestions for future research are given.

3.2 Experimental case and method

The model, EnKF settings, and data sources used in this study are all inherited from P14. Two experiments are conducted using a SM and DM MP scheme, respectively, in which ensemble forecasts are initialized from the final EnKF analyses for the 8-9 May 2008 MCS. The SM ensemble (EXP_S) and the DM ensemble (EXP_D) use the same configuration during the EnKF analysis period as the corresponding control experiments EXP_S_M_3_5/EXP_S and EXP_D_M_3_5/EXP_D from P14. A brief summary of the case and experiment settings is provided below.

3.2.1 System overview

On 8 May 2007, an MCS developed in western Texas and moved to the northeast into southwestern and central Oklahoma during the evening hours (approximately 0000-0500 UTC 9 May). During the day on 8 May, a positively-tilted upper level trough and seasonably warm, moist air at the surface led to the development of widespread convection over western Texas. The cool outflow from these storms helped to initiate additional convection and contributed to upscale growth over time as the storms became organized into a convective line. Ahead of the line, isolated supercell storms developed in northwest Texas and southwest Oklahoma. The developing MCS interacted with two of these storms, leading to the development and maintenance of a line end vortex (LEV) near the northern end of the MCS (P14, Schenkman et al. 2011). During the 0100 – 0500 UTC 9 May timeframe the system remained in the asymmetric

stage of MCS development, with a broad area of leading stratiform precipitation, an intense leading convective line, and a trailing region of stratiform precipitation (Fig. 3.1), with term definitions based on Fritsch and Forbes (2001)). Widespread heavy rain was observed with this MCS, and four tornadoes were reported near the LEV (NWS 2012). For a more detailed discussion of the development, structure, and impacts of this MCS, we refer the reader to P14, Schenkman et al. (2011), and Snook et al. (2011).

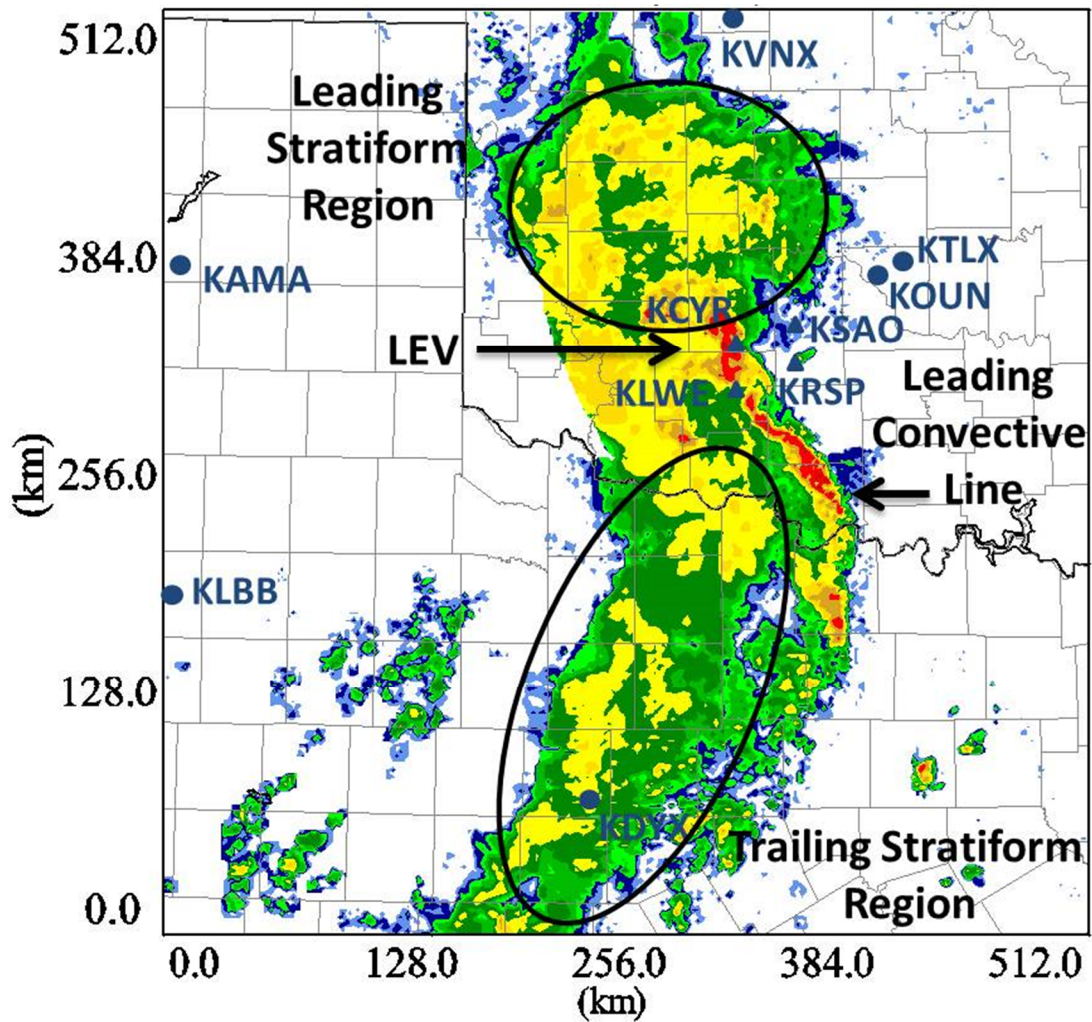


Fig. 3.1. Mosaic of observed reflectivity (dBZ) from KAMA, KDYX, KFWS, KLBB, KTLX, and KLVN at 0200 UTC at about 2 km above ground. The locations of all radars assimilated are marked. Also, notable MCS features including the line end vortex (LEV), leading convective line, leading stratiform region, and trailing stratiform region are given. Reproduced from Putnam et al. (2014).

3.2.2 Forecast model settings

The forecast model used is the Advanced Regional Prediction System (ARPS, Xue et al. 2000; Xue et al. 2001; Xue et al. 2003). ARPS is a fully-compressible, non-hydrostatic, three-dimensional atmospheric model suitable for convective-scale simulation and prediction. ARPS predicts the three-dimensional wind components (u, v, w), pressure (p), potential temperature (θ), water vapor mixing ratio (q_v), as well as the mixing ratios for cloud water (q_c), rain (q_r), snow (q_s), ice (q_i), graupel (q_g), and hail (q_h) for a SM MP scheme. For a DM MP scheme, the model also predicts the hydrometeor number concentrations (N_{tx} , where x refers to individual hydrometeor species). Additional parameterizations used include NASA Goddard Space Flight Center long- and shortwave radiation, 1.5-order turbulent kinetic energy (TKE)-based subgrid-scale turbulence closure and convective boundary layer parameterization schemes, and a two-layer land surface/soil-vegetation model. More details on the model physics can be found in Xue et al. (2001). The model domain used consists of 259×259 grid points in the horizontal with a 2 km horizontal grid spacing and a stretched vertical grid using 53 vertical grid points with a minimum grid spacing of 100 m and average grid spacing of 500 m. The model terrain is interpolated to the 2 km grid from a 30 arcsecond high resolution USGS dataset.

The full experiment consists of a 1-hour (h) spin-up period, 1-h data assimilation period, and a 3-h ensemble forecast. During the spin-up period, a 1-h deterministic forecast on the 2 km model grid is initialized from the NCEP North American Mesoscale Model (NAM) analysis at 0000 UTC. The 3-h NAM forecast from 0000 UTC valid at 0300 UTC and the NAM analysis at 0600 UTC provide lateral boundary

conditions during the forecast. At 0100 UTC, smoothed random perturbations are added to the 1-h spin-up forecast (Tong and Xue 2008, Snook et al. 2011) to initialize a 40-member ensemble for performing the EnKF data assimilation cycles. The first assimilation is performed at 0105 UTC and the last at 0200 UTC, with an assimilation cycle length of 5 minutes. Only radar data are assimilated. Further details on the data assimilation are given below. Following the assimilation period, the final ensemble analyses are used to initialize 3-h ensemble forecasts from 0200 UTC through 0500 UTC.

3.2.3 Data sources

As in Snook et al. (2011) and P14, Level-II Z and radial velocity (V_r) data from five WSR-88D S-band radars in Oklahoma and Texas are assimilated. These include KTLX of Twin Lakes, Oklahoma City, Oklahoma, KVNK of Vance Air Force Base, Oklahoma, KAMA of Amarillo, Texas, KLBB of Lubbock, Texas, and KDYX of Abilene, Texas. Together, these five radar sites provide full coverage of the MCS during the DA period. KFDR (Fredrick, Oklahoma) is also located near the MCS, but level-II data from KFDR are unavailable during the assimilation window. Z and V_r data are also assimilated from four experimental X-band radars maintained by the Engineering Research Center (ERC) for Collaborative and Adaptive Sensing of the Atmosphere (CASA, McLaughlin et al. 2009) in southwestern Oklahoma. These radars, KCYR (Cyril, Oklahoma); KSAO (Chickasha, Oklahoma); KLWE (Lawton, Oklahoma); and KRSP (Rush Springs, Oklahoma), provide additional low-level radar coverage over a portion of the MCS near the LEV. The National Severe Storms

Laboratory's dual-pol S-band radar KOUN is used for verification. The locations of radars used in this study are marked in Fig. 3.1.

Radar observations are interpolated to the model grid horizontally, but are left at the height of the radar elevation scan in the vertical, following Xue et al. (2006). The observations are interpolated to the time of each assimilation cycle using the previous and subsequent volume scan. Quality control procedures, include despeckling, ground clutter removal, and velocity dialiasing, are applied to the radar data prior to assimilation. For the CASA X-band Z observations, attenuation correction is performed before the data are assimilated (Chandrasekar et al. 2004).

3.2.4 Ensemble Kalman filter settings

The EnKF algorithm used is an implementation of the ensemble square root filter (EnSRF) of Whitaker and Hamill (2002). As mentioned earlier, the ensemble is first initialized at 0100 UTC by adding random, smoothed, Gaussian perturbations to the 1-h spin-up forecast. Perturbations with a standard deviation of 2 m s^{-1} are added to u , v , and w and a standard deviation of 2 K to θ (using positive values only) across the entire model domain. Additional perturbations with a standard deviation of $.001 \text{ kg kg}^{-1}$ are added to the hydrometeor mixing ratios and water vapor but they are confined to regions of precipitation where Z is greater than 5 dBZ. The perturbations are smoothed following Tong and Xue (2008) and use a horizontal correlation length scale of 8 km and vertical scale of 5 km.

Processed Z and V_r data from the nine radars are assimilated every 5 minutes between 0105 UTC and 0200 UTC. This includes clear-air Z data from the WSR-88D radars, which Tong and Xue (2005) have shown helps to suppress development of

spurious convection. Clear-air data from the CASA network are not used because of uncertainties associated with the X-band attenuation (a Z of zero may be due to complete attenuation). Assimilation of V_r is limited to regions where $Z > 20$ dBZ. The radar observation operator used is that of Jung et al. (2008a), which is different from that used in Snook et al. (2011) and the same as that in P14. A horizontal and vertical covariance localization radius of 6 km is used for both Z and V_r based on the correlation function of Gaspari and Cohn (1999).

The observation error and covariance inflation methods used are the same as in P14. They were chosen based on preliminary experiments using various configurations. Radar observation error values of 5 dBZ for Z and 3 m s^{-1} for V_r are used. Multiplicative inflation (Anderson 2001) with a factor of 1.25 is applied to the prior ensemble for grid points where $Z > 20$ dBZ in order to maintain ensemble spread and produce a closer to optimal consistency ratio value (Dowell et al. 2004) throughout the assimilation period than could be achieved using lower values of observation error and other covariance inflation methods such as additive noise (Dowell and Wicker 2009) and relaxation to prior ensemble (Zhang et al. 2004).

3.2.5 Microphysics schemes used and their configurations

The two control experiments differ solely in terms of the microphysics scheme used. EXP_S uses a combination of three different SM MP schemes. Using multiple MP schemes within the ensemble was shown to increase ensemble spread and improve root-mean-square innovation (RMSI) during the assimilation period by Snook et al. (2011). Of the 40 ensemble members, 16 use the Lin scheme (Lin et al. 1983), 16 use the WRF single-moment 6-class WSM6 scheme (Hong and Lim 2006), and 8 use the

simplified NWP scheme (NEM) of Schultz 1995). Fewer NEM members are included because NEM member forecasts did not tend to perform as well as members using the other SM schemes. The intercept parameter used for rain (N_{or}) is reduced by a factor of 10 from the typical value of $8 \times 10^6 \text{ m}^{-4}$ to $8 \times 10^5 \text{ m}^{-4}$, following Snook and Xue (2008), who found that the reduced N_{or} value led to a lower and more realistic evaporation rate and associated surface cold pool intensity.

The DM experiment, EXP_D, uses the Milbrandt and Yau (MY, 2005b) scheme. During the assimilation period, the shape parameters (α) for rain and hail vary inversely between 0.0 and 2.0 in 0.5 increments for each member to increase ensemble spread. All other hydrometeor categories use $\alpha = 0$; furthermore α is set to 0 for all categories in the forecasts after 0200 UTC. As in Snook et al. (Snook et al. 2011) and P14, the graupel category of the MY scheme is turned off to more closely resemble the majority of members in EXP_S which did not predict graupel.

3.3 Results of experiments

In this section, ensemble forecast results from EXP_S and EXP_D are presented. The results are divided into two parts: (1) an evaluation of the overall forecast quality using Z mosaics and (2) verification of simulated dual-pol variables against KOUN observations. Evaluations include qualitative discussion of system structure and feature placement, evaluation of probabilistic forecasts, as well as quantitative verification. We also discuss methods and challenges as they relate to dual-pol variables.

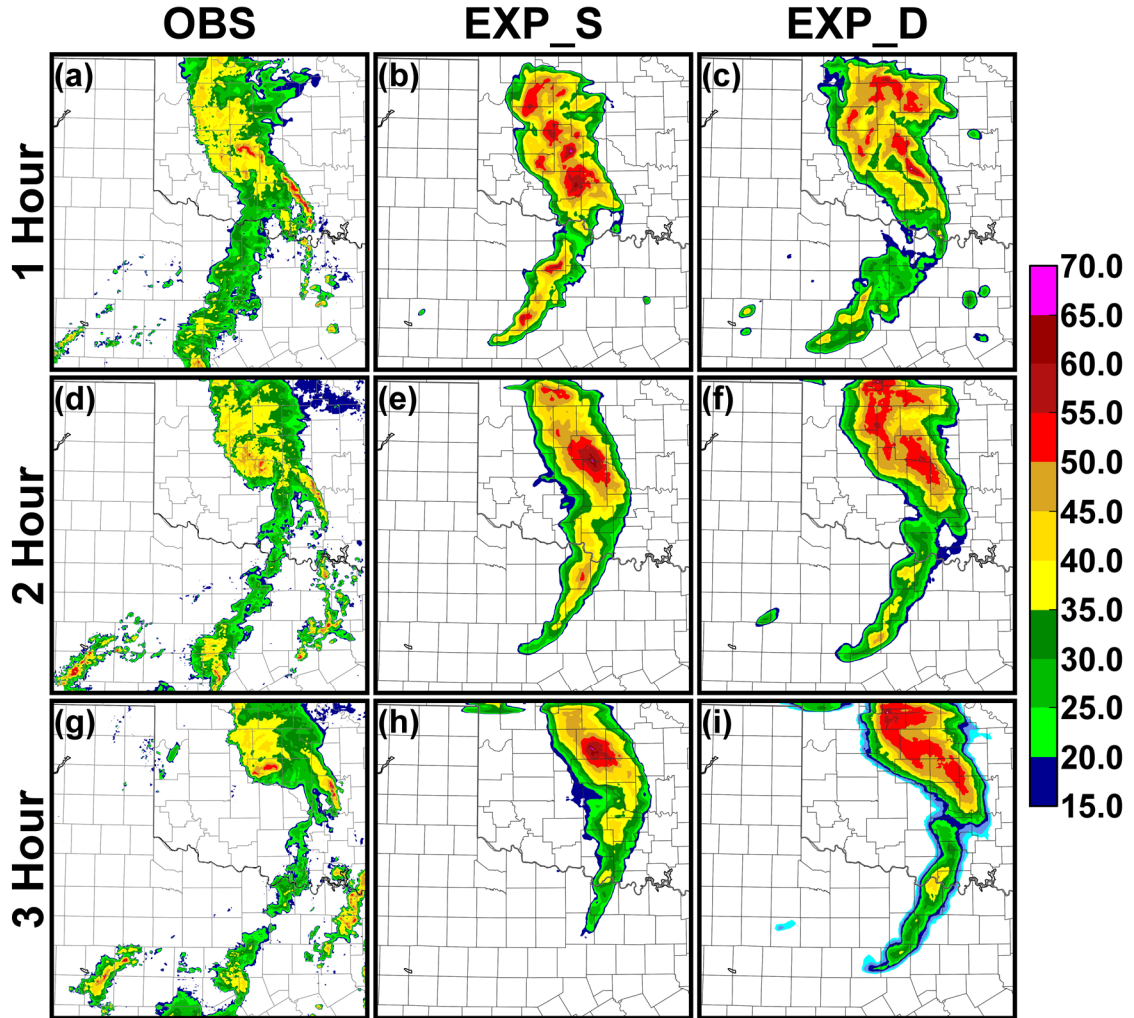


Fig. 3.2. Mosaic of (a,d,g) observed reflectivity (dBZ) as in Fig. 3.1 as well as probability matched ensemble mean reflectivity for (b) EXP_S and (c) EXP_D at 0300 UTC/1-h forecast, (d-f) 0400 UTC/2-h forecast, and (g-f) 0500 UTC/3-h forecast.

3.3.1 Ensemble forecasts of radar reflectivity

3.3.1.1 Qualitative evaluation of reflectivity mosaics

Ensemble forecasts of the MCS are evaluated at 1, 2, and 3-h of forecast time by verifying the probability matched ensemble mean (PMEM; Ebert 2001) forecasts of Z from EXP_S and EXP_D against mosaics of observed Z at model level 10, which is approximately 2 km AGL (Fig. 3.2). Model level 10 is the lowest level where complete

radar coverage of the MCS is available. The mosaic of observed Z is created by combining observations from the five WSR-88D radars used in the assimilation, with observations interpolated to the model grid as discussed above in section 3.2.3. Where multiple radars observe a specific grid point, the highest value of Z is used in the mosaic. The PMEM is used instead of a regular ensemble mean because Z can vary greatly over small distances, leading to under-prediction of intensity and over-prediction of areal coverage when ensemble members with even slightly-displaced convective features are averaged. The PMEM ranks all Z values in the domain from highest to lowest for both the ensemble mean and the full ensemble, then reassigns values from the full ensemble probability density function of Z to the grid location with the same rank in the ensemble mean; this process helps mitigate the aforementioned biases introduced by taking the ensemble mean (Ebert 2001; Clark et al. 2009).

Unlike in P14, the simulated radar variables in the results use a different, more complex observation operator than was used for EnKF DA. This operator, outlined in Jung et al. (2010), uses a lookup table of scattering amplitudes for all hydrometeors calculated using the T-matrix method (Vivekanandan et al. 1991; Bringi and Chandrasekar 2001). The simpler operator used during EnKF DA, based on Jung et al. (Jung et al. 2008a), uses a fitted approximation to the T-matrix values for rain, and uses the Rayleigh approximation for ice species. The simpler operator is used during DA to reduce computational expense, while the more advanced operator is used for forecast verification because it allows for a more realistic comparison to observations.

The PMEM of Z in EXP_S contains a region of anomalously high Z (>55 dB) centered near the LEV (see Fig. 3.1), and there is little distinction between regions of

stratiform and convective precipitation (Fig. 3.2b,e,h). The intensity of the trailing stratiform precipitation is also over-forecast. On the other hand, the PMEM of Z in EXP_D (Fig. 3.2c,f,i) contains broader precipitation coverage in the leading stratiform region and a convective line with greater southern extent, though it does over-forecast the precipitation intensity in the leading stratiform region. The ensemble spread of Z is lower in EXP_D than in EXP_S (not shown); only one MP scheme is used in EXP_D, leading to closer agreement among members and higher ensemble mean values (Snook et al. 2012). These results are similar to those obtained in deterministic forecasts of this case in P14, where the authors found the size sorting of smaller raindrops rearward in the leading convective line when using a DM scheme (absent in EXP_S) led to greater evaporative cooling and a stronger cold pool that helped maintain a more realistic MCS structure. They also found that the cold pool in EXP_S is disorganized, contributing to the development of spurious convection near the LEV. It should be noted that neither EXP_S nor EXP_D predict the small clusters of storms that develop in the southeast and southwest portion of the domain in the observations, likely in part because this convection developed mostly after the DA period.

3.3.1.2 Probabilistic forecasts for reflectivity

Uncertainty within the ensemble forecast due to, e.g., initial condition and model errors, can be considered by producing probabilistic forecasts of Z from the forecast ensemble. High-resolution, convection-permitting NWP forecasts are particularly sensitive to timing and location errors as forecast lead time increases due to the small spatial and temporal scales of convective storms (Lorenz 1969; Roberts 2008). To account for this sensitivity, we use the neighborhood ensemble probability (NEP)

method (Ebert 2008; Roberts and Lean 2008; Schwartz et al. 2009b), which, at each model grid point, produces a probabilistic forecast using a collection of nearby points in all ensemble members rather than relying solely on data from that single grid point in each member. In this way, NEP accounts for spatial uncertainty as well as uncertainty conferred by the ensemble. Appropriate specification of the neighborhood is important; in this study we use a circular neighborhood with a radius of 5 km, which is appropriate for the grid spacing used and convective features predicted (Snook et al. 2012; 2015). NEP is calculated for $P[Z > 20 \text{ dBZ}]$ (Fig. 3.3) and $P[Z > 40 \text{ dBZ}]$ (Fig. 3.4) at the same vertical level 10 as in Fig. 3.2. The 20 dBZ threshold is used to consider overall precipitation coverage in the MCS, including the stratiform regions, while the 40 dBZ threshold is chosen to focus on areas of heavy, convective precipitation. In Fig. 3.3 and Fig. 3.4, the observed Z contours for the corresponding threshold are also plotted.

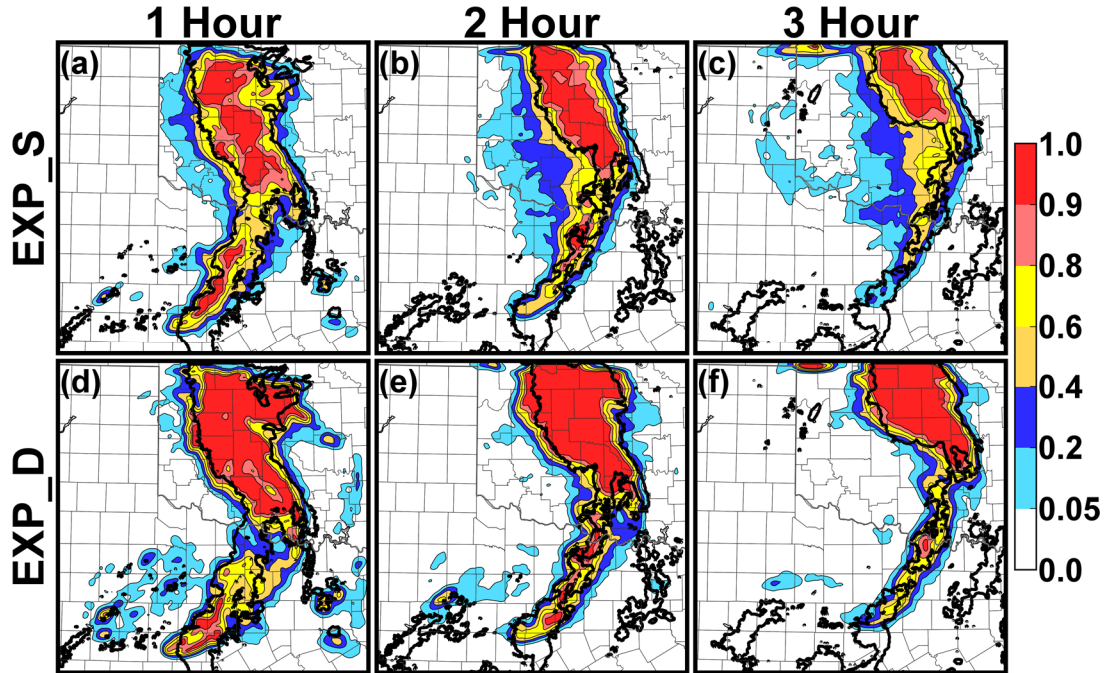


Fig. 3.3. Probability of reflectivity exceeding 20 dBZ at 2 km AGL for EXP_S at (a) 1 h, (b) 2 h, and (c) 3 h forecast times and (d-f) EXP_D. The thick black line outlines observed reflectivity exceeding 20 dBZ.

As was noted in the PMEM forecasts, the NEP forecasts of Z for EXP_D exhibit improved precipitation structure and feature placement compared to EXP_S. At the 20 dBZ threshold, the region of high $P[Z > 20 \text{ dBZ}]$ in EXP_D (Fig. 3.3d-f) closely matches the observed region of 20+ dBZ Z , particularly in the leading stratiform region and leading convective line. In particular, EXP_D predicts broad area of very high probability (> 0.9) that closely matches the observed leading stratiform region in terms of position, shape, and motion throughout the forecast period. In contrast, EXP_S (Fig. 3.3a-c) exhibits high probability (> 0.8) for only about half of the observed region of 20+ dBZ Z during the first two hours of the forecast, and even less in the 3-h forecast. EXP_S also has a substantial region of moderately high probabilities (up to 0.8) to the west of the MCS where no precipitation is observed. Considering the individual SM microphysics schemes within EXP_S, the LIN members exhibit the best agreement with observations in terms of forecast coverage and intensity of Z ; WSM6 members generally over-forecast the extent of the trailing stratiform region, while NEM members under-forecast the extent of both the trailing and leading stratiform regions (not shown). These results are consistent with those of Snook et al. (2012), which, using a similar ensemble with the same MP schemes, found that the RMS innovation of Lin members during the forecast period was lower than that of WSM6 and NEM members. In both EXP_D and EXP_S, low probabilities are predicted for the trailing stratiform precipitation region; overall, this region is the worst forecast portion of the MCS.

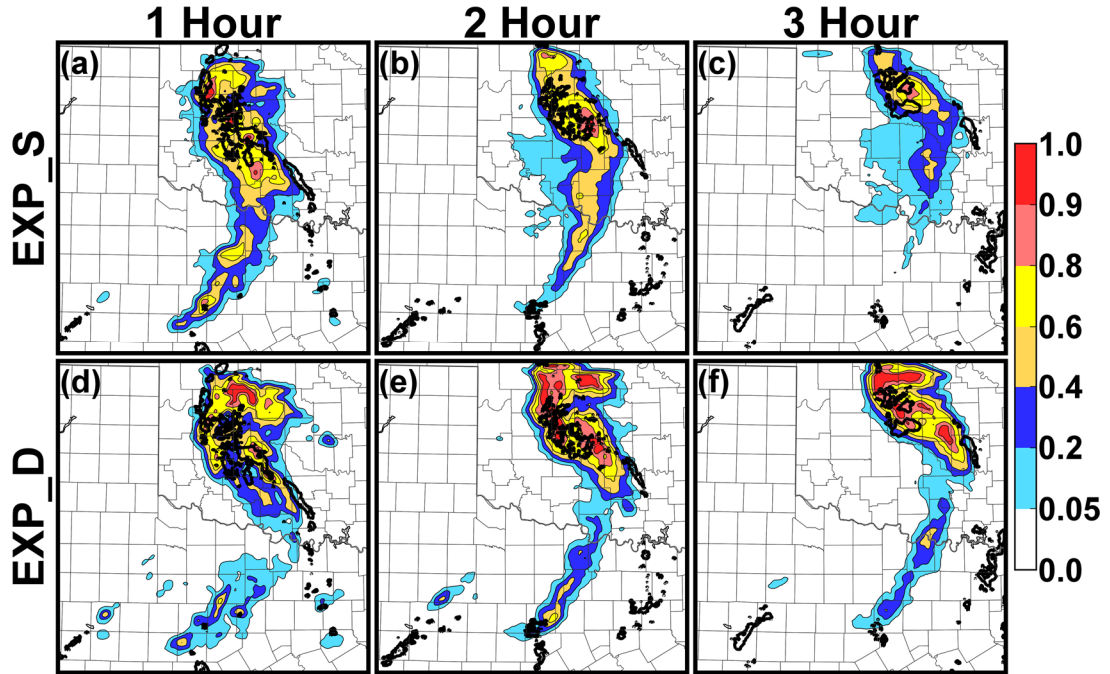


Fig. 3.4. Probability of reflectivity exceeding 40 dBZ at 2km agl for EXP_S at (a) 1-h, (b) 2-h, and (c) 3-h forecast times and (d-f) EXP_D. The thick black line outlines observed reflectivity exceeding 40 dBZ.

Although overall precipitation coverage ($Z > 20$ dBZ) is generally good for both cases, the $P[Z > 40 \text{ dBZ}]$ associated with heavier convective precipitation exhibits greater error. EXP_S has only a small overlap of low probabilities (0.05-0.2) with the observed 40 dBZ region in the 1-h forecast (Fig. 3.4a); EXP_D has greater overlap throughout the forecast period (Fig. 3.4d-f), but the predicted probabilities remain low. The convective line has a width of a few km and will be more susceptible to spatial error as forecast lead time increases compared to the stratiform regions, even with the consideration of a 5 km neighborhood. EXP_D also has higher probabilities in the convection near the LEV on the north end of the MCS. However, there are areas of high probability in the stratiform region as well, where EXP_D over-forecasts Z intensity. The over-forecast in intensity is in part due the height of the model grid used in Fig.

3.2-3.4 being close to the melting layer, where high Z occurs due to the presence of large, oblate, and wet hydrometeors. MP schemes thus far used with the simulator have shown a tendency to delay melting until warmer temperatures at lower elevations compared to observations due to overestimated evaporative cooling (Jung et al. 2008a). Because radar coverage is incomplete below this level, though, this issue is difficult to avoid. A modified melting model in the radar simulator that includes temperature information to help account for the delay is considered for future work.

3.3.1.3 Quantitative evaluation of reflectivity forecasts

Qualitative evaluations based on the PMEM (Fig. 3.2) show quite skillful forecasts in terms of Z but there are still apparent spatial errors that would adversely affect quantitative skill scores. The NEP of $Z > 40$ dBZ used to identify the leading convective line indicated how small spatial error can lead to lower Z probabilities. When considering features with small spatial scales, scores such as the equitable threat score, which consider hits, misses, and false alarms in a deterministic point by point framework, are susceptible to a ‘double-penalty’: a forecast with even a modest spatial displacement in a feature not only misses the observed feature but also produces a false alarm because the forecast feature is not coincident with any observed feature (Ebert and McBride 2000; Rossa et al. 2008; Mittermaier et al. 2013). Therefore, quantitative measures that consider the probability of an event within a neighborhood are considered.

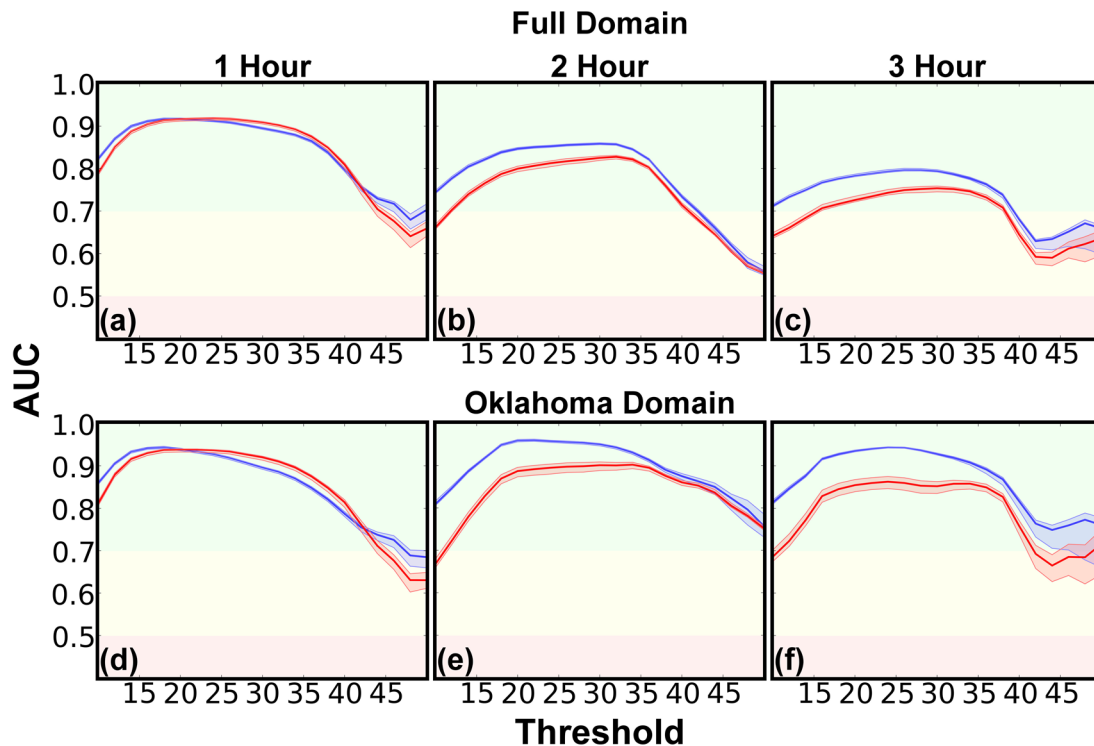


Fig. 3.5. Area under the relative operating characteristic curve (AUC) for EXP_S (red line and shading) and EXP_D (blue line and shading) at (a) 1-h, (b) 2-h, and (c) 3-h forecast times at 2 km AGL for the full experiment domain and also (d-f) a subdomain covering Oklahoma.

The first metric considered is the area under the relative operating characteristic (ROC) curve (AUC, Mason 1982; Mason and Graham 1999). The AUC is a summary skill score that compares the probability of detection and the probability of false detection for a given event over a range of probability thresholds; in this case the event is Z exceeding a given threshold within a neighborhood with a 5 km radius. Possible AUC values range from 0.0 to 1.0, with 1.0 indicating a perfect forecast (no false alarms or misses). AUC values of 0.5 or below indicate that the forecast has no useful skill. AUC is calculated for EXP_S and EXP_D using Z thresholds ranging from 10 dBZ to 50 dBZ for 1, 2, and 3-h forecast times (Fig. 3.5), and a bootstrap procedure is used to resample the ensemble 1000 times to determine the 5th to 95th percentile range,

which is shaded. Background shading is included to indicate the areas of useful forecast skill (green; $AUC > 0.7$), low skill (yellow; $0.5 < AUC < 0.7$), and no skill (red; $AUC < 0.5$). Calculations are performed over the full experiment domain (Fig. 3.5a-c) as well as an Oklahoma subdomain positioned to cover the leading stratiform region and leading convective line, where both forecasts performed better compared to the trailing line (Fig. 3.5d-f).

Both experiments generally produce high AUC values, except for the very highest Z thresholds, associated with intense convective precipitation; confidence in AUC at these thresholds is low, however, because the sample size of Z exceeding these thresholds is quite small, and the regions in question are very small in spatial extent. AUC also, as expected, decreases with increasing forecast time. In general, EXP_D shows improvement over EXP_S in skill, especially for moderate Z thresholds representing the stratiform region in the later hours.

The AUC increases overall for both experiments when calculations are limited to the Oklahoma subdomain (Fig. 3.5d-f). In the 1-h forecast, AUC is similar in EXP_S and EXP_D, but in the 2 and 3-h forecasts, EXP_D outperforms EXP_S in terms of AUC at nearly all thresholds. In particular, EXP_D has an AUC value over 0.9 for thresholds of 20-25 dBZ throughout the forecast period over the Oklahoma subdomain (Fig. 3.5d-f), indicating a highly skillful forecast of general precipitation coverage of the leading stratiform region. EXP_D also exhibits useful skill ($AUC > 0.7$) for higher Z thresholds representing convective precipitation throughout the forecast period over the Oklahoma subdomain, suggesting that the poorer scores over the full domain are partially due to the overly quick dissipation of the trailing convective line and the

newly-developed convection in the southern portion of the domain, while the leading convective line is generally well forecast.

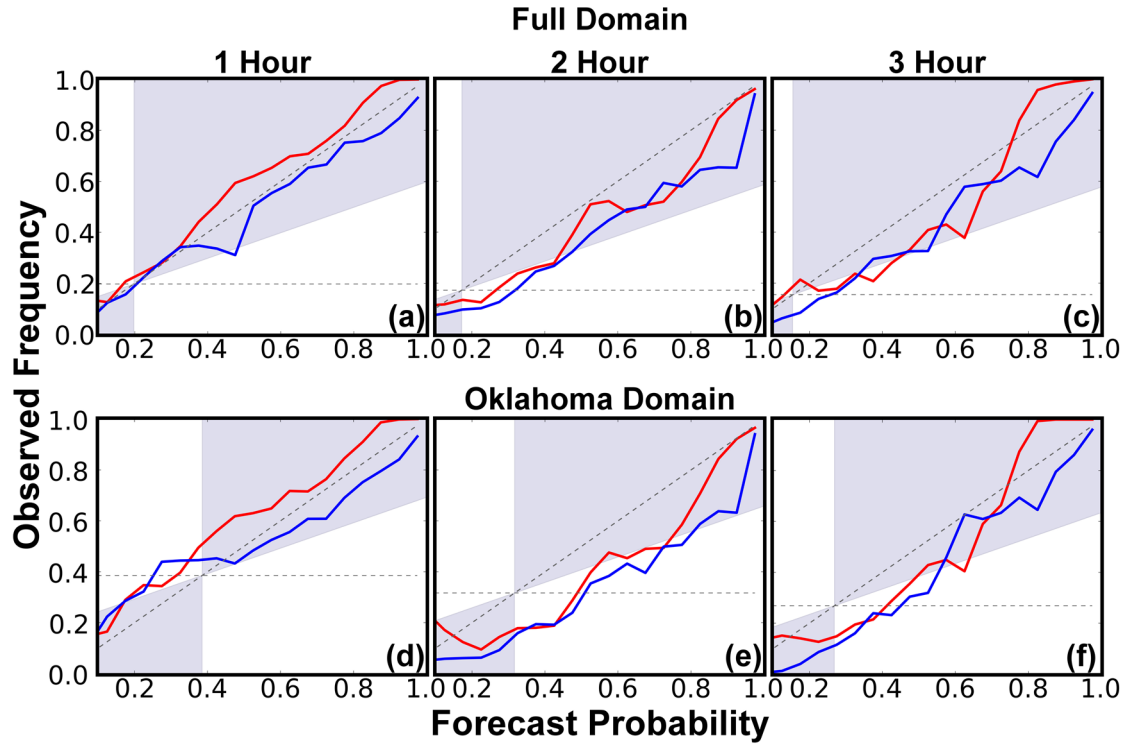


Fig. 3.6. Reliability diagrams calculated for reflectivity exceeding 20 dBZ for EXP_S (red line) and EXP_D (blue line) at (a) 1-h, (b) 2-h, and (c) 3-h forecast times at 2 km AGL for the full experiment domain and also (d-f) a subdomain covering Oklahoma.

Reliability and sharpness diagrams are examined next. A probabilistic forecast is considered reliable when the probability of an event forecast to occur closely corresponds to the rate at which the event actually occurs (Brown 2001). Reliability diagrams are calculated for $P[Z > 20 \text{ dBZ}]$ using a 5 km radius neighborhood at 1, 2, and 3-h forecast times (Fig. 3.6). In these reliability diagrams, perfect reliability is indicated by the one-to-one diagonal and the shaded region indicates a skillful forecast. Areas where the calculated reliability lies above the diagonal indicate that Z is under-forecast (forecast probability is lower than the observed frequency); conversely, areas

below the diagonal indicate that Z is over-forecast (forecast probability is higher than the observed frequency). Sharpness diagrams, which are histograms of the calculated probability values, are shown in Fig. 3.7. An ideal forecast will have many values near 1.0 or 0.0, distinguishing sharply between events and non-events. Calculations are again performed over both the full domain and Oklahoma subdomain.

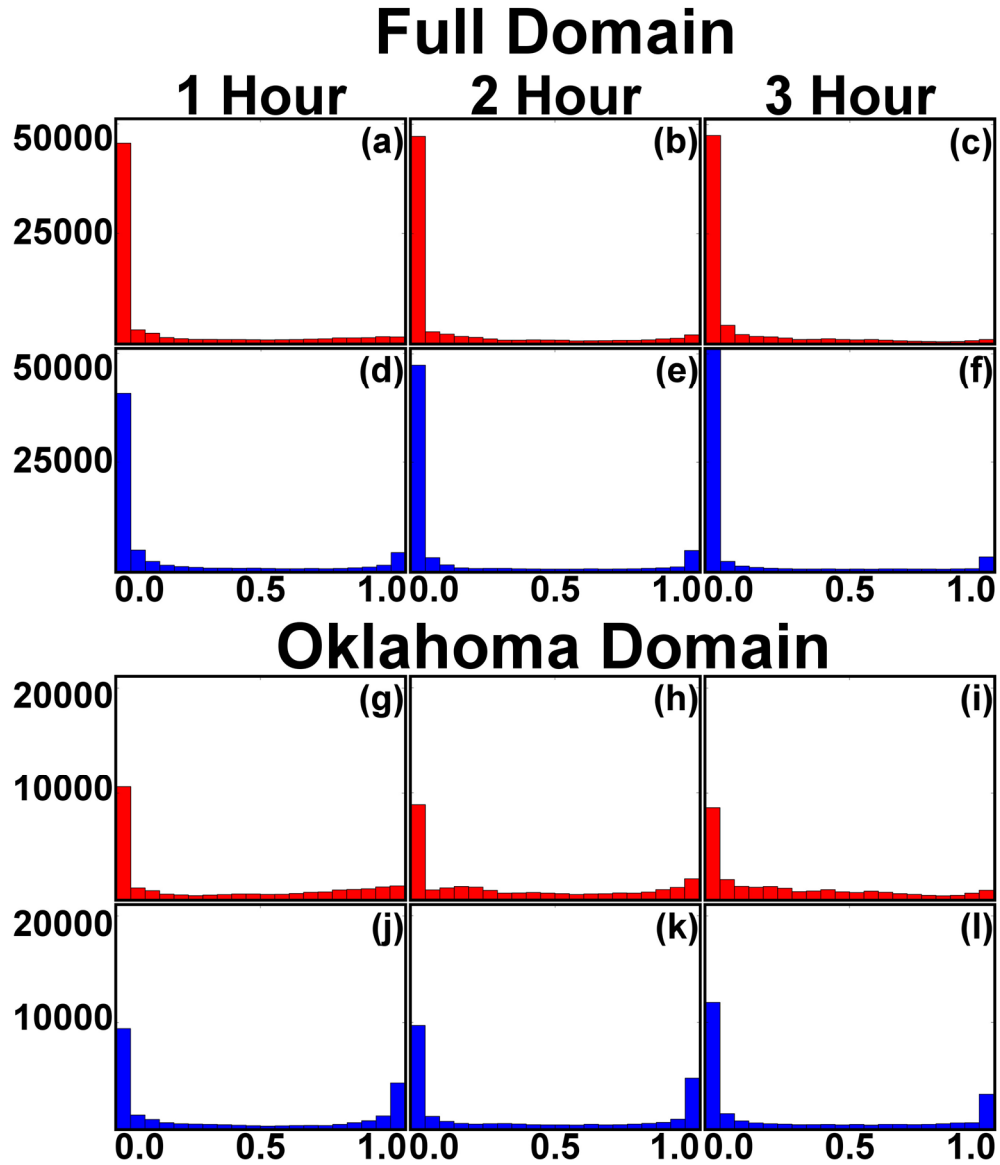


Fig. 3.7. Sharpness diagrams calculated for reflectivity exceeding 20 dBZ for EXP_S (red) at (a) 1-h, (b) 2-h, and (c) 3-h forecast times and (d-f) EXP_D (blue) at 2 km AGL for the full experiment domain and also (g-l) a subdomain covering Oklahoma.

Overall, there is not much difference in the reliability of EXP_S and EXP_D either on the full domain or the Oklahoma subdomain. For the 1-h forecast time (Fig. 3.6a,d), both forecasts show good reliability, with the region of $Z > 20$ dBZ slightly under-forecast in EXP_S and slightly over-forecast in EXP_D. For the 2 and 3-h forecast times (Fig. 3.6b,c,e,f), precipitation coverage is generally over-forecast in both experiments. EXP_D does show greater sharpness than EXP_S, particularly over the Oklahoma domain (Fig. 3.7j-l). Both experiments have a large number of probabilities of 0.0 that represent the large areas where precipitation is not observed, but EXP_D has a much higher number of points with probabilities close to 1.0 where the ensemble predicts precipitation with very high confidence. As indicated by the AUC (Fig. 3.5) and the qualitative evaluation of NEP forecasts (Fig. 3.3), this region of very high confidence agrees well with observations in EXP_D, outperforming EXP_S.

3.3.2 Ensemble forecasts of polarimetric variables

3.3.2.1 Qualitative evaluation of predicted polarimetric variables

The PMEM is calculated as in Fig. 3.2 for simulated Z , Z_{DR} , and K_{DP} as though the ensemble forecasts of EXP_S and EXP_D were observed by KOUN at 1-h (Fig. 3.8), 2-h (Fig. 3.9), and 3-h (Fig. 3.10) forecast times; KOUN observations at the corresponding times are provided for comparison. The simulated fields are shown at the 0.5° elevation; this choice of the lowest elevation is because dual-pol radar signatures tend to be the strongest at the low levels where size sorting effects (Dawson et al. 2014) and rain water species dominate. Also, the lower elevation is less affected by the melting layer. The difference in Z between the forecasts over the KOUN observing region is similar to the PMEM mosaics considered earlier (Fig. 3.2); EXP_D exhibits

improved representation of the leading convective line and better coverage of the stratiform region compared to EXP_S, though it somewhat overestimates intensity due to a low melting layer.

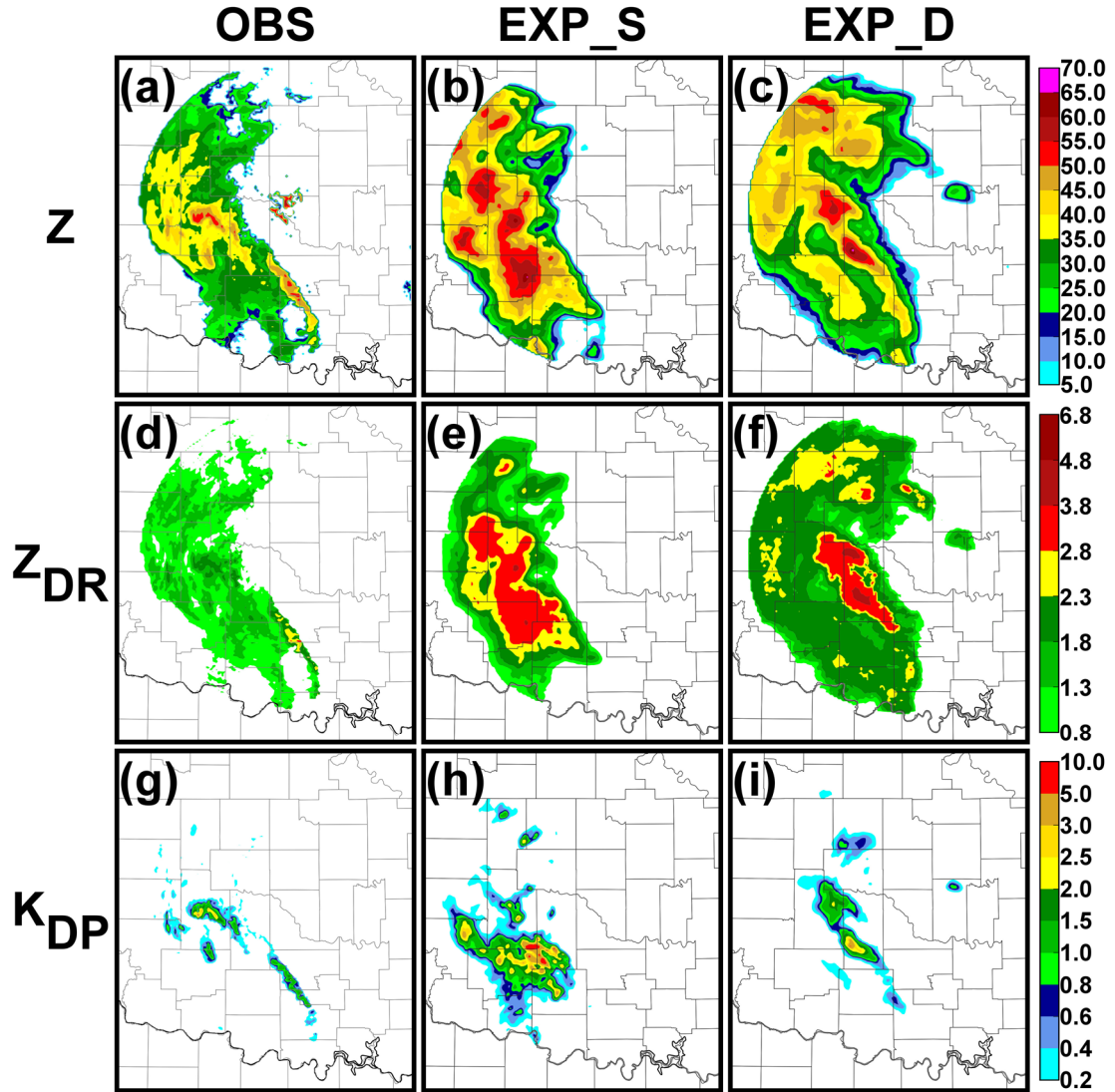


Fig. 3.8. (a) Observed reflectivity (dBZ) and simulated reflectivity from (b) EXP_S and (c) EXP_D at 0300 UTC/1-h forecast at a 0.5° tilt from KOUN, as well as (d-f) differential reflectivity (dB) and (g-i) specific differential phase (°km⁻¹).

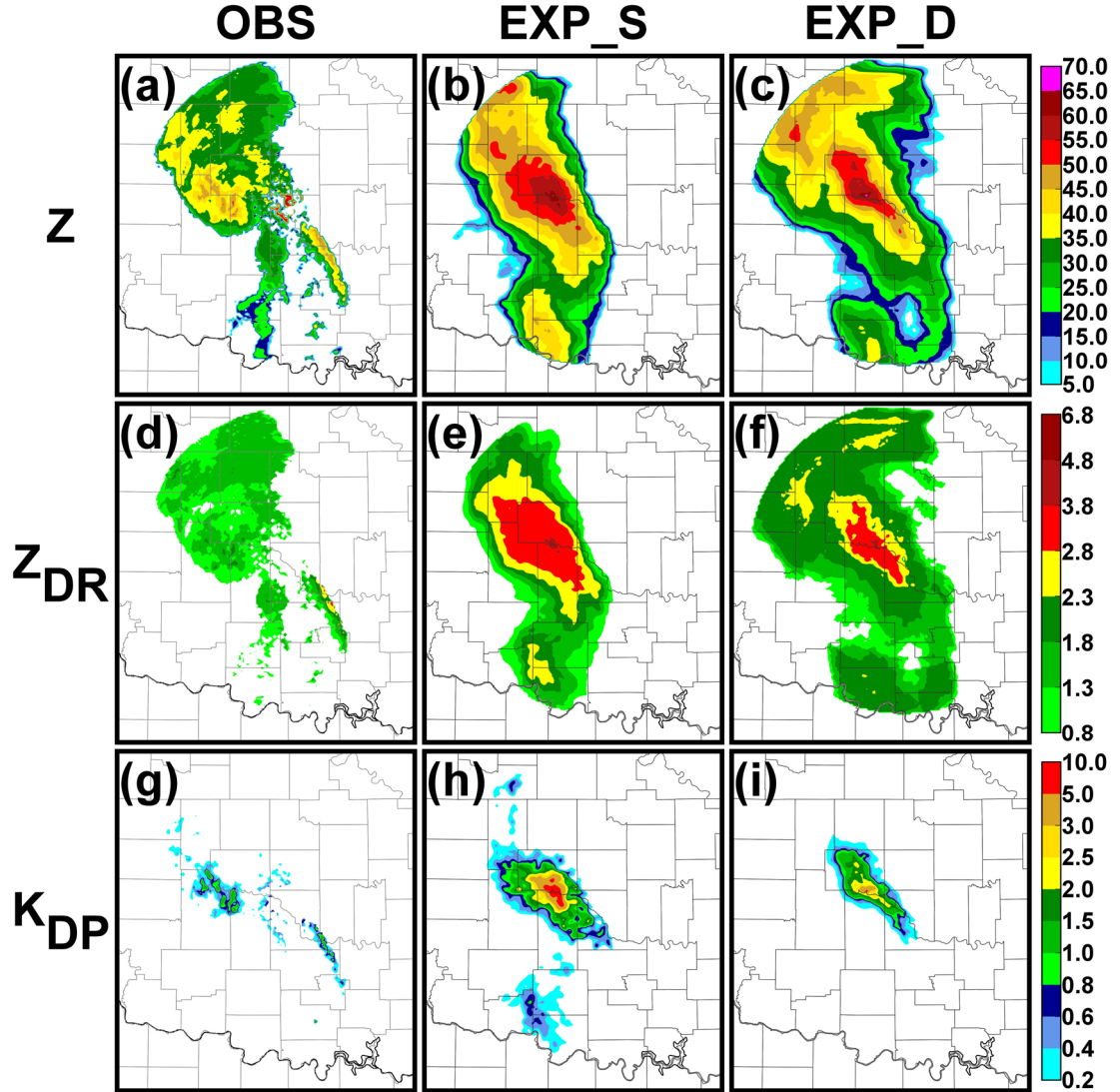


Fig. 3.9. As in Fig. 3.8 but at 0400 UTC with 2-h forecast results.

There are two notable differences between EXP_D and EXP_S in terms of their forecast dual-pol fields. First, the areal coverage of high Z_{DR} values ($Z_{DR} > 2.3\text{dB}$), a threshold that distinguishes the convective region from the stratiform region in the observations, is over-forecast in EXP_S. The highest Z_{DR} values predicted by EXP_S are coincident with the poorly-organized region of intense convection within the system due to the monotonic relationship between the Z and Z_{DR} (e.g., Fig. 3.8e). The Z_{DR}

values in EXP_D (Fig. 3.8f), while slightly higher than the observations (Fig. 3.8d), still show a similar general distribution of high and low Z_{DR} regions compared to the observations, indicating a distinct difference in maximum raindrop size between the convective and stratiform regions that is maintained throughout the entire forecast period. P14 found that these MCS features were maintained by an improved cold pool due to increased evaporative cooling from the advection of small raindrops rearward by the DM scheme.

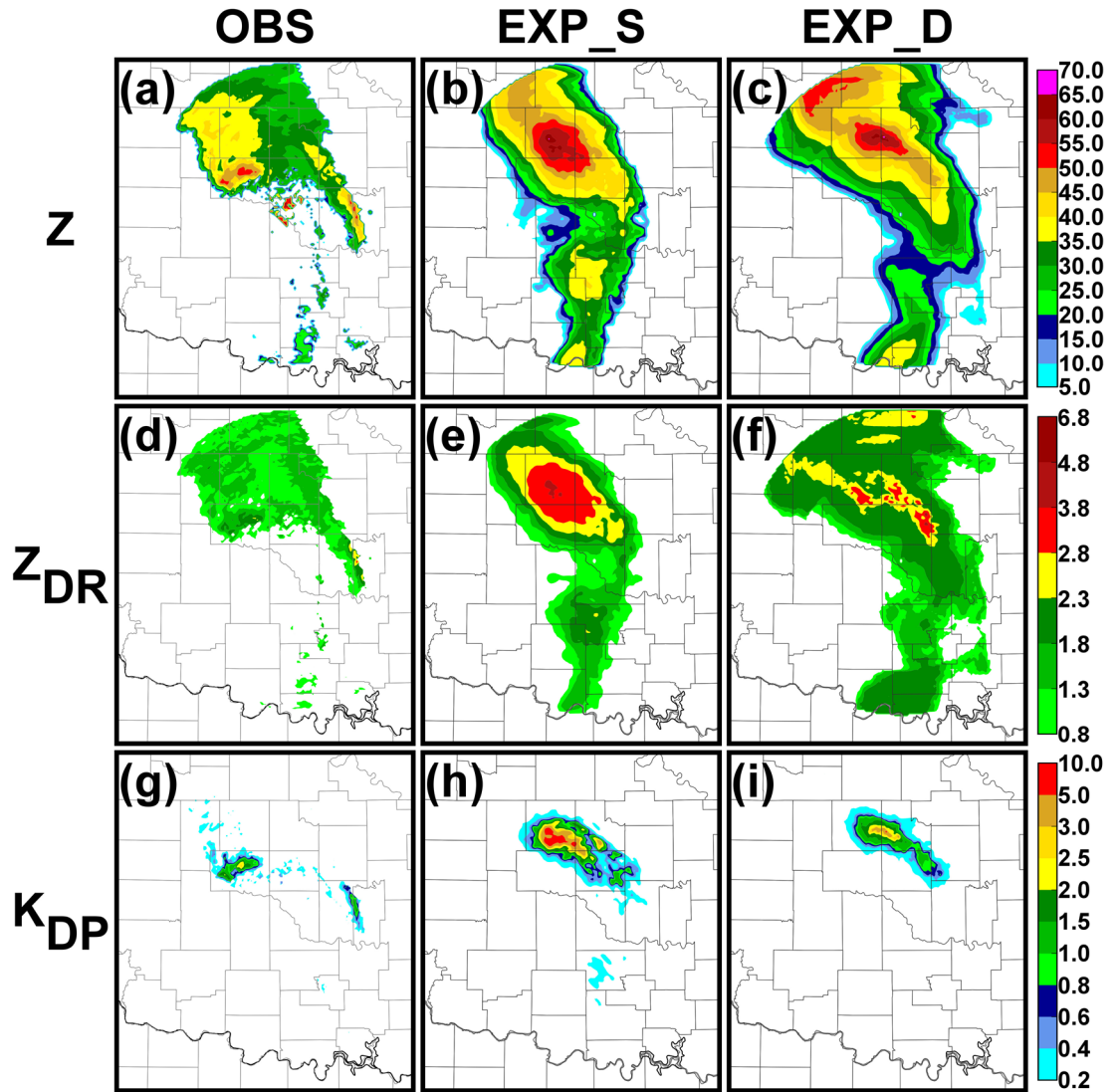


Fig. 3.10. As in Fig. 3.8 but at 0500 UTC with 3-h forecast results.

The second notable difference is that the K_{DP} values in EXP_S are unrealistically high when compared to the observations, with values peaking at nearly 10° km^{-1} , suggesting that EXP_S greatly over-forecasts liquid water content in the convective precipitation. By comparison, K_{DP} in EXP_D is much closer to the observations. The difference in K_{DP} values during the forecast in the current study is notable when compared to P14, where dual-pol variables were considered only for the analysis (not for forecasts). In the P14 analysis, K_{DP} values were generally quite similar between SM and DM experiments, with K_{DP} slightly underestimated compared to the observations due to a high hail bias. However, the Z_{DR} patterns differ between the SM and DM analyses in P14 and in the forecasts of EXP_S and EXP_D in the current study. These differences in Z_{DR} occur in the stratiform region. The region of non-zero K_{DP} values is mainly confined to the leading convective line. The unrealistically-high K_{DP} values in EXP_S occur by the first forecast hour. Rain development in the stratiform region of the MCS is heavily dependent on the transport of frozen hydrometeors in the mid and upper levels of the MCS from the convective to the stratiform region. There is very little hydrometeor transport from the convective line to stratiform region in the SM case (P14), and therefore there is a higher precipitation rate in the convective line. While the difference in K_{DP} values in the convective region between the SM and DM experiment is less substantial in the analysis, the improved development and maintenance of the MCS when using the DM scheme leads to improved representation of Z_{DR} and K_{DP} fields, compared to the observations, throughout the forecast (Fig. 3.8-Fig. 3.10).

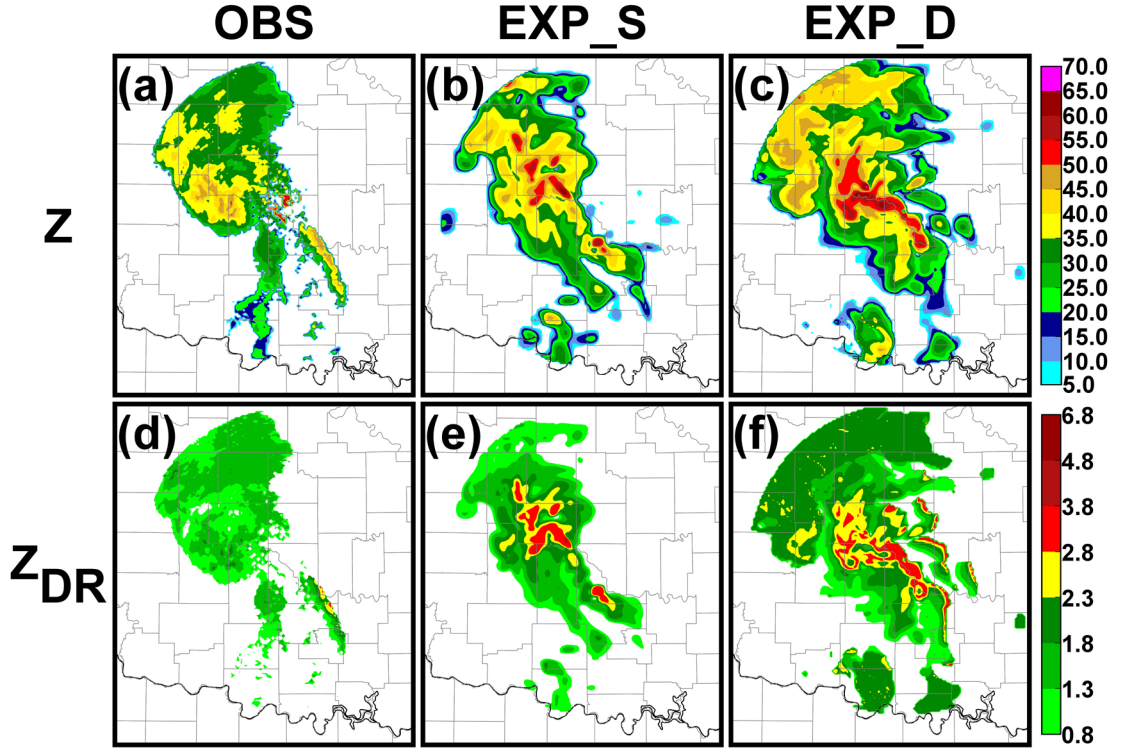


Fig. 3.11. (a) Observed reflectivity (dBZ) and simulated reflectivity from (b) EXP_S member 14 and (c) EXP_D member 39 at 0400 UTC/2-h forecast at a 0.5° tilt from KOUN, as well as observed (d) and simulated (e-f) differential reflectivity (dB).

The patterns in the dual-pol variables that reflect microphysical processes can be subtle; one such pattern is increased Z_{DR} along the leading convective line due to size sorting. Though the PMEM helps to alleviate some of the biases introduced by taking an ensemble mean, it can smear such high-detail patterns. For this reason, the best individual ensemble member from each experiment is examined in order to bring to light distinct pattern differences within the predicted dual-pol fields (Fig. 3.11). The 2-h forecast of EXP_S member 14 and EXP_D member 39 are chosen based upon a qualitative examination of the ensemble members that considers placement of system features, Z_{DR} patterns, and overall value range. The best EXP_S member contains precipitation extending southeastward where the observations have the leading

convective line, but the intensity and extent is rather limited compared to the best EXP_D member. As expected, areas of high Z_{DR} coincide with areas of high Z in the EXP_S member. In the EXP_D member, however, high Z_{DR} values are located along the eastern/leading edge of the leading convective line, a pattern consistent with the presence of size sorting of raindrops within the convective line, with smaller raindrops being advected rearward in the line while larger raindrops remain. At least physically such features are realistic.

3.3.2.2 Probabilistic forecasts of polarimetric variables

In section 3.3.1.2, probabilistic forecasts were used to evaluate the ensemble forecast precipitation coverage of stratiform and convective precipitation, based on 20 and 40 dBZ Z thresholds, respectively. A distinct variation in the Z_{DR} values also occurs, with Z_{DR} increasing where larger raindrops are present along the leading edge of the convective line. To evaluate how well the two experiments forecast the high Z_{DR} signatures, the probability of $Z_{DR} > 2.3$ dB at the 1, 2, and 3-h forecast time is calculated (Fig. 3.12). The threshold of $Z_{DR} = 2.3$ dB is chosen based on the observed values in this case (Fig. 3.8d, 3.9d, 3.10d), and the observed $Z_{DR} = 2.3$ dB contour is shown as a thick black line. EXP_S has a broad expanse of relatively high probability of $Z_{DR} > 2.3$ dB over the stratiform region, a result consistent with the overall pattern of Z_{DR} in Fig. 3.8e, 3.9e, and 3.10e. This region of high $P[Z_{DR} > 2.3 \text{ dB}]$ is significantly displaced from the observed leading convective line. In EXP_D, there is some overlap of low to moderate probabilities of $Z_{DR} > 2.3$ dB with the observed 2.3 dB contour in the 1-h forecast, and some overlap of low probabilities at the 2 and 3-h forecasts. Though the regions of moderate $P[Z_{DR} > 2.3 \text{ dB}]$ in EXP_D do not exactly match the observed region of high

Z_{DR} , the geographic distribution of higher probability follows a north-northwest to south-southeast orientation, similar to the observed leading convective line, and substantially improved compared to the more circular pattern found in EXP_S. The EXP_D probabilistic forecast of Z_{DR} thus has greater practical value, indicating moderate probability of an arc of larger raindrops relatively near the observed leading convective line, correctly indicating the existence and general direction of motion of leading convection in the MCS within the ensemble forecast.

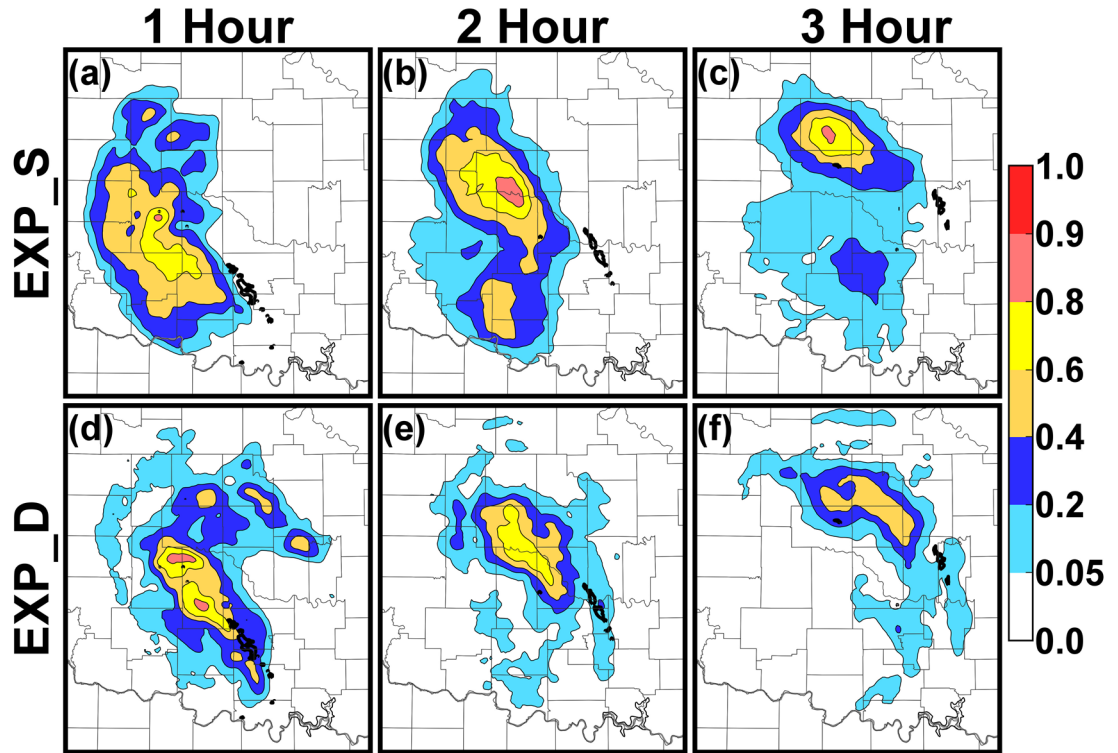


Fig. 3.12. Probability of differential reflectivity exceeding 2.3 dB at a 0.5° tilt for EXP_S at (a) 1-h, (b) 2-h, and (c) 3-h forecast times and for (d-f) EXP_D.

3.3.2.3 Quantitative verification of polarimetric variables

The same concerns for how small spatial errors can affect quantitative skill scores of Z discussed in section 3.3.1.3 are even greater when considering skill scores for predicted dual-pol variables. Dual-pol signatures follow patterns associated with

microphysical processes that occur at very small scales, such as the size-sorting of raindrops along the leading convective line. With this potential limitation in mind, the AUC is calculated for Z_{DR} (0.0 to 2.7 dB) and K_{DP} (0.0 to 1.5 ° km⁻¹) for the 1, 2, and 3-h forecasts (Fig. 3.13) using a 5 km neighborhood radius as was done in Fig. 3.5 for Z . Both experiments have similar, skillful AUC values for predicting Z_{DR} at thresholds of 0.0 to 1.0 dB (Fig. 3.13a-c). For higher thresholds, the AUC for EXP_S indicates very poor skill, while EXP_D still produces a skillful forecast. AUC for Z_{DR} is better in EXP_D due to the lower Z_{DR} values throughout the leading stratiform region, which agree much more closely with observations than the forecast of EXP_S. The Z_{DR} associated with the leading convective line also has a good overlap with observed values in EXP_D. EXP_S outperforms EXP_D for the considered thresholds of K_{DP} due to erroneous broader coverage in EXP_S that overlaps the observations and the displacement error in EXP_D. K_{DP} coverage is significantly less than either Z or Z_{DR} ; AUC is particularly sensitive to the probability of detection and therefore EXP_D scores are poorer. Additionally, the significant high bias in K_{DP} in EXP_S is not accounted for at these thresholds chosen based on observed values; the AUC threshold limit is set to 1.5 ° km⁻¹ because few observations exceed this value. K_{DP} is poorer qualitatively in comparison to EXP_D, but limitations in the quantitative scores used lead to poor and misleading results.

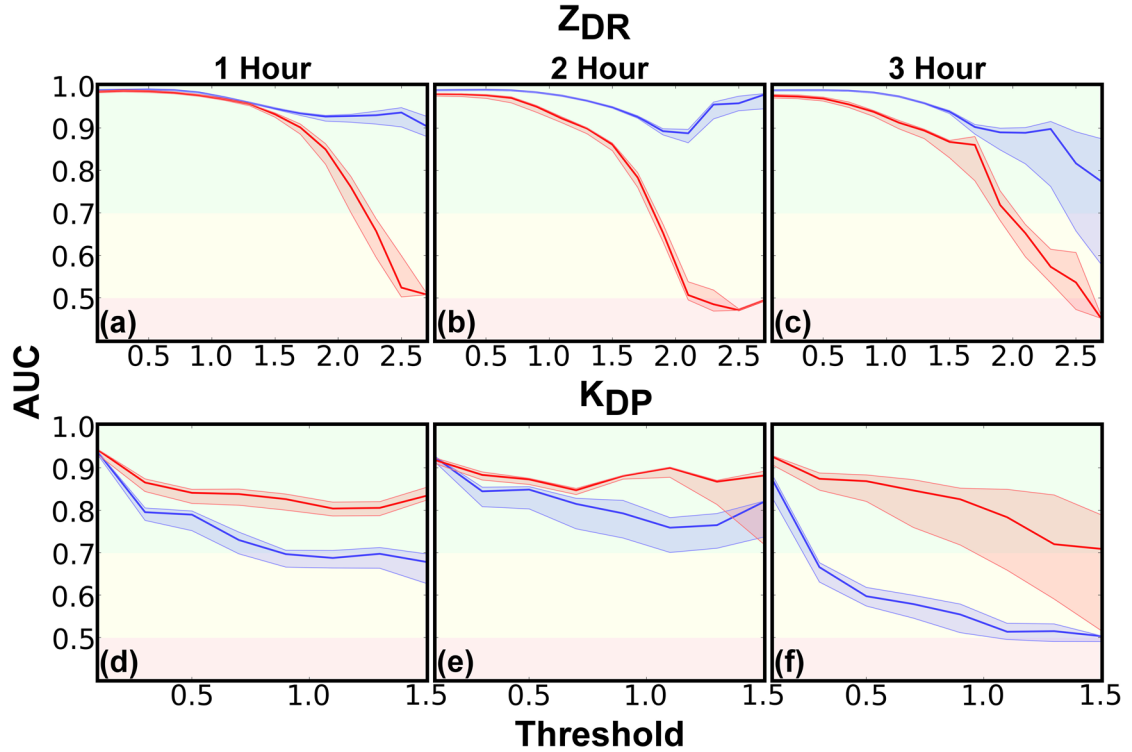


Fig. 3.13. Area under the relative operating characteristic curve (AUC) for differential reflectivity (dB) for EXP_S (red line and shading) and EXP_D (blue line and shading) at (a) 1-h, (b) 2-h, and (c) 3-h forecast times at a 0.5° tilt as well as for (d-f) specific differential phase ($^\circ \text{ km}^{-1}$).

Due to the large impact of spatial error on the quantitative skill scores for the dual-pol variables, other quantitative methods of evaluation not reliant on location are useful. Domain-wide histograms of the simulated dual-pol variables can be used to identify significant biases in the forecast. Histograms of the simulated values from all members of EXP_S and EXP_D as well as the observed values are plotted in Fig. 3.14. The values from EXP_S and EXP_D are normalized by the size of the ensemble for comparison to the observations. For observed Z, values associated with the widespread stratiform precipitation lead to a peak between about 30 to 35 dBZ throughout the experiment period (Fig. 3.14a-c). The EXP_D ensemble forecast Z values match the observed distribution in this range better than EXP_S during the first two forecast

hours. Both experiments over-forecast the geographic extent of the convective precipitation, and over-forecast the intensity of Z in part due to the influence of the melting layer, leading to a higher number of $Z > 50$ dBZ values compared to the observations, though this high bias is slightly greater in EXP_S than in EXP_D for forecast hours one and two.

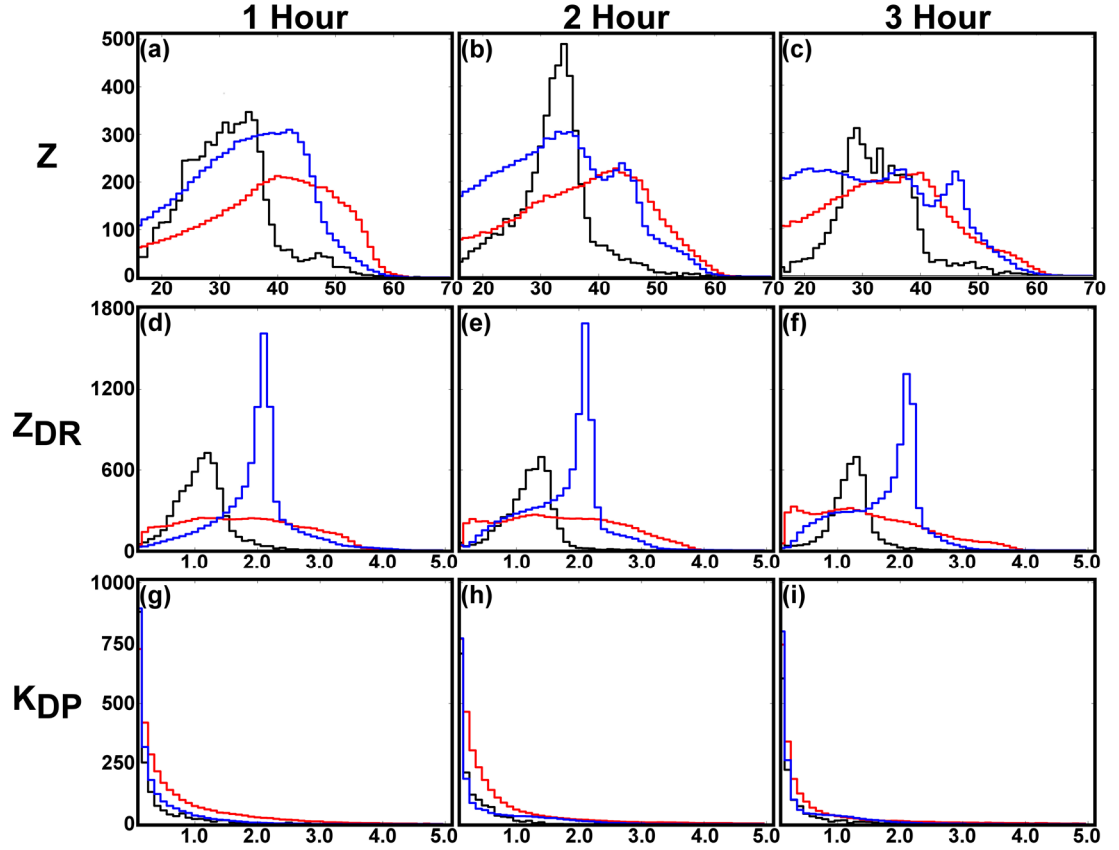


Fig. 3.14. Histograms of observed (black) KOUN and simulated reflectivity (dBZ) values from EXP_S (red) and EXP_D (blue) at (a) 0300, (b) 0400, and (c) 0500 UTC at a 0.5° tilt as well as (d-f) observed and simulated differential reflectivity (dB) values and (g-i) observed and simulated specific differential phase ($^\circ \text{ km}^{-1}$) values. The values in EXP_S and EXP_D are normalized by the size of each ensemble.

Differences between EXP_S and EXP_D are readily apparent in histograms of the predicted dual-pol values (Fig. 3.14d-i). Observed Z_{DR} values (Fig. 3.14d-f) peak at about 1.0 to 1.5 dB due to the broad coverage of moderately-sized raindrops in the

leading stratiform region. EXP_D over-forecasts the coverage of the leading stratiform precipitation, leading to an overall high-bias in the Z_{DR} histogram, and slightly over-forecasts the location of the histogram peak in Z_{DR} values, but the overall histogram pattern is similar to that of the observations. EXP_S, on the other hand, has a uniform distribution of Z_{DR} values throughout the forecast period, with no evidence of the peak seen in the observations and in EXP_D, due to the lack of broad coverage of stratiform precipitation in EXP_S. EXP_S also has a larger number of very high values ($Z_{DR} > 3.0\text{dB}$) resulting from the unorganized region of intense convection in the center of the system. Relatively little bias is noted in the K_{DP} histograms for EXP_D, producing histograms similar to that produced by the dual-pol observations (Fig. 3.14g-i). EXP_S over-forecasts the total coverage of non-zero K_{DP} values, again suggesting a high-bias in liquid water content overall compared to the observations. This substantial high-bias in liquid water content in convective precipitation skews EXP_S towards high values, with grid volumes exhibiting $K_{DP} > 3.0 \text{ } ^\circ \text{ km}^{-1}$, particularly in the 1-hour forecast (Fig. 3.14g).

3.4 Summary and conclusions

Ensemble forecasts initialized from cycled EnKF ensemble analyses are produced for a mesoscale convective system (MCS) that occurred over Oklahoma and northern Texas on 8-9 May 2007 using single-moment (SM, Lin et al. 1983) and double-moment (DM) microphysics (Milbrandt and Yau 2005b) schemes. Qualitative and quantitative probabilistic methods are used to examine the MCS structure and precipitation distribution for the SM (EXP_S) and DM (EXP_D) experiments. Additionally, predicted dual-polarization (dual-pol) radar variables and their

probabilistic forecasts are also evaluated against available dual-pol radar observations, and discussed in connection with model predicted microphysical states and structures. The current study expands on the work of Putnam et al. (2014) which focused on the EnKF data assimilation and the deterministic forecasting aspects of the same two experiments that used SM and DM microphysics schemes, respectively. This paper focuses on ensemble probabilistic forecasting of reflectivity and the simulated dual-pol radar variables associated with the 8-9 May 2007 MCS.

EXP_D produces a very good qualitative and quantitative prediction of the both the overall precipitation coverage of the system (considering a threshold region of $Z > 20$ dBZ). EXP_S under-forecasts the leading stratiform precipitation and produces a large, poorly-organized region of convection rather than an organized leading convective line. EXP_D has higher forecast skill, measured in terms of the area under the relative operating characteristic curve (AUC), for 2 and 3-h forecasts of the stratiform precipitation and leading convective line comprising the northern portion of the MCS. EXP_D also provides ensemble forecasts with greater sharpness, as well as one in which the highest precipitation probabilities match regions of observed precipitation at a higher frequency.

EXP_D better represents the microphysics-related features in the MCS throughout the forecast period. This is notable in terms of Z_{DR} values, where the dual-moment ensemble forecast shows a clear distinction between the convective and stratiform precipitation regions, similar to that seen in the final EnKF analysis in Putnam et al. (2014), which continues throughout the forecast period. Additionally, EXP_D implies more realistic liquid water content in the convective region than

EXP_S, where unrealistically high K_{DP} values suggest the liquid water content has been over-forecast, associated with the unorganized system structure and precipitation development in the forecasts.

Producing meaningful probabilistic forecasts for dual-polarization (dual-pol) variables proves challenging. Dual-pol signatures are often produced by physical processes within convective systems with very small spatial scales; scales of less than a few kilometers often. These small-scale structures are smeared when probabilistic forecasts are generated using neighborhood-methods or a probability-matched ensemble mean. When individual ensemble members are examined, though, EXP_D shows superior predicted dual-pol fields compared to EXP_S, producing a notable arc of high Z_{DR} along the leading convective line in the MCS, resulting from size-sorting as smaller raindrops are advected rearward in the line while large raindrops fall faster along the leading edge. Such size-sorting processes are not represented in EXP_S, where Z_{DR} shows a monotonic relationship with Z . Probabilistic forecasts of Z_{DR} for EXP_D, while not particularly accurate in matching the location of the observations, still indicate the presence of this arc of large raindrops along the leading convective line and the general direction and speed of motion of the line.

This is the first study to consider explicit ensemble-based probabilistic forecasting of simulated dual-pol radar variables, and it highlights several challenges for future work. Even on high resolution grids capable of resolving microphysical patterns that occur on small spatial scales, quantitative verification scores for dual-pol signatures that usually have very small spatial scales (even compared to convective storms) suffer from a double penalty: forecasts of precipitation variables not only miss the location of

the observations (a ‘miss’), but also occur in a nearby location where the event was not observed (a ‘false alarm’). Some probabilistic neighborhood-based metrics are used in this case, including the AUC, to help account for spatial errors, but the distance and orientation of patterns in the simulated variables still presents a challenge when using such methods. Scores for dual-pol variables, specifically K_{DP} , are poorer as the threshold considered increases, despite the neighborhood radius of 5 km used, due to both the small spatial scale of the patterns being considered and discrepancy in the range of forecast values versus observed values. Although using a larger neighborhood may alleviate to a larger extent the effect of spatial error, the probabilistic forecasts produced using progressively larger neighborhood radii will be more and more smoothed, losing the resolution necessary to capture small-scale features and negating their intended purpose. Additional methods of quantitatively evaluating dual-pol variables include histograms, which can provide information on general biases without considering spatial error. In such histograms produced for this case, high biases in the number of large drops and overall liquid water content, as suggested by the high biases in predicted K_{DP} values, are identified in EXP_S, likely due to the representation of convective precipitation within EXP_S. Possible future quantitative verification methods for dual-pol fields include object-based methods (e.g. Davis et al. 2006, Johnson et al. 2013, Zhu et al. 2015) that match similar storm features in observations to those in the forecasts to better compare dual-pol variable patterns; this, and other forecast evaluation methods for dual-pol fields, remains a promising area for future research endeavors. More studies evaluating and improving microphysics

parameterizations and the dual-pol radar simulators are also needed (e.g., Johnson et al. 2016b; Putnam et al. 2016).

Chapter 4 Assimilation of Polarimetric Radar Data using EnKF: Experiment Setup and Sensitivity Testing

4.1 Introduction

Convective storms feature complex cloud microphysical and dynamical processes that interact with one another to lead to a diverse microphysical state, or the variation of different hydrometeor types and their particle size distributions (PSDs). For example, small raindrop evaporation in convective downdrafts increases the transport and intensity of colder air to the surface and has a significant effect on the surface cold pool (Snook and Xue 2008). In a reverse example, storm relative wind shear leads to the size sorting of hydrometeors, where larger hydrometeors fall closer to the updraft of a supercell while smaller hydrometeors are advected further outward in the forward flank (Kumjian and Ryzhkov 2012; Dawson et al. 2014). It is these highly non-linear chaotic processes and complex microphysical states that contribute to fast error growth in convection allowing model (CAM) forecasts, even when there are only slight deviations in the initial model state compared to the atmospheric state (Lorenz 1969; Larson et al. 2005; Wang et al. 2012). Data assimilation, or optimally combining a background model state with available observations, is used to best replicate the state of these convective storms for analysis and forecast initialization (Kalnay 2002). However, observations of the microphysical state of convective storms used for assimilation have thus far been limited to one parameter, reflectivity (Z). It is vital that we increase the amount of observed information during data assimilation as new meteorological observation systems become available, including the use of dual-polarimetric (dual-pol) radar observations, to improve the model microphysical state.

Dual-pol radars provide additional observations of the atmospheric microphysical state compared to Z alone, which is mainly a bulk representation of the number and size of the combination of hydrometeors present. The additional dual-pol parameters include differential reflectivity (Z_{DR}), which provides information on the axis ratio of hydrometeors, and specific differential phase (K_{DP}), which provides information on the liquid water content of hydrometeors (Bringi and Chandrasekar 2001). In addition, specific combinations and patterns of these parameters can be used to identify the known important microphysical and dynamical processes in convective storms, known as polarimetric signatures (Kumjian and Ryzhkov 2008). For example, the Z_{DR} arc signature seen in the forward flank of supercells is indicative of the aforementioned hydrometeor size sorting due to storm-relative wind shear (Kumjian and Ryzhkov 2008; Kumjian and Ryzhkov 2012; Dawson et al. 2014 Dawson et al. 2014) . Another signature, the K_{DP} foot, is a region of increased precipitation rate near the surface due to melting hail shedding rain drops and may serve as an indicator of the location of the forward flank downdraft (FFD) (Romine et al. 2008; Crowe et al. 2012). The recent dual-pol upgrade of the national WSR-88D radar network provides CONUS-wide coverage of dual-pol observations (ROC 2013), which had previously been limited to a few experimental and mobile radars. These vital dual-pol parameters are now consistently available nationwide for both research and future operational assimilation purposes with CAMs.

The assimilation and forecast performance of a CAM in terms of representing a wide variety of atmospheric microphysical states important microphysical processes is inherently tied to the cloud microphysics scheme used. Most microphysics schemes

currently used represent the PSDs of hydrometeors in bulk form with the gamma distribution

$$N(D)_x = N_{0x} D_x^{\nu_x(1+\alpha_x)-1} e^{-(\Lambda_x D)^{\nu_x}}, \quad (4.1)$$

where $N(D)_x$ is the number of hydrometeors of category x with diameter D in a unit volume (Ulbrich 1983; Milbrandt and Yau 2005a). The distribution includes four free parameters: 1) the slope parameter Λ_x ; 2) the intercept parameter N_{0x} ; 3) the dispersion parameter α_x , also referred to as the shape parameter; and 4) the dispersion parameter ν_x . Most schemes assume $\nu_x = 1$ for most hydrometeor categories and the distribution simplifies to

$$N(D)_x = N_{0x} D_x^{\alpha_x} e^{(-\Lambda_x D)}. \quad (4.2)$$

Microphysics schemes are classified by the number of these free parameters they update based on microphysical state variables predicted in the model. A single-moment (SM) scheme predicts mixing ratio (q) and updates Λ_x , a double-moment (DM) scheme also predicts number concentration (N_i) and updates N_{0x} , while a tripe-moment (TM) scheme also predicts radar reflectivity (z) and updates α_x . Previous studies have shown that CAMs require advanced multi-moment microphysics schemes (i.e. at least DM) to replicate microphysical processes like sedimentation (size-sorting, Wacker and Seifert 2001; Milbrandt and Yau 2005a) and the associated dual-pol signatures (Jung et al. 2010; Kumjian and Ryzhkov 2012). In fact, Jung et al. (Jung et al. 2010) demonstrated in simulations of dual-pol variables with a SM and DM MP scheme that the SM MP scheme could not replicate several signatures, including the Z_{DR} arc and mid-level Z_{DR} ring. Other signatures which were apparent in the SM scheme simulations were often unrealistic, including the underestimation of K_{DP} values in the K_{DP} foot.

Because dual-pol observations are indirect measurements, and due to the bulk representation of hydrometeor PSDs in most convective-scale models, forward operators are required to connect the observations to the model microphysical state variables. A polarimetric radar data (PRD) simulator is used to connect the model microphysical state variables to dual-pol observations and can be used as the forward operator in assimilation experiments. Since the values of the polarimetric variables are by definition impacted significantly by how the radar wave scatters in both the horizontal and vertical direction, it is important that the form and assumptions of the PRD simulator operator best replicate the interaction of the radar wave with the hydrometeors of all sizes and physical states.

Li and Mecikalski (Li and Mecikalski 2012) developed a PRDS with operators based on derived relations between Z_H , Z_{DR} , and K_{DP} from Bringi and Chandrasekar (Bringi and Chandrasekar 2001), but only provide relations for rain for a SM MP scheme and include several assumptions. Jung et al. (2008a) developed a more advanced set of operators for a SM MP scheme that included direct relations of the polarimetric variables and the model microphysical state variables, an axis-ratio relation for raindrops, a melting model, and radar wave scattering amplitude function fitted to the T-matrix method for rain and the Rayleigh approximation for ice hydrometeors. Xue et al. (Xue et al. 2010) and Jung et al. (Jung et al. 2010) expanded on these operators by adding the ability to use MM MP schemes and include look-up tables of actual T-matrix scattering amplitudes for all hydrometeors. Pfeifer et al. (2008) also developed a PRDS called SynPolRad which includes T-matrix scattering amplitude in the operator calculations. However, their calculation for the dielectric constant represents melting

hydrometeors as water coated with ice, while the dielectric constant calculation in the Jung et al. (2008a) melting model represents melting hydrometeors as ice coated with water which will have a significant impact on the simulated variables. The dielectric constant for water is significantly greater than ice and increases simulated Z . This matches the observed Z increase associated with melting hydrometeors because melting begins on the hydrometeor surface and the water coated melting hydrometeor appears as a large raindrop. SynPolRad also does not include an operator for K_{DP} .

The ensemble Kalman filter (EnKF, Evensen 1994; Evensen 2003) is particularly well suited for the assimilation of polarimetric variables due to these highly non-linear operators and multi-moment microphysics schemes required to take better advantage of the additional polarimetric variable information. The EnKF has been successful in previous convective scale assimilation studies with multi-moment microphysics schemes for real data cases (Jung et al. 2012; Yussouf et al. 2013; Putnam et al. 2014; Wheatley et al. 2014; Yussouf et al. 2015; Snook et al. 2016). The EnKF approximates the background model error through the flow-dependent error covariance between ensemble members and does not require an adjoint model as in 3DVAR and 4DVAR. The adjoint model is particularly difficult to develop for non-linear observation operators and MM schemes which include ice hydrometeors. The EnKF is also advantageous for MM schemes because forward operators for radar variables can be used to directly update the model microphysical state variables. Additionally, the cross-covariances between model state variables in the ensemble update state variables that are updated by observations via the forward operators (Snyder and Zhang 2003).

One concern with the EnKF is that updating the numerous microphysical state variables in a MM MP scheme is a significantly underconstrained problem when relying on only two independent observations (Z and V_r). For example, in a DM scheme, there are as many as 12 state variables; 6 hydrometeor categories each with a q and N_r . However, Xue et al. (2010) showed encouraging results in the ability of the EnKF to update 10 state variables associated with a DM Milbrandt and Yau (Milbrandt and Yau 2005b) MP scheme in the presence of model error. The assimilation of additional dual-pol variables will aid in providing additional independent information to update all the numerous microphysical state variables.

Previous research for the assimilation of polarimetric variables is very limited – in both OSSE and observed experiments - and has not included the advanced operators and microphysics schemes required to take the best advantage of the additional dual-pol information as possible. Jung et al. (Jung et al. 2008b) assimilated Z_{DR} , reflectivity difference (Z_{DP}), and K_{DP} in addition to Z and V_r in an EnKF OSSE experiment using the forward operators developed in Jung et al. (Jung et al. 2008a). Analyses with the additional dual-pol variables improved the root mean square errors (RMSEs) of the microphysical state variables as well as all other model variables. However, this study used the SM Lin (Lin et al. 1983) scheme and forward operators that use fitted T-matrix scattering amplitudes for rain. Li and Mecikalski (Li and Mecikalski 2012) assimilated both Z_{DR} and K_{DP} , in addition to Z and V_r , for both a mesoscale convective system (MCS) and isolated convective storm case. The results showed that forecasts initialized with the additional dual-pol variables provided a positive impact on short-term forecasts in terms of both storm structure and location. However, the study uses a warm-rain SM

Kessler (Kessler 1969) MP scheme along with the 3DVAR DA method that only updates q_r via very simple Z equations, such as from Kessler (Kessler 1969). Additionally, the results are focused on comparing intensity, structure, and location of Z and not evaluating the analyzed microphysical state with the dual-pol observations, including polarimetric signatures that are representative of important atmospheric microphysical processes. Between these studies, it is clear that the impact of dual-pol observations for a real data assimilation experiment on the microphysical state has not been investigated. The impact these new dual-pol observations have on the model state must first be understood before the observations can be used to help initialize convective-scale forecasts.

The purpose of this chapter is to examine for the first time the impact that assimilating dual-pol parameters has on EnKF-analyzed supercell storms for real data cases while using a fully DM ice microphysics scheme and advanced polarimetric forward operators. Two high impact tornadic supercell cases from 10 May 2010 and 20 May 2013 are chosen to assess the robustness of the results across multiple cases. A new method to pre-calculate a portion of the forward operator is developed to use the advanced Jung et al. (Jung et al. 2010) operators so that the calculated T-matrix scattering amplitudes for all hydrometeors can be utilized for the first time during assimilation without increasing the assimilation time. The advanced operators have been used with a real case for model MP scheme verification (Putnam et al. 2016), but assimilation experiments have not yet been conducted due to the previous computational expense. Specific goals include verifying the assimilated dual-pol observations and evaluating the model microphysical state through comparisons of

raindrop size with dual-pol observations, changes in the PSDs between experiments, and comparisons with retrieved PSD parameters using the dual-pol observations. Additionally, several sensitivity tests run during the experiment are presented as a template to help guide future research in real case dual-pol assimilation.

The remainder of this Chapter contains the following sections. Section 4.2 contains a meteorological overview of the supercell cases considered. In section 4.3, the background model, microphysics scheme, and the new look-up table observation operators are described for control experiments assimilating Z , Z and Z_{DR} , and Z and K_{DP} . Section 4.4 contains sensitivity test results which vary such aspects as the EnKF model error treatment methods, radar filtering procedure, observations errors, and configuration of radars assimilated. The best results from section 4.4 will be analyzed in Chapter 5.

4.2 Overview of case studies

4.2.1 The 20 May 2013 New Castle-Moore, OK tornadic supercell case

On 20 May 2013 an outbreak of tornadoes occurred across the southern Plains. Most notably, one supercell storm over central Oklahoma produced a violent tornado that tracked across the southern Oklahoma City metropolitan area during the mid-afternoon hours (SPC 2016b). At 1800 UTC 20 May, an upper level low pressure system was in place over the north-central United States with a large region of strong, southwesterly flow at 500 mb extending southward to the southern plains, providing significant deep shear for rotating updrafts (Fig. 4.1a). At the surface, a cold front trailed from an associated surface low in the Northern Plains southward into Oklahoma, with a dryline intersecting the front just to the west of Oklahoma City. A broad and

extremely moist warm sector existed ahead of this cold front/dry line intersection with widespread mixed layer CAPE values greater than 3000 J kg^{-1} (Fig 4.1b). Widespread storms began to develop after 1800 UTC, with one such storm developing just to the southwest of Oklahoma City. This storm produced a tornado that began shortly before 2000 UTC and remained on the ground for over 40 minutes, tracking from New Castle to Moore. The tornado was rated EF5 after causing widespread catastrophic damage across Moore with a total cost of several billion dollars (Burgess et al. 2014). For more information on this case, the reader is referred to Burgess et al. (2014), Zhang et al. (2015), and Kurdzo et al. (2015). This case occurred after the dual-pol upgrade of all WSR-88D network radars and was in close proximity to KTLX providing more than adequate coverage of dual-pol observations.

4.2.2 The 10 May 2010 Moore-Harrah, OK and Norman-Pink, OK tornadic supercells case

An intense outbreak of tornadoes occurred across Oklahoma on 10 May 2010, including multiple violent tornadoes within the Oklahoma City metropolitan area. A seasonably strong short-wave trough advanced eastward over the southern plains during the morning, leading to rapid surface cyclogenesis and an impressive northward advance of highly unstable air over Oklahoma. At about 230 UTC 10 May, a 994 mb surface low was located over southern Kansas with a southeastward oriented warm front extending over central Oklahoma and a southward oriented dryline over western Oklahoma followed closely by a southeastward advancing cold front (Fig. 4.2a).

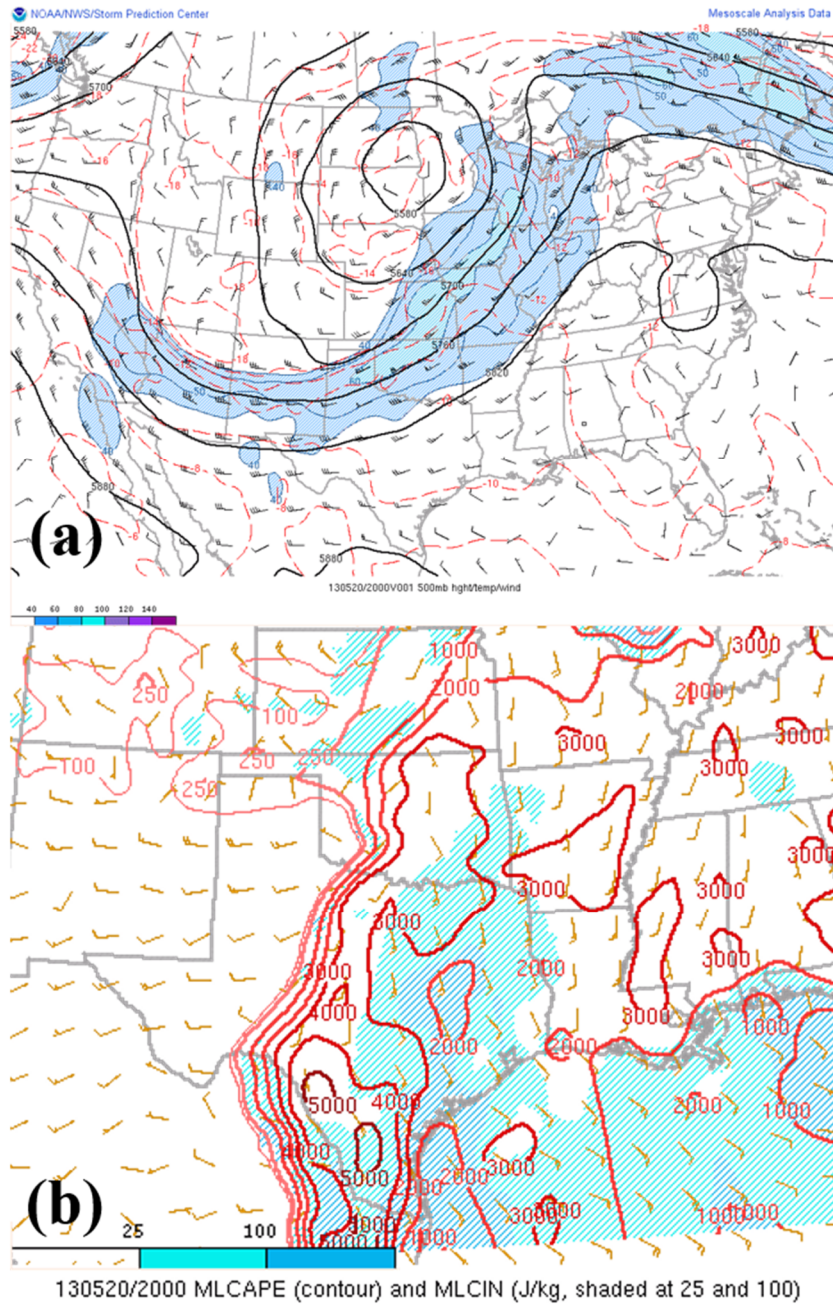


Fig. 4.1. (a) 500 mb wind barbs, wind fields (colorfill, 20 knot interval), height contours (60-dam interval), and air temperature (red dashed lines, 2 °C intervals) as well as (b) Mixed layer CAPE (red contours) and CIN (colorfill) (J kg^{-1}) analyses from the Storm Prediction Center (SPC) at 2000 UTC 20 May 2013.

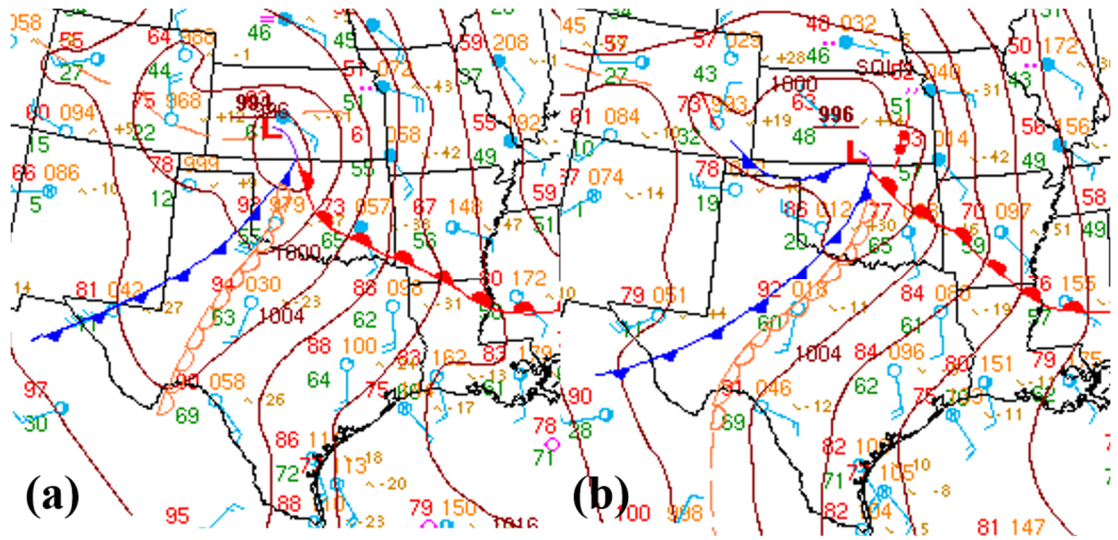


Fig. 4.2. (a) 2100 UTC 10 May 2010 and (b) 0000 UTC 11 May 2010 Storm Prediction Center surface analyses. Note the marked locations of the warm front, dryline, cold front, and surface low.

Supercell storms initiated rather early over northern Oklahoma and southern Kansas with the first tornadoes occurring around 1900 UTC (SPC 2016a). By 0000 UTC, the dryline had advanced to the I-35 corridor and multiple supercell storms rapidly developed ahead of it just to the west of Oklahoma City (Fig. 4.2b). Two storms that tracked over the southern portions of the metropolitan area in very close proximity to one another both produced multiple tornadoes, including two violent tornadoes (Fig. 4.3, NWS 2016). The first violent tornado began at 2220 UTC near Moore and tracked northeastward for 30 minutes before lifting near Harrah (tornado ‘I1’ in Fig 4.3). This was quickly followed by a tornado that developed in south Norman and tracked northeastward for nearly 30 minutes and dissipated near Pink (tornado ‘J1’ in Fig. 4.3). At approximately 2245 UTC, the northern Moore storm split and the right, more southern split quickly produced a third strong tornado just west of Shawnee (tornado ‘L1’ in Fig 4.3). Amazingly, this group of storms produced several additional low

intensity tornadoes during this time frame. The storms were observed by the National Severe Storm Laboratory’s dual-pol S-band experimental and research radar, KOUN, located in north Norman, as well as the nearby WSR-88D radar KTLX. Additional observational overviews of this case include Palmer et al. (2011) and Bodine et al. (2013).

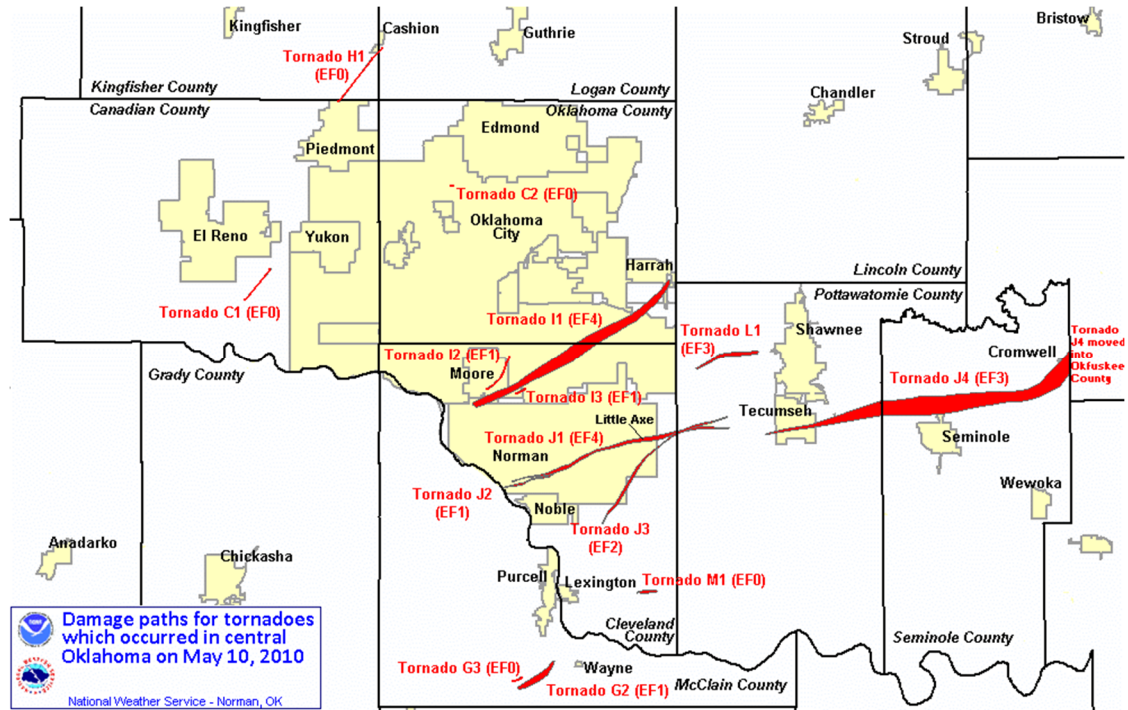


Fig. 4.3. Norman Weather Service Office tornado damage survey paths from 10 May 2010 tornado outbreak.

4.3 Method

In this section, the general model and MP scheme experiment settings, radar data, and observation operator information for the control experiments are introduced. For the 20 May 2013 case, the experiment configuration is inherited from Snook et al. (2016), while in the 10 May 2010 case the configuration is designed similarly to Jung et al. (2012). For simplicity, the 10 May 2010 case will be referred to as ‘M10’ and the 20

May 2013 case as ‘M20’. Including different cases with different configuration settings will increase the reliability of our findings. The forecast model and general EnKF configuration settings for the experiments from both cases are discussed in sections 4.3.1 and 4.3.2 while section 4.3.3 contains further details on the dual-pol variable assimilation. Further details on the radar data processing are given in section 4.4.4 and an explanation of the observation operators is given in 4.4.5.

4.3.1 Prediction model and microphysics scheme

For this study, we have used the Advanced Regional Prediction System forecast model (ARPS, Xue et al. 2000; Xue et al. 2001; Xue et al. 2003). Briefly, ARPS is a three-dimensional, fully-compressible, non-hydrostatic, convection allowing model. The state variables predicted include the three-dimensional wind components (u, v, w), pressure (p), potential temperature (θ), and water vapor mixing ratio (q_v), as well as microphysical state variables determined by the MP scheme to be described later. Solar radiation is parameterized using the National Aeronautics and Space Administration (NASA) Goddard Space Flight Center long- and shortwave radiation scheme while Sub-grid scale turbulence is parameterized with a 1.5-order turbulent kinetic energy (TKE) scheme. The soil model includes two layers with parameterized surface fluxes for sensible and latent heat as well as moisture. Additional details on the model physics parameterizations are given in Xue et al. (2001).

The Milbrandt and Yau (Milbrandt and Yau 2005b) DM MP scheme is used. In addition to the previous state variables, the scheme includes the prediction of mixing ratios for cloud water (q_c), ice (q_i), rain (q_r), snow (q_s), graupel (q_g), and hail (q_h) as well as their respective number concentrations (N_{ic} , N_{ii} , N_{ir} , N_{is} , N_{ig} , and N_{ih}). For M10, the

prediction of graupel is not included. The additional predicted state variables for graupel were found not to have a significant impact on the storm evolution in Jung et al. (Jung et al. 2012). However, the prediction of graupel is included for M20 case to remain consistent with Snook et al. (2016) and provide an additional contrast between the experiments.

4.3.2 Experiment configuration and EnKF settings

4.3.2.1 20 May 2013 experiment configuration

The M20 configuration is inherited from Snook et al. (2016); the details on this configuration are summarized here. The model grid is 603 x 653 grid points in the horizontal with a stretched vertical grid consisting of 63 levels with a minimum spacing at the surface of 50 m and average spacing of 425 m. The grid spacing is 500 m in order to resolve the highly detailed processes that contribute to the highly localized presentation of polarimetric patterns and signatures. The terrain for the grid is interpolated from USGS with a resolution of 30 seconds of arc. For reference, the experiment domain and observations of the storms of interest near Moore, OK are plotted in Fig. 4.4.

The experiment timeline consists of a 30 minute spin-up period followed by a 1.5 hour assimilation window (Fig. 4.5). An initial ensemble of 40 members is obtained via interpolation from the 4 km regional CAPS Spring Experiment storm scale ensemble forecasts (SSEF, Kong 2013) at 1800 UTC 20 May 2013. The external boundary conditions are also interpolated from the SSEF. Random, Gaussian storm scale perturbations (Tong and Xue 2008), smoothed with a 2D recursive filter with a decorrelation length scale of 6 km in the horizontal and vertical are added to u and v , using

a mean standard deviation of 0.5 m s^{-1} , as well as to potential temperature (θ) with a mean standard deviation of 0.5 K . A 30 minute spin-up forecast from 1830 UTC to 1900 UTC is run prior to assimilation.

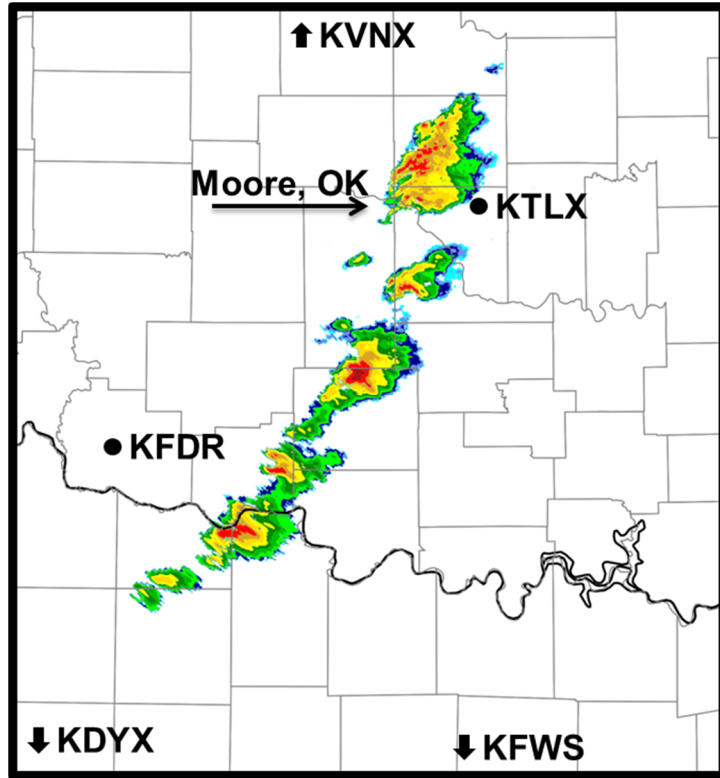


Fig. 4.4. 20 May 2013 experiment domain and location of radars included. Observed reflectivity (Z , dBZ) at the 0.5° tilt from KTLX at 1938 UTC 20 May 2013 is included.

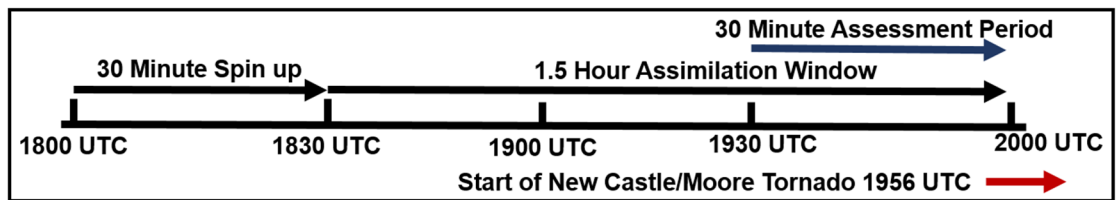


Fig. 4.5. Diagram of experiment timeline including the spin-up forecast, assimilation window, 30 minute assessment period, and times of tornadoes from the storms of interest.

The ensemble square root filter (EnSRF, Whitaker and Hamill 2002) is used to assimilate both radar and surface observations at 5 minute intervals over a 1.5 hour period from 1830 UTC to 2000 UTC. Two experiments are conducted, one in which Z and V_r are assimilated (experiment CZ, short for ‘control Z’) and one in which Z_{DR} is assimilated in addition to Z and V_r (experiment CZZDR, short for ‘control Z and Z_{DR} ’). The names Z and Z_{DR} are used in order to emphasize the different number of precipitation-related radar observations that are assimilated while noting that V_r is assimilated in all cases. An experiment for K_{DP} is not included for this case because the observations were particularly noisy and not consistent across the storms. All variables in all experiments are assimilated from five WSR-88D network radars located within and near the domain: KDYX, KFDR, KFWS, KTLX, and KVNK (see Fig. 4.4). Z_{DR} is available from all radars since this case occurred after the WSR-88D upgrade (ROC 2013). Observations of precipitation are assimilated at every other grid point because initial experiments showed this increased model stability. Clear air observations are assimilated every 4 grid points. The volume scans for each radar are not synchronized. At each assimilation time, the previous volume scan closest to the assimilation time within the 5 minute forecast window is used. If there is no volume scan during this time, then the observations are not assimilated from that radar. Data greater than 5 minutes prior to assimilation for KDYX and KFWS is used during the initial analysis at 1830 UTC since there were no prior cycles before this. A summary of the volume scans used for each radar is given in Table (4.1).

Assim Time (UTC)	Observation Time (UTC)				
	<i>KDYX</i>	<i>KFDR</i>	<i>KFWS</i>	<i>KTIX</i>	<i>KVNX</i>
183000	182126	182536	182140	182625	182726
183500	183106	183033	183114	183118	183210
184000		183935		183949	183957
184500	184046	184326	184049	194338	184258
185000		184718		184742	184901
185500	185026	185109	185024	185133	185203
190000		185904	185520	185953	185805
190500	190005	190310	190017	190411	190408
191000	190945	190714	190513	190826	190710
191500		191131	191011	191243	191312
192000	191925	191548	191507	191658	191928
192500		192422	192500	192116	192230
193000	192953	192839	192956	192949	192844
193500	193432	193256	193452	193405	193158
194000	193913	193713	193949	193821	193813
194500	194356	194130	194445	194238	194440
195000	194836	194547	194942	194655	194740
195500	195315	195422	195439	195111	195354
200000	195753	195838	195934	195941	195708

Table 4.1. Table of radar volume start times for each assimilation cycle for the 20 May 2013 case.

The observation error in both experiments is 6.0 dBZ for Z and 4.0 m s⁻¹ for V_r . These values follow recent assimilation experiments on this scale and are optimal based on our previous studies. Experiments with lower observation errors for Z were tried but resulted in instability in the ensemble. Clear-air Z observations are assimilated, which has been shown to help suppress spurious convection (Tong and Xue 2005), while V_r observations are assimilated when $Z > 10$ dBZ. The assimilation of Z_{DR} is further discussed in section 4.3.3. Surface observations are assimilated from all available Automatic Surface Observing System (ASOS) and Automatic Weather Observing System (AWOS) observation sites within the domain. These observations include u , v ,

air temperature T , dewpoint temperature T_D , and air pressure p . The observation errors are 1.5 m s^{-1} for u and v , 2.0 K for T and T_D , and 2.0 hpa for p . A summary of the observation errors is given in Table 4.2.

	Surface Obs					Profiler Obs	
	$U \text{ (ms}^{-1}\text{)}$	$V \text{ (ms}^{-1}\text{)}$	$T \text{ (K)}$	$T_D \text{ (K)}$	$Pa \text{ (hpa)}$	$U \text{ (ms}^{-1}\text{)}$	$V \text{ (ms}^{-1}\text{)}$
20-May	1.5	1.5	2.0	2.0	2.0	2.5	2.5
10-May	1.5	1.5	2.0	2.0	NA	2.5	2.5

Table 4.2. Table of conventional observation error values for both the 20 May 2013 and 10 May 2010 experiments.

Other EnKF configuration settings include using a covariance localization radius for the radar observations of 3 km in both the horizontal and vertical directions using the correlation function of Gaspari and Cohen (Gaspari and Cohn 1999). For the surface observations, the horizontal radius is 500 km and the vertical radius is 6 km. To help account for filter divergence, we use the ‘relaxation to prior spread’ covariance inflation method of Whitaker and Hamill (Whitaker and Hamill 2012), with an inflation coefficient of 0.95. In other words, 95% of the prior spread is restored.

4.3.2.2 10 May 2010 experiment configuration

For the M10 case, the experiment domain is 531×363 in the horizontal with 53 vertical levels. As in the M20 case, the horizontal grid spacing is 500 m and the vertical grid has a minimum spacing of 50 m and an average spacing of 425 m. For reference, the domain and storms of interest are plotted in Fig 4.6. Similar to the M20 case, there is an approximately 30 minute spin-up forecast from 2100 UTC to shortly after 213130 UTC and then a 1.5 hour assimilation window (Fig. 4.7). The initial ensemble members are nested within a 4 km regional ARPS model ensemble nested within a 40 km North

American ensemble. Briefly, the North American ensemble uses a GSI-based, coupled EnKF-En3DVar hybrid assimilation system created for the Rapid Refresh (RAP) model over 0000 UTC 8 May 2010 to 2100 UTC 16 May 2010 (Pan et al. 2014). The nested 4 km regional ensemble is initialized at 1800 UTC 10 May 2010 and has a domain size of 443 x 483 in the horizontal with 53 vertical levels; the domain covers the CAPS VORTEX II domain used during the 2010 Spring Experiment (Kong 2010). The 4 km ensemble members are interpolated individually down to the 4 km grid from respective members of the 40 km ensemble, which also provide the lateral boundary conditions for each member. A MPI-OPEN MP hybrid parallel EnSRF system is used to assimilate both radar and conventional observations every hour over a 6 hour period. The model MP scheme is SM Lin (Lin et al. 1983) and the observation operators for radar data assimilation are from Jung et al. (Jung et al. 2008a). The 500 m grid ensemble members are interpolated down individually from 4 km ensemble analysis at 2100 UTC, including the terrain. Dry lateral boundary conditions for 2100, 2200, and 2300 UTC are also interpolated from each 4 km member to the 500 m grid. Random, Gaussian storm scale perturbations, smoothed using a 2D recursive filter with a de-correlation length scale of 6 km in the horizontal and 3 km in the vertical, are added to each member of the interpolated ensemble prior to the spin-up forecast. The standard deviation of the perturbations is 2 m s^{-1} for u , v , and w , 1.0K for θ , and $.2 \text{ g kg}^{-1}$ for water vapor (q_v), cloud water mixing ratio (q_c), rain water mixing ratio (q_r), cloud ice mixing ratio (q_i), snow mixing ratio (q_s), and hail mixing ratio (q_h). The perturbations for w and the hydrometeor mixing ratios are confined to within a 4 km horizontal and 2 km vertical radius of grid points where observed radar echoes from KTLX exceed 30.0

dBZ to avoid initiating spurious convection. Additionally, the perturbations for θ are positive only.

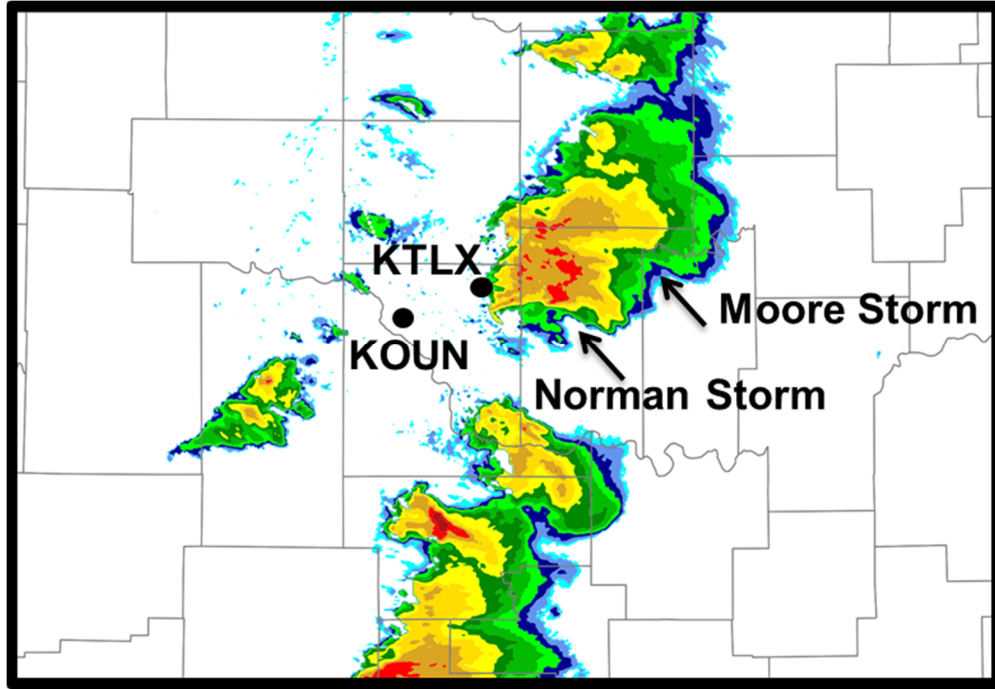


Fig. 4.6. 10 May 2010 experiment domain and location of radars included. Observed reflectivity (Z , dBZ) at the 0.5° tilt from KOUN at 2250 UTC 10 May 2010 is included.

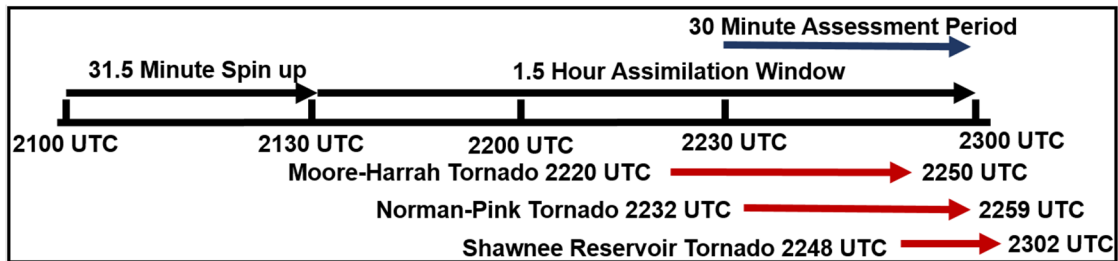


Fig. 4.7. Diagram of experiment timeline including the spin-up forecast, assimilation window, 30 minute assessment period, and times of tornadoes from the storms of interest.

Radar, surface, and profiler observations are assimilated from 213130 UTC to 230130 UTC at 4 minute 30 second intervals. Two experiments are conducted, one which assimilates Z and V_r from KTLX (experiment CZ) and one which assimilates Z

and V_r from KTLX plus Z_{DR} from the National Severe Storms Laboratory's S-band dual-pol research radar, KOUN (experiment CZZDR). An additional experiment assimilating K_{DP} from KOUN in addition to Z and V_r from KTLX is conducted based on the results for sensitivity testing with the control experiments. KOUN is included since this case occurred prior to the WSR-88d dual-pol upgrade. All radar observations are assimilated at every other grid point. The 4 minute 30 second intervals are used because the radar volumes from KTLX on this day were set to a slightly faster speed than the normal approximately 5 minute volume scan. The KTLX volumes for each cycle are chosen following the M20 case, with the closest volume started prior to the assimilation time used. The KOUN volume with a start time closest to the KTLX volume used at each assimilation time provides the dual-pol observations for each cycle. A table of the volume scan times used for each assimilation time is given in Table 4.3. The observation error is 5 dBZ for Z , 3 m s^{-1} for V_r . Surface observations for u , v , T , and T_D are assimilated from all ASOS, AWOS, and Oklahoma Mesonet stations within the domain. The observation error is 1.5 m s^{-1} for u and v and 2K for T and T_D . Profiler observations of u and v are available at 2200 UTC and assimilated at the assimilation time immediately following with an observation error of 2.5 m s^{-1} . A summary of the observation errors for this case is included in Table 4.2.

Assim Time (UTC)	Observation Time (UTC)	
	KTLX	KOUN
213130	212924	213043
213600	213337	213502
214030	213752	
214500	214218	214231
214930	214909	214650
215400	215323	215108
215830	215736	215527
220300	220151	215945
220730	220604	220403
221200	221017	220821
221630	221436	221240
222100	221850	221658
222530	222304	222116
223000	222717	222533
223430	223132	222951
223900	223545	223409
224330	224205	223827
224800	224627	224556
225230	225041	225014
225700	225453	225432
230130	225929	225851

Table 4.3. Table of radar volume start times for each assimilation cycle for the 10 May 2010 case.

Additional EnKF settings for this case include a covariance localization radii for radar observations of 3 km in the horizontal and vertical using the Gaspari and Cohen (1999) correlation function. The covariance localization radii are 60 km in the horizontal and 6 km in the vertical for the surface observations and 800 km in the horizontal and 6 km in the vertical for the profiler observations. The model error treatment methods used for this case are a combination of relaxation to prior spread with an inflation coefficient of 1.0 and multiplicative inflation (Anderson 2001) with an

inflation factor of 1.2. Additionally, during each forecast period, the shape parameters of rain and hail are varied between 0.0 and 2.0 in 0.05 increments between each ensemble member. Varying the shape parameter in our previous experiments has been shown to help improve ensemble spread and the analysis (Xue et al. 2010; Jung et al. 2012).

4.3.3 Dual-pol observation assimilation settings

The assimilation of the dual-pol variables is treated differently than for Z and V_r . First, Z_{DR} (and K_{DP} for M10) is assimilated after Z and V_r are analyzed. The ARPS EnSRF usually assimilates each variable at each grid point. For this study, Z and V_r are assimilated at each grid point and, after that analysis is completed, Z_{DR} is assimilated. It is believed that Z_{DR} has a greater impact on the analysis in this way. This occurs by default for the M10 case because the Z_{DR} and K_{DP} observations are assimilated from a second radar after Z and V_r are assimilated. Second, dual-pol observations are assimilated at grid points 2000 m AGL or less. This excludes observations within and above the melting layer for which the simulation of the dual-pol variables via the observation operators contains more uncertainty. This specifically applies to dry and wet snow, which can vary significantly in terms of size, shape, and density, factors that become increasingly difficult to model during melting since mixed-phase hydrometeors are not predicted in the model. Future studies, including a follow-up study to Johnson et al. (Johnson et al. 2016a), will investigate simulated dual-pol variables above the melting layer before they are used in assimilation studies.

The observation error for Z_{DR} is 0.6 dB and is approximately twice the typical Z_{DR} observation error (Doviak and Zrnica 1993; Ryzhkov et al. 2005) to account for

errors in the observation operator. Only values of $Z_{DR} > 0.3$ dB are assimilated based on thresholds determined in Jung et al. (2008b). The authors found through a comparison of simulated errors in Z and Z_{DR} that there is no discernable independent information from Z_{DR} values below this threshold due to noise. The K_{DP} error for the M10 case is $0.3 \text{ } ^\circ \text{ km}^{-1}$ and slightly lower than that used for Z_{DR} due to a significantly higher threshold used for assimilation, $0.9 \text{ } ^\circ \text{ km}^{-1}$. K_{DP} observations are noisier compared to Z_{DR} (Jung et al. 2008b).

4.3.4 Radar data processing

The presence of ground clutter and other biological scatterers has a significant impact on the dual-pol observations. In most cases for Z , the values of these observations during the daytime hours are low enough or non-existent to the point that they will have little impact on the analysis. However, the Z_{dr} observations cover the full spectrum of typical values seen with precipitation and thus must be removed. The Park et al. (Park et al. 2009) hydrometeor classification algorithm (HCA) is used to classify and then remove observations determined to be from ground clutter or biological scatters. This applies to all radars in the M20 case and KOUN in the M10 case. For the 20 May 2013 case, many ρ_{HV} values are particularly low in the convective regions, potentially due to non-uniform beam filling; these values are often lower than 0.8. Values this low typically correspond to ground clutter and biological scatterers in the HCA algorithm. The use of the texture parameters $SD(Z)$ and $SD(\Phi_{DP})$ helps regulate this but some values are still wrongly classified by the algorithm. A small number of observed values are removed that should not be due to these anomalously low values. The removal of ground clutter and biological scatterers elsewhere is judged to be more

vital, particularly for Z_{DR} which contains anomalously large values when clutter is present. Manual ground clutter removal is performed on KTLX for the M10 case since it had not yet been upgraded to dual-pol capabilities.

Additional preprocessing of the radar data includes performing automatic velocity dealiasing on all radars from the M20 case and KOUN from the M10 case. The KTLX observations from M10 require manual unfolding because the Nyquist velocity is not consistent throughout the radar volume. The V_r data were manually unfolded for this case in (Wang et al. 2016). For this study, SOLO is also used to remove ground clutter. A 5-point along-the-radial median filter is applied to all variables. K_{DP} is calculated from filtered specific differential phase (Φ_{DP}) using a least squares fit algorithm detailed in Ryzhkov and Zrnic (1996). Low precipitation ($Z < 40$ dBZ) echoes are heavily filtered with 25 range gates and heavy precipitation ($Z > 40$ dBZ) echoes are lightly filtered with 9 range gates. The observations are interpolated to the model grid in the horizontal but left at the radar tilt elevation in the vertical (Xue et al. 2006). Since K_{DP} is quite noisy, a second 9-point square median filter is used on the interpolated observations. Finally, several bad radials from KOUN for the M10 case were listed as missing to avoid assimilating corrupt data.

4.3.5 Observation operators

Our previous studies have used the observations operators originally developed in Jung et al. (2008a) (eg. Jung et al. 2012, Putnam et al. 2014). These operators contain a melting model and raindrop axis ratio relation, and use a fitted approximation to T-matrix scattering amplitudes for rain and the Rayleigh approximation for ice hydrometeors. A more advanced set of operators were developed in Jung et al. (Jung et

al. 2010). The improvements included an updated axis ratio for rain (Brandes et al. 2002) that improves upon the prior relation modeling more spherical shapes. Additionally, full T-matrix scattering amplitudes calculated for a range of diameters for all hydrometeor categories were used. The new operators lead to more realistic simulated dual-pol values. For example, Z_{DR} values with these operators are lower compared to the prior operators due to the revised axis-ratio relation for rain. Z values are also better approximated for large, melting hail where the scattering of the radar wave by hydrometeors of this size enters the Mie regime. However, due to the new axis ratio relation and table of scattering amplitudes, these operators require numerical integration over the particle size distribution that adds a significant amount of computational time during assimilation.

A modified set of the observation operators from Jung et al. (Jung et al. 2010) has been developed to increase computational speed without sacrificing much accuracy. The operators require the use of look-up tables of T-matrix scattering amplitudes. To speed up the calculation, a portion of the calculation is computed based on ranges of possible PSD parameter values prior to assimilation and stored in look-up tables. Specifically, the tables are based on the Λ_x (and α_x) parameter of the PSD. In this experiment, only Λ_x is considered since in these experiments a DM MP scheme is used and the α_x values are 0 for all hydrometeors during assimilation.

As an example, the horizontal Z_{hh} (generally discussed as Z) observation operator for rain is given as:

$$Z_{hh} = \frac{4\lambda^4}{\pi^4 |K_w|^2} \int |f_a(\pi)|^2 N_0 e^{-\Lambda D} dD , \quad (4.3)$$

where Z_{hh} is the horizontal radar reflectivity factor, λ is the wavelength of the radar, K_w is the dielectric factor for water, and $f_a(\pi)$ is the backscattering amplitude along the major axis (adapted from equation 3 from Jung et al. (Jung et al. 2010)). For reference, in Jung et al. (2008a), when a fitted approximation to the T-matrix scattering amplitudes is used, a power law function is used in place of $|f_a(\pi)|$. Next, a summation over rain diameters from 0.04 to 7.96 mm is computed:

$$Z_{hh} = \frac{4\lambda^4}{\pi^4 |K_w|^2} N_0 \sum_{i=1}^{100} |f_a(\pi)|^2 e^{-\Lambda D} dD . \quad (4.4)$$

N_0 can be calculated outside the summation because it is not dependent on diameter. The summation portion of the expression is pre-calculated based on Λ_r values at 1 m^{-1} increments, which for simplicity will be referred to as $S(\Lambda_r)$. During assimilation, Λ_r is calculated based on the model predicted q_r and N_r . Since the increment range of Λ_r is known, the corresponding $S(\Lambda_r)$ value can be quickly looked up from the pre-calculated table. If the model calculated Λ_r value is between two Λ_r values in the table, the associated $S(\Lambda_r)$ values are interpolated. Pre-calculated look-up tables for this part of the expression are computed for all hydrometeors categories and all possible water fractions detailed in Jung et al. (2010) for their equations 3, 4, and 5. Although there are some small errors in the calculated variables using the modified operator, the improvement in the calculated variables using these operators compared to using the Jung et al. (2008a) operators is judged to be greater than any subsequent errors in the calculation due to the look-up tables. A more detailed example is given in Appendix A1.

4.4 Dual-pol assimilation sensitivity tests

The EnKF assimilation of dual-pol observations is a new area of research and thus there is little prior information on successful EnKF configuration settings. Several initial tests are run that vary the settings of the initial control experiment to narrow down the best configuration for both cases. These include testing different model error treatment methods, using additional radar filtering methods, and altering the configuration of the radar data and observations that are assimilated.

The results are compared by calculating the root mean square error (RMSE) for the ensemble mean (enmean) analysis of both the lowest radar tilt and all observed data points in the domain below the 2000 m AGL threshold where Z_{DR} is assimilated during the 30 minute assessment period (Table 4.4 for M20, Table 4.5 for M10). For convenience, these will be referred to as the ‘lowest tilt domain’ and the ‘ Z_{DR} domain’. The RMSE is calculated for areas where the observations exceed 5.0 dBZ for Z and 0.1 dB for ZDR . RMSE for Vr is calculated where the Z observations greater than 5.0 dBZ exist.

Ideally, the best analysis will have lower error over both domains, and the lowest tilt domain is included because the observations nearest to the surface are where dual-pol signatures associated with size-sorting are most prominent. Additional qualitative comparisons of the features and where they may differ most from the observations will be considered as well. The goal is to find experiment settings that will lead to an analysis that best represents the values and patterns of the observed Z_{DR} , particularly for the storms of interest for each case, while also not increasing error for Z significantly. This applies to all cases, even when Z_{DR} is not assimilated, since it is

desired that the Z experiments without Z_{DR} best replicate Z_{DR} signatures so that the changes in the analysis when Z_{DR} is assimilated can be properly compared. Simulated Z_{DR} from the enmean analysis is compared to observed Z_{DR} for experiments when Z_{DR} is not assimilated. Although most attention will be paid to Z and Z_{DR} , V_r is included for reference and it is still important that error in V_r is not increased significantly in any test.

Z_{DR} Domain Average RMSEs

	KTLX Z	KTLX ZDR	KTLX Vr		KTLX Z	KTLX ZDR	KTLX Vr
CZ	10.2	1.33	2.35	CZZDR	10.75	1.26	2.58
				OZZDR	10.44	1.25	2.47
MZ	9.9	1.34	2.36	MZZDR	10.61	1.27	2.34
PZ	9.13	1.34	1.82	PZZDR	9.15	1.3	1.98
RCZ	10.6	1.38	2.5	RCZZDR	11.21	1.3	2.6
RFZ	9.46	1.19	2.59	RFZZDR	10.17	1.06	2.61
				RFREZZDR	10.63	1.04	2.71

Lowest Tilt Domain Average RMSEs

	KTLX Z	KTLX ZDR	KTLX Vr		KTLX Z	KTLX ZDR	KTLX Vr
CZ	7.65	1.26	2.4	CZZDR	8.18	1.17	2.48
				OZZDR	8.13	1.16	2.48
MZ	7.32	1.27	2.3	MZZDR	7.93	1.15	1.26
PZ	7.9	1.28	1.86	PZZDR	8.24	1.26	2.01
RCZ	8.33	1.31	2.46	RCZZDR	8.85	1.19	2.5
RFZ	7.26	1.14	2.57	RFZZDR	7.77	0.96	2.61
				RFREZZDR	8.55	0.94	2.69

Table 4.4. Table of calculated average RMSEs over the assessment window period for both the Z_{DR} and lowest tilt domains for the 20 May 2013 case. Blue cells indicate RMSEs lower than the control experiment and orange cells indicate RMSEs higher than the control experiment.

4.4.1 The 20 May 2013 tornadic supercells case

4.4.1.1 Observation assimilation order

The observation assimilation order in the control experiment for Z_{DR} is chosen to isolate Z_{DR} from the other traditional variables assimilated (Z and V_r). In the CZZDR, Z and V_r are first assimilated at every grid point and then Z_{DR} is assimilated separately after. In sensitivity experiment ‘OZZDR’, Z , V_r , and Z_{DR} are assimilated at every grid point in one pass.

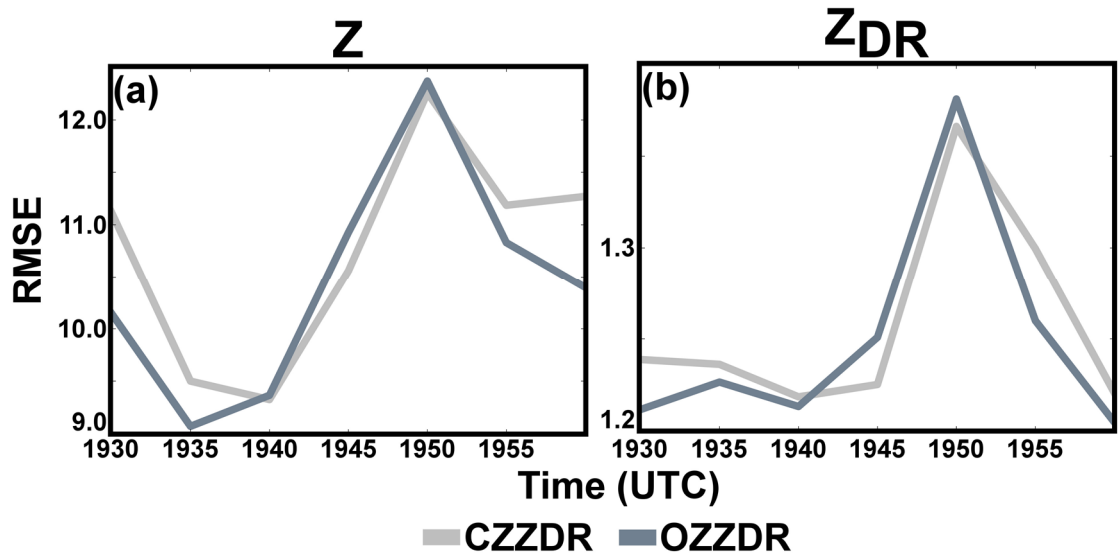


Fig. 4.8. Time plot of analyzed (a) Z (dBZ) and (b) Z_{DR} (dB) RMSE values calculated over the Z_{DR} domain for experiments CZZDR and OZZDR over the assessment window (1930 – 2000 UTC).

The total average RMSE during the assessment period for both experiments is calculated compared to KTLX for the lowest tilt and ZDR domains and listed as part of Table 4.4. The values in OZZDR are slightly worse for analyzed Z . However, the analyzed values of Z_{DR} are basically the same, showing that the analysis when Z_{DR} is assimilated separately and after Z and V_r does not have any significant negative impact. The RMSEs for the Z_{DR} assimilation domain at each analysis over the assessment period

are plotted in Fig. 4.8. There are analyses where one experiment has more error over the other but the average calculation shows that these roughly even out. Plots of analyzed Z and Z_{DR} compared to KTLX observations at the 0.5° tilt are included in Fig. 4.9. The analysis time chosen to present is 1940 UTC since this is when analyzed Z and Z_{DR} from both experiments have RMSEs that are similar and relatively low compared to other times. The domain shown only contains observations that are within the Z_{DR} assimilation domain. Qualitatively, there does not appear to be a significant difference between the results. In fact, analyzed Z_{DR} in OZZDR has an improved pattern in the Z_{DR} arc region of the Moore storm; the decrease in Z_{DR} immediately north of this region is improved compared to the observations. Ultimately, assimilating Z_{DR} after the other variables is desirable, especially if it does not show any significant negative impact, because it keeps the experiments for this case consistent with those in the M10 case, since a separate radar is used for Z_{DR} and those observations are assimilated after Z and V_r as well.

4.4.1.2 Model error treatment methods

Many methods exist to increase the spread between ensemble members, which is used to estimate model error, to prevent filter divergence. Filter divergence occurs when the filter solution begins to diverge from the observations because more weight is erroneously put on the background model state than the new observations. The relaxation to prior spread covariance inflation is used in the control experiment. Preliminary results show areas of weak precipitation in the forward flank of the analyzed storms in this case. Additional model error treatment methods are tried in

order to increase spread and improve the analysis fit to the observations in the low precipitation areas.

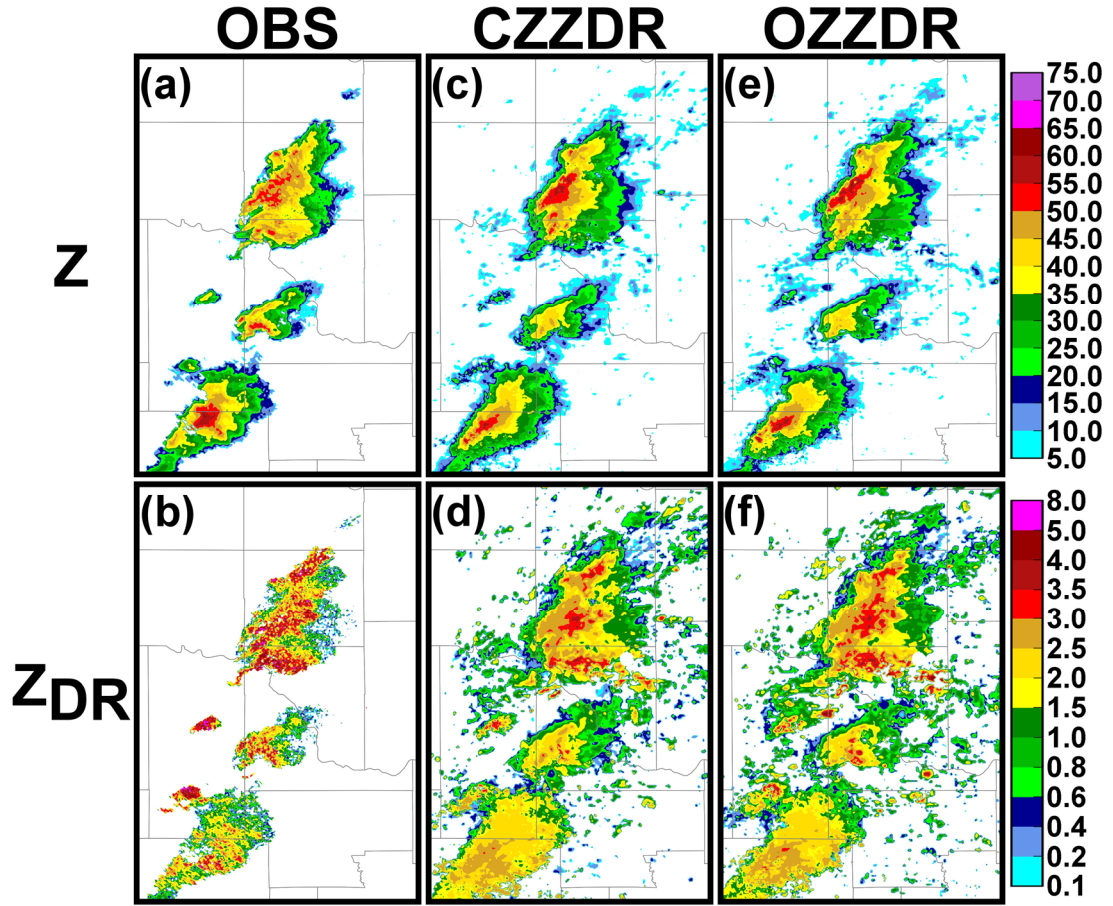


Fig. 4.9. (a) Reflectivity (dBZ) and (b) differential reflectivity (dB) at the 0.5° tilt from KTLX at 1938 UTC as well as from the ensemble mean analyses of experiments (c-d) CZZDR and (e-f) OZZDR at 1940 UTC.

First, sensitivity experiments using multiplicative covariance inflation are conducted (Anderson 2001), one which Z assimilates Z and V_r (experiment ‘MZ’) and one which assimilates Z, V_r and Z_{DR} (experiment ‘MZZDR’). The multiplicative inflation is used in addition to the relaxation to prior spread inflation. The inflation factor is 1.2 and the inflation is only applied where $Z > 20$ dBZ in order to avoid increasing spurious precipitation. Second, sensitivity experiments with additive

perturbation, also referred to as additive noise, are performed; one which assimilates Z and V_r (experiment ‘PZ’) and one that assimilates Z , V_r , and Z_{DR} (experiment ‘PZZDR’). The additive perturbations are used in addition to the relaxation to prior spread inflation (Dowell and Wicker 2009). Perturbations of θ at ± 1.0 K are added in areas where observed $Z > 10.0$ dBZ in order to increase convective circulations and thus increase the ensemble spread in precipitation regions.

The calculated average RMSEs over the assessment period show inconsistent results. Over the Z_{DR} domain, the analyzed Z and V_r are improved in MZ, PZ, MZZDR, and PZZDR compared to the CZ and CZZDR cases. However, simulated Z_{DR} in MZ and PZ as well as analyzed Z_{DR} in MZDR and PZDR all have slightly higher average error values. Some of these values change for the lowest tilt domain. MZ and PZ both have slightly higher error than CZ. Analyzed V_r is improved in all cases.

The individual RMSEs for each analysis for both domains over the assessment window are included in Fig. 4.10. The RMSE for Z in MZ and PZ is lower than for CZ for the Z_{DR} domain at later times in the window. This is similar for the lowest tilt domain but the difference is nowhere near as significant for PZ, and CZ actually outperforms PZ early in the period. The RMSE for Z in CZZDR, MZZDR, and PZZDR has similar values, but with the PZDR results differing more significantly from CZZDR compared to MZZDR. The pattern of RMSE values for Z in CZ generally follows the amount temporal error between the assimilation time and the scan time for the lowest tilts of the KTLX volume that are assimilated at that time. In other words, when the assimilation time is more similar to the time of the lowest KTLX tilts, there is lower error in Z ; The pattern in RMSE for the additional model error treatments methods

seems to show that they perform similar or even worse when the lowest tilt times line up more favorably with the assimilation time and better when there is greater temporal error between the lowest tilt times and assimilation time. This pattern generally follows for Z in CZZDR, with the caveat that the MZZDR results are more similar to CZZDR.

The temporal pattern also follows for the simulated and analyzed Z_{DR} RMSEs for CZ and CZZDR compared to their respective model error treatment method experiments. CZZDR outperforms PCZZDR for the Z_{DR} domain for most times except around 1950 UTC, when there is a greater amount of temporal error between the lowest radar tilts of KTLX and the assimilation time, but outperforms PCZZDR for all times for the lowest tilt domain. The analyzed Z_{DR} in MZZDR is relatively closer to CZZDR than PCZZDR.

Analyzed Z and simulated Z_{DR} from the enmean analysis for the 0.5° tilt for KTLX for CZ, MZ, and PZ at 1940 UTC are plotted in Fig. 4.11 and the results from CZZDR, MZZDR, and PZZDR are plotted in Fig. 4.12. Analyzed Z in MZ and PZ appears to show a slightly better fit compared to CZ in the right forward flank of the Moore storm. Z in CZ is overestimated to some extent in the precipitation core in the storm immediately north of the Moore storm compared to PZ as well. However, the precipitation coverage for each storm is erroneously more expansive in PZ compared to CZ, and this has a negative impact on the simulated Z_{DR} . High values of Z_{DR} extend well downshear in the forward flanks of the storms compared to CZ and the observations. Additionally, the Z_{DR} values in CZ are more similar to the observations compared to MZ and PZ where these values are underestimated, particularly in PZ.

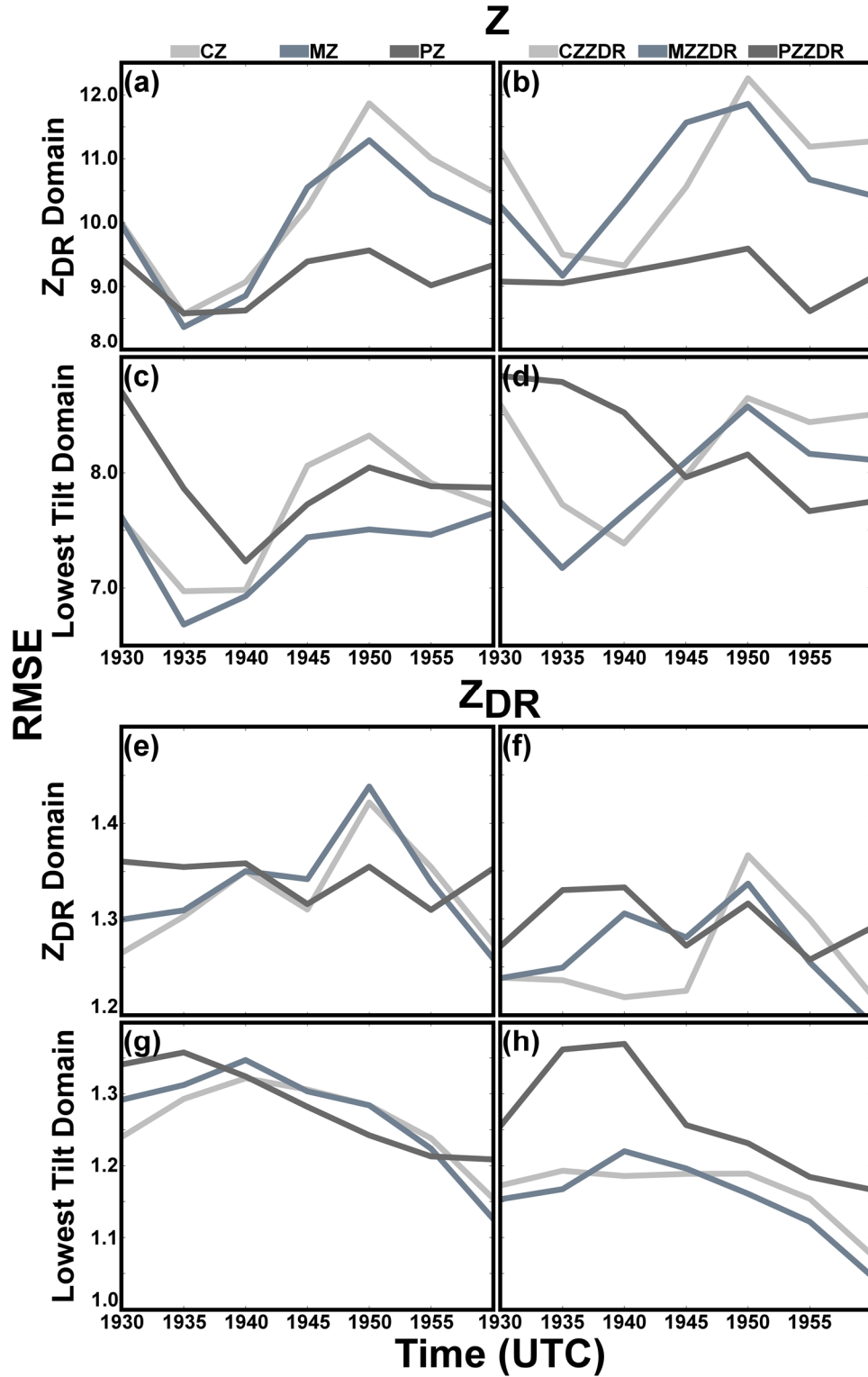


Fig 4.10. Time plot of analyzed Z (dBZ) RMSE values for the (a-b) Z_{DR} domain and (b-c) lowest tilt domain and analyzed Z_{DR} (dB) RMSE values for the (e-f) Z_{DR} domain and (g-h) lowest tilt domain calculated over the assessment window (1930 – 2000 UTC) for the model error treatment experiments.

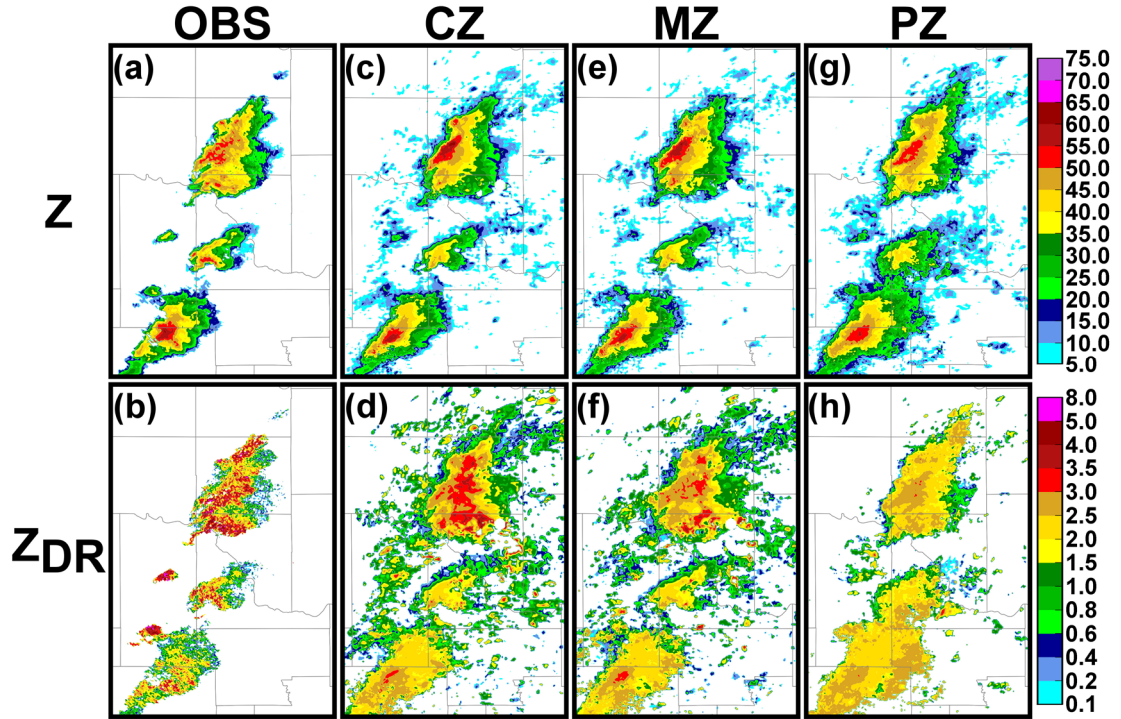


Fig. 4.11. (a) Reflectivity (dBZ) and (b) differential reflectivity (dB) at the 0.5° tilt from KTLX at 1938 UTC as well as from the ensemble mean analyses of experiments (c-d) CZ and (e-f) MZ and (g-h) PZ at 1940 UTC.

The analyzed Z_{DR} in PZZDR is also lower than the observations, which is of particular concern because improvement should be seen since this field is analyzed compared to PZ. The assimilation of Z_{DR} for MZZDR improves the analysis compared to MZ, but it is important to have a control that properly represents observed Z_{DR} patterns in order to gauge the degree of improvement assimilating Z_{DR} provides. The analyzed Z_{DR} for MZZDR in the southeast portion of the Z_{DR} arc of the Moore storm is also very noisy. The goal of the sensitivity experiments is to help improve these areas. Since the RMSE results show inconsistent improvements, particularly for Z_{DR} , the results for this sensitivity experiment are judged to be inconclusive. The treatment methods appear to have a positive impact on the traditionally assimilated variables (Z

and V_r) compared to the Z_{DR} values. However, there is no significant overall improvement quantitatively for Z_{DR} and evaluation of the analyzed fields from a sample analysis shows that the analyzed Z_{DR} patterns are better in CZZDR. In particular, between both RMSE calculations and qualitative evaluation, there is a negative impact on the low level analyzed Z_{DR} fields in PZZDR compared to CZZDR. Further study is needed in this area and perhaps the temporal error can be considered when applying additional treatment methods.

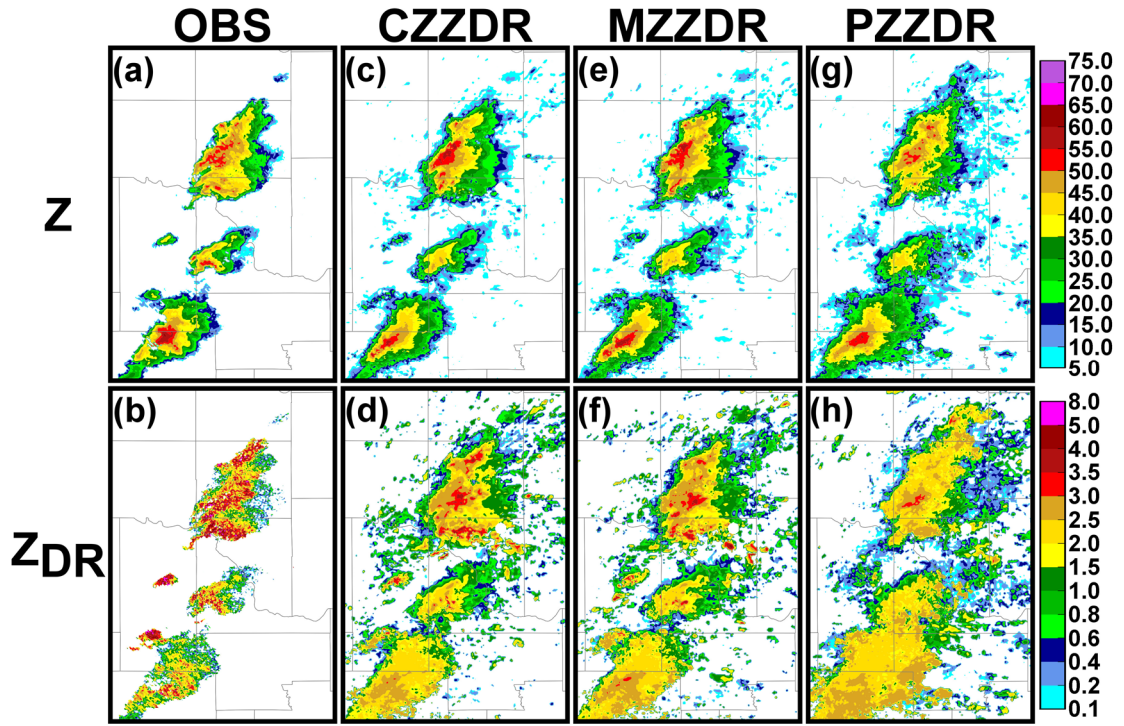


Fig. 4.12. (a) Reflectivity (dBZ) and (b) differential reflectivity (dB) at the 0.5° tilt from KTLX at 1938 UTC as well as from the ensemble mean analyses of experiments (c-d) CZZDR and (e-f) MZZDR and (g-h) PZZDR at 1940 UTC.

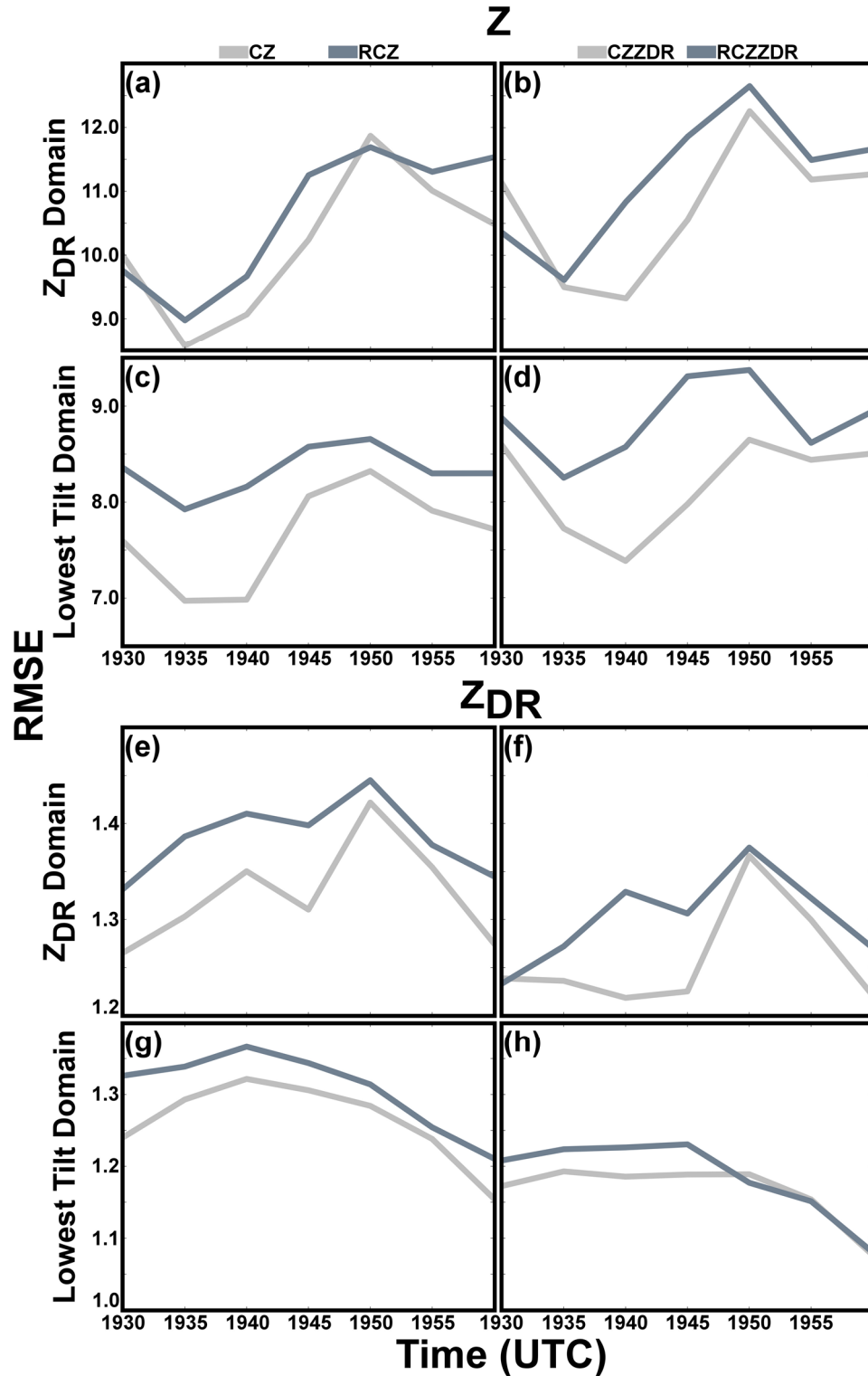


Fig 4.13. Time plot of analyzed Z (dBZ) RMSE values for the (a-b) ZDR domain and (b-c) lowest tilt domain and analyzed ZDR (dB) RMSE values for the (e-f) ZDR domain and (g-h) lowest tilt domain calculated over the assessment window (1930 – 2000 UTC) for the radar configuration experiments.

4.4.1.3 Radar configuration

The configuration chosen for the control experiment includes assimilating multiple observations from multiple radars. Specifically, with the focus on the Moore storm and other storms in the Oklahoma City area, there could be an oversaturation of Z observations assimilated since this region is covered by 3 separate radars included in this experiment. For testing purposes, an experiment was run with a new configuration of radars and observed variables. KVNK is not included since its coverage overlaps the KTLX coverage for the storms of interest and does not cover much of the rest of the domain. The coverage of KFDR overlaps the storms of interest as well, but since it also provides coverage for a significant portion of the domain, V_r is still assimilated. Also, Z_{DR} is only assimilated from KTLX since the Z_{DR} observations from the other radars will not have an effect on the storms of interest with the height limit imposed on Z_{DR} observations. Finally, the grid spacing for clear air Z observations assimilated is lowered from every 4 grid points to every 2 grid points. This is the smallest grid spacing that can be used without causing instability in the model based on previous tests done for this case. Experiments are performed assimilating Z and V_r (radar configuration experiment ‘RCZ’) and assimilating Z , V_r , and Z_{DR} (radar configuration experiment ‘RCZZDR’).

The average RMSE calculations for both domains for all variables do not show improvement for either RCZ or RCZZDR, compared to CZ and CZZDR, with this new configuration (Table 4.4). The individual RMSE calculations over the assessment window show more rapid error growth in RCZ and RCCZDR in terms of analyzed Z , especially for the lower tilt domain (Fig. 4.13). As discussed in the previous section on

model error treatments methods, the scan times of the lower KTLX tilts assimilated have less temporal error during the early part of the assessment window and increase during the middle part. When there is greater temporal error between the KTLX observations and the assimilation times, there is a more significant impact on the results that only assimilate Z from KTLX for this area. Having the extra observations from the other radars appears to have a positive impact during this time period for the control experiments.

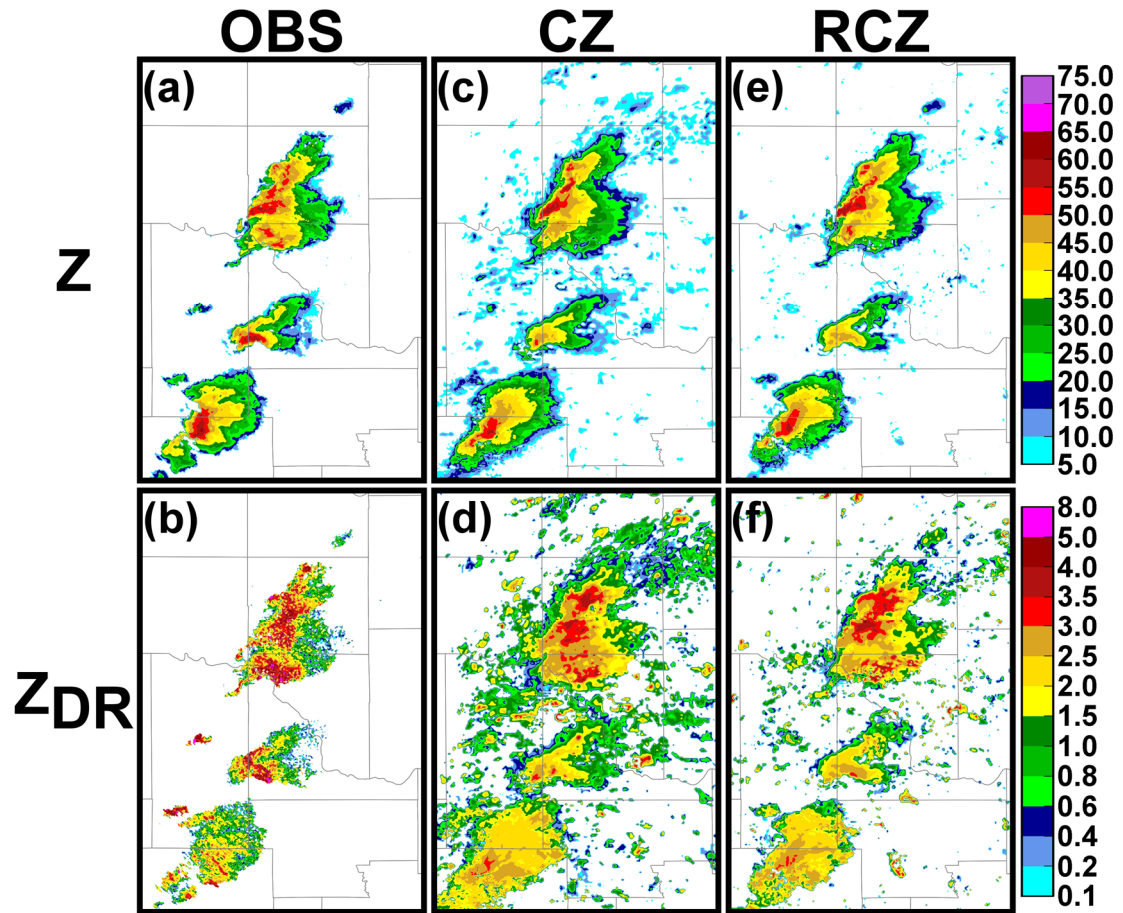


Fig. 4.14. (a) Reflectivity (dBZ) and differential reflectivity (dB) at the 0.5° tilt from KTLX at 1934 UTC as well as from the ensemble mean analyses of experiments (c-d) CZ and (e-f) RCZ at 1935 UTC.

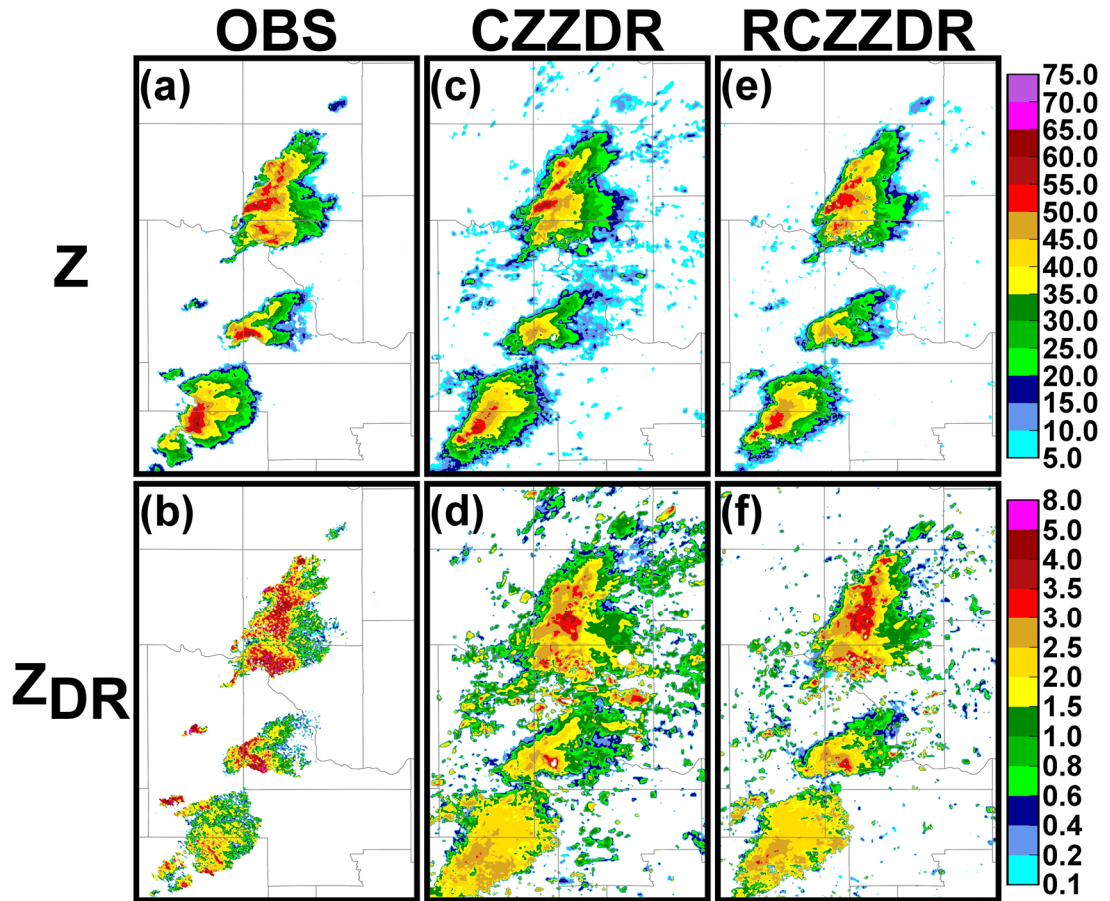


Fig. 4.15. (a) Reflectivity (dBZ) and (b) differential reflectivity (dB) at the 0.5° tilt from KTLX at 1934 UTC as well as from the ensemble mean analyses of experiments (c-d) CZZDR and (e-f) RCZZDR at 1935 UTC.

Figs. 4.14 and 4.15 contain plots of observed Z and Z_{DR} from KTLX at the same 0.5° tilt at 1935 UTC as well as the analyzed and simulated values of both variables for the pair of control and radar configuration experiments. The reduced grid spacing for the assimilation of clear air Z has a noticeable impact, reducing the amount of spurious precipitation. The analyzed values are relatively similar, though the new configuration experiments also show some improved areas, such as higher Z values in RCZ in portions of the forward flank of the Moore storm compared to CZ. The analyzed Z_{DR} in RCZZDR also appears consistently higher and a closer match to the observations in the

forward flanks for the Moore storm and the storm to its north. There are some areas where there is not improvement, such as overestimated simulated Z_{DR} in the forward flank of the Moore storm for RCZ. Overall, the new configuration shows promise for improving some aspects of the analysis. However, the RMSE calculations do not show that RCZ and RCCZDR experiment improved upon CZ and CZDR.

4.4.1.4 Radar observation filtering

Z_{DR} observations can be noisy, which can lead to instability in the analysis, and may also contain information on a scale smaller than the grid spacing used in the analysis. A 5-point median filter was used in the data for the control experiment but the observations are still rather noisy. An additional radar observation filtering pass is used in sensitivity experiments radar filter with Z , (RFZ, assimilates Z and V_r) and RFZZDR (assimilates Z and V_r plus Z_{DR}). The original 5-point filter was applied to the observations before being interpolated to the model grid. For the additional filtering pass, a 9-point median filter is used on the Z and Z_{DR} observations after they have been interpolated to the grid. In this way, they should be smoothed to the grid at a scale similar to the model analyses. Since the Z_{DR} observations have been smoothed and there is less noise, one additional experiment that assimilates Z_{DR} with a reduced observation error is included (radar filtering with reduced error experiment ‘RFREZZDR’). The error is lowered by half from 0.6 dB to 0.3 dB.

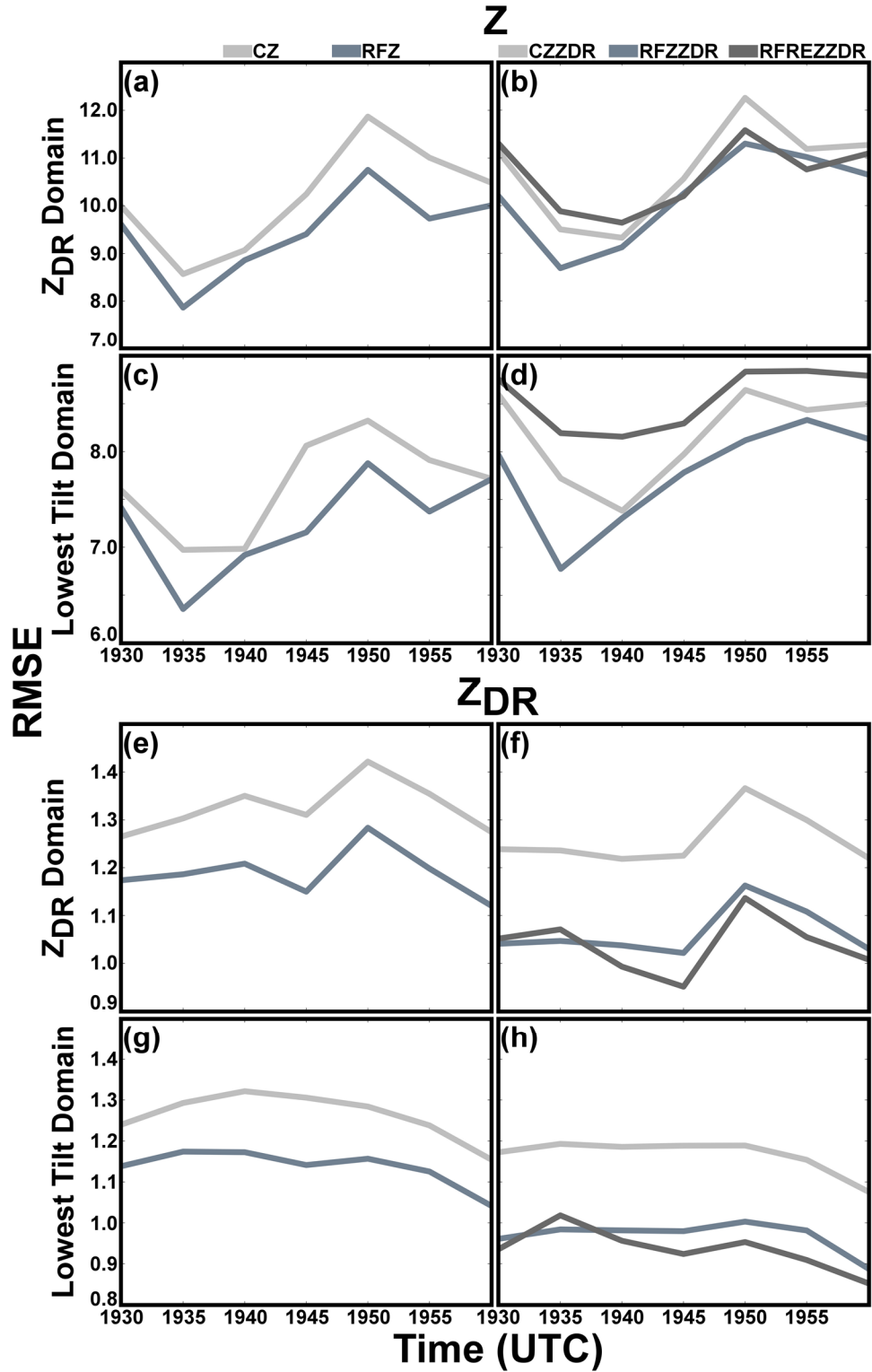


Fig 4.16. Time plot of analyzed Z (dBZ) RMSE values for the (a-b) Z_{DR} domain and (b-c) lowest tilt domain and analyzed Z_{DR} (dB) RMSE values for the (e-f) Z_{DR} domain and (g-h) lowest tilt domain calculated over the assessment window (1930 – 2000 UTC) for the radar filtering experiments.

The RFZ and RFZZDR have improved average RMSE values compared to the control experiments for all values of Z and Z_{DR} in both domains. Interestingly, RMSE values for V_r are slightly worse in each case. For experiment RFREZZDR, the average RMSE for analyzed Z_{DR} is lower than both CZZDR and RFZZDR. However, the error for analyzed Z is higher than both RFZZDR for both domains and higher than CZZDR for the lowest tilt domain. Basically, the use of filtered radar observations improved both Z and Z_{DR} in RFZZDR, while the lower Z_{DR} error in RFREZZDR improved Z_{DR} but negatively impacted Z . It is desirable to improve analyzed Z_{DR} when Z_{DR} is assimilated, but not at the expense of increasing the error in Z .

Plots of individual RMSE values for each analysis time during the assimilation window shows the use of additional radar filtering in RFZ and RFZZDR consistently provides improvement in all cases (Fig. 4.16). Unlike the model error treatment methods tested, the radar filtering does not negatively impact the simulated Z_{DR} for RFZ compared to CZ and instead provides improved results. This is desirable when evaluating the benefits assimilating Z_{DR} may provide an analysis when those results are compared. The plots also show how the improvement seen in RFZZDR and RFREZZDR is relatively similar compared to CZDR. There is still significant improvement when higher Z_{DR} observation error is used without negatively impacting analyzed Z .

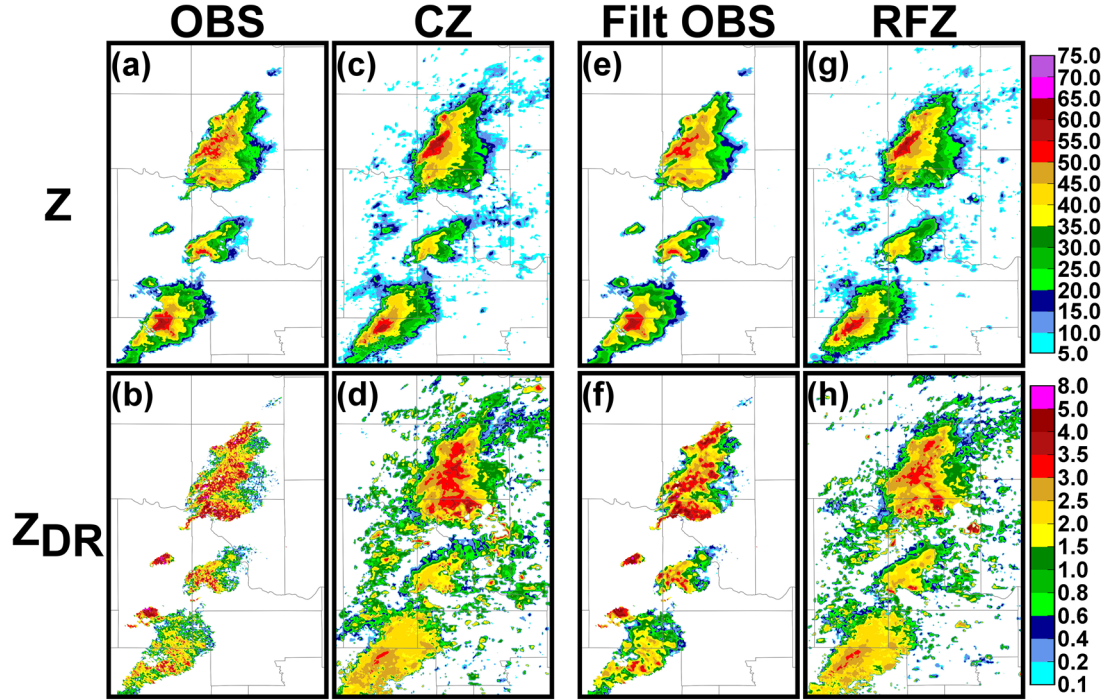


Fig. 4.17. (a) Reflectivity (dBZ) and (b) differential reflectivity (dB) at the 0.5° tilt from KTLX at 1938 UTC and from the ensemble mean analysis of (c-d) CZ at 1940 UTC as well as the filtered (e) reflectivity and (f) differential reflectivity from KTLX and the ensemble mean analysis of (g-h) RFZ.

The improvement in the radar filtering results compared to the control experiment can also be seen qualitatively. Results for all experiments are plotted at 1940 UTC, which is an analysis time when the results are similar and the errors are relatively low, in Figs. 4.17 and 4.18. The observations for both Z and Z_{DR} before and after the additional filtering are included for comparison. Analyzed Z in RFZ shows an improved fit with increased values in the forward flank of the Moore storm compared to CZ. An area of particular importance to represent is the Z_{DR} arc in the Moore storm. In CZZDR, analyzed Z_{DR} for this area is not consistent and is also very noisy, reflecting the difficulty of analyzing a noisy field like Z_{DR} on the model grid. RFZZDR shows some significant improvement in the Z_{DR} pattern in this area which is important for

eventual evaluation compared to the control experiment. The increased error in analyzed Z for the REREZZDR experiment can be seen in the Moore storm and the storm to its north, where Z values are lower compared to both RFZZDR and CZDR. Additionally, there the high Z_{DR} in the forward flank of the Moore storm is very noisy and less consistent compared to RFZZDR. RFREZZDR does not provide an improved analysis in this important area while RFZZDR does.

Overall, the results using the additional radar observation filtering are encouraging, specifically for dual-pol variables. One potential drawback is that some of the details in the observations are lost as more filtering is applied to the observations. However, this additional filtering results in similar patterns in the observed variables compared to the simulated variables so it appears that the scale of observed features which can be analyzed on the grid used has not been negatively affected by the additional filtering. Future studies that use different scales will need to continue to investigate filtering methods.

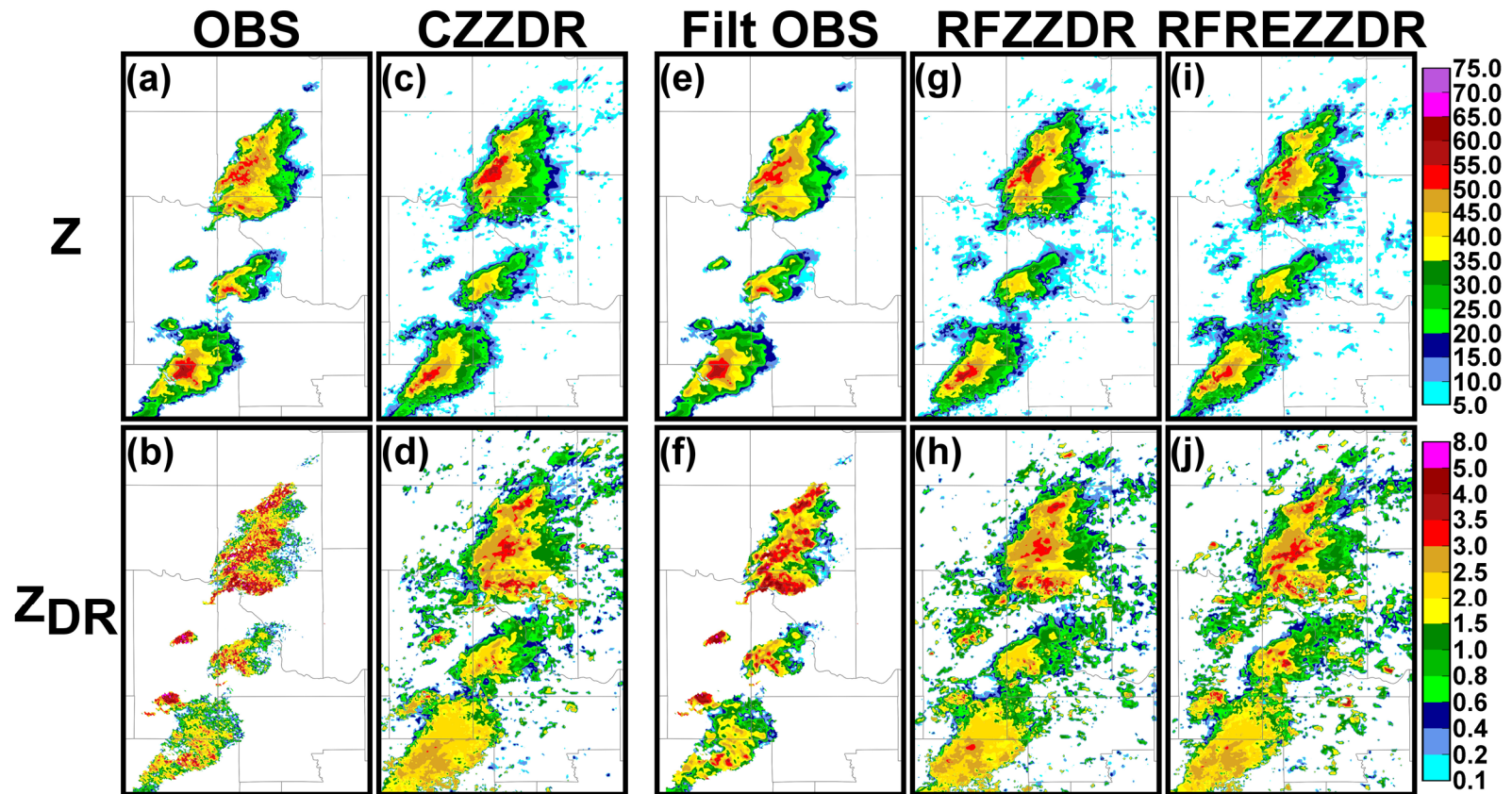


Fig. 4.18. (a) Reflectivity (dBZ) and (b) differential reflectivity (dB) at the 0.5° tilt from KTLX at 1938 UTC and from the ensemble mean analysis of (c-d) CZZDR at 1940 UTC as well as the filtered (e) reflectivity and (f) differential reflectivity from KTLX and the ensemble mean analyses of (g-h) RFZZDR and (i-j) RFREZZDR.

Z_{DR} Domain Average RMSEs

	KTLX Z	KOUN ZDR	KTLX Vr		KTLX Z	KOUN ZDR	KTLX Vr
CZ	8.48	1.37	2.25	CZZDR	9.92	1.28	2.27
PZ	9.81	1.34	2.13	PZZDR	9.56	1.27	2.16
RFZ	7.18	1.27	2.58	RFZZDR	8.81	1.15	2.59
				RFREZZDR	10.37	1.14	2.62

Lowest Tilt Domain Average RMSEs

	KTLX Z	KOUN ZDR	KTLX Vr		KTLX Z	KOUN ZDR	KTLX Vr
CZ	7.4	1.19	2.01	CZZDR	8.8	1.07	2.02
PZ	9.6	1.27	1.78	PZZDR	9.39	1.17	1.81
RFZ	6.51	1.12	2.63	RFZZDR	8.2	0.99	2.6
				RFREZZDR	9.53	0.96	2.6

Table 4.5 Table of calculated average RMSEs over the assessment window period for both the Z_{DR} and lowest tilt domains for the 10 May 2013 case. Blue cells indicate RMSEs lower than the control experiment and orange cells indicate RMSEs higher than the control experiment.

4.4.2 The 10 May 2010 tornadic supercells case

Similar to the M20 case, some initial sensitivity experiments are performed to improve on the initial control experiment. The experiments follow those for the M20 case with a couple of exceptions. First, Z_{DR} is already assimilated separately from Z and V_r because the observations come from a separate radar (KOUN) assimilated after the Z and V_r observations from KTLX, so no experiment that alters the assimilation order of the observations is included. Second, multiplicative inflation is already included in the control experiment so only an additive noise test is conducted for the model error treatment test section. Finally, this experiment only uses KTLX, as well as KOUN for Z_{DR} , and therefore there is little to change about the radar configuration in a similar way to the radar configuration experiments developed for M20. The average RMSE calculations across the assessment window are repeated for this case. It should be noted

that the RMSE for Z and V_r are calculated against the observations KTLX and the RMSE for Z_{DR} is calculated against the observations KOUN to remain consistent with the assimilation experiments.

4.4.2.1 Model error treatment methods

Additive perturbations are used in addition to the relaxation to prior spread and multiplicative covariance assimilation methods in experiments that assimilate Z and V_r (experiment ‘PZ’) and that assimilating Z , V_r , and Z_{DR} (experiment ‘PZZDR’). Similar to the M20 case, perturbations of θ at ± 1.0 K are added in areas where observed $Z > 10.0$ dBZ. The average RMSEs over the assessment window for both the Z_{DR} domain and low tilt domain are higher in the two perturbation experiment PZ compared to the control experiments except for simulated Z_{DR} from PZ for the Z_{DR} domain which is only .03 dB different than CZ (Table 4.5). In contrast to the M20 case, where additive perturbations showed some improvement for the traditionally assimilated variable, Z , particularly for the Z_{DR} assimilation domain, in this case do not show improvement for PZ. Interestingly, the average RMSE of analyzed Z in PZZDR for the Z_{DR} domain is lower. This appears to be related to the temporal error between the low tilts in the KTLX volume and the assimilation time that was noted for the M20 case. The perturbations help for this experiment when there is higher temporal error. However, the RMSEs for each individual assimilation time also show that PZ and PZZDR have consistently higher error compared to the control experiments for the low tilt experiment domain, an area of particular focus for this experiment (Fig. 4.19).

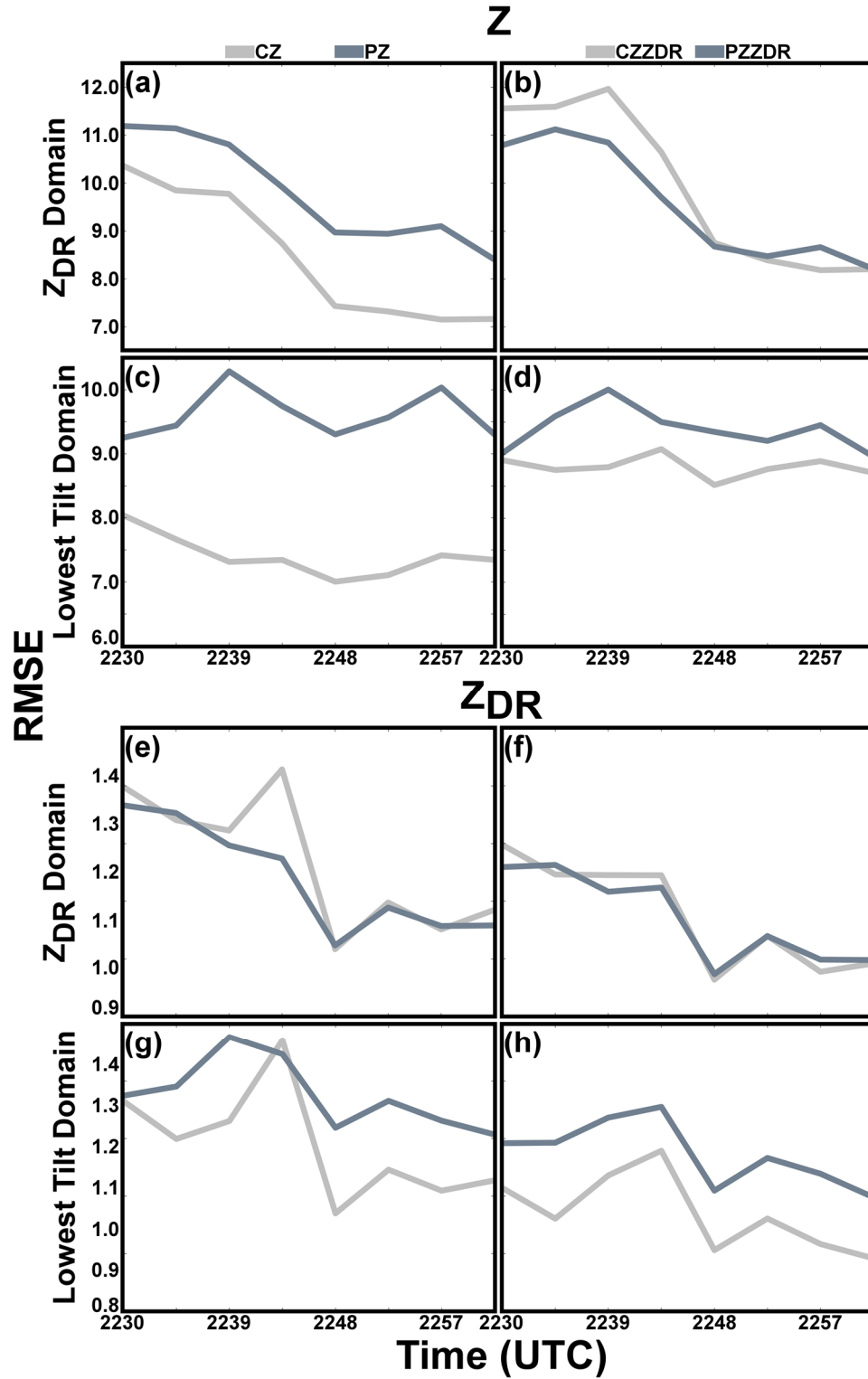


Fig 4.19. Time plot of analyzed Z (dBZ) RMSE values for the (a-b) Z_{DR} domain and (b-c) lowest tilt domain and analyzed Z_{DR} (dB) RMSE values for the (e-f) Z_{DR} domain and (g-h) lowest tilt domain calculated over the assessment window (2230 – 2301 UTC) for the model error treatment experiments.

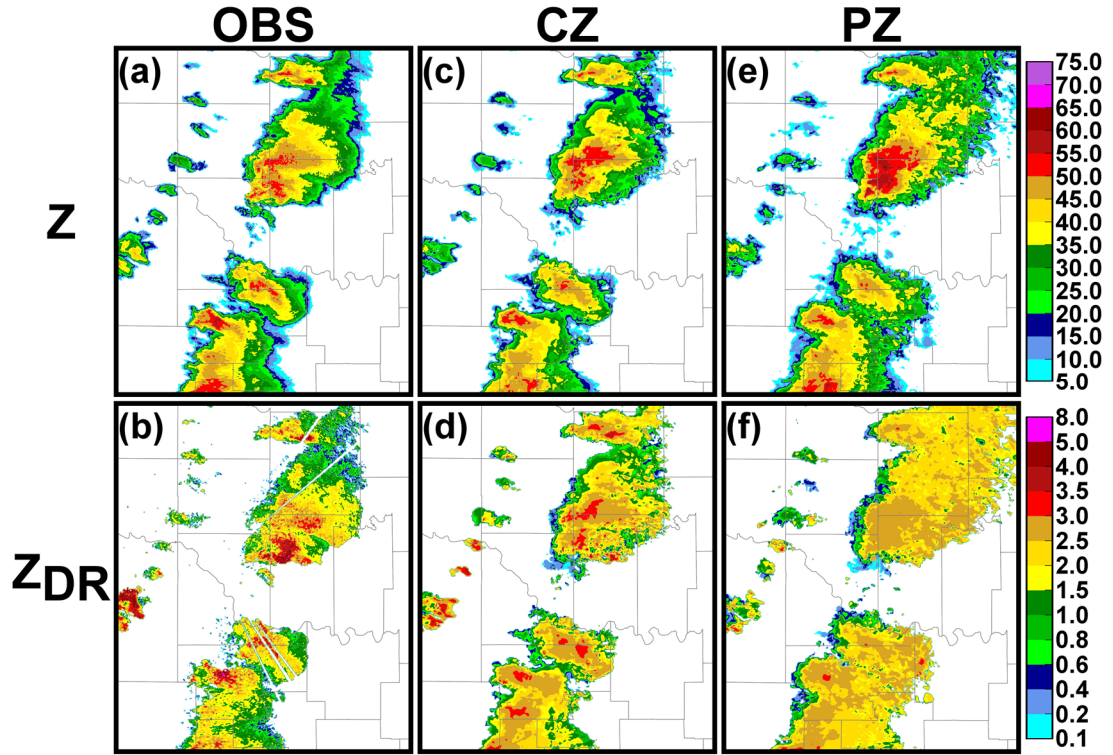


Fig. 4.20. (a) Reflectivity (dBZ) at the 0.5° tilt from KTLX at 2246 UTC and (b) differential reflectivity (dB) from KOUN at 2246 UTC as well as from the ensemble mean analyses of experiments (c-d) CZ and (e-f) PZ at 2248 UTC.

Individual plots of the variables at the lowest, 0.5° tilt are included in Figs. 4.20 and 4.21 for 2248 UTC, chosen because it is an optimal time in which the individual RMSE values for each experiment are similar and also relatively low in error compared to the rest of the assessment window. As for the error calculations, the plots of Z are from KTLX and the plots of Z_{DR} are from KOUN. Analyzed Z in PZ is significantly higher in the core of the Norman and Moore storms (Fig. 4.20). Additionally, the far northeastern portion of the forward flank of the Moore storm is significantly over-forecast. The simulated Z_{DR} values show little deviation compared to the Z ; the Z values remain relatively consistent throughout each storm in PZ, particularly for the forward flank portion furthest downshear from the updraft of each storm, while there is a much

more significant amount of variation in CZ. The individual RMSEs in Fig. 4.19 are noted to be worse for analyzed Z in CZZDR for this experiment and the values and patterns in Fig. 4.21 reflect that. The high Z values associated with the heaviest precipitation cores in the Moore and Norman storm are similarly overestimated compared to PZZDR; CZ improved on PZ in this area. However, the similar lack of significant variation noted in simulated Z_{DR} for PZ is also seen in the analyzed Z_{DR} for PZZDR. This is of particular concern because this experiment assimilates Z_{DR} ; the Z_{DR} value should show variation across the storms as in the observations (Fig. 4.21). Overall, the additive perturbations do not appear to have a net positive affect for these experiments.

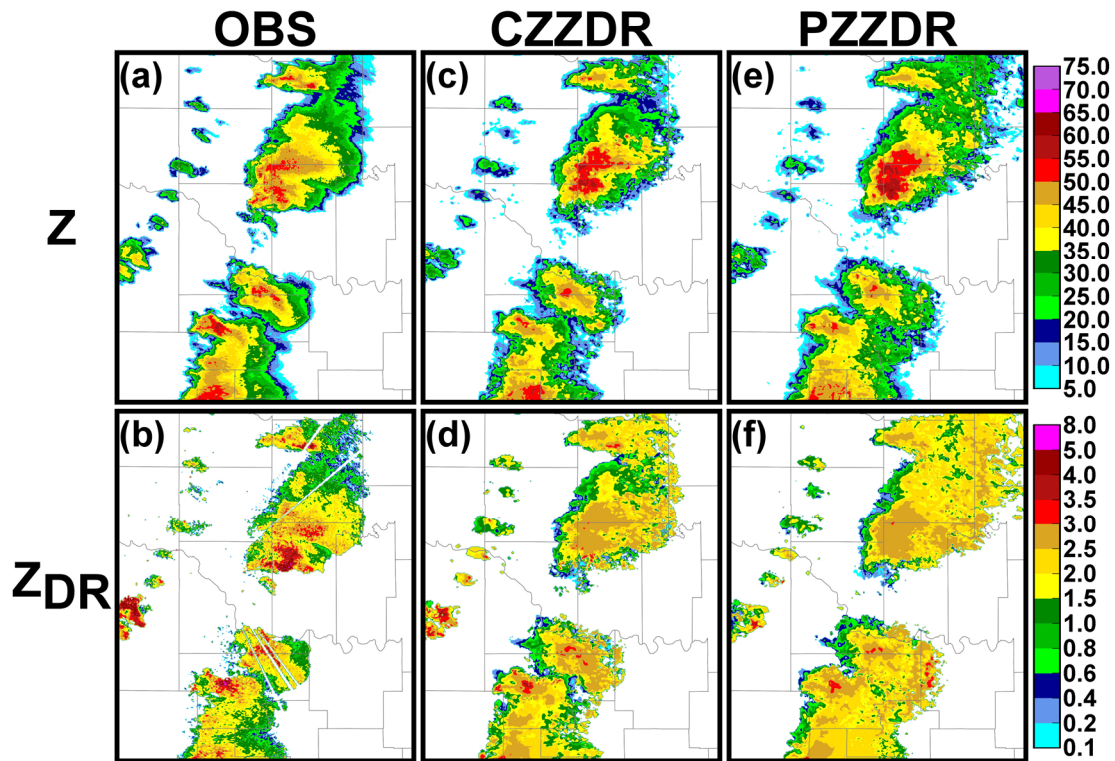


Fig. 4.21. (a) Reflectivity (dBZ) at the 0.5° tilt from KTLX at 2246 UTC and (b) differential reflectivity (dB) from KOUN at 2246 UTC as well as from the ensemble mean analyses of experiments (c-d) CZZDR and (e-f) PZZDR at 2248 UTC.

4.4.2.2 Radar observation filtering

The same additional 9-point median filter applied to the Z and Z_{DR} observations after they are interpolated to the model grid are used in similar experiments for this case. Experiment RFZ assimilates Z and V_r while experiment RFZZDR assimilates Z , V_r , and Z_{DR} . An additional experiment is also conducted that assimilates Z_{DR} with a reduced observation error of 0.3 dB. The domain average RMSEs for Z and Z_{DR} both RFZ and RFZZDR are lower compared to the control experiments. The individual RMSEs calculated for RFZ and RFZZDR at each assimilation time are also consistently lower, or at least very similar, to the results from the control experiments (Fig. 4.22). As in the M20 case, experiment RFREZZDR with the reduced observation error for Z_{DR} shows a similar improvement compared to CZZDR for analyzed Z_{DR} as RFZZDR but has increased the RMSE values for analyzed Z .

The two versions of observations before and after the additional filtering as well as the model results are plotted in Figs. 4.23 and 4.24. The newly filtered observations appear to improve the analysis of patterns seen in the variables for RFZ and RFZDR. For example, the downshear extent of the high Z values associated with heavy precipitation in the forward flank of the Norman storm is improved (Fig. 4.23). This improvement is even greater in Z_{DR} for RFZ and RFZDR. The Z_{DR} values are higher further downshear in the forward flank for the Norman storm in both cases which is more similar to the observations. This is obviously important when Z_{DR} is assimilated but also important for the Z experiments because, as previously mentioned, any improvements seen when Z_{DR} is assimilated will be more robust if the experiments that only assimilate Z are consistent with the observations.

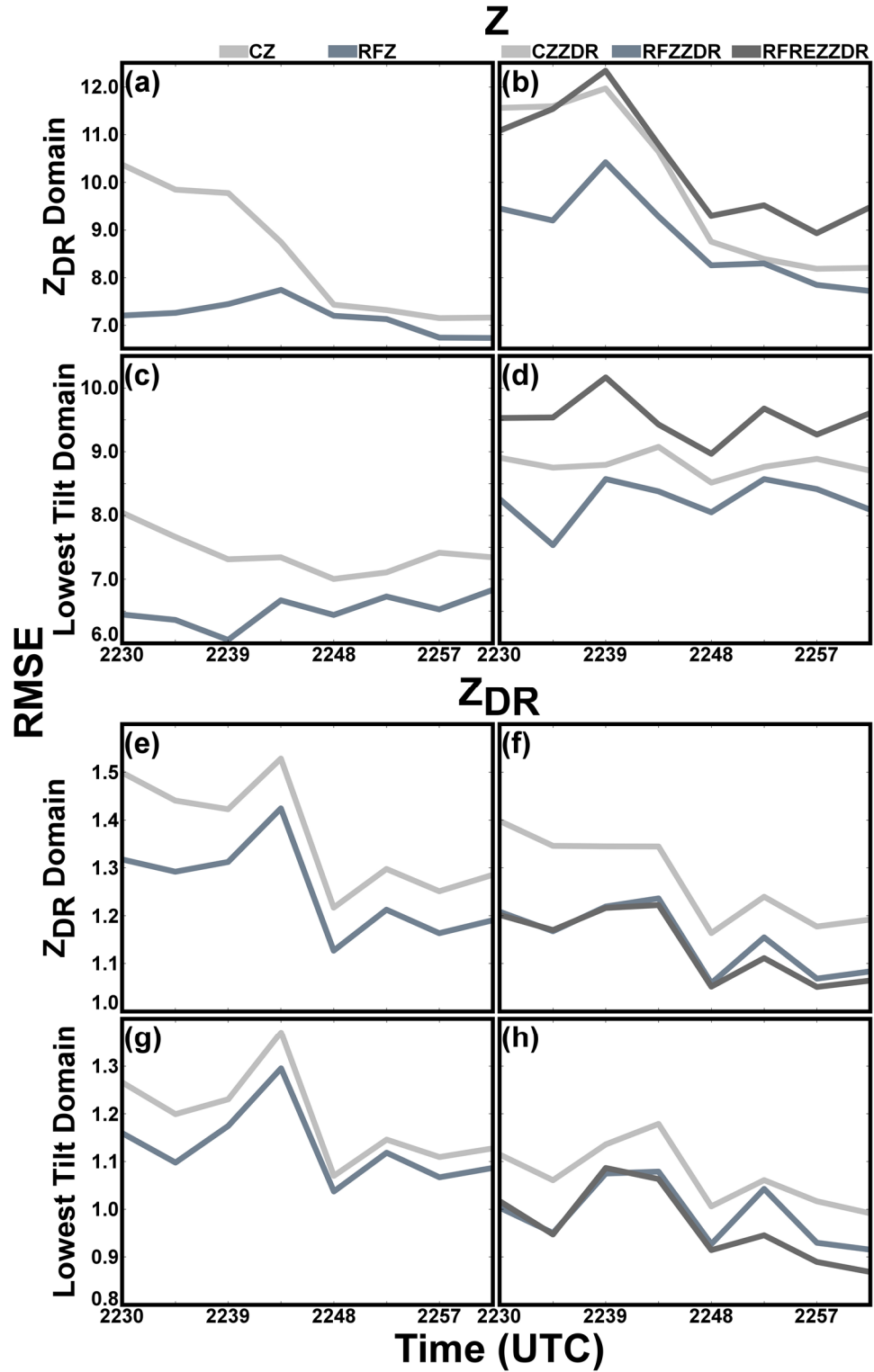


Fig 4.22. Time plot of analyzed Z (dBZ) RMSE values for the (a-b) Z_{DR} domain and (b-c) lowest tilt domain and analyzed Z_{DR} (dB) RMSE values for the (e-f) Z_{DR} domain and (g-h) lowest tilt domain calculated over the assessment window (2230 – 2301 UTC) for the radar filtering experiments.

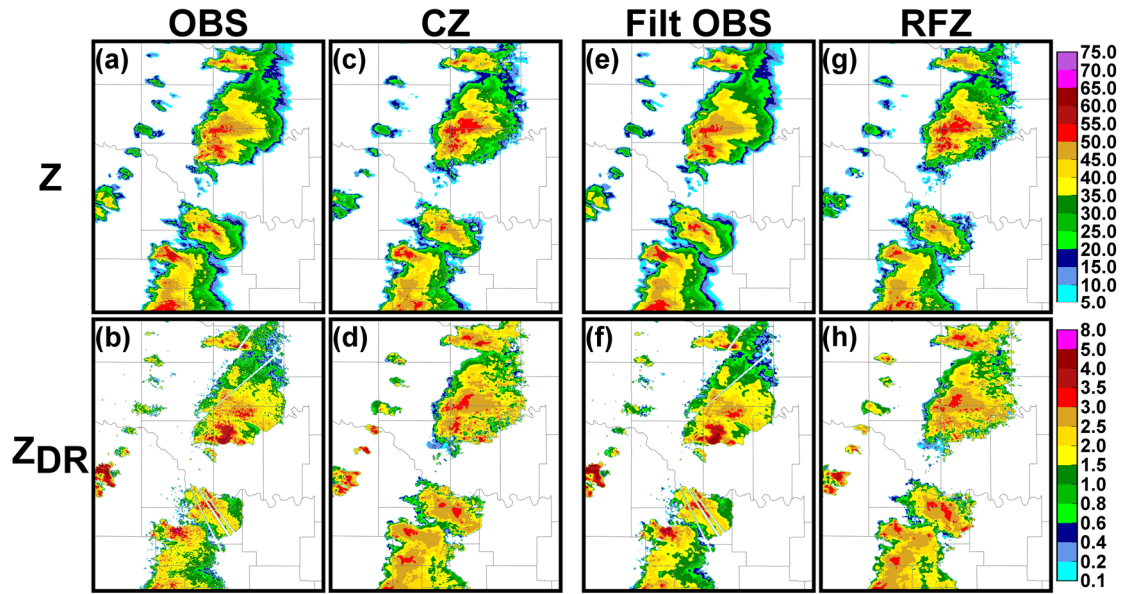


Fig. 4.23 (a) Reflectivity (dBZ) at the 0.5° tilt from KTLX at 2246 UTC and (b) differential reflectivity (dB) from KOUN at 2246 UTC and from the ensemble mean analysis of (c-d) CZ at 2248 UTC as well as the filtered (e) reflectivity and (f) differential reflectivity from KTLX and KOUN and the ensemble mean analyses of (g-h) RFZ.

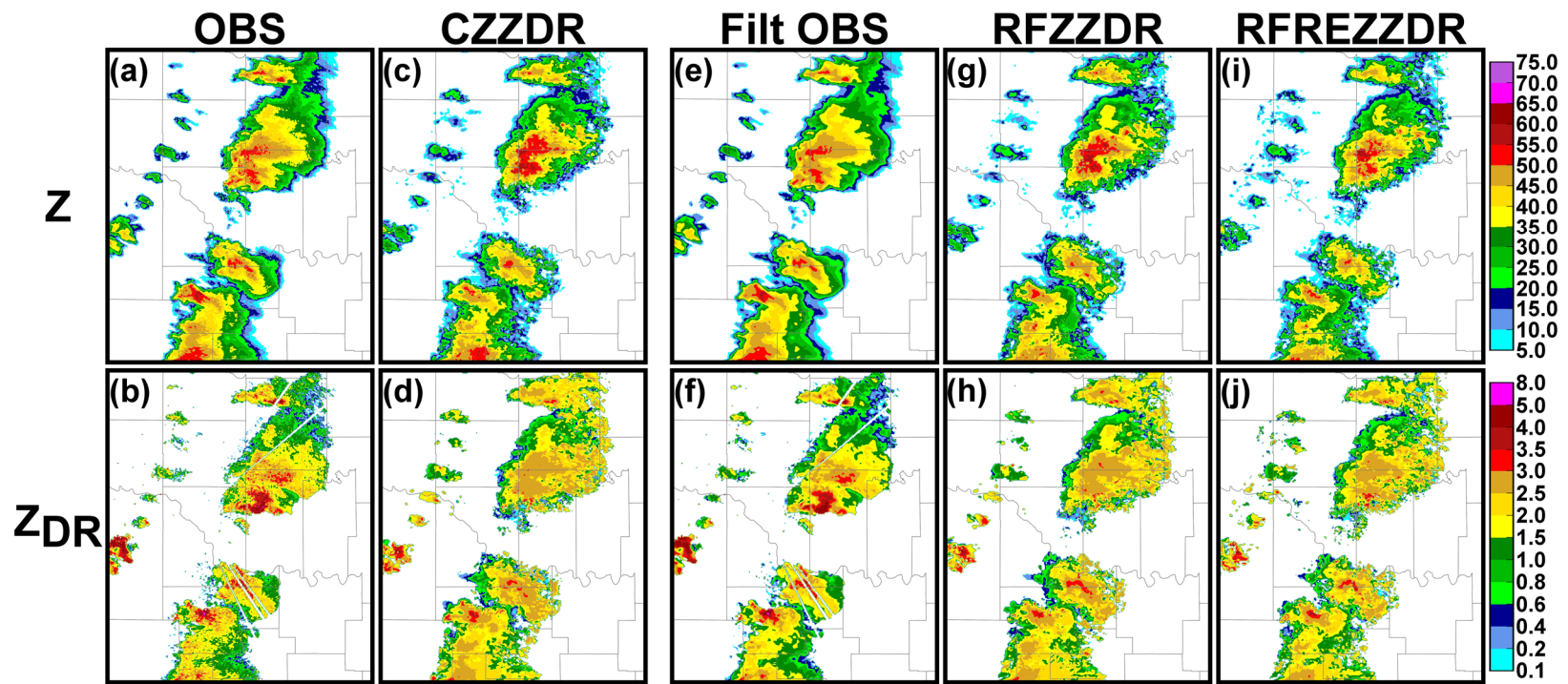


Fig. 4.24 (a) Reflectivity (dBZ) at the 0.5° tilt from KTLX at 2246 UTC and (b) differential reflectivity (dB) from KOUN at 2246 UTC and from the ensemble mean analysis of (c-d) CZZDR at 2248 UTC as well as the filtered (e) reflectivity and (f) differential reflectivity from KTLX and KOUN and the ensemble mean analyses of (g-h) RFZ and (i-j) RFREZZDR.

4.5 Conclusions

Sensitivity tests are run for control experiments CZ, which assimilates Z and V_r , and CZZDR, which assimilates Z , V_r , and Z_{DR} , for both the May 20 (M20) and May 10 (M10) cases. The tests included using a different assimilation order for Z_{DR} (M20 case), using additional model error treatment methods (M20 and M10 case), altering the configuration of which radars and which observations are assimilated (M20 case), and assimilating observations with additional filtering methods (M20 and M10 case). The focus of the experiments is to improve the analysis of Z and Z_{DR} in the lower model levels where the new dual-pol assimilation experiments will assimilate Z_{DR} observations and be evaluated. The results are compared by calculating the average RMSE for all observations during an assessment window, the last 30 minutes of the assimilation period, for both the domain over which Z_{DR} is assimilated as well as the lowest radar tilt. Individual RMSE values and the analyzed variables plotted at the lowest radar tilt are also considered.

The model error treatment methods experiments show some improvement compared to the control but, in general, they are inconclusive. For example, analyzed Z is improved in MZ and PZ compared to CZ. However, Z_{DR} values are erroneously lower in the model error treatment experiments compared to the control experiments in areas of heavy precipitation and erroneously high in areas far downshear in the forward flank, particularly for PZ and PZZDR. The new radar configuration experiments, exclusive to the M20 case, have higher average RMSE values overall and have consistently higher RMSE values for each assimilation time. RC and RCZZDR have less spurious precipitation compared to their control counterparts, but when evaluated against

observations they did not show improvement. On the other hand, the radar filtering experiments show consistent improvement in the RMSE values as well as notable qualitative improvements in the patterns of the analyzed variables. Specifically, the values are more consistent and higher in value than the control experiments where such patterns exist in the observations.

The impact of different treatment methods on the two cases differs. For the radar filtering experiments, the results improve upon the control experiment for both cases. However, for the model error treatment methods, the addition of the additive perturbations shows some improvement in some of the analyzed variables in PZ for the M20 case but generally shows no improvement in the M10 case.

An interesting finding from the model error treatment and radar configuration experiments is how they appear to provide different results depending on the temporal error between the radar observations and the assimilation time. The model error treatment methods improve upon the control analyses when there is greater temporal error between the scan times for the lowest observed tilts in the KTLX radar volume and the time at which those observations are assimilated. On the other hand, in the radar configuration experiment, the RMSE increases when there is more temporal error, indicating the additional observations that are assimilated from other radars in the control experiment help better analyze the storm when the lower observed tilts from nearby KTLX are delayed compared to the assimilation time.

A lower observation error for Z_{DR} is used for one radar filtering experiment, but this results in noisier analyzed Z_{DR} and increased the error in analyzed Z . The analyzed Z_{DR} in experiment RFZZDR with the original Z_{DR} error still has a similar fit to the

observations as when the reduced error was used while also fitting observed Z better. The model error treatment methods, specifically for the M20 case, have a positive impact on some values for the traditionally assimilated radar variables, Z and V_r , but have an overall negative impact on Z_{DR} in the analysis whether it is assimilated or not.

The results that are chosen for further analysis to evaluate the impact of assimilating the dual-pol variables in part 2 (chapter 5) are those which used the additional radar filtering, RFZ and RFZZDR for both cases. The results of those experiments show consistent improvement for the various evaluation methods for both the Z and Z_{DR} experiments. It is also clear, however, that further study of configurations for the assimilation of dual-pol variables is needed.

Chapter 5 Assimilation of Polarimetric Radar Data using EnKF: Evaluation of Analyses

5.1 Introduction

In this chapter, a more in depth investigation of the results for experiments RFZ and RFZZDR from Chapter 4 are presented for both cases, which were judged to produce the best results during sensitivity testing. For convenience, the ‘RF’ will be dropped from the experiment name, leaving experiments ‘Z’ and ‘ZZDR’. Since there are two cases, the dates are added to the experiment names to differentiate them; the 20 May 2013 case experiments are ‘M20Z’ and ‘M20ZZDR’ and the 20 May 2010 case experiments are ‘M10Z’ and ‘M10ZZDR’. The experiment setup for each case included a 30 minute assessment window at the end of the assimilation period where results would be compared to observations. These windows roughly coincided with the storms of interest in each case maturing as well as moving within close vicinity to KTLX (M20) and KOUN (M10), so that assessment could take place with observations as close to the surface as possible. The noted storms of interest are the Moore storm for the M20 case and the Moore and Norman storms for the M10 case. There are also other nearby storms closely associated with these that will be addressed too.

Detailed focus will be placed on one analysis from each case. This analysis is chosen based on the RMSE calculations for the lowest tilt from the previous section for both ensemble mean analysis (enmean) Z and Z_{DR} . For the first case considered, M20, the RMSE for enmean Z is relatively low at 1940 UTC for both the M20Z and M20ZZDR experiments while the error for analyzed enmean Z_{DR} is relatively consistent throughout the assessment period. Qualitative comparisons of the analyses with the

lowest RMSE error were considered in choosing 1940 UTC. The evaluation will first compare the dual-pol variables from each result to the observations. Then, different measurements of the PSD through drop size and parameter values will be considered to assess what impacts the additional assimilation of Z_{DR} have on the estimate of the model microphysical state.

5.2 The 20 May 2013 tornadic supercells case

5.2.1 Evaluation of analyzed dual-pol variables

The enmean analyzed Z and simulated Z_{DR} from M20Z and analyzed Z and analyzed Z_{DR} from M20ZZDR for 1940 UTC are compared to KTLX observations at the 0.5° tilt (Fig. 5.1). The subdomain is focused on the Moore storm of interest and the storm immediately to its north, which will be referred to as the OKC storm for convenience. The storm identities are noted in Fig. 5.1. The analyzed Z from both experiments is relatively similar. The Z values in both analyses are more similar to the observations in the OKC storm. The analyzed Z in the southeastern portion of the forward flank is underestimated in both cases. Sensitivity experiments conducted in Chapter 4 were not able to improve the analysis of these regions in any significant manner. Based on the Z pattern in both cases for both storms, it appears that precipitation is advected further downshear in the forward flank, with respect to the environmental wind shear (roughly oriented west-southwest to east-northeast), and underestimated in the region adjacent to the updraft relative to the storm motion (southeast portion of the forward flank), particularly for the Moore storm, which was moving nearly due east at this time.

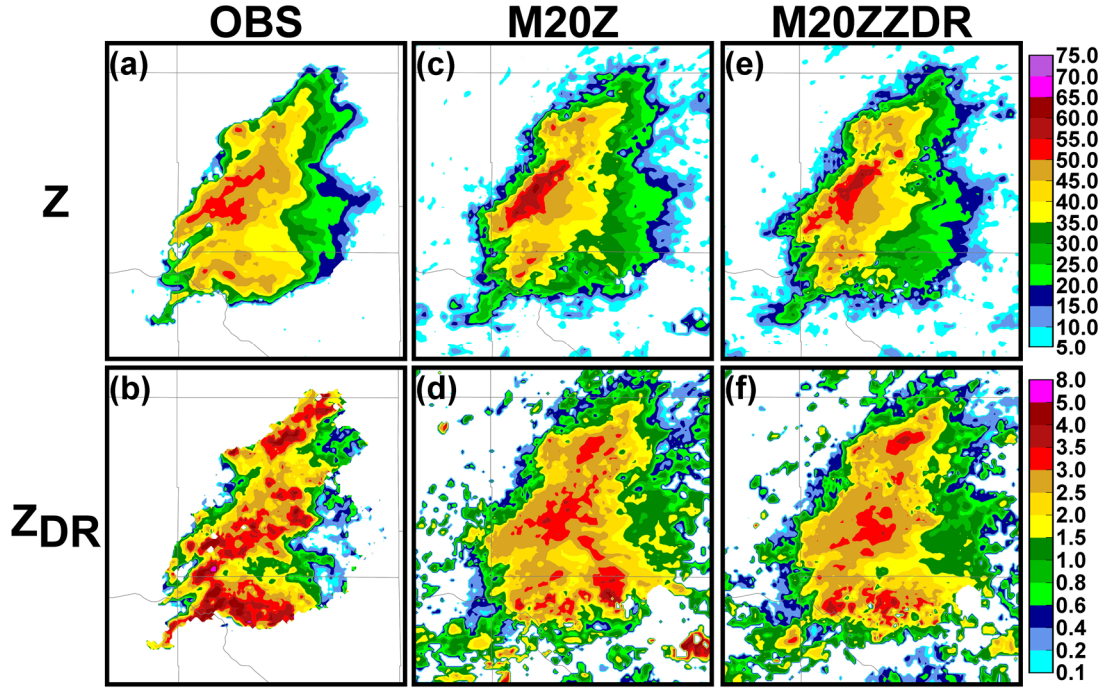


Fig. 5.1. (a) Reflectivity and (b) differential reflectivity (dB) at the 0.5° tilt from KTLX at 1938 UTC as well as from the ensemble mean analyses of (c-d) M20Z and (e-f) M20ZZDR at 1940 UTC.

The impact of assimilated Z_{DR} is most noticeable for the Moore storm. Simulated Z_{DR} in M20Z is lower in the Z_{DR} arc region and higher immediately to the north compared to the observations. In M20ZZDR, analyzed Z_{DR} is increased along an east-west oriented axis consistent with the Z_{DR} arc in the observations. The analyzed Z_{DR} values are also lower immediately to the north. In other words, the Z_{DR} arc for the Moore storm is more defined when Z_{DR} is assimilated. When combined with the OKC storm, the analyzed Z_{DR} pattern in M20ZZDR distinguishes between the high Z_{DR} values within the right (relative to storm motion) forward flank of both storms and the local minimum in between.

The differences in analyzed Z between the model results and observations and simulated Z_{DR} for M20Z and analyzed Z_{DR} for M20ZZDR for the observations from the

same 0.5° KTLX tilt are plotted in Fig. 5.2. The observations are included for reference. The warm, orange colors indicate where the model results are higher than the observations and the cool, blue colors indicate where the model results are lower than the observations. Areas with little change relative to the observations are noted in gray. The Z values for both experiments are similar. The noted areas from Fig. 5.1 where Z is underestimated in the southeastern portion of the forward flank for both storms is obvious from the dark blue colors.

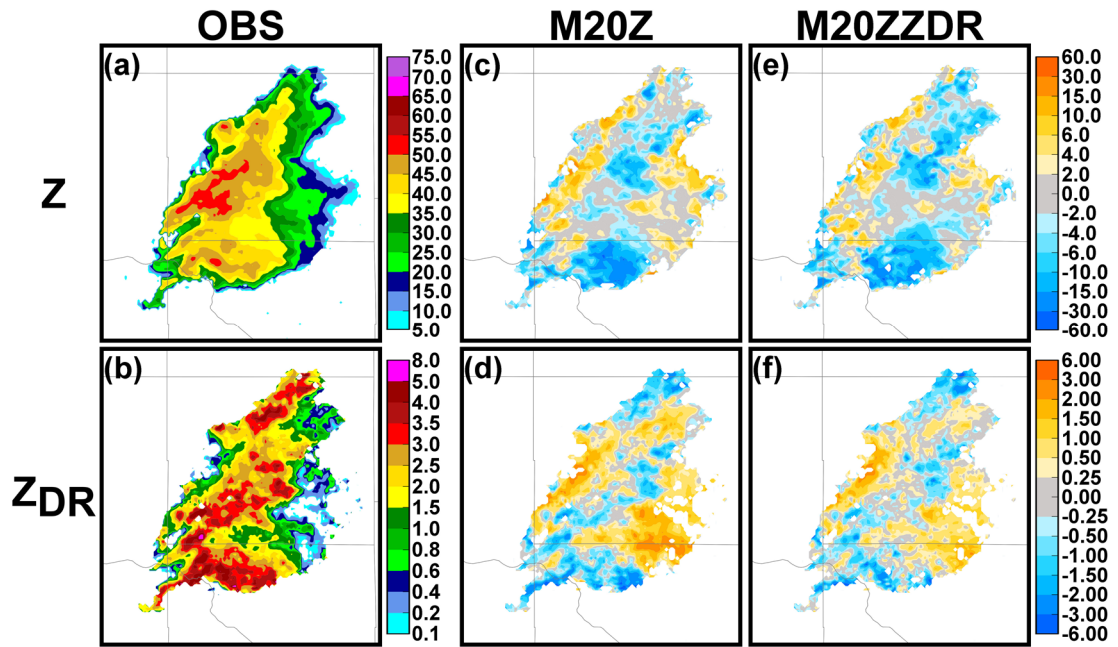


Fig. 5.2. (a) Reflectivity (dBZ) and (b) differential reflectivity (dB) at the 0.5° tilt from KTLX at 1938 UTC and the difference between the (c) analysis reflectivity and the observations and (d) differential reflectivity and the observations for M20Z and (e-f) M20ZZDR at 1940 UTC.

The impact of assimilating Z_{DR} is clearly seen when comparing the Z_{DR} differences between the experiments. For the Moore storm in particular, the magnitude of the differences between analyzed Z_{DR} and the observations for M20ZZDR are less compared to M20Z. Simulated Z_{DR} values that are too high in the central and eastern

portions of the forward flank of the Moore storm in M20Z are still slightly higher but with a lesser magnitude in M20ZZDR. Z_{DR} values in M20Z that are too low in the southern portion of the forward flank where the observed Z_{DR} arc exists are still somewhat lower but with a lesser magnitude in M20ZZDR. A larger portion of the Moore storm in M20ZZDR is within the ‘gray’ region where the differences between the analyzed and observed Z_{DR} are less than 0.25 dB in magnitude.

The fact the patterns of analyzed Z between the experiments are relatively similar is not insignificant. Ultimately, the goal is to provide an improved analysis of the observations. However, the Z_{DR} analysis is improved which should indicate through investigation of the model microphysical state that the similar analyzed Z pattern in M20ZZDR better represents the observed microphysical state. In other words, when Z alone is assimilated, there are a multitude of possible combinations of PSDs that can fit those values of Z . However, they will be in error compared to the observations. The assimilation of Z_{DR} provides additional information on the observed microphysical state to better replicate the observed PSDs that lead to the Z values seen. An analysis with Z alone that matches the observations well may provide a good fit in terms of precipitation coverage, but the actual microphysical state of the model may contain significant error compared to the observed state.

For one last assessment of the Z_{DR} values, the differences between M20Z and M20ZZDR are plotted in Fig.5.3 in the same way as Fig. 5.2 but compared to each other rather than the observations. The Z_{DR} observations are included for comparison. The differences are most apparent in the Moore storm. The Z_{DR} analysis has higher values of Z_{DR} , sometimes in significant magnitudes, along the southern edge of the forward flank

where the Z_{DR} arc is located. Additionally, the analyzed Z_{DR} in M20ZZDR is lower to the northeast of the Z_{DR} arc where PSDs with lower maximum drop sizes and more small drops would be expected. This reflects the pattern of values in the Z_{DR} observations. Values greater than 3.0 dB are located within the Z_{DR} arc and decrease to less than 1 dB further downshear in the forward flank.

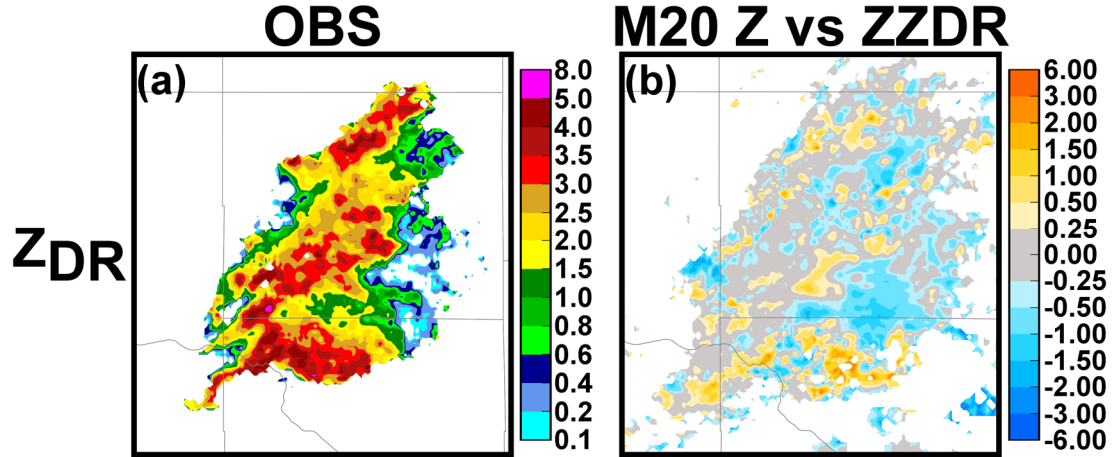


Fig. 5.3. (a) Differential reflectivity (dB) at the 0.5° tilt from KTLX at 1938 UTC and difference in differential reflectivity between (b) M20Z and M20ZZDR at 1940 UTC.

5.2.2 Evaluation of model microphysical state

It is important to further investigate how the differences seen in the values of the dual-pol variables in the analyses compared to observations when Z_{DR} is assimilated impact the estimate of the model microphysical state variables. A few values associated with the model PSDs are evaluated in this section. First, rain mean mass diameter ($D_{nr.}$) at model grid level 2 (first level above the surface) is plotted in Fig. 5.4. Analyzed Z contours at 20 dBZ intervals are overlaid on the plots. The Z_{DR} observations from the 0.5° KTLX tilt are included for reference. Both storms are located very close to KTX so the 0.5° tilt observations are close to the surface.

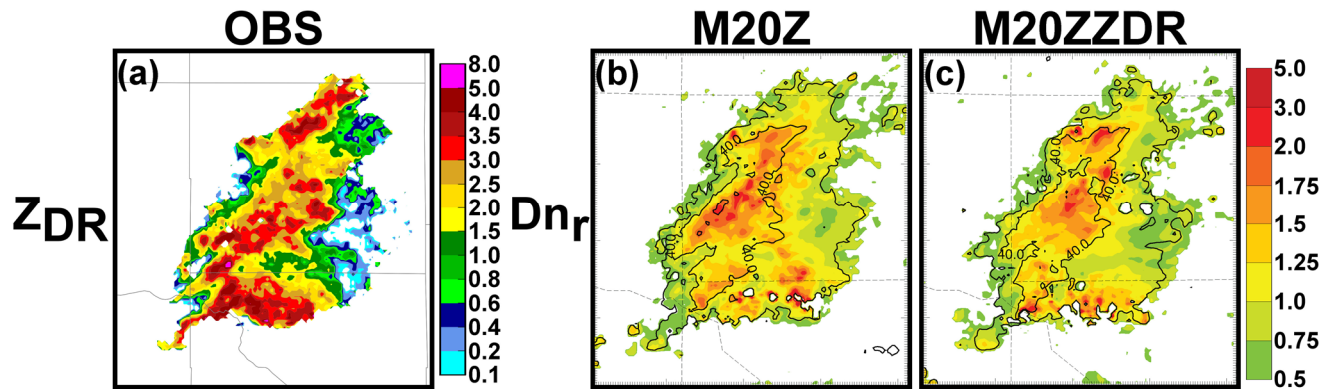


Fig. 5.4. (a) Differential reflectivity (dB) at the 0.5° tilt from KTLX at 1938 UTC as well as mean mass diameter (mm) at the first model level above the surface for the ensemble mean analysis of (b) M20Z and (c) M20ZZDR at 1940 UTC. Reflectivity contours are overlaid on the mean mass diameter plots in 20 dBZ intervals.

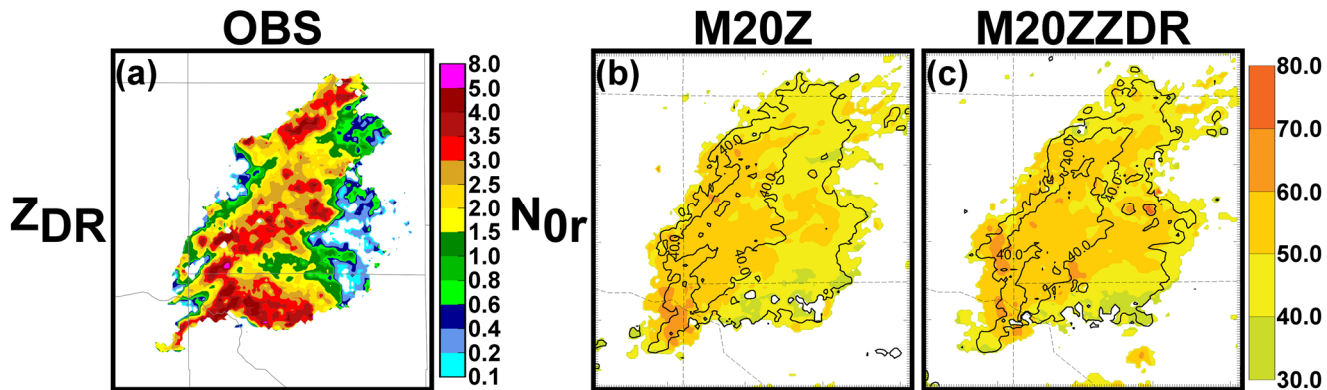


Fig. 5.5. (a) Differential reflectivity at the 0.5° tilt from KTLX at 1938 UTC as well as rain intercept parameter (mm⁻⁴, $10\log_{10}$ scale) at the first model level above the surface for the ensemble mean analysis of (b) M20Z and (c) M20ZZDR at 1940 UTC. Reflectivity contours are overlaid on the intercept parameter plots in 20 dBZ intervals.

The pattern of D_{nr} values in M20ZZDR better reflects the observed Z_{DR} pattern compared to M20Z. It is expected that PSDS associated with high Z_{DR} values will have higher mean mass diameter values, and vice versa for low Z_{DR} values. Specifically, there are higher mean mass diameters on the immediate southern edge of the forward flank of the Moore storm co-located with the Z_{DR} arc in the observations. Additionally, the D_{nr} values are lower immediately to the north in the central and northern portions of the forward flank. These differences between M20Z and M20ZZDR indicate that the improvement in the analyzed Z_{DR} patterns seen in section 5.2.1 in M20ZZDR is reflected in the model microphysical state. Also of note, the pattern of higher D_{nr} values in the OKC storm in M20ZZDR better matches areas of high Z_{DR} in the observations compared to M20Z. The comparison of the Z_{DR} values did not show as much of an impact in this area but it is clear that there was still a positive impact on the microphysical state.

The intercept parameter for rain N_{0r} , one of the parameters of the rain PSD, is plotted for the same model grid level 2 in Fig. 5.5. Analyzed Z contours at 20 dBZ intervals are overlaid on the plots. The Z_{DR} observations are again included for reference. It is expected that high Z_{DR} values are associated with PSDs with lower N_{0r} values, representing distributions with long tail ends and larger drops, and that low Z_{DR} values are associated with PSDS with higher N_{0r} values, representing distributions with a much higher number of small drops and a lower maximum drop size. The evaluation of Z_{DR} values in section 5.2.1 noted that there is a local minimum in Z_{DR} seen in the observations and M20ZZDR between the Moore and OKC storms between the higher values associated with the Z_{DR} arc in both storms. The N_{0r} values in M20ZZDR are

higher than in M20Z for this region, indicating an increase in the number of small drops present in the model which is expected given the low Z_{DR} values in the observations.

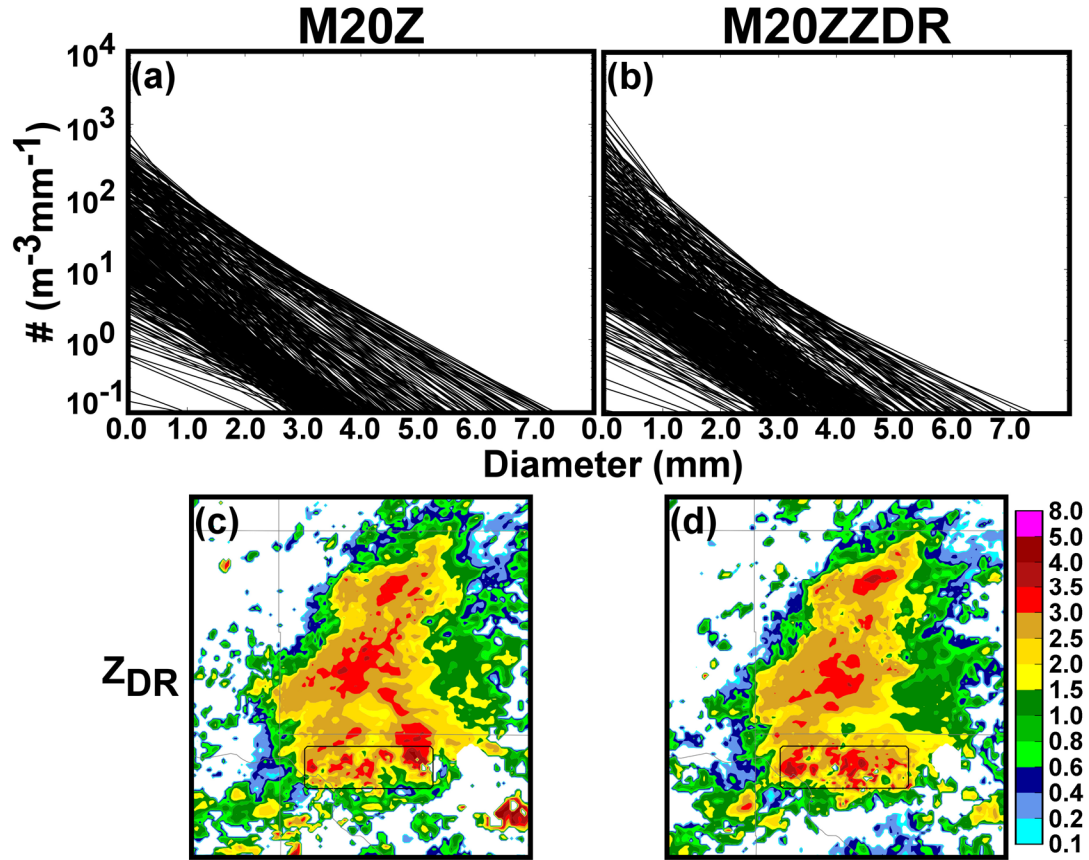


Fig. 5.6. Individual rain DSDs at each model grid point from the first level above surface for (a) M20Z and (b) M20ZZDR at 1940 UTC as well as (c) simulated and (d) analyzed differential reflectivity reference images from M20Z and M20ZZDR as plotted from the 0.5° tilt of KTLX with a black box indicating the region from which the DSDs are included.

Individual rain DSDs at the first level above the surface (model grid level 2) from both experiments are plotted in Figs. 5.6 and 5.7. A subdomain is used in each figure to highlight separate areas of interests in the storm and a black box that outlines this subdomain is plotted on included simulated (M20Z) and analyzed (M20ZZDR) Z_{DR} plots from Fig. 5.1 for reference. Fig. 5.6 focuses on the southern portion of the forward flank of the Moore storm associated with the Z_{DR} arc and Fig. 5.7 focuses on the

northern portion of the forward flank of the Moore storm. The DSDs with the largest drop sizes present (up to 7 mm diameter) are similar (Fig. 5.6). However, there is a notable increase in the concentration of DSDs with larger drop sizes from the 3.0 to 4.0 mm range to 4.0 to 5.0 mm range in M20ZZDR compared to M20Z. This region in both experiments appears to contain similar maximum drop sizes but there is a relative increase in the number of DSDs with larger drop sizes when Z_{DR} is assimilated in M20ZZDR. The DSDs in Fig. 5.7 are again somewhat similar but there is a general increase in the N_{0r} values in the M20ZZDR experiment. It is expected that the DSDs in this region would have an increased number of small drops based on the lower observed Z_{DR} .

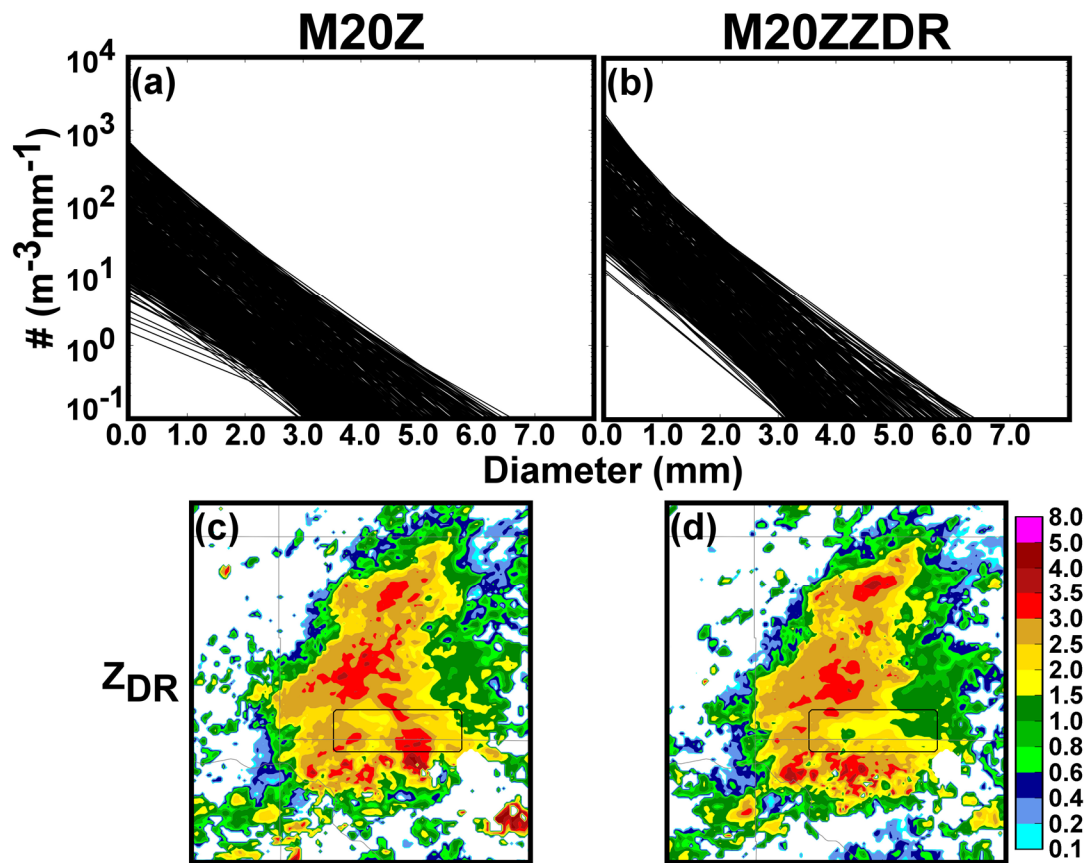


Fig. 5.7. As in Fig. 5.6, but for a different reference area indicated by the black box in (c-d).

These experiments use NWP to estimate the model microphysical state. Another area of observational research attempts to retrieve information about the observed DSDs using dual-pol radar observations and known relationships between the DSD parameters. In one such method, introduced in Zhang et al. (2001), Λ_r is first found by creating a table of calculated Z_{DR} values based on a range of potential Λ_r values using a Z_{DR} equation that has been modified to include calculated T-matrix scattering amplitudes for rain (Jung et al. 2010). The table is searched based on the observed Z_{DR} value to find the closest Λ_r used to calculate a similar Z_{DR} value. Next, the observed Z value and calculated Λ_r are used to calculate N_{or} . The model estimated N_{or} values at the first level above the surface for both experiments are compared to retrieved N_{or} values from the lowest 0.5° tilt from KTLX in Fig. 5.8. The observed Z_{DR} is included for reference as well as the hydrometeor classifications for the observations based on the method of Park et al. (2009). The N_{or} values are only retrieved in areas that are identified as pure rain (the big drops, rain, and heavy rain categories). The retrieved N_{or} values are somewhat higher than the model estimated values. However, the pattern of increasing and decreasing values better matches the M20ZZDR experiment. Higher values of N_{or} extend out further in the northern portions of the forward flank for both the Moore storm and the storm to its north over Oklahoma City. This matches the pattern in the observations, where the relative highest values of N_{or} extend out in the northern portions of the forward flank where more smaller drops are present, compared to the southern portion where the Z_{DR} arc is located. A more detailed analysis of these retrieved values is needed, but the initial results show an encouraging improvement in

the match between M20ZZDR and the observations compared to M20Z and the observations.

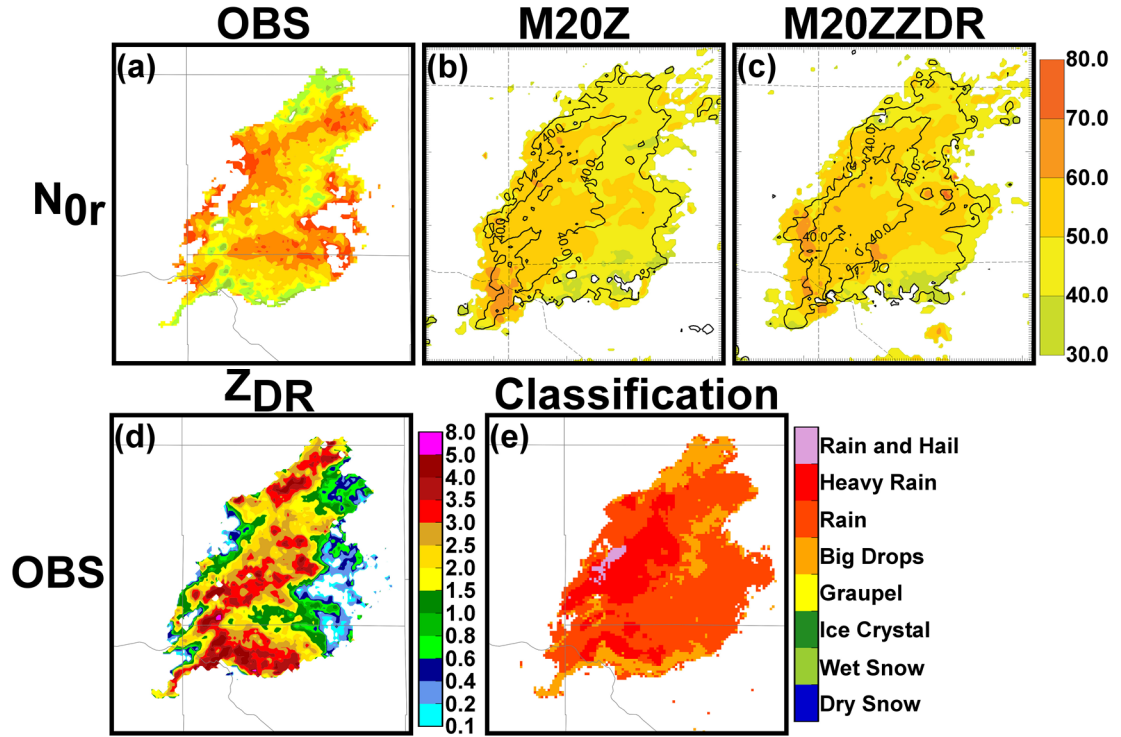


Fig. 5.8. (a) Retrieved rain intercept parameter values (mm^{-4} , 10Log_{10} scale) from KTLX observations at the 0.5° tilt as well as calculated rain intercept parameter values at the first model level above the surface for the ensemble mean analysis of (b) M20Z and (c) M20ZZDR at 1940 UTC. Reflectivity contours are overlaid on the intercept parameter plots in 20 dBZ intervals. Also, (d) observed Z_{DR} from the 0.5° tilt of KTLX and (e) hydrometeor classifications of the observations from KTLX.

5.3 The 10 May 2010 tornadic supercells case

As for the 20 May 2013 case, the radar configuration experiment results, RFZ and RFZZDR from chapter 4 for this 10 May 2010 case are evaluated. The ‘RF’ is dropped and the experiments will be referred to as ‘M10Z’ and ‘M10ZZDR’. The analyses from 2248 UTC are chosen for evaluation because this is the best combination of low RMSEs for Z and Z_{DR} at this point.

5.3.1 Evaluation of analyzed dual-pol variables

The mean analyzed Z and simulated Z_{DR} from M10Z and analyzed Z and analyzed Z_{DR} from M10ZZDR for 2248 UTC are compared to KOUN observations of Z at the 0.5° tilt (Fig. 5.9). There are actually three storms at this point; there is the southern Norman storm, the northern Moore storm, and a right split supercell from the Moore storm which will be referred to as the Shawnee storm since it produced a tornado that occurred over the Shawnee reservoir. The analyzed Z is best for the Moore storm in both experiments. For the Norman storm, as in the M20 case, the right, or southern, portion of the forward flank has underestimated Z values compared to the observations. There is not the same degree of improvement in analyzed Z_{DR} in M10ZZDR compared to simulated Z_{DR} in M10Z as is seen when comparing the similar experiments in the M20 case. There are some areas where the analyzed Z_{DR} in M10ZZDR shows a closer fit to the observations. For example, the simulated Z_{DR} in the western part of the Moore storm in M10Z is too high and the analyzed Z_{DR} values in M10ZZDR are lower. However, there isn't much improvement noted with any of the maximums in the Z_{DR} observations associated with the Z_{DR} arcs in each storm. Higher values of Z_{DR} extend further eastward in the Norman storm in M10ZZDR compared to M10Z, which is more similar to the observations, but there only a few points that are greater than 3.0 dB, which cover a significant area in the observations. The Z_{DR} values for both experiments are also too high far downshear in the forward flank of the Moore storm. This is actually worse in M10ZZDR compared to M10Z for some locations in the northeastern portion of the forward flank.

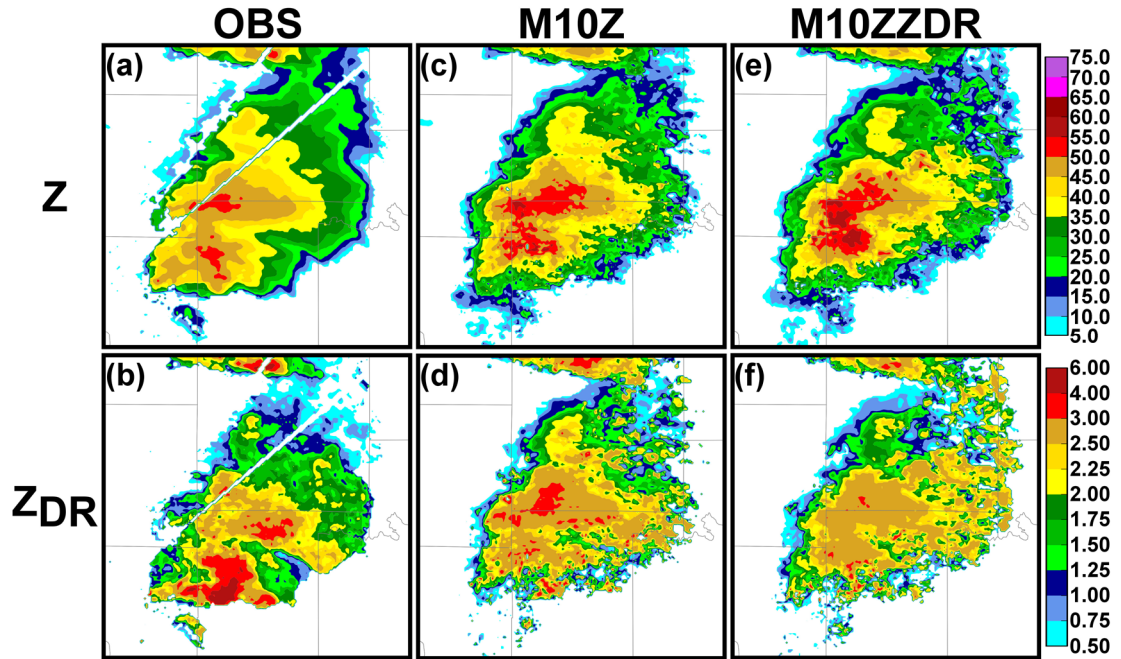


Fig. 5.9. (a) Reflectivity (dBZ) and (b) differential reflectivity (dB) at the 0.5° tilt from KOUN at 2246 UTC as well as from the ensemble mean analyses of (c-d) M10Z and (e-f) M10ZZDR at 2248 UTC.

Z and Z_{DR} difference plots between the experiments and the observations and Z_{DR} difference plots between M10ZZDR and M10Z are included in Figs. 5.10 and 5.11, respectively. The difference plots with respect to the observations help accentuate even slight improvements in M10ZZDR. The magnitudes of the differences in M10ZZDR are noticeably lower compared to M10Z. This is most apparent for the Moore storm and least apparent for the Norman storm, which is not analyzed well. The magnitude of the difference between M10ZZDR and M10Z and the observations in the Z_{DR} arc region are relatively similar. In fact, based on Fig. 5.11, large areas of Z_{DR} in the results are very similar and even in areas where there are differences, these differences do not show a discernable pattern. The only area where there are consistent differences is far downshear in the forward flank of the Moore storm. The analyzed Z_{DR} in M10ZZDR is

erroneously higher in the northeastern portion of the forward flank, but improves upon M10Z in the northern portion (Z_{DR} should be low in this region based off the observations). The analyzed Z_{DR} in M10ZZDR may have a somewhat improved fit to the observations compared to simulated Z_{DR} in M10Z, but the notable patterns in Z_{DR} that M20ZZDR appeared to capture for that case are not as apparent in this case.

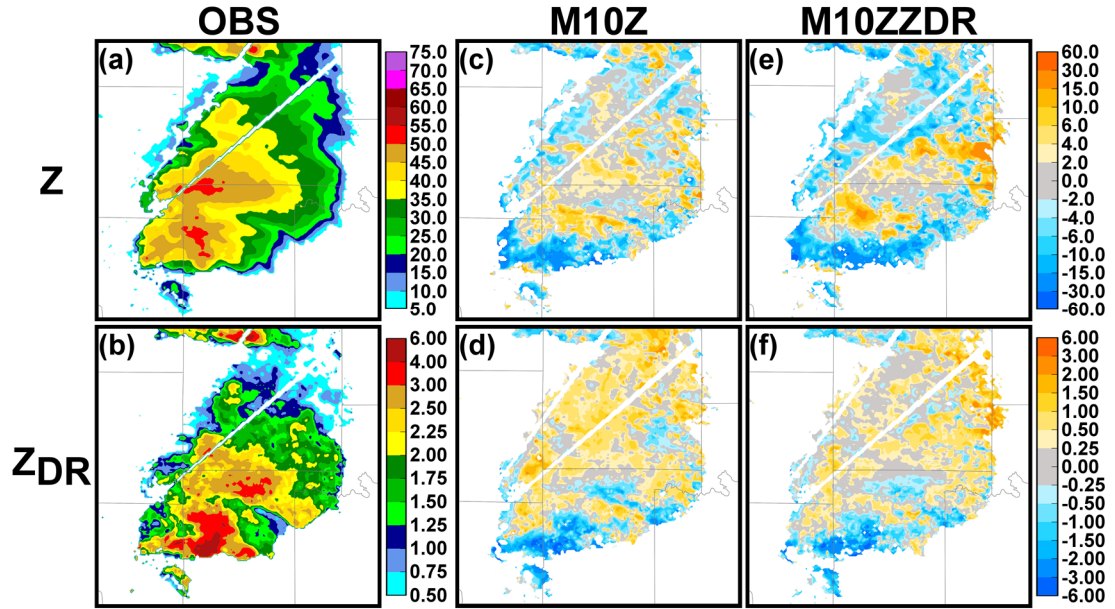


Fig. 5.10. (a) Reflectivity (dBZ) and (b) differential reflectivity (dB) at the 0.5° tilt from KOUN at 2246 UTC and the difference between the (c) analysis reflectivity and the observations and (d) differential reflectivity and the observations for M10Z and (e-f) M10ZZDR at 2248 UTC.

K_{DP} is also assimilated for the M10 case. Less attention was paid to K_{DP} in prior sections because it was not assimilated for both cases. Also, K_{DP} is more closely associated with high Z values compared to Z_{DR} . Therefore, in the sensitivity experiments, attention was focused on Z_{DR} since the observation patterns can differ significantly from Z . Fig. 5.12 contains KOUN observations of Z , Z_{DR} , and K_{DP} at the 0.5° tilt as well as enmean analyzed Z and simulated Z_{DR} and K_{DP} from M10Z and analyzed Z , simulated Z_{DR} , and analyzed K_{DP} from M10ZKDP for 2248 UTC.

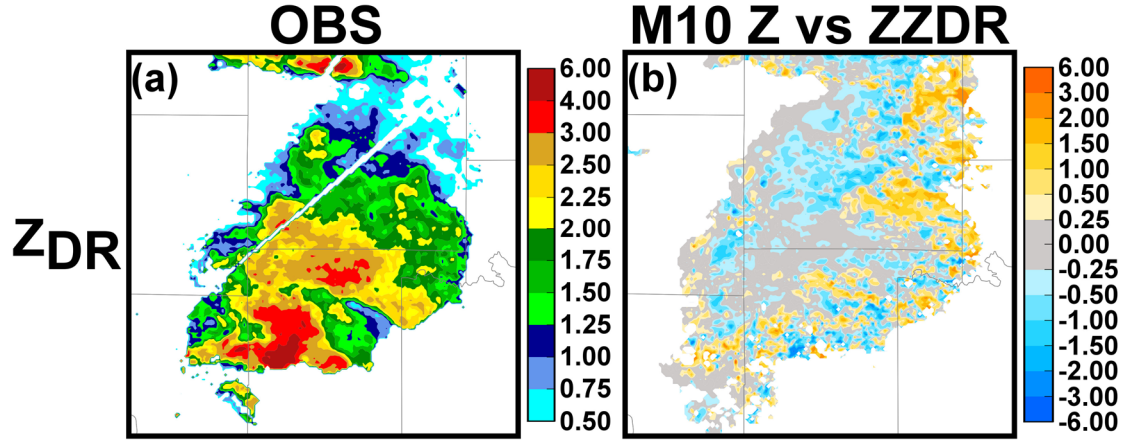


Fig. 5.11. (a) Differential reflectivity (dB) at the 0.5° tilt from KTLX at 2246 UTC and difference in differential reflectivity between (b) M10Z and M10ZZDR at 2248 UTC.

The impact of the assimilated K_{DP} is significant in M10ZKDP. The observed K_{DP} values are high in the center of each storm, where the heaviest precipitation and highest rain rates occur. The coverage and intensity of the K_{DP} values is remarkably similar to the observations. The K_{DP} values in M10ZKDP are higher than for the simulated K_{DP} values in M10Z which are underestimated. However, the analyzed Z is overestimated in M10ZKDP. The Z values are significantly higher compared to the Z observations where high K_{DP} observations are present. The coverage of precipitation on the forward flank of the Moore storm is also erroneously extended to the northeast.

The Z_{DR} values in M10ZKDP are increased compared to M10Z as well, indicating that model PSDS associated with the increased K_{DP} have higher sized raindrops relative to the observations. The use of a fixed shape parameter or a triple-moment scheme may prove beneficial in this case. The higher K_{DP} values in the observations are normally associated with PSDs that have a significant number of medium size drops. A triple-moment (TM) scheme with a variable shape parameter could fit PSDs that have a higher number of medium sized drops.

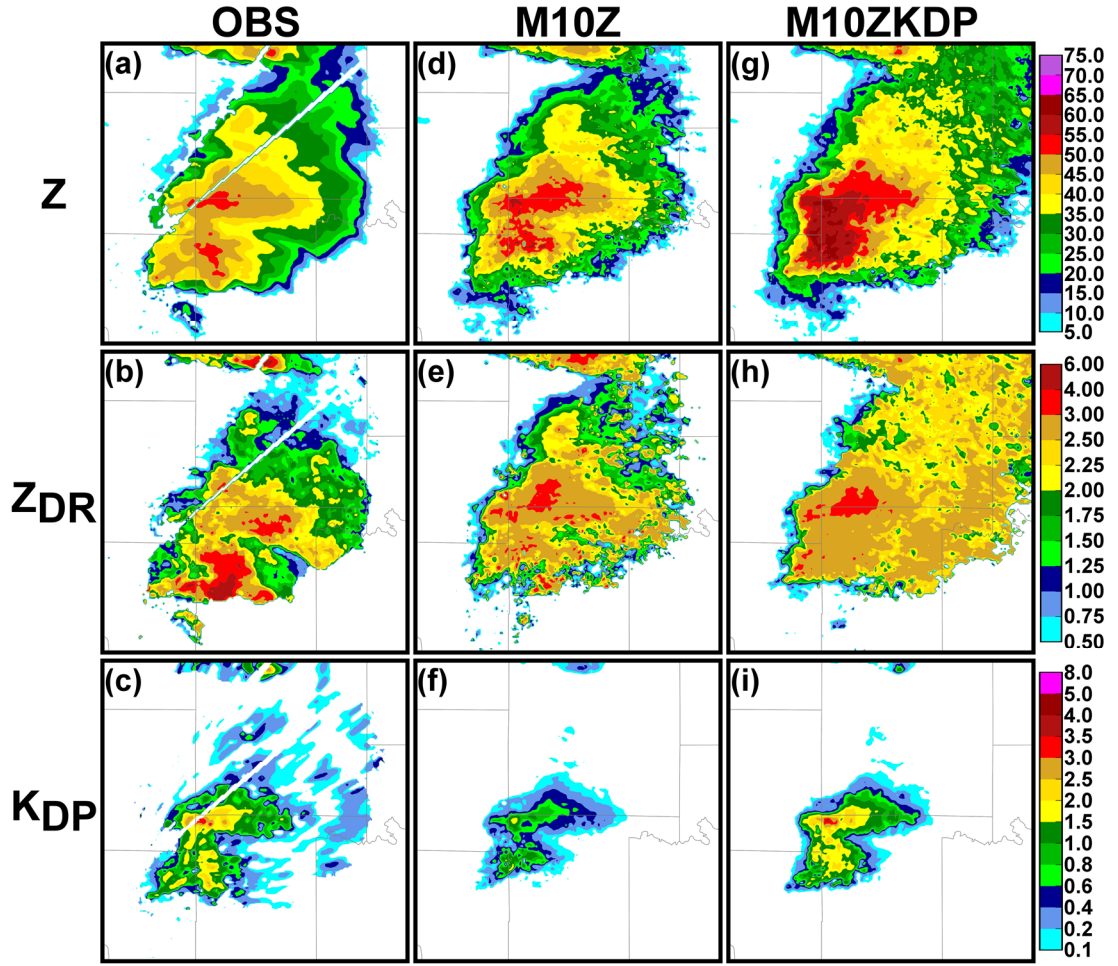


Fig. 5.12. (a) Reflectivity (dBZ), (b) differential reflectivity (dB), and (c) specific differential phase ($^{\circ} \text{ km}^{-1}$) at the 0.5° tilt from KOUN at 2246 UTC as well as from the ensemble mean analyses of (d-f) M10Z and (g-i) M10ZKDP at 2248 UTC.

5.3.2 Evaluation of model microphysical state

Mean mass diameter (D_{nr}) at model grid level 2 (first level above the surface) in M10Z and M10ZZDR is plotted in Fig. 5.13. Analyzed Z contours at 20 dBZ intervals are overlaid on the plots. The Z_{DR} observations at the 0.5° tilt from KOUN are included for reference. D_{nr} is lower in the western portion of the Moore storm where the Z_{DR} observations indicate more medium sized drops. There was a decrease in analyzed Z_{DR} in M10ZZDR noted for this location in the previous section. Additionally, D_{nr} is higher

in the southeastern portion of the Shawnee storm which corresponds to higher Z_{DR} values. This improvement is not as noticeable in the plots of analyzed Z_{DR} , so even though the analyzed Z_{DR} in M10ZZDR does not appear to improve much compared to M10Z, there still has been an improvement in the model microphysical state. There are lower D_{nr} values in M10ZZDR compared to M10Z for the western portion of this storm as well.

Both cases have high D_{nr} values along the eastern edges of the forward flanks of the supercells. This is an odd artifact and not expected theoretically, since smaller drops would be expected far downshear from the updraft, and is erroneous based on the observed Z_{DR} values. Plots of N_{or} , included in Fig. 5.14, show that the N_{or} in the experiments is very low in these locations, likely leading to the erroneously high Z_{DR} values. Overall, the patterns in the N_{or} values are very similar between the two cases. There are some noted improvements in the PSDs for M10ZZDR based on D_{nr} , but there is little improvement in the microphysical state overall for the M10ZZDR experiment for this M10 case compared to the corresponding experiment in the M20 case.

Since K_{DP} is sensitive to the amount of liquid water present in the radar volume, the impact on the model microphysical state should be seen in the values of rain mixing ratio q_r . Fig 5.15 contains plots of q_r for both M10Z and M10ZKDP at model grid level 2 as well as the corresponding K_{DP} observations from KOUN at a 0.5° tilt for reference. The q_r values are increased significantly, roughly following the pattern of the observed K_{DP} values in both location and intensity. It is clear based on the comparison of M10Z to the observations that the water content is lower in the model than compared to the

observations, but the DM scheme may not be able to fit the observed PSDs properly for M10ZKDP.

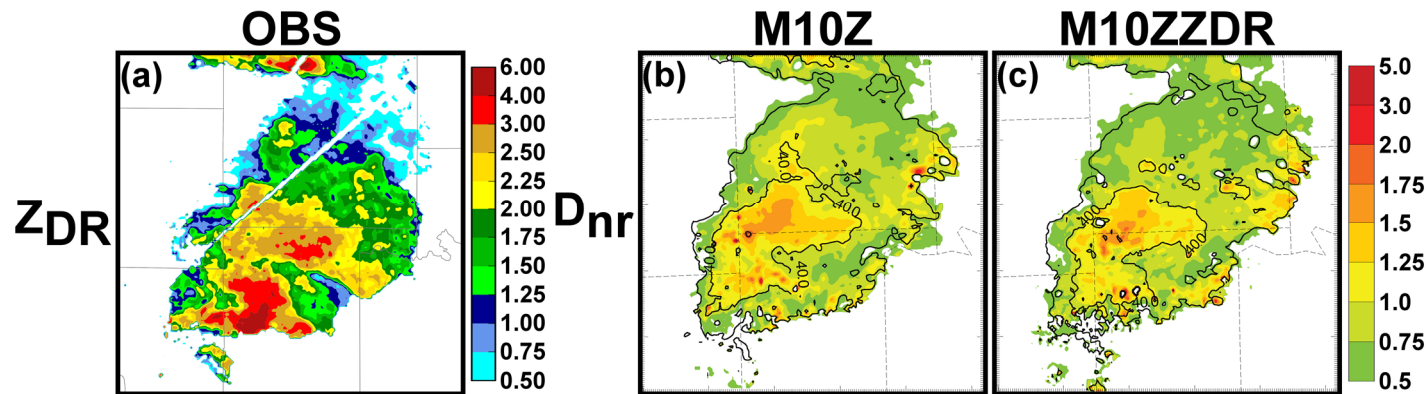


Fig. 5.13. (a) Differential reflectivity (dB) at the 0.5° tilt from KOUN at 2246 UTC as well as mean mass diameter (mm) at the first model level above the surface for the ensemble mean analysis of (b) M10Z and (c) M10ZZDR at 2248 UTC. Reflectivity contours are overlaid on the mean mass diameter plots in 20 dBZ intervals.

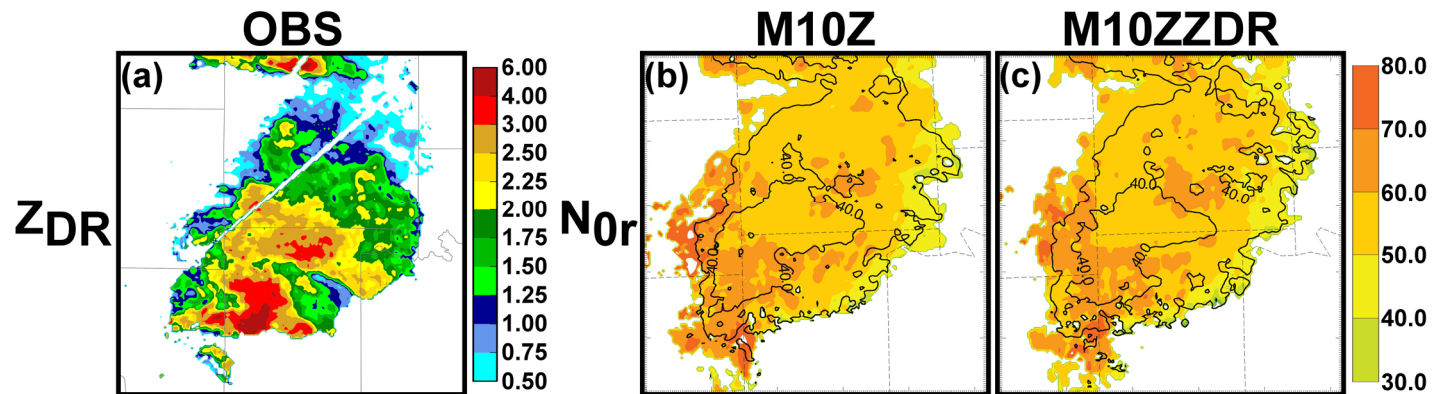


Fig. 5.14. (a) Differential reflectivity at the 0.5° tilt from KOUN at 2246 UTC as well as rain intercept parameter (mm^{-4} , 10Log_{10} scale) at the first model level above the surface for the ensemble mean analysis of (b) M10Z and (c) M10ZZDR at 2248 UTC. Reflectivity contours are overlaid on the intercept parameter plots in 20 dBZ intervals.

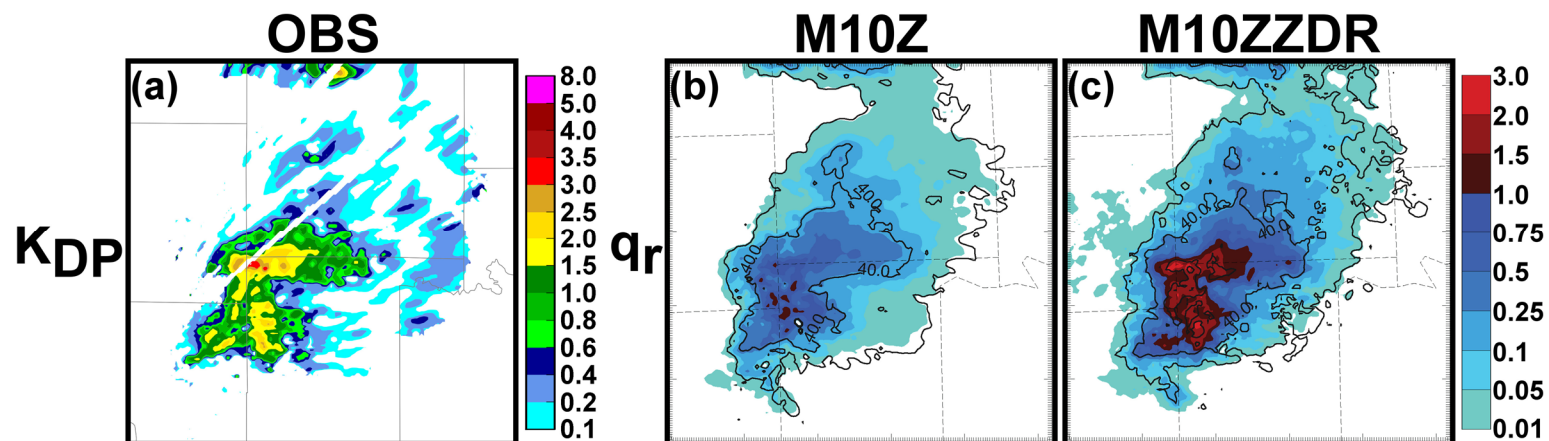


Fig. 5.15. (a) Observed specific differential phase at the 0.5° tilt from KOUN at 2246 UTC as well as rain mixing ratio (g kg^{-1}) at the first model level above the surface for the ensemble mean analysis of (b) M10Z and (c) M10ZZDR at 2248 UTC. Reflectivity contours are overlaid on the mixing ratio plots in 20 dBZ intervals.

5.4 Summary and conclusions

Dual-pol observations are assimilated for the first time for real supercell cases using an advanced double-moment (DM) microphysics schemes and an advanced forward operator that includes full T-matrix scattering amplitude calculations. Two areas of interest from two cases are considered: Tornadic supercells that occurred east of Norman and Moore, OK during the 10 May 2010 tornado outbreak (M10 case) and the supercell that produced the EF-5 Moore tornado from 20 May 2013 (M20 case). There two experiments for each case, ‘Z’ which assimilates Z and V_r , and experiment ‘ZZDR’ which assimilates Z_{DR} in addition to Z and V_r . The configuration settings for these experiments were determined in Chapter 4. The M10 case also includes an experiment that assimilates K_{DP} , ‘M10ZKDP’.

The analyzed Z_{DR} in M20ZZDR shows a better fit to observed Z_{DR} compared to M20Z. The M20ZZDR results better fit patterns of high Z_{DR} , such as the Z_{DR} arc, and regions of low Z_{DR} further downshear in the forward flank. Perhaps more importantly, the analyzed Z in M20ZZDR is not significantly different compared to M20Z and the observations. This means the additional Z_{DR} observations improved the model PSDs relative to the observed microphysical state to fit the same Z values as M20Z. This demonstrates the value of having additional observations of the storm microphysical state compared to Z alone. Evaluation of rain mean mass diameter (D_{nr}) and rain intercept parameter (N_{0r}) at the surface show that the additional Z_{DR} observations have improved the model microphysical state. Regions where Z_{DR} is high in the observations have an increased D_{nr} and vice versa compared to M20Z. Additionally, the N_{0r} is higher for regions of low observed Z_{DR} compared to M20Z. Also, individual plots of rain DSDs

from regions of observed low and high Z_{DR} show that the intercept parameter is higher in M20ZZDR where observed Z_{DR} is low and a greater number of larger drops where observed Z_{DR} is high. Finally, patterns in retrieved N_{0r} values from KTLX observations better match the N_{0r} patterns in M20ZZDR even though the actual values are a bit higher in the retrieved values.

The results are not as encouraging for the M10 case. There is not much difference between the analyzed Z_{DR} values in M10ZZDR compared to M10Z relative to the observations. While there are some noticeable improvements in both the analyzed dual-pol variables and evaluation of the microphysical state, these improvements are low in magnitude and very limited in area. More specifically, the improved patterns of these variables in the M20 case associated with notable features like the Z_{DR} arc in the observations are not noted for the M10 case. Also, the southeastern portion of the forward flank of the Norman storm is predicted very poorly.

Experiment M10ZKDP, which assimilated K_{DP} , shows a remarkably improved fit to the observations compared M10Z. However, the analyzed Z values are overestimated, particularly where high K_{DP} values are present in the observations. An analysis of rain mixing ratio q_r shows that the assimilation of K_{DP} significantly increases q_r . Since the analysis of Z has been erroneously increased the PSD appears to have been altered but not in a way that improves the model microphysical state relative to the observed state. The use of a TM scheme might provide a better fit for heavy precipitation areas where a large amount of medium sized drops are present.

Chapter 6 Summary and Conclusions

6.1 Summary

In convection allowing models (CAMs), in which model microphysics (MP) schemes are used, the MP schemes play a crucial role in properly representing microphysical processes and states. On this convective scale, even a slight deviation in the estimation of the model microphysical state compared to the true atmospheric microphysical state can quickly lead to significant error in forecasts (Lorenz 1969). Most model MP schemes predict a given number of microphysical hydrometeor types and represent their particle size distributions (PSDs) using a simplified gamma distribution (Ulbrich 1983). Up to three independent parameters govern this distribution: the slope (Λ_x), intercept (N_{0x}), and shape (α_x) parameters, which are determined by predicted model microphysical state variables. Most current research and operational models use either single-moment (SM) schemes, where only Λ_x is independently updated, and double-moment schemes (DM), where Λ_x and N_{0x} are independently updated. Advanced data assimilation (DA) methods, such as the ensemble Kalman filter (EnKF), are used to optimally combine a background model state with observations to reduce error in the initial model microphysical state of a forecast.

Weather radar currently provides the best spatial and temporal observations of severe, convective storms. The national WSR-88D network was recently upgraded to dual-polarimetric (dual-pol) capabilities which include several new parameters in addition to reflectivity (Z) and radial velocity (V_r). These include differential reflectivity (Z_{DR}), which is sensitive to the shape of the hydrometeors in the radar volume, and

specific differential phase (K_{DP}), which is sensitive on the amount of liquid water present in the radar volume. Simulated dual-pol variables from the model convective storms can be compared to the observations to provide a more thorough comparison of the model microphysical state, including additional details on the types of hydrometeors present and their PSDs. Additionally, dynamic and microphysical processes lead to distinct patterns of observed dual-pol parameters values, or signatures, in both supercell storms and mesoscale convective systems (MCS) that can be used as evidence for comparing these true atmospheric microphysical processes with the model performance. The new nation-wide observations offer an unprecedented opportunity to further investigate and estimate the model microphysical state, vital to improving convective scale forecasts, in ways not previously possible.

The goal of this dissertation is to assess the microphysical state of multi-moment MP scheme forecasts as well as to improve the estimation of the microphysical state for forecasts of severe, convective storms through the use of simulated and observed dual-pol variables and ensemble based methods. The use of ensembles, including for DA using the EnKF, provides a helpful way to compare multiple MP schemes, assess uncertainty in forecasts, and assimilate observations using complex and highly non-linear observation operators and model microphysics schemes. This is accomplished through three separate studies that 1) compare and contrast the simulated polarimetric variables and signatures for an ensemble of forecasts containing multiple microphysics schemes, 2) produce probabilistic ensemble forecasts of dual-pol variables using multi-moment schemes, and finally 3) assimilate dual-pol observations using the EnKF to improve the estimation of the model microphysical state.

In the first study (Chapter 2), simulated dual-pol variables from several members of the CAPS Storm Scale Ensemble Forecasts (SSEF) as part of the Spring Experiment (Kong 2013) which used different MP schemes are compared to dual-pol observations. This included 4-hour regional forecasts for both a mesoscale convective system (MCS) case from 20 May 2013 and a 21-hour regional forecast for a supercell case from 20 May 2013. Particular attention is paid to the types of hydrometeors in each scheme and how their particle size distributions are represented so that the observation operators used to simulate the variables best replicate the results of each scheme. Some schemes are fully DM (Milbrandt and Yau (MY) and Morrison (MOR)), some were partially DM (do not update PSD parameters for all hydrometeor types, Thompson (TOM) and WDM6), and one was SM (WSM6).

The fully DM MY and MOR scheme, which are the only schemes DM for graupel and hail, have simulated Z_{DR} values that represent patterns and signatures associated with size-sorting compared to the other schemes; Dawson et al. (2014) showed that the size-sorting graupel and hail are more responsible for the Z_{DR} arc signature in a supercell than that of rain. The MY and MOR, which are DM for snow compared to the other schemes, as well as TOM, which uses an advanced PSD for snow, better represent the stratiform precipitation region in the MCS case. The results for WDM6, which differs from WSM6 only in the prediction of a second moment for rain, closely mirror the results of WSM6, further indicating the prediction of a second moment for all hydrometeor types is important for forecasting severe convection. There are also notable biases present in the forecasts, including the over-prediction of graupel

in the MY and MOR case and the under-forecast of simulated KDP values compared to observations, indicative of a lower liquid water content in the model.

In the second study (Chapter 3), probabilistic forecasts are made of a MCS from 9 May 2007 in Oklahoma using SM and DM MP schemes. These experiments are referred to as EXP_S and EXP_D, respectively. The results show that EXP_D better represents the structure of the MCS as well as the forecast microphysical state compared to EXP_S, particularly when considering the difference in PSDs between the stratiform precipitation and convective precipitation in the leading convective line. In terms of Z , EXP_D produces higher probabilities of $Z > 20\text{dBZ}$, indicative of overall precipitation coverage, for both the leading convective line and stratiform precipitation regions of the MCS. Quantitative probabilistic skill scores show that the EXP_D forecast is more skillful at predicting the coverage of Z for most thresholds at two and three hour forecast times, particularly the lower thresholds associated with stratiform precipitation. The EXP_D forecast is also sharper, indicating higher confidence in the forecasts in predicting where precipitation occurs and does not occur.

Probabilistic prediction of simulated dual-pol variables Z_{DR} and K_{DP} show EXP_D produces more realistic values compared to the observations. The K_{DP} values are over-forecast in EXP_S and are associated with intense, disorganized convection. Also, the pattern of Z_{DR} values in the EXP_S forecast does not differentiate between the convective and stratiform regions. On the other hand, Z_{DR} values in EXP_D are higher in the leading convective line, where size sorting leads to a greater number of large rain drops, and lower in the stratiform region, where the precipitation is less intense and contains fewer large drops and more small drops. Quantitative skill scores for those

features that are more localized, such as the high Z_{DR} values associated with size sorting along the leading convective line, as well as the more intense convection in the leading convective line when considering Z , have much poorer scores for both forecasts, though EXP_D does show some improvement overall.

In the final study, for the first time, the EnKF is used to assimilate dual-pol observations from two real cases using an advanced DM MP scheme and advanced forward operators that include full T-matrix scattering amplitude calculations. The results are preliminary in nature since this is a new area of research, but there are still several important findings and notable issues encountered. Two tornadic supercell cases are considered from 10 May 2010 (M10) and 20 May 2013 (M20) in Oklahoma.

In the first part of the study (Chapter 4), sensitivity tests are conducted relative to a control experiment in order to improve the analyses in the lower model levels of the domain where Z_{DR} is assimilated, as well as understand how the settings impact the results. In one test, different model error treatment methods are used, including multiplicative inflation and additive perturbations. Both treatments improve the analysis in terms of RMSE for the traditionally assimilated variables (Z and V_r), particularly at times when there is high temporal error between the time of the low level radar observation scans and when these observations are assimilated. However, the treatment methods tend to have a negative impact on the Z_{DR} analysis. When additive perturbations are used, the Z_{DR} values are underestimated compared to observations. In another test, radar observations are filtered on the model grid to remove noise and smooth the observations to the scale of the model grid. In these experiments, the RMSE values are improved for both analyzed Z and Z_{DR} . Qualitative evaluation of the results

shows the analyses have an improved fit to the observations as well. These analyses are used for evaluation in part two of this study. One goal of these tests is to help improve the Z analysis which is underestimated in the forward flanks of several storms of interest. However, even after testing multiple experiment configurations, the precipitation intensity is still underestimated.

The analyzed dual-pol variables and their impact on the estimation of the model microphysical state are evaluated compared to observations in the second part of the study (Chapter 5). For each case, the experiment that assimilates Z only is referred to by ‘Z’, the experiment that assimilates Z_{DR} in addition to Z is ‘ZZDR’, and for the M10 case, the experiment that assimilates K_{DP} is referred to as ‘ZKDP’. For the 20 May 2013 case, experiment M20ZZDR has an improved fit to observed Z_{DR} values while remaining similar to MCZ in terms of the fit to the Z observations. This is important since the additional variables are meant to provide further information on the model PSDs, not negatively impact the fit to observations already assimilated. An evaluation of the model microphysical state shows that the raindrop mean mass diameter (D_{nr}) is increased in regions where high Z_{DR} values are assimilated and the rain intercept parameter (N_{or}) is higher where low Z_{DR} observations are assimilated. The results are much poorer in the M10 case. The analyzed Z_{DR} is lower than the observations in the Z_{DR} arc region of multiple storms. The D_{nr} fields in M10ZZDR only show a slight improvement compared to M10Z.

In the M10ZKDP experiment, the analyzed K_{DP} values are improved significantly compared to M10Z with respect to the observations, but the Z values are overestimated. An analysis of rain mixing ratio q_r shows the liquid water content in the

model is significantly increased in areas where high K_{DP} values are assimilated. The Z_{DR} values are higher compared to the observations as well, indicating that the additional water content in the model PSDs is included in larger raindrops than the observations. The use of a triple-moment scheme with a variable shape parameter, which allows for PSDs with a peak number of drops that are medium-sized, may improve the estimate.

There are several challenges noted in each of the three studies, some of which impacted more than one of the studies. These challenges include the verification methods, especially quantitative. Typical quantitative methods are not useful for polarimetric signatures that are isolated in nature and vary greatly over a small distance. In the Spring Experiment project, the fractions skill score (FSS) is used because it considers the fraction of grid points in a neighborhood where both model and observed variables are above a given threshold, effectively accounting for spatial bias in a forecast as the neighborhood size increases. However, some of the MP schemes do not produce simulated dual-pol values as high as the observations. The use of percentile values helped somewhat improve the comparisons. This applies to the ensemble probabilistic forecasts as well. Probabilistic predictions of Z_{DR} and the associated skill scores suffer from substantial location bias due to the highly localized nature of specific patterns and values of Z_{DR} associated with microphysical and dynamical processes.

Another challenge is improving the analyses of experiments using dual-pol variables. In both cases considered in this study, portions of the analyzed Z in the storms are significantly underestimated. This negatively impacts the assimilation of the dual-pol variables in some regions, particularly for the 10 May 2010 case. Several

additional sensitivity experiments with different settings are attempted and all but those that include additional radar filtering provide no overall improvement in the analyses.

6.2 Future work

Both the results from our research and the challenges encountered inspire future work. For example, for the Spring Experiment, it is a goal to eventually extend the qualitative and quantitative evaluations of MP schemes over the entire Spring Experiment period, such that they can be used to provide forecasters with potential additional information on severe weather threats, such as high K_{DP} indicative of a flash-flooding threat, as well as provide statistically more reliable assessment on the performance and behaviors of MP schemes and perhaps also their weather regime and/or convective storm dependency. Such information can be useful to developers of the MP schemes for them to improve the schemes. The results can also provide guidance to the choice of MP schemes to use in dual-pol data assimilation studies; to successfully assimilate dual-pol data using direct assimilation methods, the MP schemes used have to be able to replicate observed polarimetric values and signatures. If a scheme that does not replicate certain signatures well, any improvement gained in the data assimilation will also be quickly lost in the forecast period.

Improved quantitative methods for assessing simulated and observed dual-pol variables must also be developed. Quantitative assessment proved challenging with current skill scores, including those that consider a neighborhood of values, due to the highly localized patterns and signatures of the variables. The Neighborhood methods did show some improvement, but neighborhoods with increasing size will quickly smear the specific patterns important to assessing the microphysical state, such as the

Z_{DR} arc signatures associated with size sorting forward flank adjacent to the updraft supercells. If the neighborhood is too large, high values of Z_{DR} from elsewhere in the supercell, or from other supercells, will indicate that certain thresholds were met but do not account for the location which defeats the purpose of the assessment. In the future, object based methods could perhaps improve scores, by associating signatures in the model and observations to remove location bias. The observation operators must also continue to be refined to improve the values simulated. This work paid specific attention to precipitation near the surface, and specifically rain. Values for simulated variables in the melting layer and for frozen precipitation showed more error compared to the observations.

For dual-pol observation assimilation, the most significant question that remains as estimates of the microphysical state are refined is what impact these improved estimates will have on short-term forecasts compared to when dual-pol variables are not assimilated. The benefit from assimilating the additional variables and the length at which the benefit lasts for forecasts must be properly assessed. This includes qualitative and quantitative measures of how significant the impacts are and how long these impacts last into the forecast period. Planned future work includes launching several forecasts at nearby time intervals for assessment. There are also obviously many areas still to investigate in the analyses as well, including the covariance structures and the related impact on other model state variables besides the microphysical state variables. For example, it will be interesting to note whether the assimilation of Z_{DR} in the Z_{DR} arc region has any impact on the wind fields in the model, which are tied to the size sorting of hydrometeors that leads to the Z_{DR} arc. Finally, only separate experiments to

assimilate Z_{DR} and K_{DP} were conducted. Future experiments can assimilate both observations and examine the impacts.

References

- Aksoy, A., D. C. Dowell, and C. Snyder, 2009: A multi-case comparative assessment of the ensemble Kalman filter for assimilation of radar observations. Part I: Storm-scale analysis. *Mon. Wea. Rev.*, **137**, 1805-1824.
- Aksoy, A., D. C. Dowell, and C. Snyder, 2010: A multi-case comparative assessment of the ensemble Kalman filter for assimilation of radar observations. Part II: Short-range ensemble forecasts. *Mon. Wea. Rev.*, **138**, 1273–1292.
- Anderson, J. L., 2001: An ensemble adjustment Kalman filter for data assimilation. *Mon. Wea. Rev.*, **129**, 2884-2903.
- Bodine, D., R. Palmer, and G. Zhang, 2013: Dual-Wavelength Polarimetric Radar Analyses of Tornadoic Debris Signatures. *Journal of Applied Meteorology and Climatology*, **53**, 242-261.
- Brandes, E. A., G. Zhang, and J. Vivekanandan, 2002: Experiments in rainfall estimation with a polarimetric radar in a subtropical environment. *J. Appl. Meteor.*, **41**, 674-685.
- Bringi, V. N. and V. Chandrasekar, 2001: *Polarimetric Doppler Weather Radar*. Cambridge, 636 pp.
- Brown, B. G., 2001: Verification of Precipitation Forecasts: A Survey of Methodology Part II: Verification of Probability Forecasts at Points. National Center for Atmospheric Research.
- Bryan, G. H. and H. Morrison, 2012: Sensitivity of a Simulated Squall Line to Horizontal Resolution and Parameterization of Microphysics. *Mon. Wea. Rev.*, **140**, 202–225.
- Bryan, G. H., J. C. Wyngaard, and J. M. Fritsch, 2003: Resolution requirements for the simulation of deep moist convection. *Mon. Wea. Rev.*, **131**, 2394-2416.

- Burgess, D. W., K. Ortega, G. Stumpf, G. Garfield, C. Karstens, T. Meyer, B. Smith, D. Speheger, J. Ladue, R. Smith, and T. Marshall, 2014: 20 May 2013 Moore, Oklahoma, tornado: Damage survey and analysis. *Wea. Forecasting*, **29**, 1229-1237.
- Chandrasekar, V., S. Lim, N. Bharadwaj, W. Li, D. McLaughlin, V. N. Bringi, and E. Gorgucci, 2004: Principles of networked weather radar operation at attenuating frequencies. *Proc. Third European Conf. on Radar Meteorology and Hydrology*, 109-114.
- Chen, F. and J. Dudhia, 2001: Coupling an Advanced Land Surface-Hydrology Model with the Penn State-NCAR MM5 Modeling System. Part I: Model Implementation and Sensitivity. *Mon. Wea. Rev.*, **129**, 569.
- Cintineo, R., J. A. Otkin, M. Xue, and F. Kong, 2014: Evaluating the Performance of Planetary Boundary Layer and Cloud Microphysical Parameterization Schemes in Convection-Permitting Ensemble Forecasts Using Synthetic GOES-13 Satellite Observations. *Mon. Wea. Rev.*, **142**, 163–182.
- Clark, A. J., W. A. Gallus, Jr., M. Xue, and F. Kong, 2009: A comparison of precipitation forecast skill between small convection-permitting and large convection-parameterizing ensembles. *Wea. Forecasting*, **24**, 1121-1140.
- Clark, A. J., S. J. Weiss, J. S. Kain, I. L. Jirak, M. Coniglio, C. J. Melick, C. Siewert, R. A. Sobash, P. T. Marsh, A. R. Dean, M. Xue, F. Kong, K. W. Thomas, Y. Wang, K. Brewster, J. Gao, X. Wang, J. Du, D. R. Novak, F. E. Barthold, M. J. Bodner, J. J. Levit, C. B. Entwistle, T. L. Jensen, and J. Correia, 2012: An Overview of the 2010 Hazardous Weather Testbed Experimental Forecast Program Spring Experiment. *Bulletin of the American Meteorological Society*, 10.1175/bams-d-11-00040.1.
- Crowe, C. C., C. J. Schultz, M. Kumjian, L. D. Carey, and W. A. Peterson, 2012: Use of dual-polarization signatures in diagnosing tornado potential. *Electron. J. Oper. Meteor.*, **13**, 57-78.
- Davis, C., B. Brown, and R. Bullock, 2006: Object-Based Verification of Precipitation Forecasts. Part II: Application to Convective Rain Systems. *Mon. Wea. Rev.*, **134**, 1785-1795.

- Dawson, D. T., II, M. Xue, and J. A. Milbrandt, 2009: High resolution real-data simulations of the 3 May 1999 tornadic storms with multi-moment microphysics, Under preparation.
- Dawson, D. T., II, L. J. Wicker, E. R. Mansell, and R. L. Tanamachi, 2012: Impact of the Environmental Low-Level Wind Profile on Ensemble Forecasts of the 4 May 2007 Greensburg, Kansas, Tornadic Storm and Associated Mesocyclones. *Mon. Wea. Rev.*, **140**, 696–716.
- Dawson, D. T., II, E. R. Mansell, Y. Jung, L. J. Wicker, M. R. Kumjian, and M. Xue, 2014: Low-level ZDR signatures in supercell forward flanks: The role of size sorting and melting of hail. *J. Atmos. Sci.*, **71**, 276-299.
- Doviak, R. and D. Zrnic, 1993: *Doppler Radar and Weather Observations*. 2nd ed. Academic Press, 562 pp.
- Dowell, D., F. Zhang, L. J. Wicker, C. Snyder, and N. A. Crook, 2004: Wind and temperature retrievals in the 17 May 1981 Arcadia, Oklahoma supercell: Ensemble Kalman filter experiments. *Mon. Wea. Rev.*, **132**, 1982-2005.
- Dowell, D. C. and L. J. Wicker, 2009: Additive noise for storm-scale ensemble data assimilation. *J. Atmos. Oceanic Technol.*, **26**, 911-927.
- Dowell, D. C., L. J. Wicker, and C. Snyder, 2011: Ensemble Kalman filter assimilation of radar observations of the 8 May 2003 Oklahoma City supercell: Influence of reflectivity observations on storm-scale analysis. *Mon. Wea. Rev.*, **139**, 272–294.
- Du, J., J. McQueen, G. DiMego, Z. Toth, D. Jovic, B. Zhou, and H. Chuang, 2006: New dimension of NCEP Short-Range Ensemble Forecasting (SREF) system: Inclusion of WRF members. *Preprint, WMO Expert Team Meeting on Ensemble Prediction System*, Exeter, UK, 5pp.
- Dudhia, J., 2011: State of physics parameterizations *NWP Workshop on Model Physics with an Emphasis on Short-Range Prediction* Camp Springs, MD.
- Ebert, E. E., 2001: Ability of a poor man's ensemble to predict the probability and distribution of precipitation. *Mon. Wea. Rev.*, **129**, 2461-2480.

- Ebert, E. E., 2008: Fuzzy verification of high-resolution gridded forecasts: A review and proposed framework. *Meteorological Applications*, **15**, 51-64.
- Ebert, E. E. and J. L. McBride, 2000: Verification of precipitation in weather systems: determination of systematic errors. *Journal of Hydrology*, **239**, 179–202.
- Evensen, G., 1994: Sequential data assimilation with a nonlinear quasi-geostrophic model using Monte Carlo methods to forecast error statistics. *J. Geophys. Res.*, **99**, 10143-10162.
- Evensen, G., 2003: The ensemble Kalman filter: Theoretical formulation and practical implementation. *Ocean Dynamics*, **53**, 343-367.
- Fritsch, J. M. and G. S. Forbes, 2001: Mesoscale convective systems. *Meteor. Monogr.*, **50**, 323-358.
- Gao, J.-D., M. Xue, K. Brewster, and K. K. Droegemeier, 2004: A three-dimensional variational data analysis method with recursive filter for Doppler radars. *J. Atmos. Ocean. Technol.*, **21**, 457-469.
- Gaspari, G. and S. E. Cohn, 1999: Construction of correlation functions in two and three dimensions. *Quart. J. Roy. Meteor. Soc.*, **125**, 723-757.
- Hodur, R. M., 1997: The Naval Research Laboratory's Coupled Ocean/Atmosphere Mesoscale Prediction System (COAMPS). *Mon. Wea. Rev.*, **125**, 1414-1430.
- Hong, S.-Y. and J.-O. J. Lim, 2006: The WRF single-moment 6-class microphysics scheme (WSM6). *J. Korean Meteor. Soc.*, **42**, 129-151.
- Hu, M., M. Xue, and K. Brewster, 2006a: 3DVAR and cloud analysis with WSR-88D level-II data for the prediction of Fort Worth tornadic thunderstorms. Part I: Cloud analysis and its impact. *Mon. Wea. Rev.*, **134**, 675-698.

- Hu, M., M. Xue, J. Gao, and K. Brewster, 2006b: 3DVAR and cloud analysis with WSR-88D level-II data for the prediction of Fort Worth tornadic thunderstorms. Part II: Impact of radial velocity analysis via 3DVAR. *Mon. Wea. Rev.*, **134**, 699-721.
- Janjic, Z., 2002: Nonsingular implementation of the Mellor–Yamada level 2.5 scheme in the NCEP Mesomodel. NCEP Office Note 437, NOAA/NWS, 61.
- Janjic, Z. I., 1994: The step-mountain eta coordinate model: Further developments of the convection, viscous sublayer, and turbulence closure schemes. *Mon. Wea. Rev.*, **122**, 927-945.
- Johnson, A., X. Wang, F. Kong, and M. Xue, 2013: Object-Based Evaluation of the Impact of Horizontal Grid Spacing on Convection-Allowing Forecasts. *Mon. Wea. Rev.*, **141**, 3413–3425.
- Johnson, M., Y. Jung, D. Dawson, and M. Xue, 2016a: Comparison of simulated polarimetric signatures in idealized supercell storms using two-moment bulk microphysics schemes in WRF. *Mon. Wea. Rev.*, **144**, 971-996.
- Johnson, M., Y. Jung, D. Dawson, and M. Xue, 2016b: Comparison of simulated polarimetric signatures in idealized supercell storms using two-moment bulk microphysics schemes in WRF. *Mon. Wea. Rev.*, **144**, 971–996.
- Jung, Y., G. Zhang, and M. Xue, 2008a: Assimilation of simulated polarimetric radar data for a convective storm using ensemble Kalman filter. Part I: Observation operators for reflectivity and polarimetric variables. *Mon. Wea. Rev.*, **136**, 2228-2245.
- Jung, Y., M. Xue, and G. Zhang, 2010: Simulations of polarimetric radar signatures of a supercell storm using a two-moment bulk microphysics scheme. *J. Appl. Meteor. Climatol.*, **49**, 146-163.
- Jung, Y., M. Xue, and M. Tong, 2012: Ensemble Kalman filter analyses of the 29-30 May 2004 Oklahoma tornadic thunderstorm using one- and two-moment bulk microphysics schemes, with verification against polarimetric data. *Mon. Wea. Rev.*, **140**, 1457-1475.

- Jung, Y., M. Xue, G. Zhang, and J. Straka, 2008b: Assimilation of simulated polarimetric radar data for a convective storm using ensemble Kalman filter. Part II: Impact of polarimetric data on storm analysis. *Mon. Wea. Rev.*, **136**, 2246-2260.
- Kain, J. S. and J. M. Fritsch, 1993: Convective parameterization for mesoscale models: The Kain-Fritsch scheme. *The Representation of Cumulus Convection in Numerical Models*, Meteor. Monogr., Amer. Meteor. Soc., 165-170.
- Kalnay, E., 2002: *Atmospheric Modeling, Data Assimilation, and Predictability*. Cambridge University Press, 341 pp.
- Kalnay, E., B. Hunt, E. Ott, and I. Szunyogh, 2006: Ensemble forecasting and data assimilation: two problems with the same solution? *Predictability of Weather and Climate*, T. Palmer and R. Hagedorn, Eds., Cambridge University Press, 734 pp.
- Kessler, E., 1969: *On the Distribution and Continuity of Water Substance in Atmospheric Circulations*. Vol. 32, Meteor. Monogr., 84 pp.
- Kong, F., 2010: 2010 CAPS Spring Forecast Experiment Program Plan, 14 pp.
- Kong, F., 2013: 2013 CAPS Spring Forecast Experiment Program Plan, 24 pp.
- Kong, F., M. Xue, D. Bright, M. C. Coniglio, K. W. Thomas, Y. Wang, D. Weber, J. S. Kain, S. J. Weiss, and J. Du, 2007: Preliminary analysis on the real-time storm-scale ensemble forecasts produced as a part of the NOAA hazardous weather testbed 2007 spring experiment. *22nd Conf. Wea. Anal. Forecasting/18th Conf. Num. Wea. Pred.*, Salt Lake City, Utah, Amer. Meteor. Soc., CDROM 3B.2.
- Kumjian, M. R. and A. V. Ryzhkov, 2008: Polarimetric signatures in supercell thunderstorms. *J. Appl. Meteor. Climatol.*, **47**, 1940-1961.
- Kumjian, M. R. and A. V. Ryzhkov, 2012: The Impact of Size Sorting on the Polarimetric Radar Variables. *J. Atmos. Sci.*, **69**, 2042-2060.

- Kurdzo, J. M., D. J. Bodine, B. L. Cheong, and R. D. Palmer, 2015: High-Temporal Resolution Polarimetric X-band Doppler Radar Observations of the 20 May 2013 Moore, Oklahoma, Tornado. *Mon. Wea. Rev.*, **143**, 2711-2735.
- Lakshmanan, V., A. Fritz, T. Smith, K. Hondl, and G. Stumpf, 2007: An Automated Technique to Quality Control Radar Reflectivity Data. *J. Appl. Meteor. Climatol.*, **46**, 288-305.
- Larson, V. E., J.-C. Golaz, H. Jiang, and W. R. Cotton, 2005: Supplying local microphysics parameterizations with information about subgrid variability: Latin hypercube sampling. *J. Atmos. Sci.*, **62**, 4010-4026.
- Lean, H. W., P. A. Clark, M. Dixon, N. M. Roberts, A. Fitch, R. Forbes, and C. Halliwell, 2008: Characteristics of High-Resolution Versions of the Met Office Unified Model for Forecasting Convection over the United Kingdom. *Mon. Wea. Rev.*, **136**, 3408-3424.
- Lei, T., M. Xue, and T. Yu, 2009: Multi-scale analysis and prediction of the 8 May 2003 Oklahoma City tornadic supercell storm assimilating radar and surface network data using EnKF. *Extended abstract, 13th Conf. of IOAS-AOLS, AMS Meetings 2008*, Paper 6.4.
- Li, X. and J. R. Mecikalski, 2012: Impact of the Dual-Polarization Doppler Radar Data on Two Convective Storms with a Warm-Rain Radar Forward Operator. *Mon. Wea. Rev.*, **140**, 2147-2167.
- Lim, K.-S. S. and S.-Y. Hong, 2010: Development of an Effective Double-Moment Cloud Microphysics Scheme with Prognostic Cloud Condensation Nuclei (CCN) for Weather and Climate Models. *Mon. Wea. Rev.*, **138**, 1587-1612.
- Lin, Y.-L., R. D. Farley, and H. D. Orville, 1983: Bulk parameterization of the snow field in a cloud model. *J. Climat. Appl. Meteor.*, **22**, 1065-1092.
- Lorenz, E. N., 1969: Atmospheric predictability as revealed by naturally occurring analogues. *J. Atmos. Sci.*, **26**, 636-646.
- Mahale, V., G. Zhang, and M. Xue, 2014: Fuzzy logic classification of S-band polarimetric radar echoes to identify three-body scattering and improve data quality. *J. Appl. Meteor. Clim.*, **53**, 2017-2033.

- Mansell, E. R., 2010: On Sedimentation and Advection in Multimoment Bulk Microphysics. *J. Atmos. Sci.*, **67**, 3084–3094.
- Mason, I. B., 1982: A model for the assessment of weather forecasts. *Aust. Meteor. Mag.*, **30**, 291-303.
- Mason, S. J. and N. E. Graham, 1999: Conditional probabilities, relative operating characteristics, and relative operating levels. *Wea. Forecasting*, **14**, 713-725.
- Maxwell-Garnett, J. C., 1904: Colors in metal glasses and in metallic films. *Philos. Trans. Roy. Soc. London*, **Ser. A**, 203.
- McLaughlin, D., D. Pepyne, V. Chandrasekar, B. Philips, J. Kurose, M. Zink, K. Droegemeier, S. Cruz-Pol, F. Junyent, J. Brotzge, D. Westbrook, N. Bharadwaj, Y. Wang, E. Lyons, K. Hondl, Y. Liu, E. Knapp, M. Xue, A. Hopf, K. Kloesel, A. DeFonzo, P. Kollias, K. Brewster, R. Contreras, B. Dolan, T. Djaferis, E. Insanic, S. Frasier, and F. Carr, 2009: Short-wavelength technology and the potential for distributed networks of small radar systems. *Bull. Amer. Meteor. Soc.*, **90**, 1797-1817.
- Mellor, G. L. and T. Yamada, 1982: Development of a turbulence closure model for geophysical fluid problems. *Rev. Geophys.*, **20**, 851-875.
- Milbrandt, J. A. and M. K. Yau, 2005a: A multi-moment bulk microphysics parameterization. Part I: Analysis of the role of the spectral shape parameter. *J. Atmos. Sci.*, **62**, 3051-3064.
- Milbrandt, J. A. and M. K. Yau, 2005b: A multi-moment bulk microphysics parameterization. Part II: A proposed three-moment closure and scheme description. *J. Atmos. Sci.*, **62**, 3065-3081.
- Mittermaier, M. and N. Roberts, 2010: Intercomparison of spatial forecast verification methods: Identifying skillful spatial scales using the fractions skill score. *Weather and Forecasting*, **25**, 343-354.

- Mittermaier, M., N. Roberts, and S. A. Thompson, 2013: A long-term assessment of precipitation forecast skill using the Fractions Skill Score. *Meteor. Appl.*, **20**, 176–186.
- Morrison, H., J. A. Curry, and V. I. Khvorostyanov, 2005: A new double-moment microphysics parameterization for application in cloud and climate models. Part I: Description. *J. Atmos. Sci.*, **62**, 1665–1677.
- Morrison, H., G. Thompson, and V. Tatarskii, 2009: Impact of cloud microphysics on the development of trailing stratiform precipitation in a simulated squall line: Comparison of one- and two-moment schemes. *Mon. Wea. Rev.*, **137**, 991–1007.
- NWS, cited 2012: Storm Data and Unusual Weather Phenomena - May 2007. [Available online from <http://www.srh.noaa.gov/media/oun/stormdata/oun200705.pdf>.]
- NWS, cited 2014: The Tornado Outbreak of May 20, 2013. [Available online from <http://www.srh.noaa.gov/oun/?n=events-20130520>.]
- NWS: Information About the May 10, 2010 Tornado Outbreak in Oklahoma. [Available online from <http://www.srh.noaa.gov/oun/?n=events-20100510>.]
- Palmer, R., D. Bodine, M. Kumjian, B. Cheong, G. Zhang, Q. Cao, H. Bluestein, A. Ryzhkov, T. Yu, and Y. Wang, 2011: Observations of the 10 May 2010 Tornado Outbreak Using OU-PRIME: Potential for New Science with High-Resolution Polarimetric Radar. *Bull. Amer. Meteor. Soc.*, **92**.
- Pan, Y., K. Zhu, M. Xue, X. Wang, M. Hu, S. G. Benjamin, S. S. Weygandt, and J. S. Whitaker, 2014: A regional GSI-based EnKF-variational hybrid data assimilation system for the Rapid Refresh configuration: Results with a single, reduced resolution. *Mon. Wea. Rev.*, **142**, 3756–3780.
- Park, H. S., A. V. Ryzhkov, D. S. Zrnić, and K.-E. Kim, 2009: The Hydrometeor Classification Algorithm for the Polarimetric WSR-88D: Description and Application to an MCS. *Wea. Forecasting*, **24**, 730–748.

- Pfeifer, M., G. C. Craig, M. Hagen, and C. Keil, 2008: A Polarimetric Radar Forward Operator for Model Evaluation. *J. Appl. Meteor. Climatol.*, **47**.
- Posselt, D. J., X. Li, S. A. Tushaus, and J. R. Mecikalski, 2015: Assimilation of dual-polarization radar observations in mixed- and ice-phase regions of convective storms: Information content and forward model errors. *Mon. Wea. Rev.*, **143**, 2611-2636.
- Putnam, B. J., M. Xue, Y. Jung, N. Snook, and G. Zhang, 2014: The Analysis and Prediction of Microphysical States and Polarimetric Radar Variables in a Mesoscale Convective System Using Double-Moment Microphysics, Multinetwork Radar Data, and the Ensemble Kalman Filter. *Mon. Wea. Rev.*, **142**, 141–162.
- Putnam, B. J., M. Xue, Y. Jung, G. Zhang, and F. Kong, 2016: Simulation of polarimetric radar variables from 2013 CAPS spring experiment storm scale ensemble forecasts and evaluation of microphysics schemes. *Mon. Wea. Rev.*, Conditionally accepted.
- Roberts, N., 2008: Assessing the spatial and temporal variation in the skill of precipitation forecasts from an NWP model. *Meteor. Appl.*, **15**, 163-169.
- Roberts, N. M. and H. W. Lean, 2008: Scale-selective verification of rainfall accumulations from high-resolution forecasts of convective events. *Mon. Wea. Rev.*, **136**, 78-97.
- ROC, N.: WSR-88D Dual Polarization Deployment Progress. [Available online from <http://www.roc.noaa.gov/WSR88D/PublicDocs/DualPol/DPstatus.pdf>.]
- Rogers, E., G. DiMego, T. Black, M. Ek, B. Ferrier, G. Gayno, Z. Janjic, Y. Lin, M. Pyle, V. Wong, W. S. Wu, and J. Carley, 2009: The NCEP North American Mesoscale Modeling System : Recent changes and future plans. *23rd Conference on Weather Analysis and Forecasting/19th Conference on Numerical Weather Prediction*, Omaha, NE, 2A.4.
- Romine, G. S., D. W. Burgess, and R. B. Wilhelmson, 2008: A Dual-Polarization-Radar-Based Assessment of the 8 May 2003 Oklahoma City Area Tornado Supercell. *Mon. Wea. Rev.*, **136**, 2849–2870.

- Rossa, A., P. Nurmi, and E. Ebert, 2008: Overview of methods for the verification of quantitative precipitation forecasts. *Precipitation: Advances in Measurement, Estimation and Prediction*, S. Michaelides, Ed., Springer, 540pp.
- Ryzhkov, A. and D. S. Zrnich, 1996: Assessment of rainfall measurement that uses specific differential phase. *J. Appl. Meteor.*, **35**, 2080–2090.
- Ryzhkov, A. V., S. E. Giangrande, V. M. Melnikov, and T. J. Schuur, 2005: Calibration issues of dual-polarization radar measurements. *J. Atmos. Ocean. Tech.*, **22**, 1138–1155.
- Schenkman, A., M. Xue, A. Shapiro, K. Brewster, and J. Gao, 2011: The analysis and prediction of the 8–9 May 2007 Oklahoma tornadic mesoscale convective system by assimilating WSR-88D and CASA radar data using 3DVAR. *Mon. Wea. Rev.*, **139**, 224–246.
- Schultz, P., 1995: An explicit cloud physics parameterization for operational numerical weather prediction. *Mon. Wea. Rev.*, **123**, 3331–3343.
- Schwartz, C., J. Kain, S. Weiss, M. Xue, D. Bright, F. Kong, K. Thomas, J. Levit, and M. Coniglio, 2009a: Next-day convection-allowing WRF model guidance: A second look at 2 vs. 4 km grid spacing. *Mon. Wea. Rev.*, **137**, 3351–3372.
- Schwartz, C. S., J. S. Kain, D. R. Bright, S. J. Weiss, M. Xue, F. Kong, J. J. Levit, M. C. Coniglio, and M. S. Wandishin, 2009b: Optimizing probabilistic high resolution ensemble guidance for hydrologic prediction. *Preprint, 23rd Conf. Hydrology*, Phoenix, AZ., Amer. Meteor. Soc., Paper 9.4.
- Skamarock, W. and Coauthors: A description of the Advanced Research WRF version 3. NCAR Tech. Note NCAR/TN-4751STR. [Available online from www.mmm.ucar.edu/wrf/users/docs/arw_v3.pdf.]
- Smith, T., V. Lakshmanan, G. Stumpf, K. Ortega, K. Hondl, K. Cooper, K. Calhoun, D. Kingfield, K. Manross, R. Toomey, and J. Brogden, 2016: Multi-radar Multi-sensor (MRMS) Severe Weather and Aviation Products: Initial Operating Capabilities. *Bull. Amer. Meteor. Soc.*, in press.

- Snook, N. and M. Xue, 2008: Effects of microphysical drop size distribution on tornadogenesis in supercell thunderstorms. *Geophys. Res. Letters*, **35**, L24803, doi:10.1029/2008GL035866.
- Snook, N., M. Xue, and J. Jung, 2011: Analysis of a tornadic mesoscale convective vortex based on ensemble Kalman filter assimilation of CASA X-band and WSR-88D radar data. *Mon. Wea. Rev.*, **139**, 3446-3468.
- Snook, N., M. Xue, and Y. Jung, 2012: Ensemble probabilistic forecasts of a tornadic mesoscale convective system from ensemble Kalman filter analyses using WSR-88D and CASA radar data. *Mon. Wea. Rev.*, 2126–2146.
- Snook, N., M. Xue, and Y. Jung, 2015: Multiscale EnKF Assimilation of Radar and Conventional Observations and Ensemble Forecasting for a Tornadic Mesoscale Convective System. *Mon. Wea. Rev.*, **143**, 1035–1057.
- Snook, N., Y. Jung, J. Brotzge, B. Putnam, and M. Xue, 2016: Prediction and ensemble forecast verification of hail in the supercell storms of 20 May 2013. *Wea. Forecasting*, Accepted.
- Snyder, C. and F. Zhang, 2003: Assimilation of simulated Doppler radar observations with an ensemble Kalman filter. *Mon. Wea. Rev.*, **131**, 1663-1677.
- SPC, cited 2014: SPC Filtered Storm Reports for 5/20/2013. [Available online from http://www.spc.noaa.gov/climo/reports/130520_rpts.html.]
- SPC, cited 2014: SPC Filtered Storm Reports for 5/19/2013. [Available online from http://www.spc.noaa.gov/climo/reports/130519_rpts.html.]
- SPC, cited 2016: SPC Filtered Storm Reports for 5/10/2010. [Available online from http://www.spc.noaa.gov/climo/reports/100510_rpts.html.]
- SPC, cited 2016: SPC Filtered Storm Reports for 5/20/2013. [Available online from http://www.spc.noaa.gov/climo/reports/130520_rpts.html.]

- Stensrud, D. J., M. Xue, L. J. Wicker, K. E. Kelleher, M. P. Foster, J. T. Schaefer, R. S. Schneider, S. G. Benjamin, S. S. Weygandt, J. T. Ferree, and J. P. Tuell, 2009: Convective-scale Warn on Forecast System: A Vision for 2020. *Bull. Am. Meteor. Soc.*, **90**, 1487-1499.
- Stensrud, D. J., L. J. Wicker, M. Xue, D. Dawson, N. Yussouf, D. Wheatley, T. E. Thompson, N. A. Snook, T. M. Smith, A. D. Schenkman, C. K. Potvin, E. R. Mansell, T. Lei, K. M. Kuhlman, Y. Jung, T. A. Jones, J. Gao, M. C. Coniglio, H. E. Brooks, and K. A. Brewster, 2013: Progress and challenges with Warn-on-Forecast. *Atmos. Res.*, **123**, 2-16.
- Sun, J. and N. A. Crook, 2001: Real-time low-level wind and temperature analysis using single WSR-88D data. *Wea. Forecasting*, **16**, 117-132.
- Tanamachi, R. L., L. J. Wicker, D. C. Dowell, H. B. Bluestein, D. T. Dawson, II., and M. Xue, 2013: EnKF Assimilation of High-Resolution, Mobile Doppler Radar Data of the 4 May 2007 Greensburg, Kansas, Supercell into a Numerical Cloud Model. *Mon. Wea. Rev.*, **141**, 625-648.
- Thompson, G., R. M. Rasmussen, and K. Manning, 2004: Explicit forecasts of winter precipitation using an improved bulk microphysics scheme. Part I: Description and sensitivity analysis. *Mon. Wea. Rev.*, **132**, 519-542.
- Thompson, G., P. R. Field, R. M. Rasmussen, and W. D. Hall, 2008: Explicit forecasts of winter precipitation using an improved bulk microphysics scheme. Part II: Implementation of a new snow parameterization. *Mon. Wea. Rev.*, **136**, 5095-5115.
- Tong, M. and M. Xue, 2005: Ensemble Kalman filter assimilation of Doppler radar data with a compressible nonhydrostatic model: OSS Experiments. *Mon. Wea. Rev.*, **133**, 1789-1807.
- Tong, M. and M. Xue, 2008: Simultaneous estimation of microphysical parameters and atmospheric state with radar data and ensemble square-root Kalman filter. Part I: Sensitivity analysis and parameter identifiability. *Mon. Wea. Rev.*, **136**, 1630-1648.

- Ulbrich, C. W., 1983: Natural variations in the analytical form of the raindrop size distributions. *J. Appl. Meteor.*, **22**, 1764-1775.
- Van Weverberg, K., A. M. Vogelmann, H. Morrison, and J. A. Milbrandt, 2012: Sensitivity of idealized squall-line simulations to the level of complexity used in two-moment bulk microphysics schemes. *Mon. Wea. Rev.*, **140**, 1883-1907.
- Vivekanandan, J., W. M. Adams, and V. N. Bringi, 1991: Rigorous Approach to Polarimetric Radar Modeling of Hydrometeor Orientation Distributions. *J. Appl. Meteor.*, **30**, 1053–1063.
- Wacker, U. and A. Seifert, 2001: Evolution of rain water profiles resulting from pure sedimentation: spectral vs. parameterized description. *Atmos. Res.*, **58**, 19-39.
- Wang, H., T. Auligne, and H. Morrison, 2012: Impact of Microphysics Scheme Complexity on the Propagation of Initial Perturbations. *Mon. Wea. Rev.*, **140**, 2287-2296.
- Wang, S., M. Xue, and J. Min, 2016: Four-dimensional ensemble square-root filter (4DEnSRF) and comparison to 3DEnSRF for the analysis and prediction of the 10 May 2010 central Oklahoma tornadic supercell storm. *Quarterly Journal of the Royal Meteorological Society*, Under review.
- Weiss, S. J., J. S. Kain, D. R. Bright, J. J. Levit, G. W. Carbin, M. E. Pyle, Z. I. Janjic, B. S. Ferrier, J. Du, M. L. Weisman, and M. Xue, 2007: The NOAA Hazardous Weather Testbed: Collaborative testing of ensemble and convection-allowing WRF models and subsequent transfer to operations at the Storm Prediction Center. *22nd Conf. Wea. Anal. Forecasting/18th Conf. Num. Wea. Pred.*, Salt Lake City, Utah, Amer. Meteor. Soc., CDROM 6B.4.
- Wheatley, D. M., N. Yussouf, and D. J. Stensrud, 2014: Ensemble Kalman Filter Analyses and Forecasts of a Severe Mesoscale Convective System Using Different Choices of Microphysics Schemes. *Monthly Weather Review*, **142**, 3243-3263.
- Whitaker, J. S. and T. M. Hamill, 2002: Ensemble data assimilation without perturbed observations. *Mon. Wea. Rev.*, **130**, 1913-1924.

- Whitaker, J. S. and T. M. Hamill, 2012: Evaluating Methods to Account for System Errors in Ensemble Data Assimilation. *Mon. Wea. Rev.*, **140**.
- Xue, M., K. K. Droegemeier, and V. Wong, 2000: The Advanced Regional Prediction System (ARPS) - A multiscale nonhydrostatic atmospheric simulation and prediction tool. Part I: Model dynamics and verification. *Meteor. Atmos. Physics*, **75**, 161-193.
- Xue, M., M. Tong, and K. K. Droegemeier, 2006: An OSSE framework based on the ensemble square-root Kalman filter for evaluating impact of data from radar networks on thunderstorm analysis and forecast. *J. Atmos. Ocean Tech.*, **23**, 46–66.
- Xue, M., Y. Jung, and G. Zhang, 2010: State estimation of convective storms with a two-moment microphysics scheme and an ensemble Kalman filter: Experiments with simulated radar data *Q. J. Roy. Meteor. Soc.*, **136**, 685-700.
- Xue, M., D.-H. Wang, J.-D. Gao, K. Brewster, and K. K. Droegemeier, 2003: The Advanced Regional Prediction System (ARPS), storm-scale numerical weather prediction and data assimilation. *Meteor. Atmos. Physics*, **82**, 139-170.
- Xue, M., F. Kong, K. W. Thomas, J. Gao, Y. Wang, K. Brewster, and K. K. Droegemeier, 2013: Prediction of Convective Storms at Convection-Resolving 1 km Resolution over Continental United States with Radar Data Assimilation: An Example Case of 26 May 2008 and Precipitation Forecasts from Spring 2009. *Advances in Meteorology*, **2013**, 9.
- Xue, M., K. K. Droegemeier, V. Wong, A. Shapiro, K. Brewster, F. Carr, D. Weber, Y. Liu, and D.-H. Wang, 2001: The Advanced Regional Prediction System (ARPS) - A multiscale nonhydrostatic atmospheric simulation and prediction tool. Part II: Model physics and applications. *Meteor. Atmos. Phys.*, **76**, 143-165.
- Xue, M., F. Kong, D. Weber, K. W. Thomas, Y. Wang, K. Brewster, K. K. Droegemeier, J. S. K. S. J. Weiss, D. R. Bright, M. S. Wandishin, M. C. Coniglio, and J. Du, 2007: CAPS realtime storm-scale ensemble and high-resolution forecasts as part of the NOAA Hazardous Weather Testbed 2007 spring experiment. *22nd Conf. Wea. Anal. Forecasting/18th Conf. Num. Wea. Pred.*, Amer. Meteor. Soc., CDROM 3B.1.

- Yussouf, N., J. Kain, and A. Clark, 2016: Short-term Probabilistic Forecasts of the 31 May 2013 Oklahoma Tornado and Flash Flood Event Using a Continuous-Update-Cycle Storm-scale Ensemble System. *Wea. Forecasting*, in press.
- Yussouf, N., E. R. Mansell, L. J. Wicker, D. M. Wheatley, and D. J. Stensrud, 2013: The Ensemble Kalman Filter Analyses and Forecasts of the 8 May 2003 Oklahoma City Tornado Supercell Storm using Single and Double Moment Microphysics Schemes. *Mon. Wea. Rev.*, **141**, 3388-3412.
- Yussouf, N., D. C. Dowell, L. J. Wicker, K. H. Knopfmeier, and D. M. Wheatley, 2015: Storm-Scale Data Assimilation and Ensemble Forecasts for the 27 April 2011 Severe Weather Outbreak in Alabama. *Mon. Wea. Rev.*, **143**, 3044–3066.
- Zhang, F., C. Snyder, and J. Sun, 2004: Impacts of initial estimate and observations on the convective-scale data assimilation with an ensemble Kalman filter. *Mon. Wea. Rev.*, **132**, 1238-1253.
- Zhang, G., J. Vivekanandan, and E. Brandes, 2001: A method for estimating rain rate and drop size distribution from polarimetric radar measurements. *IEEE Trans. Geosci. Remote Sens.*, **39**, 830-841.
- Zhang, G., M. Xue, Q. Cao, and D. Dawson, 2008: Diagnosing the intercept parameter for exponential raindrop size distribution based on video disdrometer observations. *J. Appl. Meteor. Climatol.*, **47**, 2983-2992.
- Zhang, Y., F. Zhang, D. J. Stensrud, and Z. Meng, 2015: Practical Predictability of the 20 May 2013 Tornadic Thunderstorm Event in Oklahoma: Sensitivity to Synoptic Timing and Topographical Influence. *Mon. Wea. Rev.*, **143**, 2973-2997.
- Zhu, K. F., Y. Yang, and M. Xue, 2015: Percentile-based neighborhood precipitation verification and its application to a landfalling tropical storm case with radar data assimilation. *Adv. Atmos. Sci.*, **32**, 1449-1459.

Appendix A Example Calculation of Forward Operator for Polarimetric Radar Observation Assimilation

An example of the modified operators using pre-calculated look-up tables is presented here. The Z_H calculation for rain is considered:

$$Z_{hh} = \frac{4\lambda^4}{\pi^4 |K_w|^2} \int (A |f_a(\pi)|^2 + B |f_b(\pi)|^2 + 2C f_a(\pi) f_b(\pi)^*) N(D) dD, \quad (A1)$$

where Z_{hh} is the horizontal radar reflectivity factor, λ is the wavelength of the radar, K_w is the dielectric factor for water, A , B , and C , include the canting angle of rain, $f_a(\pi)$ is the backscattering amplitude along the major axis, $f_b(\pi)$ is the complex backscattering amplitude along the minor axis, $f_b(\pi)^*$ is the complex conjugate of the backscattering amplitude along the minor axis, and $N(D)dD$ is the drop size distribution for rain. For rain, the mean and standard deviation of the canting angle is assumed to be 0 which leaves a simplified expression:

$$Z_{hh} = \frac{4\lambda^4}{\pi^4 |K_w|^2} \int |f_a(\pi)|^2 N(D) dD. \quad (A2)$$

The simplified gamma form of the drop size distribution:

$$N_0 D^\alpha e^{-\Lambda D} dD, \quad (A3)$$

where N_0 is the intercept parameter, α is the shape parameter, and Λ is the slope parameter, is substituted in which yields:

$$Z_{hh} = \frac{4\lambda^4}{\pi^4 |K_w|^2} \int |f_a(\pi)|^2 N_0 D^\alpha e^{-\Lambda D} dD. \quad (A4)$$

In Jung et al. (2008a), a fitted approximation to the T-matrix scattering amplitudes is used, and a power law function is used in place of $|f_a(\pi)|$. The diameters in the resulting expression can be combined and the expression can easily solved analytically.

In the Jung et al (2010) case, the equation is solved numerically by a summation over a

range of drop diameters in the PSD and associated scattering amplitudes represented by $|f_a(\pi)|^2$. As originally implemented, the reflectivity factor would then be computed by a summation over the range of possible rain diameters (100 in total):

$$Z_{hh} = \frac{4\lambda^4}{\pi^4 |K_w|^2} \sum_{i=1}^{100} |f_a(\pi)|^2 N_0 D^\alpha e^{-\Lambda D} dD . \quad (\text{A5})$$

This summation requires a double loop because both the drop size distribution and scattering amplitude are a function of diameter. A portion of this calculation is completed and stored ahead of time for fast access during assimilation. Since N_0 is not dependent on diameter, it can be removed from the summation:

$$Z_{hh} = \frac{4\lambda^4}{\pi^4 |K_w|^2} N_0 \sum_{i=1}^{100} |f_a(\pi)|^2 D^\alpha e^{-\Lambda D} dD . \quad (\text{A6})$$

The remaining summation is calculated and stored before assimilation. The pre-calculated tables are based on a range of values for Λ and α . For simplicity, the precalculated portion of the equation will be referred to by S , which is a function of Λ and α :

$$Z_{hh} = \frac{4\lambda^4}{\pi^4 |K_w|^2} N_0 S(\Lambda_i, \alpha_i). \quad (\text{A7})$$

As an example, in this experiment, a typical value of Λ would be 2000.0 m^{-1} and a α of 0. Prior to assimilation, the S has been calculated with a lambda value of at or near 2000.0 and stored. During assimilation, Λ is calculated based on the predicted microphysical state variables rain mixing ratio q_r and number concentration N_{tr} :

$$\Lambda_m = \frac{\pi \rho_w N_{tr} \Gamma(4)^{\frac{1}{3}}}{6 \rho_{air} q_r} , \quad (\text{A8})$$

where Λ_m will stand for the Λ calculated in the model during assimilation. The list of Λ_i for which S is calculated are at a constant interval so it simply requires the calculated

Λ_m to be divided by the known interval to find the table index containing the associated S value:

$$Z_{hh} = \frac{4\lambda^4}{\pi^4 |K_w|^2} N_0 S(\Lambda_m). \quad (\text{A9})$$

If the calculated Λ_m is between two of the Λ_i list values for S , then the result used is a linear interpolation between S for the Λ_i list values above and below Λ_m .